Measurement of the Timelike Electromagnetic Form Factors of the Proton at the BESIII Experiment through the Process $e^+e^- \to p\bar{p}$

Dissertation
zur Erlangung des Grades
"Doktor der Naturwissenschaften"

am Fachbereich Physik, Mathematik und Informatik
der Johannes Gutenberg-Universität Mainz

von

Christoph Rosner
geb. in München, Deutschland

Mainz, den 18. 3. 2021

Abstract

The proton, despite being one of the most important building blocks of matter in the universe, is still poorly understood in terms of its quark and gluonic structure and internal dynamics. To achieve a deeper understanding of these fundamental properties of the proton is one of the most important and challenging goals of modern nuclear physics. In the scope of this work, one of the accessible quantities that parametrises the structure and internal dynamics of the proton, the electromagnetic form factors, are measured in the timelike region with unprecedented accuracy using data taken at the BESIII experiment primarily in 2015.

Within this thesis, the process $e^+e^- \to p\bar{p}$ is investigated with the scan technique for the first time, using a dataset with a total integrated luminosity of 688.5 pb^{-1}. The Born cross section of the process is measured over the full energy range of this dataset between 2.0 and 3.08 GeV at 22 energy points, achieving a total uncertainty on the level of a few percent, dominated by the systematic uncertainty. The effective form factor of the proton is extracted from this measured cross section to allow for a comparison with older experiments. The measurement presented here is in good agreement with these previous results while achieving an improved precision. An oscillating behaviour observed in the effective form factor in previous experiments is confirmed for a part of the energy range (2.0 - 2.5 GeV) of the measurement of this work.
The main purpose of the dedicated scan dataset taken in 2015 at BESIII, the separate extraction of the individual magnetic ($|G_M|$) and electric ($|G_E|$) timelike form factors of the proton, has been achieved through the performance of an angular analysis of the data at 16 center of mass energy points. The precision of this measurement reaches a level which is comparable to results obtained in the spacelike region for the first time. Results for $|G_M|$ are in agreement with the few existing previous measurements with vastly improved accuracy, while $|G_E|$ is measured separately for the first time. The extracted ratio R=$|G_E/G_M|$ of the two form factors helps to clear up a long-standing discrepancy of the previous results from the PS170 (proton-antiproton annihilation) and BaBar (electron positron annihilation) experiments, in favour of the latter.

The results of this work significantly improve our understanding of the proton structure and dynamics within the picture of the strong interaction. The first time measurement of $|G_E|$ as well as the improved precision of existing measurements of the electromagnetic form factors in the timelike region will allow the development of new theoretical models as well as the verification (or falsification) and improvement of existing ones.

Zusammenfassung

Obwohl das Proton zu den wichtigsten Bausteinen gehört, aus denen die Materie in unserem Universum zusammengesetzt ist, ist es bis heute im Bezug auf seine Gluon- und Quark-Struktur wenig verstanden. Diese fundamentalen Eigenschaften des Protons besser zu verstehen gehört zu den wichtigsten und herausforderndsten Zielen der modernen Kernphysik. Im Rahmen dieser Arbeit wurde mit den Elektomagnetischen Formfaktoren eine der messbaren Größen, die die Struktur und innere Dynamik des Protons beschreibt, mit bisher unerreichter Präzision gemessen, indem im Jahr 2015 am BESIII Experiment erhobene Daten ausgewertet wurden.

In dieser Arbeit wurde der Prozess $e^+e^- \to p\bar{p}$ unter Verwendung von Daten mit einer integrierten Luminosität von 688.5 pb^{-1} zum ersten Mal mit Hilfe der Scan-Techik analysiert. Der Born Wirkungsquerschnitt des Prozesses wurde für alle Schwerpunktsenergien des Datensatzes zwischen 2.0 und 3.08 GeV bestimmt, wobei die erzielte Unsicherheit auf einem Niveau von wenigen Prozent liegt und von der systematischen Unsicherheit dominiert wird. Der effektive Formfaktor des Protons wurde aus diesem Wirkungsquerschnitt ermittelt, um einen Vergleich mit älteren Experimenten zu ermöglichen. Die Ergebnisse dieser Arbeit sind dabei gut vereinbar mit vorigen Messungen dieser Größen, allerdings mit deutlich höherer Präzision. Zuvor beobachtete Oszillationen des effektiven Formfaktors konnten für einen Teil der Schwerpunktsenergien des Datensatzes (2.0 - 2.5 GeV) bestätigt werden.

Mit der individuellen Bestimmung des magnetischen ($|G_M|$) und elektrischen ($|G_E|$) Formfaktors des Protons konnte das wichtigste Ziel, für welches der Datensatz von 2015 am BESIII Experiment erhoben wurde, erreicht werden. Die Formfaktoren wurden dabei mit Hilfe einer Winkelanalyse bei 16 Schwerpunktsenergien extrahiert, bei denen genügend Ereignisse des Signalprozesses erzeugt wurden. Die Präzision dieser Messung im Bereich zeitartiger Impulsüberträge erreicht dabei erstmals ein Niveau, welches mit dem von Ergebnissen im Bereich raumartiger Impulsüberträge vergleichbar ist. Die Messung von $|G_M|$ stimmt bei stark verbesserter Präzision mit Resultaten voriger Experimente überein, während $|G_E|$ zum ersten Mal separat bestimmt wurde. Das im Rahmen dieser Arbeit ermittelte Verhältnis der beiden Formfaktoren (R=$|G_E/G_M|$) kann dabei helfen, Unstimmigkeiten zwischen Ergebnissen aus dem PS170 (Proton-Antiproton Paarvernichtung) und BaBar Experiments (Elektron Positron Paarvernichtung) aufzuklären.

Die im Zuge dieser Arbeit erzielten Resultate verbessern unser Verständnis der Struktur und inneren Dynamik des Protons im Rahmen der starken Wechselwirkung signifikant. Die erstmalige Messung von $|G_E|$ sowie die deutlich erhöhte Präzision in der Messung von R und $|G_M|$ im Bereich zeitartiger Impulsüberträge wird die Entwicklung neuer theoretischer Modelle, welche die Struktur des Protons beschreiben, vorantreiben und die Bestätigung (oder Widerlegung) sowie Verbesserung existierender Modelle erlauben.

Contents

Chapter 1

Introduction

Modern physics explains the physical world of matter that we live in as an interaction between elementary particles and fundamental forces, which have mainly been discovered over the course of the last century. Elementary particles, under the influence of these fundamental forces, form bound states from microscopic scales (nucleons, atoms, molecules...) up to macroscopic scales (star systems, galaxies, galaxy clusters, black holes...).

One such bound system is the proton, one of the two nucleons along with the neutron that form the atomic nuclei of all known elements of the periodic system, and therefore make up most of the mass of the visible matter in the universe. In the simple picture described above, the proton results from the interaction between three elementary up and down quarks through the strong force, mediated by gluons. In isolation, the proton is the only known stable configuration of quarks and gluons and as such, its internal structure and the dynamics between its valance quarks, sea quarks and gluons have been the subject of intense investigations during the last 100 years.

Many questions remain unanswered: is the proton really stable, or has it a long yet finite lifetime? How does its spin originate from its constituents? One of its basic features, the radius of the proton, has recently gained a lot of attention due to new results from muonic hydrogen measurements contradicting earlier results from electron-proton scattering (see proton radius puzzle). Also in current scientific discussion, a lot of attention has been cast on the fact that only a small portion of matter in the universe is accounted for, while the largest part of the mass comes from yet unknown dark matter. However, the origin of a large part of the mass of the known matter in nucleons is also not yet fully understood. While the recently discovered Higgs boson is said to give mass to the elementary particles such as quarks, which are the constituents of the proton, the mass of these constituents only accounts for a few percent of the total proton mass. The remainder of the mass originates from the interaction of its components through the

strong force, for example by building a sea of short-lived quark-antiquark pairs, or the kinetic energy of the quarks that are confined by the strong force. To better understand that mechanism, a deeper insight into the structure and internal dynamics of the proton is crucial.

Among the measurable quantities which describe the structure and dynamics of the proton are the electromagnetic form factors (EM FFs). They represent parametrisations of the charge and magnetisation distributions within the nucleon, and can be measured in two separate regions: the timelike (TL) and spacelike (SL) region. The easiest experimental access to these observables is the electromagnetic probe, in the case of the SL region through elastic electron-nucleon scattering and in the TL region through annihilation experiments, such as electron-positron annihilation or proton-antiproton annihilation. While the former region has been investigated in numerous experiments since the 1950s and data about the SL EM FFs of the proton is fairly accurate, knowledge about the TL EM FFs is rather scarce. Results have been extracted on an effective FF, which is based on certain assumptions, but the individual electric and magnetic FF have not been measured yet, since their extraction requires data sets with high luminosity to perform an analysis of the angular distribution of the outgoing nucleons (or leptons in the time-reverse channel) and simultaneously a precise measurement of the luminosity. So far, only the ratio of the two FFs has been extracted with high uncertainties and partially contradicting results.

The data set analysed in this thesis was collected specifically to change this situation for the proton EM FFs of the TL region, as well as measure the FFs of other baryons such as neutrons and Lambda baryons. Unlike previous measurements at the BaBar experiment or BESIII which have been performed through the use of the initial state radiation technique (for details see section 2.3.2) on existing data sets taken for other purposes, the one presented here is based on a scan data set collected by the BESIII collaboration in 2015 with an integrated luminosity of 651.09 pb^{-1} which was obtained with the main purpose of extracting baryon EM FFs. Additional data taken during a previous scan in 2012 was merged with said dataset for a total luminosity of 688.5 pb^{-1}. The dataset of 2015 was taken in form of a discrete scan at 22 energy points between 2.0 and 3.08 GeV, which means a coarser energy cover compared to the continuous initial state radiation measurements. However, the very high luminosity at each scan point combined with a precise luminosity measurement based on the analysis of large angle Bhabha scattering events allows an extraction of the individual electric and magnetic FF with unprecedented accuracy. This extraction through a careful analysis of the data set described above is the main subject of this thesis and will be discussed in the following chapters.

The description of the experimental setup at the BESIII experiment, the analysis of the data, and the underlying theory in this thesis is divided in 12 chapters. Following is an overview of the different chapters and the topics they cover. Here, chapters that mainly describe my own work (chapters 6-12 and partially chapter 5) are marked in red, while chapters that are provided to better understand the basis of this work such as the experimental setup and theoretical background (chapters 2, 3, 4 and partially 5) are marked in blue. The content of these chapters mainly comprises a summary and condensation of the references quoted therein.

Chapter 2: This chapter describes the theoretical foundations, first in form of a short introduction to the standard model and then in an overview over the theory and theoretical models of nucleon EM FFs. In addition, the experimental side of the determination of nucleon EM FFs is covered by reviewing the available experimental methods as well as the current situation of performed measurements in both the SL and the TL region.

Chapter 3: This chapter describes the experimental setup of the BESIII detector at the BEPCII collider, where the data analysed in this thesis was collected, including a brief discussion about each subdetector and their most important specifications.

Chapter 4: Here, the available data sets of the BESIII experiment are introduced, including the high luminosity scan data set taken in 2015 between 2.0 and 3.08 GeV on which this work is based on.

Chapter 5: (1) The first part of this chapter gives a short introduction to the architecture of the software framework BOSS that was used in the analysis of data in this work as well as the generation of Monte Carlo samples. The most relevant Monte Carlo event generators used for the simulation of signal and background events are briefly described as well. (2) The second part of the chapter gives an overview of the generated Monte Carlo samples for the analysis of this work for both signal and background processes.

Chapter 6: Here, the event selection for the signal process $e^+e^- \to p\bar{p}$ is described and the results for the number of selected events are given for each data sample.

Chapter 7: This chapter covers an in-depth discussion of the performed background evaluation to the signal process using two independent evaluation methods.

Chapter 8: This chapter describes the determination of the cross section of the process $e^+e^- \to p\bar{p}$ after applying radiative and efficiency corrections to the selected events with signal Monte Carlo samples.

Chapter 9: The extraction of the individual EM FFs of the proton is described in this chapter via an angular analysis of the data after a differential radiative and efficiency correction using the same signal Monte Carlo samples.

Chapter 10: This chapter presents an evaluation of different sources for systematic errors for all extracted quantities that are presented in this thesis.

Chapter 11: Chapter 11 presents the final results of this work for the $e^+e^- \to p\bar{p}$ Born cross section, effective, magnetic and electric FFs as well as the ratio between the electric and magnetic FF including statistical and systematic uncertainties. The presented results are then compared and put into perspective with results of previous measurements.

Chapter 12: The final chapter of this work discusses the results presented in chapter 11 and compares them to the predictions of several theoretical approaches. Interesting phenomena such as an oscillating behaviour in the effective and individual EM FFs of the proton are investigated, before a final summary and conclusion is given.

Chapter 2

Electromagnetic Form Factors of the Nucleon

Within this chapter, the theoretical fundamentals necessary to understand the content of the following chapters are covered. At first, a brief introduction is given in section 2.1 about the so called standard model, which is the basis of all modern particle physics. Section 2.2 then gives a more specific introduction to nucleon structure investigations and the underlying theory of EM FFs of the nucleon. An overview of the current experimental situation for the different regions where the EM FFs can be explored is given in section 2.3, and the final section 2.4 of this chapter covers different theoretical approaches to the description of the nucleon EM FFs.

2.1 The standard model of particle physics

Physics as one of the oldest academic disciplines always had the ultimate goal to find an inclusive description of nature, and therefore mostly matter and the forces interacting with it. On their quest to find such a description, physicists have discovered ever smaller constituents of matter which they thought fundamental, but ultimately turned out to be divisible, consisting of even smaller parts. While the idea of a smallest, fundamental constituents of matter dates back to the old Greek philosophers Leuicippus and Democritus (5th century BC), who believed matter to be made up of *atomos* (uncuttable), the concept stayed controversial until the end of the 19th century, with prominent sceptics such as Ernst Mach. Only in the 20th century, the discovery of various particles which are, up to our knowledge today, elementary, established the view of matter being comprised of universal elementary parts as the doctrinal opinion.

The particles which we believe to be fundamental today can be divided into two categories: fundamental fermions as the constituents of matter, and fundamental bosons such as gauge bosons and the Higgs bosons as the carriers of interactions (forces). The constituent fermions in turn can be further divided into two categories: leptons, such as electrons and neutrinos, and quarks, which make up mesons and hadrons (e. g. proton and neutron). In modern physics, these elementary particles and the interactions between them are classified in the so called standard model of particle physics. The standard model was developed in the latter half of the 20th century and received its final formulation in the mid 70s. Features already predicted in this formulation, such as the top quark [1] or the Higgs boson [2, 3], have later been found experimentally, in the case of the Higgs boson in 2012 at CERN, which proves the predictive power of the model.

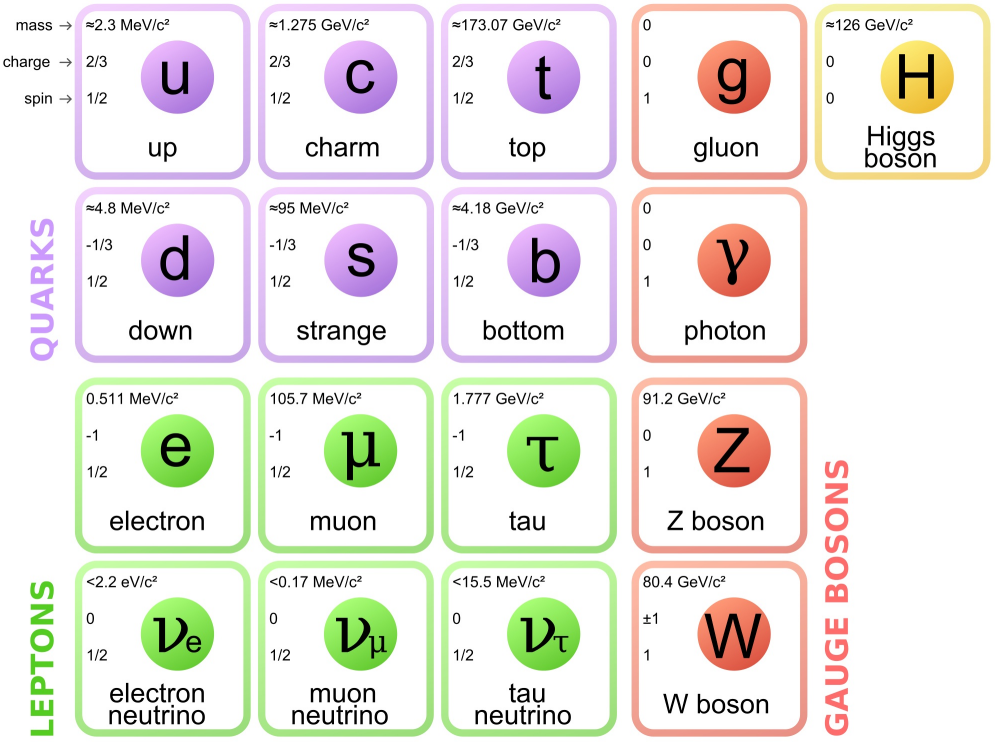

FIGURE 2.1: Overview of the elementary particles of the standard model. Column 1-3 show the three generations of fermions, column 4 the gauge bosons and column 5 the Higgs boson. Image taken from reference [4]

Figure 2.1 shows the different elements of the standard model: There are twelve elemental fermions with spin 1/2, each six quarks and six leptons, which are grouped into 3 generations based on their mass. All known stable matter in the universe is comprised of particles of the first generation, particles of higher generations (except neutrinos) eventually decay into particles of the first generation. All twelve particles have a corresponding anti-particle, which has the same mass but opposite charges and handedness.

The twelve fundamental leptons each carry different amounts and types of charges. These charges determine which gauge bosons they interact with and therefore which forces they are subjected to. Neutrinos as the weakest interacting fermions only carry weak charge, which means they only interact through the weak force mediated by W and Z bosons. They come in three flavours as electron (ν_e), muon (ν_μ) and tau (ν_τ) neutrino, and have very low, yet non-zero masses, which is known due to phenomena such as the oscillation between different neutrino flavours. To date, only upper limits of neutrino masses are known. Their corresponding charged partners, Electrons, muons and tauons, additionally carry (integer) electric charge and consequently also interact through the electromagnetic force mediated by photons. Finally, quarks carry the so called color charge in addition to fractional electric and weak charge, which allows them to interact with gluons, the gauge bosons mediating the strong force. They come in six different flavours as up (u), down (d), strange (s), charm (c), bottom (b) and top (t) quarks.

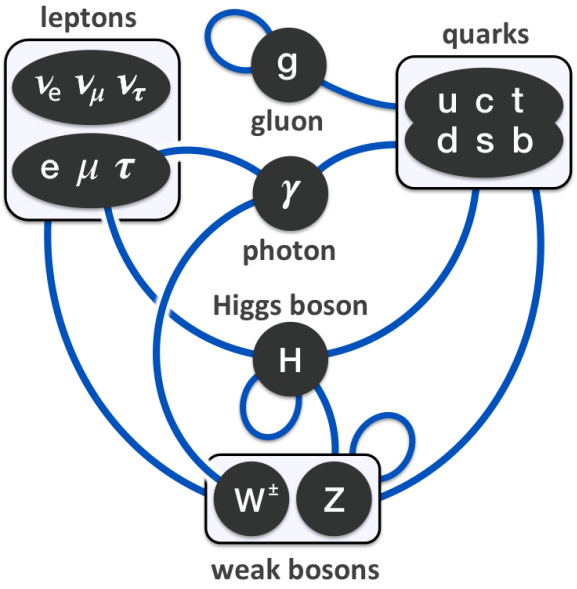

FIGURE 2.2: Illustration of the possible interactions between the fundamental particles described in the standard model, taken from reference [5]

Apart from the different fundamental fermions they affect, the three fundamental forces included in the standard model are distinguished by different characteristics. The weak force, which amongst other things plays a role in radioactive decays, is as the name suggests the weakest of these forces with a relative interaction strength compared to the strong force of approximately 10^{-6}. It also has a very low interaction length of about 10^{-18} meters due to the large mass of its mediating bosons ($m_Z \simeq 91.19 GeV$, $m_W \simeq 80.38 GeV$ [6]), which according to Heisenberg's uncertainty principle only allows them to exist for a very short time as intermediate particles. The electromagnetic

force is next in line in relative strength compared to the strong force, with a factor of $\alpha = 1/137$ (fine-structure constant) between them. Since the photon as its mediator is massless, the theoretical range of the interaction is infinite. Finally, the strong force as the strongest fundamental interaction has a few particularities. While the 8 types of gluons mediating the strong force are, like the photon, massless, and would therefore allow an infinite range of the strong interaction, they carry a color charge themselves unlike the electrically neutral photon. Gluons are thus able to strongly interact among themselves (self-coupling). Due to this phenomenon, the energy contained in the gluon field at distances above ~ 1 fm is high enough to generate new quark-antiquark pairs , a process known as hadronisation. This also leads to the so called color confinement, meaning that coloured particles such as quarks and gluons can not be isolated and instead clump together to form hadrons. Any free particle must be color neutral in the sense that it either contains all three color charges (red, green, blue) of the same strength, or the same amount of color charge and its corresponding anti-color charge (anti-red, anti-green, anti-blue).

TABLE 2.1: Summary of the four fundamental interactions of nature.

Interaction	Gravitation	Weak	Electro-magnetic	Strong
couples to	mass	weak charge	electric charge	color charge
Affected particles	all	quarks, leptons	quarks, leptons (except neutrinos)	quarks, gluons
Mediators	gravitons (hypothetical)	W, Z bosons	photons	gluons
relative strength	$\sim 10^{-38}$	$\sim 10^{-6}$	1/137	1
range [m]	∞	$\sim 10^{-18}$	∞	$\sim 10^{-15}$
current theory	General relativity (GR)	Electroweak Theory (EWT)	Quantum electrodynamics (QED)	Quantum chromodynamics (QCD)

The fourth known force of nature, the gravitation, is not yet included in the standard model. Due to its very low relative strength of about 10^{-38} compared to the strong force (and still 10^{-29} compared to the weak force), it does not play a significant role in microscopic interactions on the scale of atoms or nucleons. However, its infinite range and the fact that stable matter is, seen from a long distance, mostly electrically neutral makes it the governing force of macroscopic interactions for example between celestial bodies or galaxies. The unification of gravitational theory with the other three forces (or two, considering the successful unification of the electric and weak force) in the form

of a quantum gravity theory to a "theory of everything" is one of the most important goals of modern physics.
Currently, no such Grand Unified Theory (GUT) exists yet, therefore the interactions are each described by their own theories. In case of the electromagnetic force, the current theory is Quantum Electrodynamics (QED). The weak force is described by the Quantum Flavourdynamics (QFT), however due to its unification with the electromagnetic force, this theory is rarely used. Instead, the weak force is better understood through their common theory, the Electroweak Theory (EWT). Gravitation is up to today still best described through the General Relativity (GR), since as mentioned a quantum theory is not yet found. Finally, the current theory of the strong force is Quantum Chromodynamics (QCD), which will be treated in more detail in the next section.

The standard model in its current formulation has already been extremely successful in both the description of nature as well as the prediction of new phenomena. While it has not been falsified until today, there are still open questions and problems which the standard model has no answers to. For example, it requires the input of a high amount (19) of free numerical parameters, among them the masses of the particles, which have to be measured. The origins of these parameters are unknown, they have to be input ad hoc into the standard model which, for a fundamental theory, is highly unsatisfactory. There is also no deeper understanding why there are exactly three generations with two flavours each of fundamental fermions. Matter-antimatter asymmetry in the universe can partially be explained by CP violation, however the order of magnitude predicted by the standard model is too low. The standard model also provides no explanation for the existence of dark matter or dark energy, both of which have strong experimental indications, or the mass of neutrinos which is proved to exist due to neutrino oscillation. Current experiments, for example at the large hadron collider (LHC) at CERN, or in precision experiments at various laboratories, are therefore looking for physics beyond the standard model.

2.1.1 Quantum chromodynamics

Quantum Chromodynamics is the theory embedded in the standard model that exclusively deals with the strong interaction between quarks and gluons. It is a quantum field theory which is, similar to QED, a gauge theory. While QED is based on the abelian gauge group U(1), QCD is based on the non-abelian SU(3). Important features that follow from QCD are the already explained confinement and the asymptotic freedom of affected particles, which causes the strong interaction to become weaker with rising energy scales, leading to asymptotically free particles at very high energies. Since the spatial separation between quarks in a nucleon behaves as $\lambda\!\!\!^{-} = \frac{\hbar}{\sqrt{Q^2}}$ (here, $\hbar$ is the

reduced Planck constant and Q^2 is the momentum transfer), the same is true for bound quarks within a nucleon.

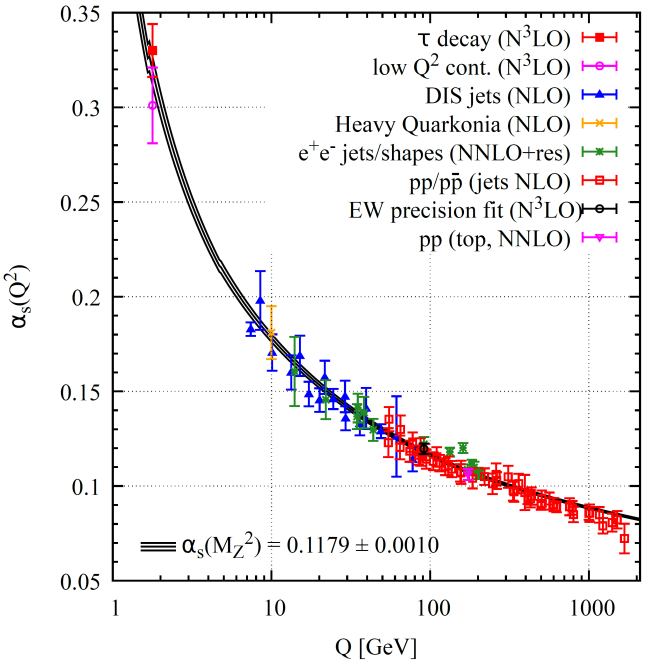

FIGURE 2.3: Summary of measurements of the running coupling constant α_s of the strong interaction as a function of the energy scale Q, taken from reference [6]

The Lagrangian of QCD is given by [7]

$$\mathcal{L}_{QCD} = \bar{\psi}_i(i(\gamma^\mu D_\mu)_{ij} - m\delta_{ij})\psi_j - \frac{1}{4}G^a_{\mu\nu}G^{\mu\nu}_a, \tag{2.1}$$

where ψ_j represents the quark field with colour index i=(red, blue, green), γ^μ are dirac matrices, D_μ is the gauge covariant derivative given in equation 2.3, m is the quark mass required as an input to the QCD, and $G^a_{\mu\nu}$ represents the gauge invariant gluonic field strength tensor given by [8]:

$$G^a_{\mu\nu} = \partial_\mu \mathcal{A}^a_\nu - \partial_\nu \mathcal{A}^a_\mu + g_s f^{abc}\mathcal{A}^b_\mu \mathcal{A}^c_\nu. \tag{2.2}$$

Here, $\mathcal{A}^a_\mu$ are the gluon fields where a is the colour index of the SU(3) colour group (a=1,2,3...8), f^{abc} are the structure constants of SU(3), and g_s is the quark gluon coupling constant.

The gauge covariant derivative is given by:

$$(D_\mu)_{ij} = \delta_{ij}\partial_\mu - \frac{1}{2}ig_s\lambda^a_{ij}\mathcal{A}^a_\mu, \tag{2.3}$$

using the same abbreviations as equation 2.2.

The strong coupling constant α_s, defined from g_s of equations 2.2 and 2.3 as $\alpha_s = \frac{g_s^2}{4\pi}$, is a running coupling constant, meaning that its strength varies considerably depending on the energy scale of the strong interaction. In dependence of this energy scale, usually given in terms of the momentum transfer of the interaction Q, α_s can be written in the leading-log approximation as [9]

$$\alpha_s = \frac{\alpha_s(\mu_R^2)}{1 + (\alpha_s(\mu_R^2)(33 - 2n_f)/12\pi) ln(|Q^2|/\mu_R^2)}, \tag{2.4}$$

where n_f is the number of considered quark flavours and μ_R is the energy scale of the renormalisation. The energy dependence of α_s can be seen in figure 2.3 in an overview of current measurements of the quantity [6]. Equation 2.4 also shows the asymptotic freedom at high energy scales, since for $Q^2 \to \infty$, α_s vanishes as long as the amount of quark flavours is below 16.

TABLE 2.2: Summary of quantum numbers of quarks in the standard model.

quark flavour	d	u	s	c	b	t
$\mathcal{B}$ - baryon number	$\frac{1}{3}$	$\frac{1}{3}$	$\frac{1}{3}$	$\frac{1}{3}$	$\frac{1}{3}$	$\frac{1}{3}$
Q - electric charge	$-\frac{1}{3}$	$+\frac{2}{3}$	$-\frac{1}{3}$	$+\frac{2}{3}$	$-\frac{1}{3}$	$+\frac{2}{3}$
I - isospin	$\frac{1}{2}$	$\frac{1}{2}$	0	0	0	0
I_z - z-component of isospin	$-\frac{1}{2}$	$+\frac{1}{2}$	0	0	0	0
s - spin	$\frac{1}{2}$	$\frac{1}{2}$	$\frac{1}{2}$	$\frac{1}{2}$	$\frac{1}{2}$	$\frac{1}{2}$
S - strangeness	0	0	-1	0	0	0
C - charm	0	0	0	+1	0	0
B - bottomness	0	0	0	0	-1	0
T - topness	0	0	0	0	0	+1

The variable coupling constant divides QCD into two regimes: the perturbative regime at high energy scales, where α_s is small enough to allow the use of pertubation theory,

and the non-perturbative regime at low energies, where pertubation theory can not be used and therefore theoretical predictions and calculations become very difficult.

2.1.2 Classification of hadrons in the standard model

Due to the colour confinement explained in section 2.1, quarks can not exist as isolated particles and therefore form bound systems known as hadrons. The standard model allows for two types of colour neutral hadrons: mesons, which in the naive quark model consist of a valence quark-antiquark pair whose colour charges cancel each other out, and baryons consisting of three valence quarks with all three colour charges.

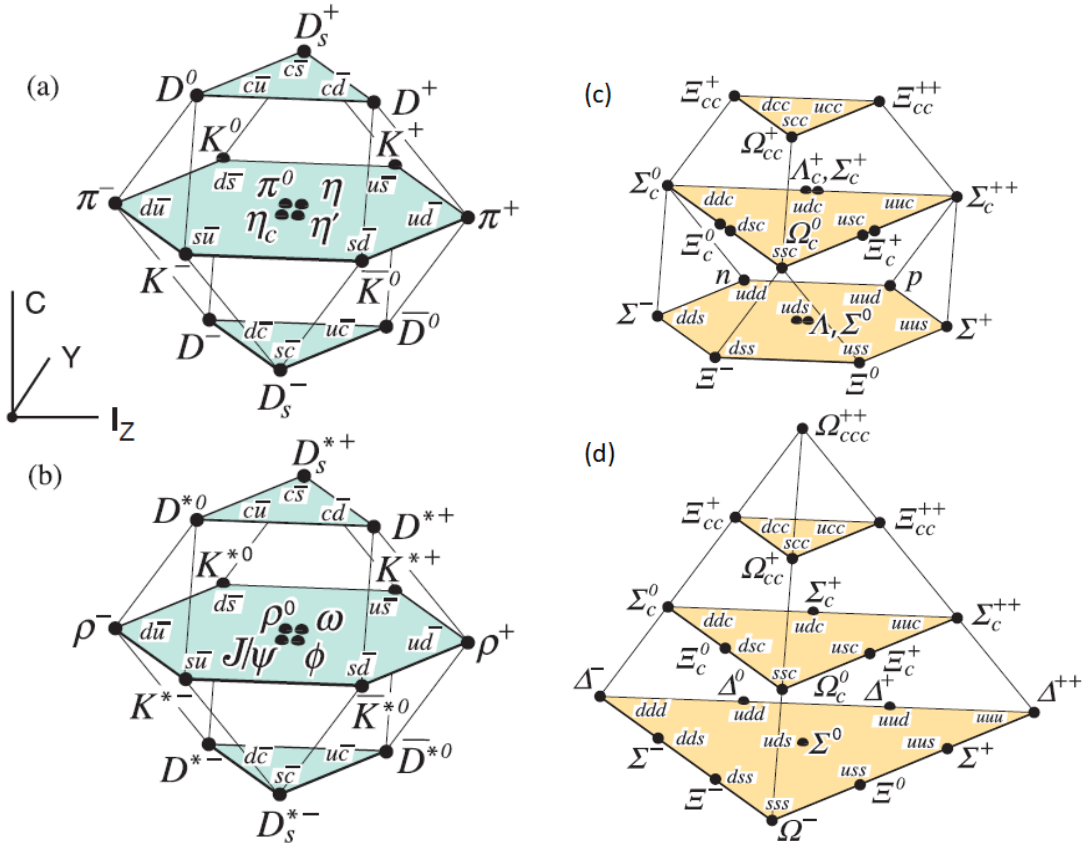

FIGURE 2.4: Overview of two-quark (mesons, left side) and three-quark (baryons, right side) bound states in the standard model. Left side: SU(4) 16-plets of (a) pseudoscalar (J=0) and vector (J=1) mesons consisting of u, d, s and c quarks as a function of the z-component of isospin I_z, charm C and hypercharge Y. Right side: SU(4) multiplets of baryons consisting of u, d, and s quarks: (c) 20-plet with an SU(3) octet and (d) 20-plet with an SU(3) decuplet. Taken from reference [6].

These composite particles are usually classified in the quark model via a set of quantum numbers. One convenient set of quantum numbers is J^{PC}, where J is the total angular momentum, P is the spatial parity, and C is the charge conjugation. In the case of

mesons, it can be shown that $P = (-1)^{l+1}$, where l is the angular momentum of the $q\bar{q}$ state. Charge conjugation represents the transformation of a particles into its antiparticle and is in the case of mesons only defined for mesons made of quarks and their own antiquarks. In these cases it can be shown that $C = (-1)^{l+s}$.
Using these quantum numbers, mesons are classified into J^{PC} multiplets, where the lowest lying states with l=0 are divided into pseudoscalar ($J^{PC} = 0^{-+}$) and vector ($J^{PC} = 1^{--}$) mesons. The exited states with l=1 are divided into scalar mesons ($J^{PC} = 0^{++}$), axial vector mesons ($J^{PC} = 1^{++}$ or 1^{+-}) and tensor mesons ($J^{PC} = 2^{++}$). In addition to J^{PC}, a number of quantum numbers can be used to further categorise mesons. Quantum numbers of the different flavoured quarks are summarised in table 2.2. In addition, a composite quantum number known as the hypercharge can be defined as:

$$Y = \mathcal{B} + S - \frac{C - B + T}{3}. \tag{2.5}$$

Quantum numbers of the composite particles such as baryons and mesons simply result from the sum of the corresponding quantum number of their constituent quarks.
Considering just the lighter quarks u, d, and s, the possible 9 combinations of quark antiquark pairs that form mesons are grouped into a singlet and an octet, following an SU(3) symmetry. Adding the next heavier quark c, this expands to an SU(4) symmetry, however this symmetry is strongly broken due to the much heavier mass of the c quark compared to u, d, and s. Nonetheless, the 16 combinations of possible quark antiquark pairs with these constituents can be divided into a singlet and an 15-plet. The resulting mesons classified in terms of their isospin z-component I_z, charm C and hypercharge Y can be seen on the left side of figure 2.4 [6].

The second type of hadrons, the baryons, are fermions with quantum number $\mathcal{B} = 1$, resulting from the sum of $\mathcal{B} = 1/3$ of their 3 constituent quarks. In addition, they consist of a sea of short-lived quark antiquark pairs of different flavours. "Ordinary" baryons are made up of only the lighter quarks, u, d, and s. These baryons are therefore subject to an approximate flavour SU(3) symmetry, and belong to multiplets on the right side of

$$3 \otimes 3 \otimes 3 = 10_S \otimes 8_M \otimes 8_M \otimes 1_A, \tag{2.6}$$

where the subscript S means symmetric, M means mixed symmetric and A means antisymmetric behaviour when interchanging two quarks of the baryon. Baryons made of only u and d quarks are nucleons (protons and neutrons) with isospin I=1/2 and

Δ baryons with isospin I=3/2. Baryons containing any number of s quarks are called hyperons, more specifically Λ, Σ, Ξ, or Ω depending on the number of s quarks they contain and their isospin. Compared to other baryons containing heavier quarks, they are fairly long lived and can even form non-stable bound states known as hypernuclei. The only known baryon that is up to our knowledge stable in isolation is the proton, while even the neutron decays (if not in a bound system) to a proton, electron and electron antineutrino with a half-life of about 10 minutes. A summary of baryons made up of u,d and s quarks can be found on the right side of figure 2.3.

2.2 Nucleon structure

Despite being the building blocks of atomic nuclei and therefore one of the most fundamental components of matter, a lot of details about the internal structure and dynamics of nuclei is still not understood until today, despite being investigated since almost 100 years. The electromagnetic interaction has in this time proven to be a powerful tool in the investigation of the nucleon structure, and is still the main sources of new insights. Most of what we know today about the proton structure has been explored in elastic and (deep) inelastic scattering experiments of for example electrons on nucleons, or in annihilation experiments of for example electron-positron annihilation into nucleon-antinucleon (or vice versa in case of the proton).

As discussed in the previous section, nucleons in the quark model consist of three of the lightest quarks (u and d) each. In case of the neutron, two d and one u quark give the neutron a total electric charge of 0, while the proton, consisting of two u and one d quark, has total electric charge 1. The sum of the rest masses of the protons constituent quarks is about 9 MeV/c^2, however the proton rest mass is over 100 times larger than that at about 938.27 MeV/c^2. Although the neutron is overall electrically neutral, its constituents carry electrical charge and therefore both the neutron and proton have electromagnetic structure and dynamics. Our current knowledge about this structure and its dynamics is encoded in functions describing the spatial distribution or dynamics of the electromagnetic charges. One of these functions are the EM FFs of the nucleon, which are the main subject of this thesis and will be discussed in further detail in the following sections.

2.2.1 Early investigations of the nucleon structure

Historically, the first explorations into the structure of nucleons have been done by scattering experiments of electrons on nucleon targets. The resulting (differential) cross

section of this process then allows conclusions about the spatial distribution of the charge of the target.

The first description of this cross section was found by Rutherford in 1911. It applies to the scattering of non-relativistic point-like particles with spin 0 and can be expressed by [10]:

$$\frac{d\sigma}{d\Omega} = \left(\frac{Z_1 Z_2 \, \alpha \, (\hbar c)}{4 E_K \, \sin^2 \frac{\theta}{2}} \right)^2 . \tag{2.7}$$

The formula gives the probability to find the electron within the solid angle of $d\Omega = 2\pi \sin(\theta) d\theta$ after being scattered by the angle θ. Z_1 is the electric charge of the scattered particle, Z_2 the charge of the target, $\alpha = \frac{e^2}{4\pi}$ (e = elementary charge) is the finestructure constant, E_K is the non-relativistic kinetic energy of the projectile, and $\hbar c \approx 197$ MeV·fm is the product of the reduced Planck constant and the speed of light in vacuum.

In 1929, Nevill F. Mott modified Rutherfords formula to account for the fact that the electron is a spin 1/2 particle. Spin effects lead to a modified cross section formula given by [11]

$$\left(\frac{d\sigma}{d\Omega} \right)^*_{Mott} = \left(\frac{d\sigma}{d\Omega} \right)_{Rutherford} \cdot \left(1 - \beta^2 \sin^2 \frac{\Theta}{2} \right), \tag{2.8}$$

where $\beta = \frac{v}{c}$ with the particle speed v. The star indicates that the recoil onto the target is neglected in this formula. While the projectile is considered to be a relativistic particle carrying spin, the target is assumed to be structureless and carry neither spin nor magnetic moment.

The approximation of a structureless scattering target however only holds true for the limit of momentum transfer $|q| = 0$, where the virtual photon mediating the interaction has a large wavelength and therefore cannot resolve the structure of the target. For higher values of $|q|$, the photon "sees" only part of the charge of the target, which leads (in case of the proton) to systematically lower cross sections compared to 2.8. This experimentally observed reduction can be parametrised as a form factor, which modifies equation 2.8 to [12]:

$$\left(\frac{d\sigma}{d\Omega} \right)_{exp} = \left(\frac{d\sigma}{d\Omega} \right)_{Mott} \cdot |F(q^2)|^2 = \left(\frac{d\sigma}{d\Omega} \right)_{Mott} \cdot \int \rho(\vec{x}) e^{i\vec{q}\vec{x}} d\vec{x}, \tag{2.9}$$

where $F(q^2)$ is the form factor of the charge distribution as a function of q. The right side of formula 2.9 links this form factor in Born approximation to the Fourier transform of the charge density of the target.

In the case of the proton, the first indications that it is not a point-like structureless particle were the experiments conducted by Stern [13] on the magnetic moment of the proton, which turned out to be about 2.8 times higher then expected for a point-like particle. Electron scattering experiments done at the Stanford High Energy Physics Laboratory by Hofstadter *et al.* [14] allowed a first measurement of a FF after equation 2.9, under the assumption of an electron proton interaction via a single virtual photon. The results of these experiments can be seen in figure 2.5 [15]. The experimentally observed cross section is systematically lower than the prediction for a point-like charge and magnetic moment distribution (curve c in the plot), which is a clear indication that the proton indeed has a substructure. Note that the lower cross section for the Mott curve compared to the experiment is due to the neglect of the magnetic moment in 2.8, which was remedied by the work described in the following.

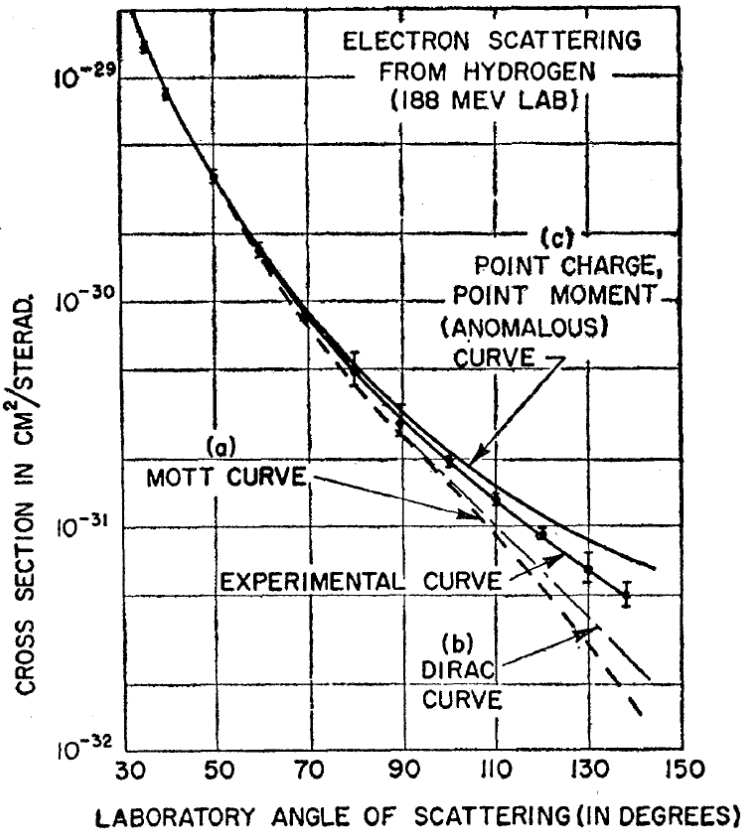

FIGURE 2.5: Experimental cross section of the electron-proton scattering performed by Hofstadter (1956) [15] as a function of the scattering angle at an electron energy of 188 MeV together with several theoretical curves. The experimental cross section is systematically lower than the theoretical curve of Rosenbluth assuming a point-like charge and anomalous magnetic moment, which indicates a non-pointlike structure of the proton.

Further interpretations of the obtained FF are possible following the work of Rosenbluth [16], by dividing the FF into parts linked to the effective charge and the effective magnetic moments of the interaction with the electron. Clementel and Villi [17] defined these parts as two separate FFs, $F_1(q) = \frac{e'}{e}$ and $F_2(q) = \frac{\kappa' e'}{\kappa_0 e}$, where e is the natural charge, e' the effective charge, and κ' is the effective anomalous magnetic moment. These FFs where later called the Dirac (F_1) and Pauli (F_2) FFs in experimental papers by Hofstadter *et al.* and others [15, 18]. In this picture, F_1 represents the deviation of the behaviour of the scattering target from a particle with point-like charge, while F_2 represents the deviation from a particle with point-like anomalous magnetic moment.
Following this work, Hofstadter was able to write the differential cross section of elastic electron-proton scattering as [15]:

$$\left(\frac{d\sigma}{d\Omega}\right) = \left(\frac{d\sigma}{d\Omega}\right)_{Mott} \cdot \frac{E_e}{E_{beam}} \left[F_1^2(Q^2) + \tau F_2^2(Q^2) + 2\tau \tan^2\frac{\theta}{2}\left(F_1(Q^2) + F_2(Q^2)\right)^2\right]. \tag{2.10}$$

Here, $\tau = Q^2/4M_p^2$ with the mass of the proton $M_p = 938.272081$ MeV/c^2 [6]. The recoil onto the target is considered with $\frac{E_e}{E_{beam}} = (1 + \frac{2E_{beam}}{M}\sin^2\frac{\theta}{2})^{-1} = (1+\tau)^{-1}$, where E_{beam} is the energy of the beam electron and E_e is the energy of the scattered electron. Q^2 is defined from the momentum transfer q as $Q^2 = -q^2$.
A more commonly used set of FFs compared to F_1 and F_2 are the so called Sachs FFs, which are simply linear combinations of the former ones:

$$G_E(Q^2) = F_1(Q^2) - \tau F_2(Q^2) \tag{2.11}$$

$$G_M(Q^2) = F_1(Q^2) + F2(Q^2) \tag{2.12}$$

Using these definitions, the cross section formula, also known as the Rosenbluth formula, can be expressed as follows:

$$\left(\frac{d\sigma}{d\Omega}\right) = \left(\frac{d\sigma}{d\Omega}\right)_{Mott} \cdot \left[\frac{G_E^2(Q^2) + \tau G_M^2(Q^2)}{1+\tau} + 2\tau G_M^2(Q^2)\tan^2\frac{\theta}{2}\right]. \tag{2.13}$$

2.2.2 Nucleon electromagnetic form factors: timelike and spacelike region

The EM FFs introduced in the last section from a historical perspective can be seen in more general terms as modifications to the point-like photon nucleon vertex which account for the structure of the interacting particle. As such, a non-pointlike particle

has a number of independent EM FFs depending on its spin S, with $N_{FF} = (2S + 1)$. In case of the proton and neutron with $S = 1/2$, this gives two independent FFs; either $F_1(Q^2)$ and $F_2(Q^2)$ or $G_E(Q^2)$ and $G_M(Q^2)$.

The EM FFs of nucleons depend on one kinematical variable, the momentum transfer Q^2 of the considered reaction. This variable divides the measurable FFs into different regions. The region with momentum transfer $Q^2 > 0$ is known as the spacelike (SL) region, while the region with $Q^2 < 0$ ($q^2 > 0$) is known as the timelike (TL) region. A subregion of the TL region is the so called unphysical region below the production threshold of the nucleon, where $0 < Q^2 < 2M_N$ with the nucleon mass M_N.

Nucleon FFs in the SL region can be measured in scattering experiments, as described in the last section. In general, the reaction is given by:

$$l^-(k_1) + N(p_1) \rightarrow l^-(k_2) + N(p_2), \tag{2.14}$$

where k_1 and k_2 are the momentum of the lepton l before and after the reaction, respectively, and p_1 and p_2 are the momentum of the nucleon N before and after the reaction, respectively. A Feynman diagram of the process in Born approximation, assuming the exchange of one virtual photon between the nucleon and the lepton, is shown in figure 2.6.

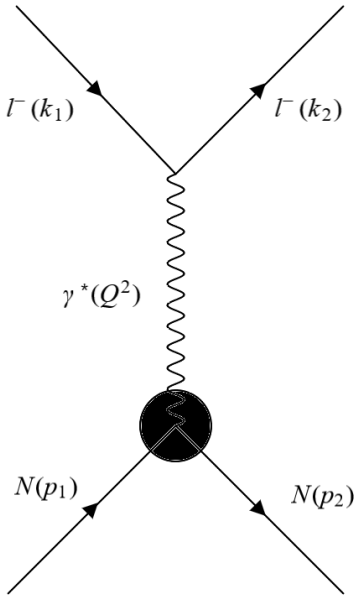

FIGURE 2.6: Feynman diagram of the elastic lepton-nucleon scattering process with single photon exchange (Born approximation).

The momentum transfer in this process is given by the momenta of the nucleon and the lepton before and after the scattering process:

$$Q^2 = -q^2 = (k_1 - k_2)^2 > 0 \tag{2.15}$$

The matrix element of the process can be written as a product of a term containing the leptonic current J^{μ}_{lep}, which can be calculated exactly from QED, and a term containing the hadronic current J^{μ}_{had} [19]:

$$-i\mathcal{M} = \frac{-ig_{\mu\nu}}{q^2}\left[ie\bar{u}(k_2)\gamma^{\nu}u(k_1)\right]\left[-ie\bar{N}(p_2)\Gamma^{\mu}(p_2,p_1)N(p_1)\right] = \frac{i}{q^2}\mathrm{J}^{lep}_{\mu}\mathrm{J}^{\mu}_{had}. \tag{2.16}$$

Here, u and N are the lepton and nucleon spinors, k_1 (k_2) and p_1 (p_2) are the incoming (outgoing) electron and neutron four-momenta, respectively, $g_{\mu\nu}$ is the metric tensor, and $\gamma^{\nu} = \gamma^0, \gamma^1, \gamma^2, \gamma^3$ are the Dirac gamma matrices.
The non-constant matrix Γ^{μ} describes the interaction between the nucleon and the virtual photon and contains the information about the structure of the nucleon. The relativistic invariance of the matrix element $\mathcal{M}$ requires Γ^{μ} to be a function depending only on p_1, p_2, and γ^{μ}. The most general form of such a matrix, considering current conservation, is [19]:

$$\Gamma^{\mu} = \gamma^{\mu}F_1^N(q^2) + \frac{i\sigma^{\mu\nu}q_{\nu}}{2M_N}F_2^N(q^2), \tag{2.17}$$

with the mass of the nucleon M_N. The cross section in laboratory frame can now be written as:

$$\frac{d\sigma}{d\Omega} = \frac{|\bar{\mathcal{M}}|^2}{64\pi^2}\cdot\left(\frac{E_e}{E_{beam}}\right)^2\cdot\frac{1}{M_N}. \tag{2.18}$$

Using equation 2.16 and 2.17, we arrive at the expression for the differential cross section given in formula 2.10, or, expressed in terms of the electric and magnetic FFs introduced in 2.11 and 2.12, at equation 2.13.

In the SL region, an interpretation of the EM FFs of the nucleon G_E and G_M is possible in a specific frame of reference. In this frame, called Breit-frame, the scattering electron only transfers a momentum $\vec{q}$ but no energy, meaning the momentum transfer becomes $q = (0, \vec{q})$. The EM FFs in the Breit-frame are associated with the Fourier transform of the charge (G_E) and the magnetic moment (G_M) spatial distributions. Therefore, G_E is usually called the electric and G_M the magnetic FF.

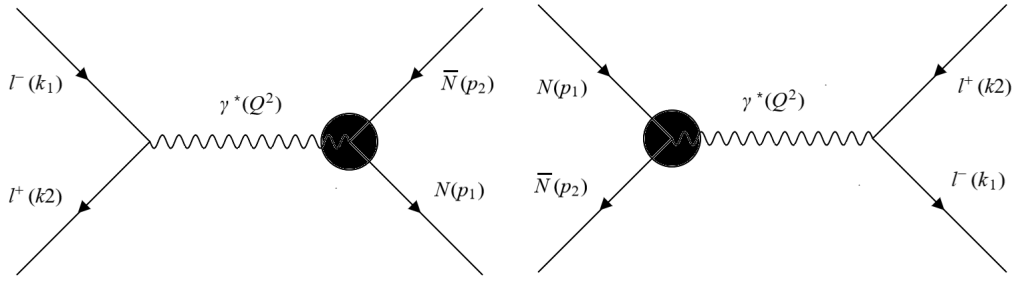

FIGURE 2.7: Feynman diagram of the Born approximation of the annihilation processes $l^+l^- \to N\bar{N}$ (left) and $N\bar{N} \to l^+l^-$ (right).

The TL region of EM FFs of the nucleon can be explored in the channel with crossed symmetry compared to 2.14,

$$l^+(k_1)l^-(k_2) \to N(p_1)\bar{N}(p_2), \quad N(p_1)\bar{N}(p_2) \to l^+(k_1)l^-(k_2). \tag{2.19}$$

Feynman diagrams of these processes are shown in figure 2.7, again in Born approximation assuming one-photon exchange. The momentum transfer in case of the annihilation channel is given by the center of mass energy of the annihilation s:

$$q^2 = s = (k_1 + k_2)^2 = (p_1 + p_2)^2, q^2 > 4M_N^2, \tag{2.20}$$

where k_1 and k_2 are the momenta of the lepton and antilepton before the annihilation or, in case of the time-reverse channel, after the pair production. p_1 and p_2 are the nucleon momenta either after the pair production or before the annihilation.
Due to crossing symmetry, the reaction can be described by the same amplitude as in the scattering case, including the same FFs F_1 and F_2 or G_E and G_M. In terms of the latter, the overall cross section can be written as:

$$\frac{d\sigma_{N\bar{N}(s)}}{d\Omega} = \frac{\alpha^2\beta C}{4s}\left[|G_M(s)|^2(1+\cos^2\theta) + \frac{4M_N^2}{s}|G_E(s)|^2\sin^2\theta\right], \tag{2.21}$$

where α is the fine-structure constant, β =v/c with the speed of the nucleon v and the speed of light c, and C is the coulomb correction factor. The angle θ is defined in the case of annihilation as the angle between the beam and the outgoing nucleons, or vice versa in the time-inversed channel.
Formula 2.21 allows a separate measurement of the two FFs $|G_E|$ and $|G_M|$ by measuring the cross section of the processes of equation 2.19 depending on the angle θ. In addition, such a measurement requires a precise knowledge of the normalisation of equation 2.21

and the luminosity of the data, as well as corrections for processes of higher order of α compared to equation 2.19.

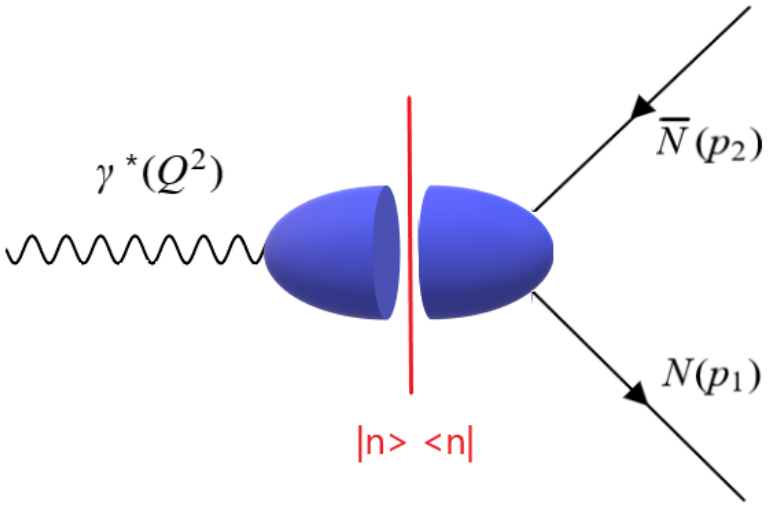

FIGURE 2.8: Spectral decomposition of the photon-nucleon vertex in the TL region based on the optical theorem.

Compared to the SL region where EM FFs of nucleons are real functions of q^2, the FFs of the TL region are complex functions of (q^2). This can be derived by using the optical theorem on the hadronic current J^{μ}_{had} as shown in figure 2.8:

$$Im[< \bar{N}(p_2)N(p_1)|J^{\mu}_{had}|0 >] \sim \sum_{n} < \bar{N}(p_2)N(p_1)|J^{\mu}_{had}|n >< n|J^{\mu}_{had}|0 > . \qquad (2.22)$$

Here, $|n >$ are on-shell hadronic intermediate states which are stable with respect to the strong force. The matrix element of equation 2.22 is non-vanishing if these intermediate states carry the same quantum numbers as the nucleon, which is the case for example for 2π, 3π, 4π states and so on. Due to that, the imaginary part of the TL EM FFs of nucleons is unequal to 0 above the production threshold of the lightest of these intermediate states $\pi^+\pi^-$, and therefore at momentum transfer $q^2 > 4m_\pi^2$ [20].

A connection between the EM FFs of the TL and the SL region is possible through the so called dispersion relations. These relations, based on unitarity and analyticity, allow to relate the real part of a function depending on a variable, for example q^2, to the integral over the imaginary part of that function from $-\infty < q^2 < \infty$. As shown above, nucleon EM FFs only have an imaginary part for $q^2 > 4m_\pi$, which reduces the integral interval to $4m_\pi < q^2 < \infty$, the TL region. Thus, the dispersion relations allow to connect the FFs in the TL region, where they are complex, to the FFs in the SL region where they are real functions of q^2. Assuming the FFs to be analytical functions, their dispersion relation can be written as [21]:

$$F(q^2) = \frac{1}{\pi}\int_{4m_\pi^2}^{\infty} \frac{Im(F(x)}{x - q^2} dx \tag{2.23}$$

Finally, the so called TL unphysical region for nucleon EM FFs lies below the production threshold of the nucleon pair of $4M_N^2$. In the case of the proton, there are suggestions to explore this region in proton-antiproton annihilation experiments, for example the planed PANDA experiment at FAIR, through the channel $p\bar{p} \to \pi_0 l^+ l^-$ [22–25], with l being either electron or muon. For the neutron, there is so far no feasible access to FFs in the unphysical region.

2.2.3 Asymptotic behaviour and boundary conditions

The normalisation at momentum transfer $q^2 = 0$ of the nucleon EM FFs follows from total charge and static magnetic moment conservation. For the Dirac and Pauli FFs, the values for proton and neutron are:

$$F_1^p(0) = Q_p = 1, \qquad F_2^p(0) = \kappa_p = \mu_p - 1 \tag{2.24}$$

$$F_1^n(0) = Q_n = 0, \qquad F_2^n(0) = \kappa_n = \mu_n, \tag{2.25}$$

where $\kappa_{p,n}$ is the anomalous magnetic moment of the proton and neutron, respectively, $\mu_p = 2.79284734462(82)$ [26] and $\mu_n = -1.91304273(45)$ [6] are the proton and neutron magnetic moment in units of the nuclear magneton $\mu_N = e\hbar/2m_p$, respectively, and Q_p and Q_n are the proton and neutron charge, respectively.
For the Sachs FFs G_E and G_M, similar conditions apply at $q^2 = 0$:

$$G_E^p(0) = Q_p = 1, \qquad G_M^p(0) = \mu_p \tag{2.26}$$

$$G_E^n(0) = Q_n = 0, \qquad G_M^n(0) = \mu_n, \tag{2.27}$$

with the same definitions as in equations 2.24 and 2.25. In addition, the Sachs FFs are equal at the production threshold of the corresponding nucleon:

$$G_E^N(4M_N^2) = G_M^N(4M_N^2), \tag{2.28}$$

which follows directly from the defining equations of the Sachs FFs, equations 2.11 and 2.12, for $\tau = 1$ and therefore $q^2 = 4M_N^2$.
The asymptotic behaviour for very large values of the momentum transfer $q^2 \to -\infty$ in the SL region can be derived from perturbative QCD (pQCD), since the strong coupling constant becomes small in this region. The Dirac and Pauli FFs behave asymptotically like [27]:

$$F_i(q^2) \underset{q^2 \to -\infty}{\sim} (-q^2)^{-1-i}, \tag{2.29}$$

with $i = 1, 2$. The two Sachs FFs G_E and G_M both behave in the same way for $q^2 \to -\infty$ [27]:

$$G_{E,M}(q^2) \underset{q^2 \to -\infty}{\sim} (-q^2)^{-2}. \tag{2.30}$$

By applying the Phragmèn–Lindelöf theorem [28, 29], the asymptotic behaviour of the SL region can be extended in any direction of the complex q^2 plane, and therefore also the TL region. Thus, both the Dirac and Pauli as well as the Sachs FFs in the TL scale with the same power law as in the space like region, and, since the FFs in the SL region are real, the asymptotic limit of the TL FFs must also be real.

2.3 Previous experimental situation for the proton electromagnetic form factors

While the previous sections where kept general about nucleon EM FFs, the experimental part of this introduction will focus on the EM FFs of the proton, which are the main subject of this work. For the proton, the experimental situation in the two kinematical regions where nucleon EM FFs can be explored (see last section) is very different: while there is a lot of experimental data available for the SL region, the situation in the TL region is much less comfortable. In this section, a brief overview over the experimental situation in both region will be given.

2.3.1 Previous experimental situation in the spacelike region

Rosenbluth separation

The main experimental method to extract proton EM FFs in the SL region is the so called Rosenbluth separation method [15], which was also the only available technique until the 1990s. The formula of the differential cross section containing the Sachs FFs, equation 2.13, can be re-written in the following notation:

$$\left(\frac{d\sigma}{d\Omega}\right) = \left(\frac{d\sigma}{d\Omega}\right)_{Mott} \cdot \left[G_E^2(Q^2) + \frac{\tau}{\epsilon} G_M^2(Q^2)\right] / (1+\tau), \tag{2.31}$$

where $\epsilon = \left[1 + 2(1+\tau)\tan^2\frac{\theta}{2}\right]^{-1}$ is the virtual photon polarisation. From equation 2.31, a reduced differential cross section of the elastic scattering process can be defined:

$$\left(\frac{d\sigma}{d\Omega}\right)_{red} = \left(\frac{d\sigma}{d\Omega}\right)_{exp} / \left(\frac{d\sigma}{d\Omega}\right)_{Mott} \cdot \frac{\epsilon(1+\tau)}{\tau} = G_M^2(Q^2) + \frac{\epsilon}{\tau} G_E^2(Q^2). \tag{2.32}$$

By measuring this reduced cross section at several different values of the kinematic factor ϵ, but the same value of Q^2, a linear dependence of the data from the two EM FFs is obtained, as can be seen in an example in figure 2.9. A linear fit to that plot returns $\frac{1}{\tau}G_E^2$ as the slope and G_M^2 as the intercept at this specific Q^2 value.

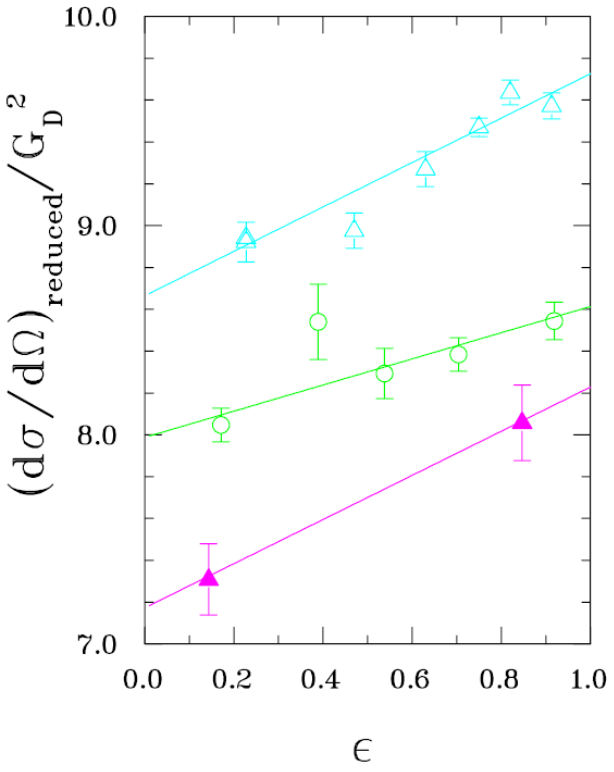

FIGURE 2.9: Rosenbluth separation of electron elastic scattering data at momentum transfer $Q^2 = 2.5$ GeV (turquoise open triangles), $Q^2 = 5$ GeV (green circles) and $Q^2 = 7$ GeV (pink filled triangles). The data is from reference [30], the plot was taken from reference [12].

Measurements of the SL FFs of various experiments with the Rosenbluth separation method are shown in figure 2.10. Here, the Sachs FFs G_E and G_M are divided by the dipole FF G_D, which is given by:

$$G_D = \frac{1}{(1 + Q^2/0.71GeV^2)^2}. \tag{2.33}$$

For lower values of Q^2, both the magnetic and the electric FF show a dipole behaviour. At higher Q^2 values, the extraction of the electric FF G_E becomes very difficult with the Rosenbluth separation method, since its term in equation 2.32 is suppressed by a factor of $1/\tau$.

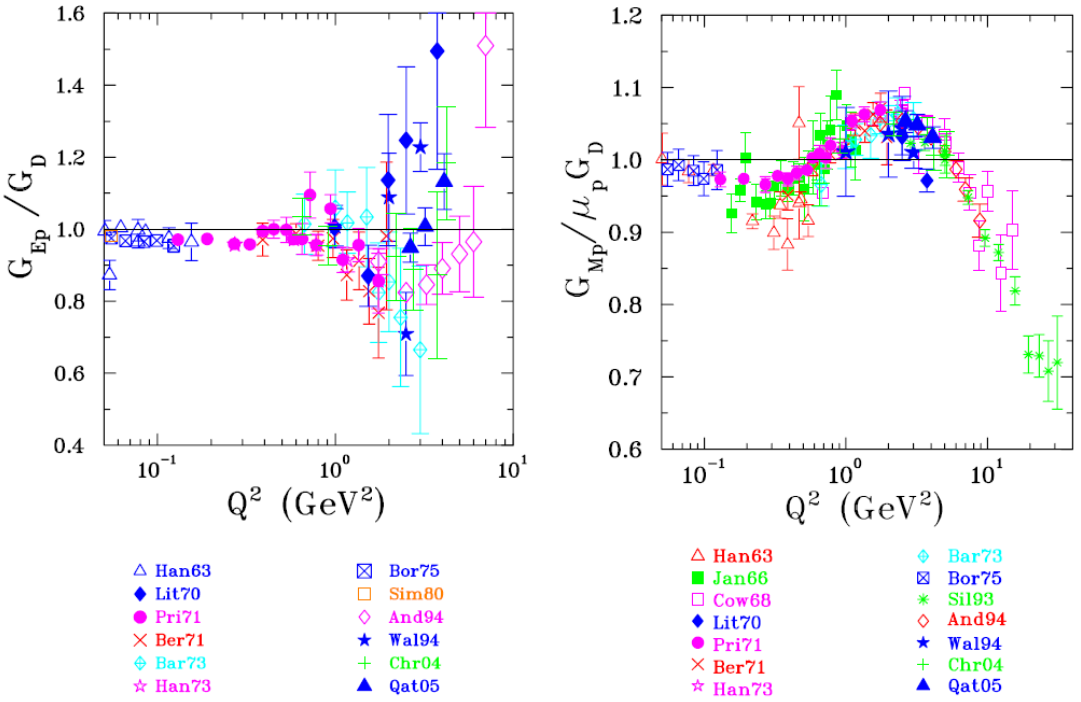

FIGURE 2.10: Measurements of the proton electromagnetic form factors in the spacelike region as a function of Q^2. The left side shows the electric, the right side the magnetic form factor divided by the dipole function G_D. The references are [31], [32], [33], [34], [35], [36], [37], [38], [39], [40], [41], [42], [43], and [44]. Plots taken from reference [12].

Double polarisation experiments

It was precisely the fact that the separate measurement of G_E becomes very difficult at high values of Q^2 using the Rosenbluth separation method that lead to the suggestion of a second method to extract EM FFs in the SL region by looking at double polarisation observables.

The first suggestion of such an experiment intended to use a longitudinally polarised electron beam and measure the polarisation of the recoiling proton. The idea was first proposed by Akhiezer and Rekalo [45, 46] in 1968, however it was only recently possible to realise it in experiments done at JLab starting in 1998 [47] due to technical advances,

for example the development of high intensity polarised electron beams and large proton polarimeters. These experiments measured polarisation observables instead of the cross section, which give access to the ratio of the electric and the magnetic FF as opposed to the individual FFs obtained from the Rosenbluth method. The longitudinal (P_l) and transversal (P_t) polarisation transfer component to the recoiling nucleon are, in the one-photon exchange approximation of elastic electron nucleon-scattering, the only non-zero components of the momentum transfer, while the normal component p_n is zero. They are related to the Sachs FFs in the following way [19]:

$$I_0 P_t = -2\sqrt{\tau(1+\tau)} G_E(q^2) G_M(q^2) \tan\frac{\theta}{2} \tag{2.34}$$

$$I_0 P_l = \frac{1}{M}\left(E_{beam} + E_e\right)\sqrt{\tau(1+\tau)} G_M^2(q^2) \tan^2\frac{\theta}{2}, \tag{2.35}$$

with $I_0 = G_E^2(q^2) + \frac{t}{\epsilon} G_M^2(q^2)$. Since the equations for the transversal and longitudinal polarisation depend on $G_E(q^2)G_M(q^2)$ and $G_M^2(q^2)$, respectively, the ratio of the two gives direct access to the ratio of the two Sachs FFs:

$$R = \frac{G_E(q^2)}{G_M(q^2)} = -\frac{p_t}{p_l}\frac{\left(E_{beam} + E_e\right)}{2M}\tan\frac{\theta}{2} \tag{2.36}$$

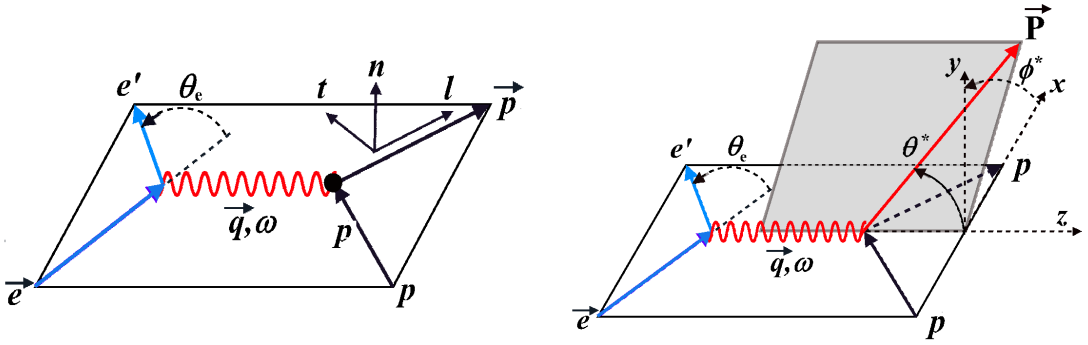

FIGURE 2.11: Left: kinematics and polarisation of the recoil nucleon in $\vec{e}p \to e'\vec{p}$. Right: kinematics and orientation of the polarisation of the target proton for $\vec{e}\vec{p} \to e'p$. The vector indicates polarisation. Plot taken from [19].

A major advantage of the technique is that the ratio of the Sachs FFs is directly obtained by a single measurement of the two recoil polarisation components for each value of q^2. Together with the fact that equation 2.36 does not require knowledge of the beam polarisation or the analysing power of the polarimeter, the systematic uncertainty of the measurement is far smaller compared to the Rosenbluth separation method.

The left side of figure 2.11 illustrates the kinematic and the polarisation of the method using the recoil polarisation method with a longitudinally polarised electron beam and an unpolarised target. A second method, where also the target is polarised, is illustrated on the right side of figure 2.11. In this method, the FFs are extracted from the beam helicity asymmetry, meaning the difference in cross section with alternating electron beam helicity states. This asymmetry is ultimately given by [19]:

$$A = \frac{\sigma_+ - \sigma_-}{\sigma_+ + \sigma_-} = -\frac{2\sqrt{\tau(1+\tau)}\tan\frac{\theta}{2}}{G_E^2(q^2) + \frac{\tau}{\epsilon}G_M^2(q^2)}[\sin\theta^*\cos\phi^* G_E G_M + \sqrt{\tau[1+(1+\tau)\tan^2\frac{\theta}{2}]}\cos\theta^* G_M^2(q^2)], \tag{2.37}$$

where σ_+ and σ_- are the cross sections for the two helicity states of the beam. θ^* and ϕ^* are defined as seen on the right side of figure 2.11.

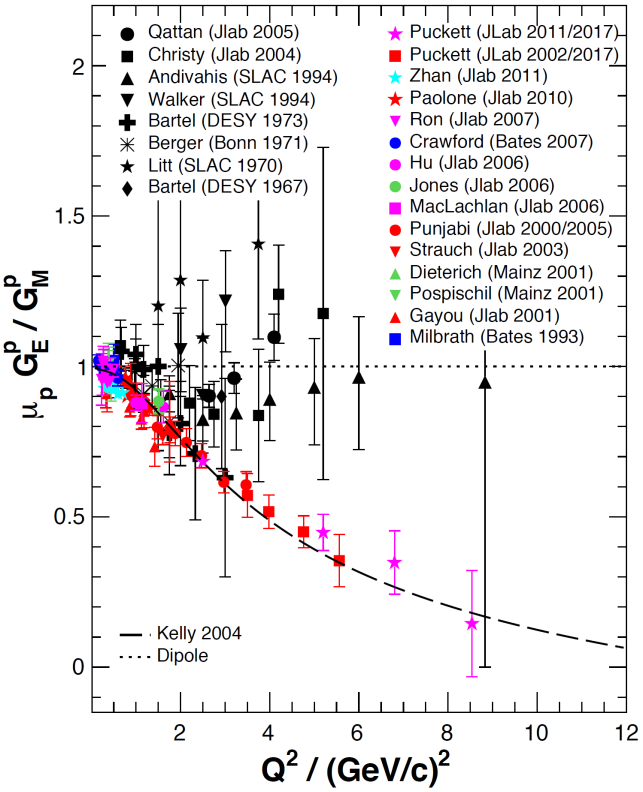

FIGURE 2.12: Ratio of the proton FFs $\mu G_E/G_M$ as a function of q^2 obtained from the polarisation method (colored symbols [48–64]) compared to those obtained from the Rosenbluth method (black symbols [30, 32, 34, 35, 37, 40–42, 44]). Plot taken from reference [65]

To be able to extract G_E from equation 2.37, the laboratory frame target polarisation must be perpendicular to $\vec{q}$ and within the reaction plane, meaning $\theta^* = \pi/2$ and $\phi^* = 0$ or 180 degree. Equation 2.37 then simplifies to [19]:

$$A_{perp} = -\frac{2\sqrt{\tau(1+\tau)}\tan\frac{\theta}{2}\frac{G_E(q^2)}{G_M(q^2)}}{(\frac{G_E(q^2)}{G_M(q^2)})^2 + \frac{\tau}{\epsilon}}. \tag{2.38}$$

From this equation, one can directly extract the ratio $R = \frac{G_E(q^2)}{G_M(q^2)}$. Since $(\frac{G_E(q^2)}{G_M(q^2)})^2$ is small especially at higher q^2, equation 2.38 is also approximately proportional to $\frac{G_E(q^2)}{G_M(q^2)}$.

Figure 2.12 shows the measurements done with the polarisation technique in comparison to the Rosenbluth data. Measurements have been performed up to a momentum transfer of about 8.5 GeV^2. While the previous Rosenbluth data indicated a FF ratio in agreement with unity, the new polarisation data shows an approximately linear monotonic decrease in R deviating from unity at about $Q^2 \approx 1\ GeV^2$. Since the magnetic FF G_M is known with small uncertainties from the Rosenbluth method, this deviation is mostly attributed to the electric FF G_E, which decreases faster than G_M with rising Q^2. The discrepancy between the two methods has been confirmed by newer experiments done at JLab [41, 42] using the Rosenbluth method, which yielded the same results as the older Rosenbluth measurements. The exact reason for this discrepancy is still up for debate, one possible explanation is the two-photon exchange process, or more precisely its interference with the one photon exchange process. In two-photon exchange, two instead of one virtual photon carry the momentum transfer Q^2. This kind of radiative corrections affects Rosenbluth data in a much more severe way compared to results from the polarisation method, where they mostly cancel out of the ratio p_t/p_l due to similar contributions to p_t and p_l, which may cause the two methods to yield different results.

2.3.2 Previous experimental situation in the timelike region

As described in section 2.2.2, proton EM FFs in the TL region are accessible through the annihilation reactions $l^+l^- \longleftrightarrow p\bar{p}$. The differential cross section, given by equation 2.21, gives access to either a separate measurement of two Sachs FFs, or $|G_M(s)|$ and the ratio of the two by rearranging the equation to:

$$\frac{d\sigma_{p\bar{p}(s)}}{d\Omega} = |G_M(s)|^2 \cdot \frac{\alpha^2\beta C}{4s}\left[(1+\cos^2\theta) + \frac{4M_p^2}{s}R^2\sin^2\theta\right], \quad R = |G_E|/|G_M| \tag{2.39}$$

While the FF ratio from equation 2.39 can also be measured without knowing the overall normalisation, the individual FF measurement requires precise knowledge thereof. Measuring any form of differential cross section also requires a sufficiently high amount of events to allow an angular analysis. Older experiments, which did not have that kind of statistic, had to settle for measuring the so called effective FF. This quantity is defined as a linear combination of the electric and magnetic FF in the following way:

$$|G(q^2)| = \sqrt{\frac{2\tau|G_M(q^2)|^2 + |G_E(q^2)|^2}{2\tau + 1}} \tag{2.40}$$

The effective FF gives an indication of the deviation of the cross section cross section from that of a point-like proton and antiproton and is still used today to compare to older experiments.

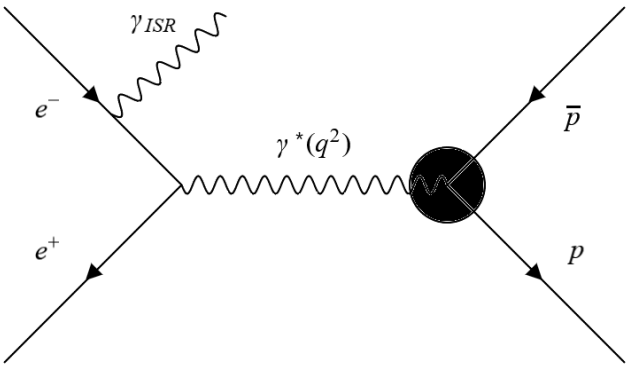

FIGURE 2.13: Feynman diagram of the initial state radiation process $e^+e^- \to p\bar{p}\gamma_{ISR}$.

In general, experiments aim to measure FFs in the TL region, be it individual FFs, their ratio, or the effective FF, over a range of momentum transfer q^2. For annihilation experiments, this can be achieved by using two different techniques. The first technique, the so called scan technique, "scans" the different values of q^2 through direct variation of the center of mass (CM) energy of the two annihilating particles. At each CM energy, the corresponding (differential) cross section of the process is measured and the FFs are extracted from it. The second technique uses data taken at a single CM energy with a high luminosity, typically at a resonance. The FFs at lower q^2 values, from the production threshold of $p\bar{p}$ at $\sqrt{s} \approx 1.876\ GeV/c^2$ up to that CM energy can then be extracted by looking at events with an initial state radiation (ISR) photon, which reduces the CM energy before the annihilation. The Feynman diagram of the process can be

seen in figure 2.13. Depending on whether the ISR photon of the process is detected directly, or indirectly for example from variables like the missing mass or momentum of the process, the method is called tagged or untagged ISR analysis, respectively.
While the luminosity of the data taken at resonances is usually high, the ISR process is a process one order higher in α compared to the Born process. Therefore its cross section is reduced by the radiator function $W(s,x)$, which in leading order is given by:

$$\frac{d\sigma_{e^+e^-\to p\bar{p}\gamma_{ISR}}(q^2)}{dq^2} = \frac{1}{s}W(s,x)\sigma_{p\bar{p}}(q^2) \tag{2.41}$$

$$W(s,x) = \frac{\alpha}{\pi x}\left(ln\frac{s}{m_e^2} - 1\right)(2 - 2x + x^2), \tag{2.42}$$

where $x = 2E^*_\gamma/\sqrt{s} = 1 - q^2/s$, E^*_γ is the ISR photon energy in the e^+e^- CM system and the electron mass m_e.

TABLE 2.3: Summary of the experimental results for the TL EM FFs using the scan technique and the reactions $e^+e^- \to p\bar{p}$ and $p\bar{p} \to e^+e^-$.

Experiment	Reaction	Pub. year	Scan points	Range [GeV]	$\mathcal{L}_{int}[pb^{-1}]$	Ref.
DM1	$e^+e^- \to p\bar{p}$	1979	4	1.925-2.180	0.4	[66]
DM2	$e^+e^- \to p\bar{p}$	1983	6	1.975-2.25	0.5	[67]
DM2	$e^+e^- \to p\bar{p}$	1990	1	2.4	0.2	[68]
ADONE 73	$e^+e^- \to p\bar{p}$	1973	1	2.1	0.2	[69]
FENICE	$e^+e^- \to p\bar{p}$	1993	1	2.1	0.1	[70]
FENICE	$e^+e^- \to p\bar{p}$	1994	4	1.9-2.4	0.3	[71]
FENICE	$e^+e^- \to p\bar{p}$	1998	1	2.1	<0.1	[72]
BES-II	$e^+e^- \to p\bar{p}$	2005	10	2.0-3.07	5	[73]
CLEO	$e^+e^- \to p\bar{p}$	2005	1	3.671	21	[74]
CMD-3	$e^+e^- \to p\bar{p}$	2015	12	1.89-2.0	6.976	[75]
M.S.T. Coll.	$p\bar{p} \to e^+e^-$	1975	2	near threshold	-	[76]
PS170	$p\bar{p} \to e^+e^-$	1991	4	near threshold	-	[77]
PS170	$p\bar{p} \to e^+e^-$	1991	4	1.94-2.05	-	[78]
PS170	$p\bar{p} \to e^+e^-$	1994	9	threshold -2.05	-	[79]
E760	$p\bar{p} \to e^+e^-$	1993	3	3.0-3.6	-	[80]
E835	$p\bar{p} \to e^+e^-$	1999	4	2.0-3.8	-	[81]
E835	$p\bar{p} \to e^+e^-$	2003	2	3.4-3.5	-	[82]

Both methods have up- and downsides: the ISR technique allows to use large, e.g. resonance, data samples taken for a different purpose and extract proton EM FFs from threshold up to the CM energy of the sample. Especially the production threshold is hard to access using the scan method due to the low momentum of the outgoing particles. However, due to the reduction in cross section by the factor $\frac{\alpha}{\pi x} \approx \frac{1}{400}$, the achievable precision is limited and can be surpassed by using a dedicated scan data set with a large luminosity.

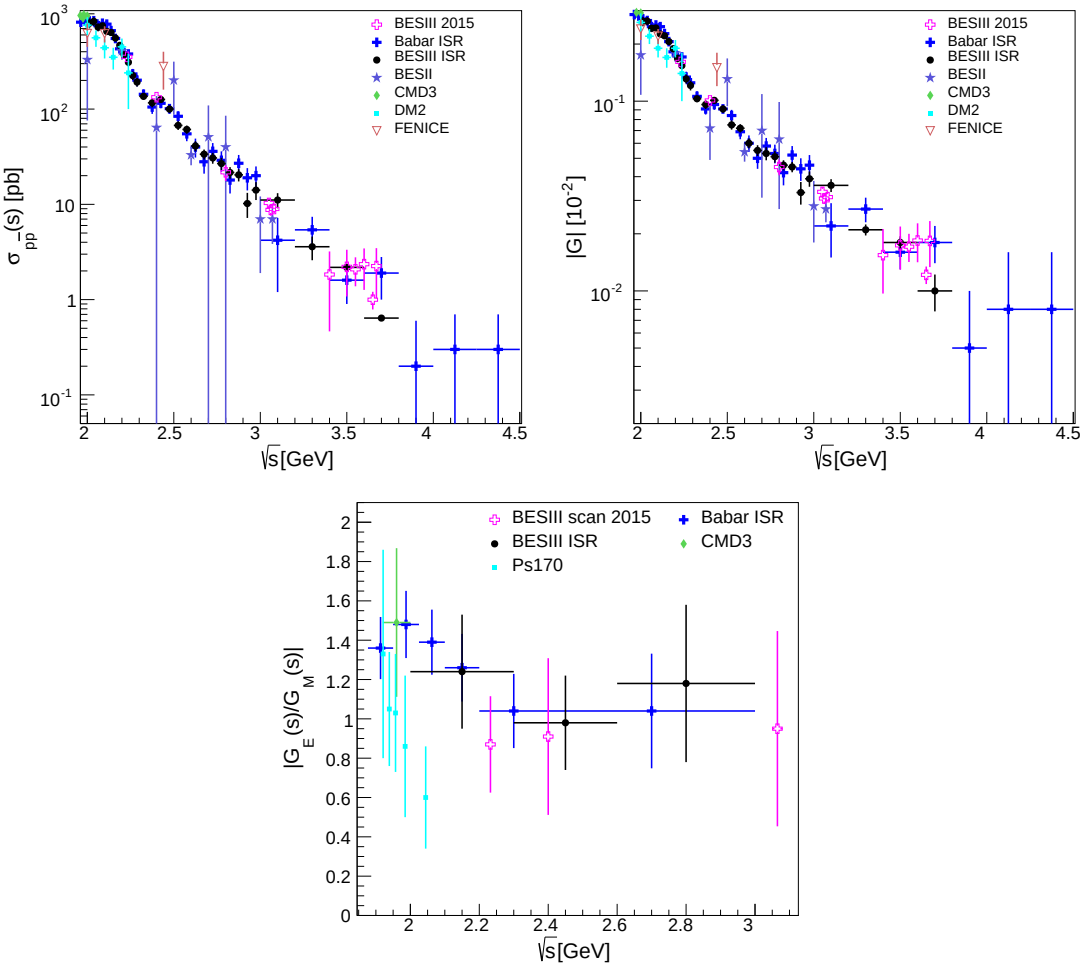

FIGURE 2.14: Upper left: Results of the cross section of the process $e^+e^- \to p\bar{p}$ from e^+e^- colliders. Upper right: Results of the effective FF of the proton $|G_{eff}$ from e^+e^- colliders [67, 72, 73, 75, 83–85]. Lower middle: Ratio R of the electric (G_E) and the magnetic (G_M) FF from e^+e^- colliders and antiproton accelerators [75, 79, 83–85].

The very first measurements of the TL EM FFs of the proton have been done via direct scan at the ADONE e^+e^- collider in Frascati in 1972 [69] in terms of the effective FF introduced in equation 2.40. A series of measurements followed in the same channel from the FENICE experiment [70–72], the DM1 [66] and DM2 experiments [67, 68] at the Orsay colliding beam facility, the BES-II experiment [73] and the CLEO experiment [74].

While first attempts to extract the TL EM FFs from the time-reversed channel started in the mid 1960s, the most important results from proton-antiproton annihilation into an electron positron pair are those of the PS170 experiment [77–79] at LEAR/CERN and the E760 [80] and E835 [81, 82] experiments at Fermilab. An overview of the measurements using the scan technique for both channels is given in table 2.3.

The most important proton TL EM FF measurements using the tagged or untagged ISR technique come from the BaBar experiment [84, 86] at the SCLAC B-factory PEP-II and recently from the BESIII experiment [85]. BaBar has measured the cross section of $e^+e^- \to p\bar{p}$ and the effective FF of the proton up to 6.5 GeV using in total 500 fb^{-1} of data collected between 1999 and 2008. In addition, BaBar was one of the experiments able to perform an angular analysis of the process due to its high luminosity, which allows to measure the ratio R of the electric and magnetic FF, shown in the lower part of figure 2.14. Another earlier experiment able to do so, PS170 in proton-antiproton annihilation, strongly disagrees with the ratio found by BaBar. The world data on the cross section of $e^+e^- \to p\bar{p}$ and the effective FF of the proton can be seen in the top part of figure 2.14, while all available results for the FF ratio are shown in the bottom. In conclusion, the experimental situation of proton EM FFs in the TL region is much less satisfying compared to the SL region. While there is a decent amount of measurements with good precision for the cross section of $e^+e^- \to p\bar{p}$ and effective FF of the proton, especially the disentangled electric and magnetic FFs are known only with low precision from few experiments, and on top of that with contradicting results.

2.4 Theoretical approaches to the proton electromagnetic form factors

This section will give an overview over the attempts from theory side to give an interpretation of the proton EM FFs. The difficulty in these attempts lies in the fact that in the few GeV energy region most relevant for the FFs, the underlying theory of QCD requires non-perturbative methods to calculate the FFs. This requires the different approaches to use approximations, which limit their respective range of application.

2.4.1 Dipole behaviour of the form factors

A very early, mostly phenomenological description of the proton EM FF behaviour was done by describing them with a simple dipole function [87]:

$$G_E(Q^2) = G_M(Q^2)/\mu_p = G_D(Q^2) = (1 + Q^2/0.71)^{-2}, \tag{2.43}$$

where μ_p is the magnetic moment of the proton. Despite the simplicity of the function, it describes the FFs well in the SL region up to the highest measured momenta of $Q^2 \simeq 31$ GeV^2 [88]. Further extensions to this parametrisation have been made to better describe the FFs in the TL region, for example an additional monopole suppression [27]:

$$G_M(Q^2) = \frac{A}{(1 + q^2/m_a^2)[1 - q^2/0.71]^2}, \tag{2.44}$$

where A and m_a are parameters that have to be determined from data.

2.4.2 Vector meson dominance model

One of the oldest attempts to describe the proton EM FFs is the vector meson dominance (VMD) model. This model assumes that, due to having the same J^{pc} quantum numbers ($J^{pc} = 1^{--}$), the interaction between the virtual photon and the nucleon can be described through the exchange of an intermediate vector meson, the lowest lying states being $\rho(770)$, $\omega(782)$ or $\phi(1020)$. Despite the fact that this is only an effective description which does not consider quark and gluon dynamics, the model describes the electromagnetic interaction of hadrons unexpectedly well at low energy.

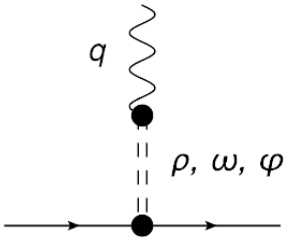

FIGURE 2.15: Coupling of the virtual photon with four momentum q to the nucleon via the exchange of an intermediate vector meson in the vector meson dominance model, from [19].

The first attempt to find a VMD based parametrisation of the nucleon EM FFs in both the SL and the TL region was performed by Massam and Zichichi in 1966 [89]. It served as a prototype for following descriptions, with one of the central ideas being the usage of the isospin components of the nucleon FFs instead of separate FFs for the proton and the neutron. This approach allows to distinguish between the contributions due to isoscalar (I=0) and isovector (I=1) mesons to the coupling:

$$F_1(q^2) = F_1^V(q^2) + F_1^S(q^2) \tag{2.45}$$

$$F_2(q^2) = F_2^V(q^2) + F_2^S(q^2), \tag{2.46}$$

where F_i^V and F_i^S (i=1,2) are the isovector and isoscaler components of the FFs, respectively. This decomposition however requires knowledge not only of the proton, but also the neutron FF in the same energy region.

Iachello, A. D. Jackson and A. Lande proposed another early parametrisation of the FFs based on VMD in 1973 [90], an approach which already predicted the linear decrease in the FF ratio G_E/G_M of the proton later observed in polarisation experiments (see section 2.3.1). The model, like the Massam and Zichichi model before, describes the interaction of the nucleon with the virtual photon in terms of VMD plus an intrinsic FF $g(Q^2)$ at the nucleon-vector meson vertex. The Iachello, Jackson and Lande (IJL) model additionally introduced the possibility for the direct coupling of the bare nucleon as a dirac particle to the photon. The isoscalar and isovector components of the Dirac and Pauli FFs in the IJL model are given by the following expressions:

$$F_1^S(q^2) = \frac{e}{2} g(q^2) \left[(1 - \beta_\omega - \beta_{phi}) + \beta_\omega \frac{M_\omega^2}{M_\omega^2 - q^2} + \beta_\phi \frac{M_\phi^2}{M_\phi^2 - q^2} \right] \tag{2.47}$$

$$F_1^V(q^2) = \frac{e}{2} g(q^2) \left[(1 - \beta_\rho) + \beta_\rho \frac{M_\rho^2}{M_\rho^2 - q^2} \right] \tag{2.48}$$

$$F_2^S(q^2) = \frac{e}{2} g(q^2) \left[(-0.120 - \alpha_\phi) \frac{M_\omega^2}{M_\omega^2 - q^2} + \alpha_\phi \frac{M_\phi^2}{M_\phi^2 - q^2} \right] \tag{2.49}$$

$$F_2^V(q^2) = \frac{e}{2} g(q^2) \left[3.706 \frac{M_\rho^2}{M_\rho^2 - q^2} \right]. \tag{2.50}$$

Here, the parameters β_ω, β_ϕ, β_ρ, and α_ϕ represent the product of the V_γ and VNN coupling constants. A fit to the proton FF in the SL region returns the following values for these parameters: $\beta_\omega = 1.102$, $\beta_\phi = 0.112$, $\beta_\rho = 0.672$, and $\alpha_\phi = -0.052$ [90]. M_ω, M_ϕ, and M_ρ are the masses of the corresponding mesons.

The IJL model was further improved by Gari and Krümpelman [91–93], who adjusted the model to fit the pQCD predictions at high Q^2 values of $F_1 \sim 1/Q^4$ and $F_2 \sim 1/Q^6$.

Extensions to the model done by Lomon included contributions of excited vector mesons such as $\rho'(1450)$ and $\omega'(1419)$ [94–96] and analytically extended the model to the TL region [97]. Modern fits using the VMD model, for example by Lomon and Pacetti, give a good parametrisation of data in both the SL and TL region. A comparison of fits of the IJL and the Gari-Krümpelman-Lomon (GKL) model can be seen in figure 2.16, where especially the improvement of the latter model for the neutron electric FF in the SL region can be seen.

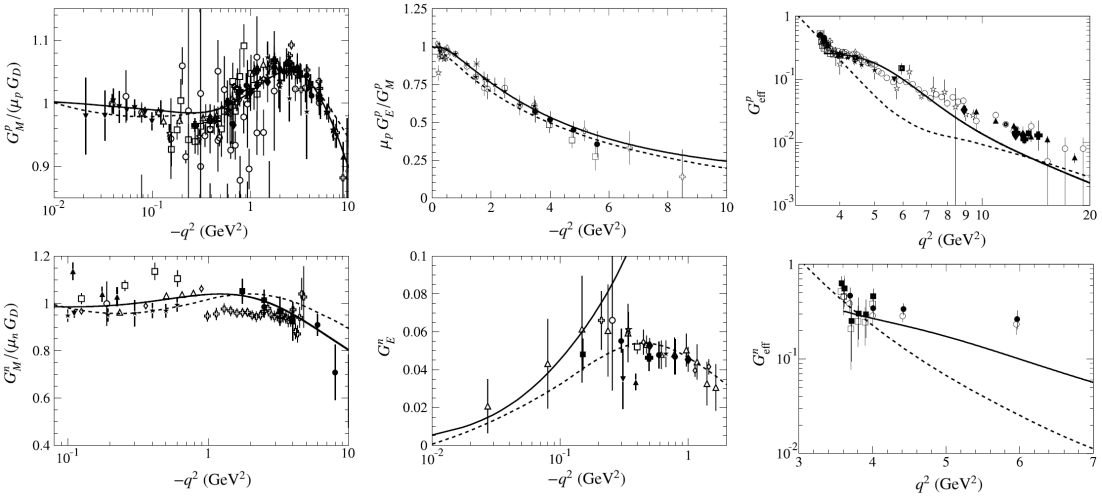

FIGURE 2.16: Parametrisations of the nucleon FFs in the SL (left 2 columns) and the TL (right column) regions from Iachello-Jackson-Lande (dashed lines) and Gari-Krümpelman-Lomon model (solid lines). References for $G_M^p(Q^2)$ and $\mu_p G_E^p(Q^2)/G_M^p(Q^2)$ are the same as in figure 2.10, data on G_M^n are from [98–107] , data on $G_E^n(Q^2)$ are from [108–116]. Data on the effective FFs G_{eff}^p and G_{eff}^n are from [66–69, 72–74, 76, 79–82, 84] and [72, 117], respectively. Figure taken from reference [27]

.

2.4.3 Perturbative QCD parametrisation

For sufficiently high values of Q^2, models based on pQCD can be used to describe the nucleon EM FFs, while at the same time, the behaviour of the FFs can be used as a test for pQCD. As mentioned before, the scaling behaviour of the FFs in this momentum transfer region can be predicted by pQCD, the first prediction coming from Brodsky and Farrar [118, 119].

In the regime of pQCD, the virtual photon interacting with a nucleon sees the nucleon as three constituent quarks moving parallel to each other along the momentum vector of the nucleon. The photon, in this picture coming from a sideways direction, interacts with one of these quarks. In order to keep the nucleon intact, the high momentum of the photon has to be distributed among the other constituent quarks via the exchange

of two hard gluons, leading again to a final state of three quarks moving in parallel as can be seen in figure 2.17.

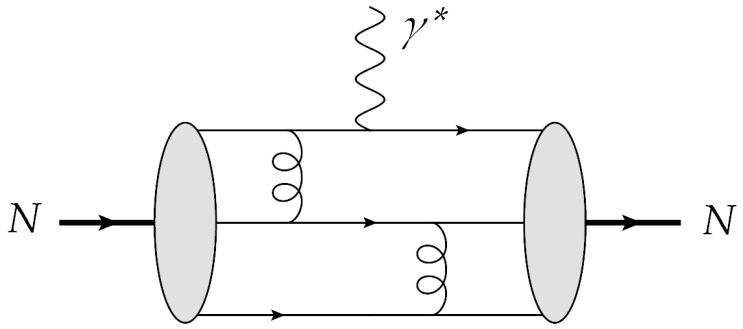

FIGURE 2.17: Diagram of the interaction of the virtual photon and the nucleon in the picture of pQCD in lowest order.

Since each gluon carries a virtuality proportional to Q^2, the pQCD prediction of the helicity conserving Dirac FF F_1 is proportional to $1/Q^4$. The four vertices of strong interaction in the reaction of figure 2.17 each contribute a factor of $\sqrt{\alpha_s}$, leading to a total scaling behaviour of:

$$G_E(Q^2) = G_M(Q^2) \underset{Q^2 \to -\infty}{\sim} \frac{\alpha_s^2(Q^2)}{Q^4} \tag{2.51}$$

The strong coupling constant α_s that the FFs are proportional to can be determined as follows:

$$ln(Q^2/\Lambda_{QCD}^2) = -\int_{\alpha_s(Q^2)}^{\infty} \frac{dx}{\beta(x)}, \tag{2.52}$$

with the QCD scale constant Λ_{QCD}. β can be expressed in the SU3 group as:

$$\beta(\alpha_s(Q^2)) = -b_0\alpha_s(Q^2)^2(1 + b_1\alpha_s(Q^2)) + \mathcal{O}(\alpha_s(Q^2)^2) \tag{2.53}$$

$$b_0 = \frac{11 - 2/3N_f}{4\pi}, \quad b_1 = \frac{153 - 19N_f}{2\pi(33 - 2N_f)}, \tag{2.54}$$

where N_f is the number of quark flavours. At first order with $b_1 = 0$, $\alpha_s(Q^2)$ becomes:

$$\alpha_s(Q^2) = \frac{1}{b_0 ln(Q^2/\Lambda_{QCD}^2)}, \quad G_{eff} \sim \frac{\alpha_0}{Q^4 ln(Q^2/\lambda_{QCD}^2)}, \tag{2.55}$$

where α_0 is a constant obtained from fitting the experimental data. Equation 2.55 is only applicable when $Q^2 >> \Lambda^2_{QCD}$, while it has a pole for $Q^2 = \Lambda^2_{QCD}$.
An analytical extension to the TL region can be derived from equation 2.55 by the following replacements:

$$Q^2 \to -q^2, \quad ln(Q^2/\Lambda^2_{QCD}) \to ln(q^2/\Lambda^2_{QCD}) - i\pi. \tag{2.56}$$

The Sachs FFs can then be expressed as:

$$|G_{E,M}(q^2)| = \frac{\alpha_0}{q^4[ln(q^2/\Lambda^2_{QCD}) + \pi^2]}, \tag{2.57}$$

where α_0 is once again a constant that has to be obtained from a fit to the TL data.
For the complex FFs in the TL region, the pQCD approach assumes a relative phase between $|G_E|$ and $|G_M|$ of zero. An experimental verification of this assumption through a measurement of the phase using polarisation observables can therefore be a test of the validity of the model.

2.4.4 Constituent quark model

Constituent quark models (CQM) have a long history in the attempts to understand the nucleon structure in terms of the quark and gluonic degrees of freedom of the QCD Lagrangian. In these models, the nucleon is treated as the ground state of a quantum mechanical system of three constituent quarks confined within a potential. The ground state nucleon in this picture is described by SU(6) spin-flavour wave functions and a completely asymmetric colour wave function.
Early formulations of CQMs focussed on the explanation of static properties of the nucleons, such as the magnetic moments and transition amplitudes. The description of nucleon FFs however requires a relativistic treatment due to the low mass of nucleon constituent quarks compared to the confinement mass scale. This becomes especially important for high values of the momentum transfer Q^2, where non-relativistic treatments lead to FF predictions far too small compared to data.

While the spectrum of the nucleon can be calculated using eigenfunctions of the poincaré invariant mass operator, the calculation of nucleon FFs requires to relate the rest frame spin and the momenta of the three quark wave function to the spin and momenta in the moving frame. The eigenfunctions of the spin and mass operator have to be extended to transform consistently under the unitarity representations of the poincaré group. Three forms of dynamics exists which differ in the generators forming the kinematic subgroup

of the poincaré group: the so called instant, point, and light-front groups. A comparison of different fits using these approaches can be seen for the SL region in figure 2.18 (left).

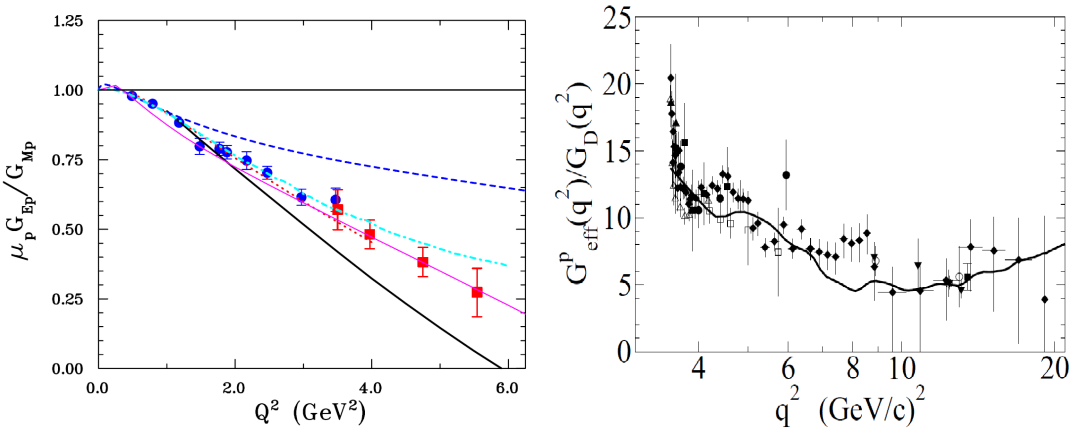

FIGURE 2.18: Left: Comparison of different relativistic CQM calculations with data for the FF ratio of the proton in the SL region. Dotted curve: front form calculation of Chung and Coester [120] with point-like constituent quarks; thick solid curve: front form calculation of Frank *et al.* [121]; dot-dashed curve: front form calculation of Cardarelli *et al.* [122, 123] with point-like constituent quarks; dashed curve: point form calculation of Boffi *et al.* [124] in the Goldstone boson exchange model with point-like constituent quarks; thin solid curve: covariant spectator model of Gross and Agbakpe [125]. The data are from [48] (solid circles) and [126] (empty squares). Figure taken from reference [12].
Right: Comparison of the prediction of the relativistic CQM of reference [127] (black solid line) with data for the effective FF of the proton in the TL region. The data are from [66, 68, 70, 73, 74, 79, 80, 82, 84]. Figure taken from reference [128].

The right side of figure 2.18 shows the prediction of a relativistic CQM for the proton FFs in the TL region, here for the effective FF. The model was built by fixing four adjusted parameters with SL experimental data and using a light-front approach. Details of the calculation can be found in reference [128].

2.4.5 Lattice QCD

Another theoretical approach to the description of the nucleon EM FFs is their calculation using Lattice QCD. It is is a non-perturbative approach to solving the QCD via a lattice gauge theory formulated on a lattice in space-time, which converges to the continuum QCD in the limit of an infinitesimally large lattice with infinite point density. Lattice QCD calculations of nucleon FFs are *ab initio* calculations from the underlying QCD theory. Since in practical lattice QCD, the achievable lattice spacing is necessarily finite, the above mentioned continuum limit of infinite point density has to be reached through extrapolation. The calculation of nucleon FFs in lattice QCD therefore requires calculations at several different values of the lattice spacing a, while at the same time,

the size of the box has to be chosen such that the nucleon fits in. This requires to increase the number of sites as the lattice spacing is decreased. In present lattice calculations, the length L of the box times the pion mass m_π is $Lm_\pi \sim 5$ [12].
Since the computational time cost of the calculations are inverse proportional to the pion mass, commonly non-physical, larger quark masses are used in these calculations. To connect the results to the physical world, a chiral extrapolation down to the real quark masses is necessary. Newest calculations, for example by Green *et al.* [129] have pion masses from 373 MeV down to near-physical values of 149 MeV, with lower pion masses reducing the systematic error associated with the extrapolation.

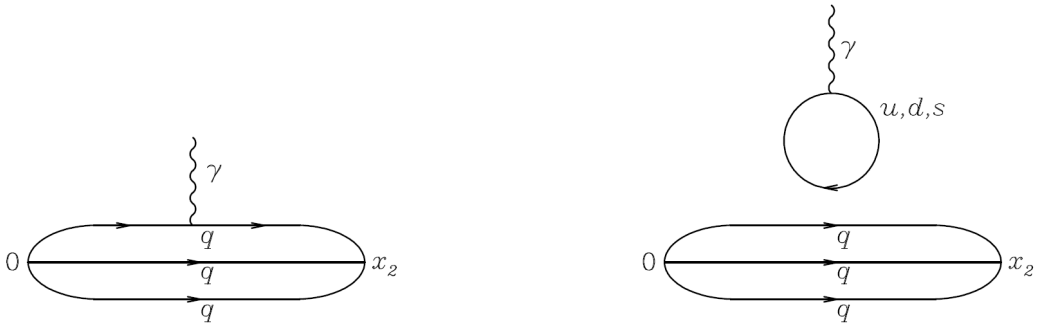

FIGURE 2.19: Diagrams of the two topologically different contributions in the calculation of nucleon FFs in lattice QCD. The left side shows the connected, the right side the disconnected diagram. Figure taken from reference [129].

To keep the physical quantities unchanged, the quark masses and bare coupling constant have to be adjusted as the lattice spacing is changed. A usual starting point for a lattice calculation is choosing the bare coupling constant g as well as the bare quark masses, which then fixes the lattice spacing. The desired physical quantity is then calculated in lattice units as a function of the quark masses, which are fixed by the pion mass in case of u and d quarks, and the kaon or ϕ in the case of the s quark. Finally, the extrapolation to the physical pion mass yields the sought after physical quantity, e.g. the nucleon mass or FFs.
Lattice results for nucleon FFs are only available for isovector FFs, since isoscalar FFs require calculations of disconnected diagrams (see figure 2.19). Unlike the connected diagrams, where a photon couples directly to one of the valence quarks, the quark loops in the disconnected diagrams are only attached to the valence quarks via gluons which are not indicated in lattice diagrams, hence the name disconnected.

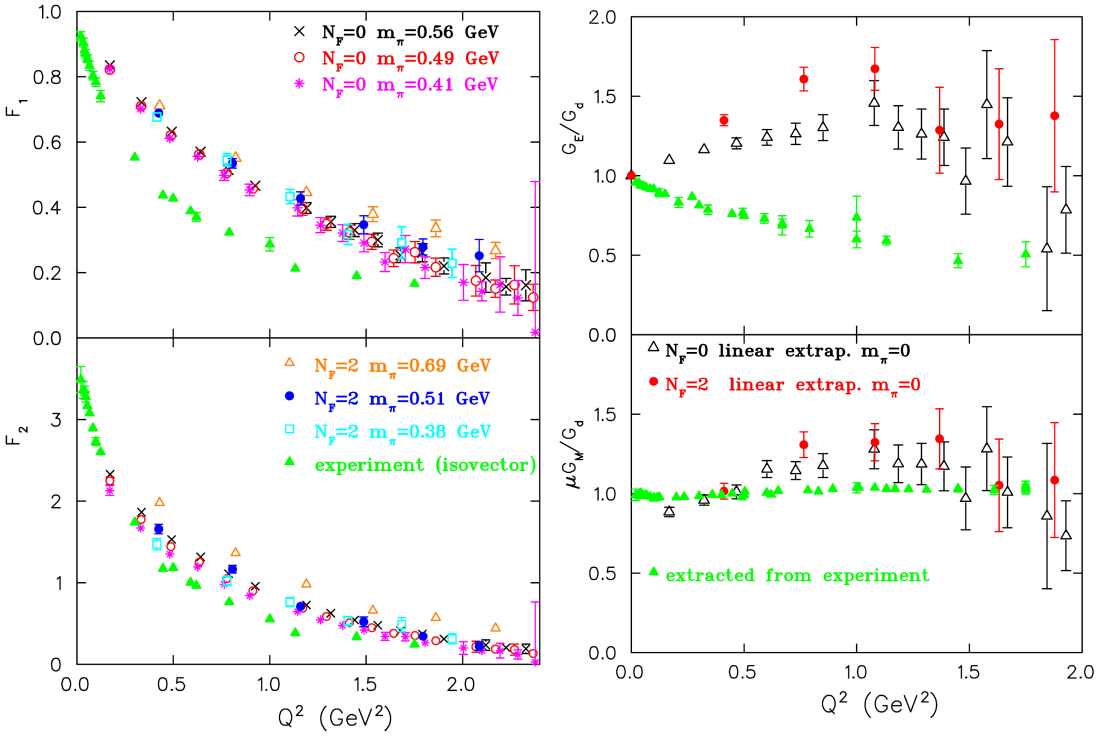

FIGURE 2.20: Lattice QCD results of the isovector FFs $F_1^V(Q^2)$ (upper left) and $F_2^V(Q^2)$ (lower left) from reference [130]. The right side shows the results for the Sachs FFS $G_E(Q^2)$ and $G_M(Q^2)$ each divided by the standard dipole FF in the chiral limit. Figure taken from reference [130].

Contributions from the disconnected diagrams require vast amounts of computing time and have therefore not been performed up to today. The isovector case can be calculated without the consideration of these diagrams, since they contribute equally to the proton and the neutron. Figure 2.20 shows results from Lattice QCD calculations for these isovector FFs in the SL region from reference [130].

2.4.6 Soft collinear effective theory

Soft collinear effective theory (SCET) can be used to describes the nucleon FFs in the region of moderate to high values of momentum transfer Q^2 by a factorisation into contributions associated with a hard and a soft scattering subprocess. SCET in this context is an effective tool to describe these subprocesses, which occur on different scales: hard rescattering with particle momenta of the order of Q^2, hard-collinear scattering with virtuallities of the order of ΛQ, as well as soft non-perturbative modes with momenta of order Λ^2 [131].

The approach was developed due to recent data in the intermediate momentum transfer range of ~5-10 GeV/c^2, e.g. taken at JLAB, which according to many phenomenological

studies could not be satisfactorily described by the hard scattering approach (see for example references [132, 133]) alone.

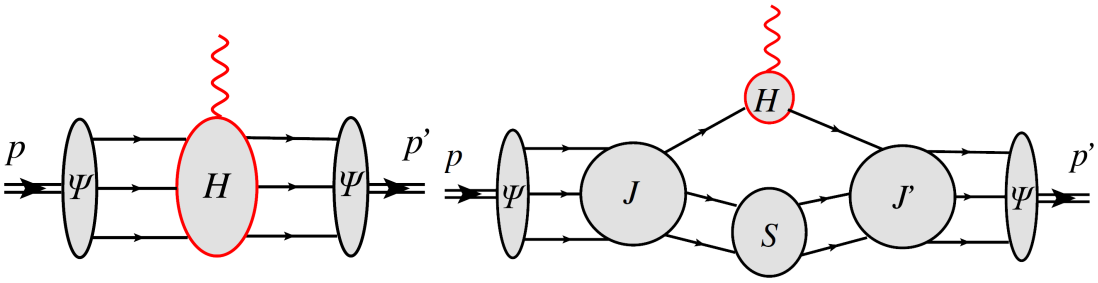

FIGURE 2.21: Reduced Feynman diagrams representing the two contributions to the virtual photon scattering of the proton within the SCET approach, the hard subprocess (left) and the soft subprocess (right). Figures taken from reference [131].

The contribution of the hard scattering process can be studied through QCD factorisation, which allows for a systematic computation of the process by order by order, with the dominant contribution being the diagram shown on the left side of figure 2.21 that represents the interaction of the virtual photon with a hard "blob" of gluons and quarks. The soft contribution can be interpreted as the hard interaction of the virtual photon with one quark, whereas the other spectator quarks remain soft (Feynman mechanism). This is shown as a reduced diagram on the right side of figure 2.21.

Combining these two contributions, the Dirac FF F_1 can be expressed as [131]

$$F_1 \simeq F_1^{(s)} + F_1^{(h)} \tag{2.58}$$

The hard scattering part is well known from the aforementioned QCD factorisation approach and can be expressed as [134]:

$$F_1^{(h)} = \int dx_i \int dy_i \mathbf{\Psi}(x_i)\mathbf{H}(x_i, y_i|Q)\mathbf{\Psi}(\mathbf{y_i}) \equiv \mathbf{\Psi} * \mathbf{H} * \mathbf{\Psi}, \tag{2.59}$$

where $\mathbf{H}$ denotes the hard coefficient function and $\mathbf{\Psi}$ denotes the nucleon distribution amplitudes.
The factorised form of the soft scattering part takes a more complicated form due to the different scales (see above) that are involved in the process [131]:

$$F_1^{(s)} = H(Q) \int Dy_i \mathbf{\Psi}(y_i) \int_0^\infty d\omega_1 d\omega_2 \mathbf{J}'(y_i, \omega_i Q) \tag{2.60}$$

$$\times \int Dx_i \mathbf{\Psi}(x_i) \int_0^\infty dv_1 dv_2 \mathbf{J}(x_i, v_i Q) \mathbf{S}(\omega_i, v_i). \tag{2.61}$$

Here, $\mathbf{\Psi}$ and $\mathbf{S}$ are nonperturbative functions describing the scattering of collinear and soft modes, H(Q) is a hard coefficient function, and $\mathbf{J}$ and $\mathbf{J}'$ are hard-collinear jet functions.

The Pauli FF F_2 can be factorised in a similar way to F_1. However, overlapping integration regions of soft and collinear contributions which lead to end-point singularities in the convolution integrals only allow for a partial factorisation of this FF. The partial factorisation can still be useful in a phenomenological analysis of the FFs in the region of intermediate Q^2, where Q^2 is large enough to allow for a power expansion, but the hard-collinear scale proportional to ΛQ is still small enough so the leading power asymptotic scale is not dominant. More details on the efforts the factorisation of F_2 can be found in reference [131].
The obtained results for the FFs F_1 and F_2 in leading order accuracy of both 1/Q and $\alpha_s(Q^2)$ can be summarised as [135]:

$$F_1(Q) \simeq e^{-S(Q,\mu)} U_1(Q,\mu) f_1(Q,\mu), \tag{2.62}$$

$$F_2(Q) \simeq \frac{4m_N^2}{Q^2} e^{-S(Q,\mu)} \left\{ U_1(Q,\mu) f_1(Q,\mu) + \frac{1}{4} \int_0^1 d\tau U_2(\tau, Q, \mu) f_2(\tau, Q, \mu) \right\}. \tag{2.63}$$

Here, $e^{-S(Q,\mu)}$ are the exponential Sudakov logarithms, U_1 and U_2 are functions describing the deviation from these logarithms, and f_1 and f_2 are the SCET-I FFs.

The QCD factorisation can be applied to both the TL and SL region of the proton EM FFs. Under the assumption of $|G_E| \simeq |G_M|$, the magnetic FF G_M in the TL region can be expressed in a simple way according to equation 2.57. Using this result, the SCET flavor combination can be written as [135]:

$$|e_u^2 f_1^u(q) + e_d^2 f_1^d(q)|^2 = \frac{4}{9} \frac{|G_M(s)|^2}{\left(1 - \rho^2 \frac{4\tau}{(1+\tau)^2}\right)} \frac{1 + \frac{1}{2} r \cos\delta + \frac{1}{16} r^2}{1 - r\cos\delta + \frac{1}{4} r^2}, \tag{2.64}$$

$$\cos\delta = \frac{\mathcal{R} f_1^u f_1^{d*}}{|f_1^u||f_1^d|}, \quad r = \frac{|f_1^d|}{|f_1^u|}, \quad \rho = \frac{1}{2}(1+\tau)\frac{|F_2|}{|F_1|}, \quad 0 < \rho < 1, \quad \tau = \frac{4m_N^2}{q^2} > 0.$$

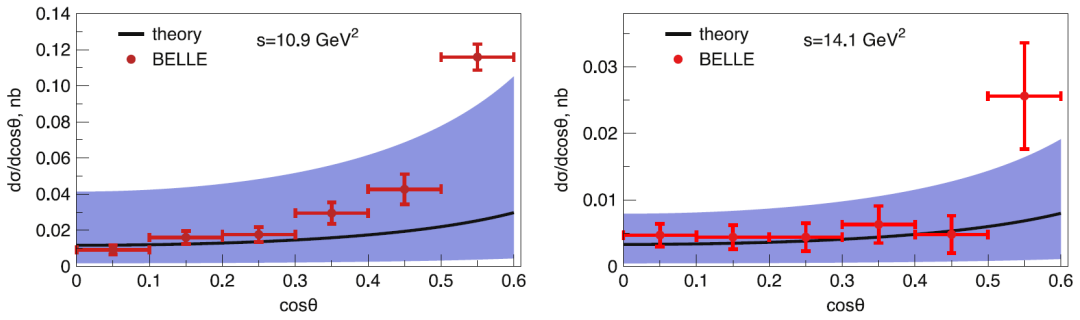

FIGURE 2.22: Prediction of the differential cross section from the SCET model for chosen parameters of $\delta \simeq 0$ and $\rho = 0.95$ compared with BELLE data [136] at two different CM energies. The left side shows a CM energy of 10.9 GeV with a chosen value of r=0.5, the right side shows a CM energy of 14.1 GeV with r=0.6, the shaded area in both plots indicates the region where $0 < \rho, r < 1$. Figure taken from reference [135].

The parameters ρ, r, and δ can not be fixed from FF data and have to be chosen. Figure 2.22 shows the predicted differential cross section $d\sigma/d\cos\theta$ up to $\cos\theta$=0.6 for two CM energy values compared with data from the BELLE experiment. The chosen values for the aforementioned parameters are $\delta \simeq 0$, $\rho = 0.95$, and r=0.5 (left plot) or r=0.6 (right plot), the shaded area gives the range of the model for $0 < \rho, r < 1$. The predicted behaviour of the integrated cross section with the restriction $\cos\theta < 0.6$ is shown in figure 2.23, once again with $\delta \simeq 0$, $\rho = 0.95$, and r=0.5. The left side shows a comparison with BELLE data, while the right shows a prediction for the future PANDA experiment.

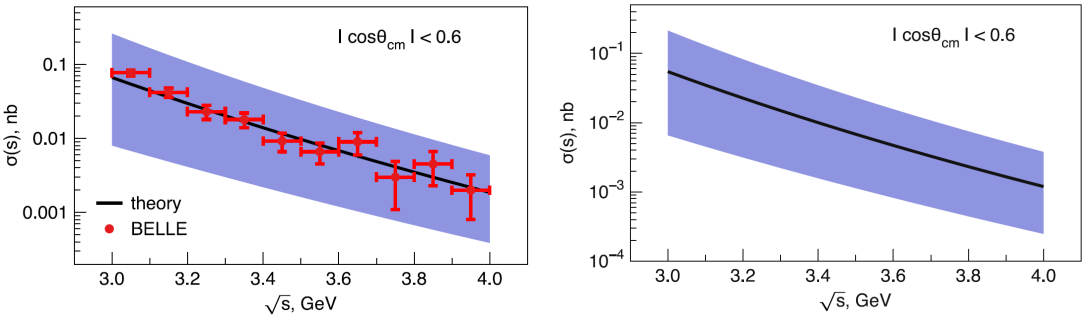

FIGURE 2.23: Prediction of the integrated cross section with the restriction $\cos\theta < 0.6$ from the SCET model. Parameters have been chosen as $\delta \simeq 0$, $\rho = 0.95$, and r=0.5, the shaded area gives the range of the model for $0 < \rho, r < 1$. The left side shows a comparison with BELLE [136] data, the right side a prediction for the future PANDA experiment. Plots are taken from reference [135].

Chapter 3

The BESIII Experiment

This chapter gives an overview of the BESIII experiment at the Institute for High Energy Physics in Beijing [137], where the data analysed within this thesis was taken. BESIII is a cylindrically symmetric multi purpose detector, consisting of several subdetectors which will be described later in this chapter. It is located at the Beijing Electron-Positron Collider II (BEPCII), which is a successor of the first Beijing Electron-Positron Collider (BEPC) operated between 1989 and 2004.

3.1 Beijing Electron-Positron Collider II

BEPCII is an upgrade of BEPC, which was a single ring electron-positron storage ring designed to operate in the τ - charm energy region [138]. BEPC had a maximum luminosity of approximately $10^{31}\ cm^{-2}s^{-1}$ and provided a beam to two experiments over its lifetime, the Beijing spectrometer (BES) [139] and the upgraded BESII.
BEPCII [140–142] was built in the existing tunnel of BEPC with a circumference of 240 meters, using a symmetric double ring design. The operating mode was changed from single-bunch to multi-bunch, which, together with the micro-beta technique (see section 3.2.1), allows for a much higher design luminosity of $10^{33}\ cm^{-2}s^{-1}$ This luminosity was reached in 2016 setting a new world record for accelerators in that energy range. The collider was optimised for a beam energy of 1.89 GeV, corresponding to a center of mass energy at the Ψ (3770) resonance.

BEPCII has a linear accelerator stage (LINAC) of 202 meters length, consisting of a positron source, an electron gun as well as klystrons to accelerate electrons and positrons to the desired energy before injection into the storage ring. This LINAC allows for injection rates of up to 50 mA/min for positrons and 200 mA/min for electrons.

TABLE 3.1: Comparison of BEPC and BEPCII design parameters, taken from reference [137]

Parameters	BEPCII	BEPC
Center of mass Energy (GeV)	2 - 4.6	2 - 5
Circumference (m)	237.5	240.4
Number of rings	2	1
RF frequency f_{rf} (MHz)	499.8	199.5
Peak luminosity at 2×1.89 GeV ($cm^{-2}s^{-1}$)	$\sim 10^{33}$	$\sim 10^{31}$
Number of bunches	2×93	2×1
Beam current (A)	2×0.91	2×0.035
Bunch spacing (m/ns)	2.4/8	-
Bunch length σ_z (cm)	1.5	~ 5
Bunch width σ_x (μm)	~ 380	~ 840
Bunch height σ_y (μm)	~ 5.7	~ 37
Relative energy spread	5×10^{-4}	5×10^{-4}
Crossing angle (mrad)	± 11	0

The storage ring can store up to 93 bunches in its 237.5 meter circumference ring with a spacing of usually 8 ns or 2.4 meters between them. This results in an overall single beam current of 0.91 A in collider mode. For the data set used in the analysis of this work, the spacing was reduced to 6 ns.

FIGURE 3.1: Aerial view of the facilities of the BEPCII collider at the institute for high energy physics in Beijing, where the BESIII detector is located.

The outer and the inner ring cross each other at two interaction points. Compared to BEPC, there is a small crossing angle between the two beams in these interaction points to allow the operation in multi-bunch mode. Located at the southern interaction point is the BESIII detector, which will be described in the following sections.

3.2 The BESIII detector

To measure the tracks and properties of the reaction products created in the interaction region of BEPCII, a cylindrical multi-purpose detector covering 93% of the full solid angle is used. It consists of a number of subdetectors fulfilling different purposes, such as a Multilayer Drift Chamber (MDC) to provide tracking information, a Time Of Flight (TOF) system to allow the separation of different particle species, an electromagnetic calorimeter (EMC) to measure energy deposition, as well as a muon counter (MUC), which helps to distinguish muons from other particles.

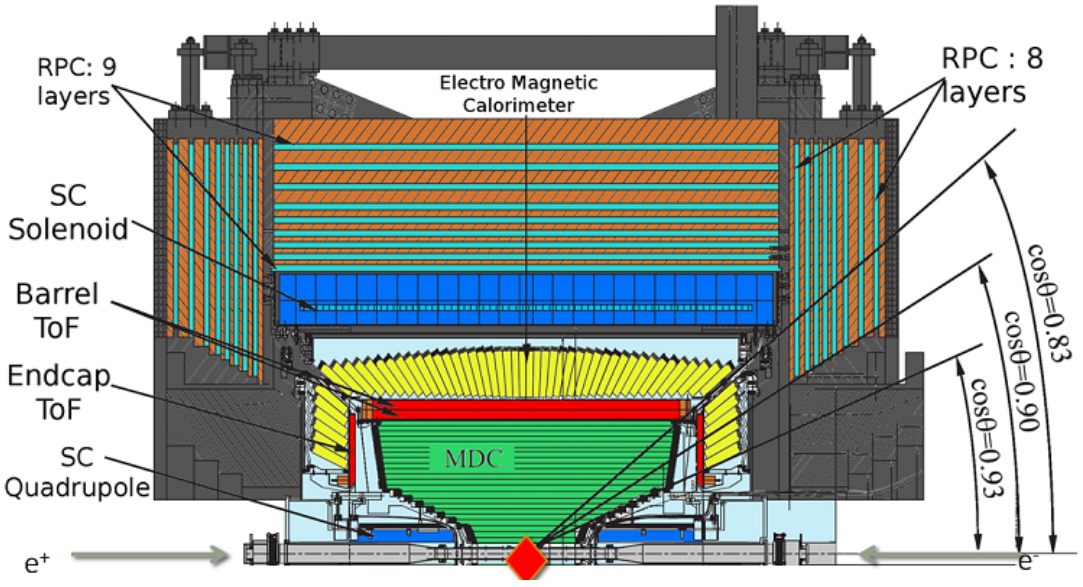

FIGURE 3.2: Overview of the BESIII Detector and its subdetectors, taken from reference [143].

These components are cylindrically arranged around the beryllium beam pipe, and are surrounded by a superconducting solenoid magnet providing a 1 Tesla magnetic field to the detector, which allows for optimal momentum measurements for charged tracks in the τ-charm region. An overview of the detector layout can be seen in figure 3.2, its main parameters are shown in table 3.2 along with those of its predecessor BESII as comparison.

3.2.1 Interaction region

As mentioned before, the two beams cross each other in the interaction region under a crossing angle of ± 11 mrad. This relatively large angle allows for a close packing of beam bunches without parasitic collisions, which increases the possible luminosity. In addition, a final beam focussing through the use of the micro beta technique is employed

TABLE 3.2: Performance parameters of different subdetectors of BESIII compared with BESII, taken from reference [137]

Subdetector	parameter		BESIII	BESII
MDC	Single wire $\sigma_{r\phi}$ (μm)		130	130
	σ_p /p (1 GeV/c)		0.5%	2.4%
	σ (dE/dx)		6 %	8.5%
EMC	σ_E /E (1GeV)		2.5%	20%
	Position resolution (1 GeV)		0.6 cm	3 cm
TOF	σ_T (ps)	Barrel	100	180
		End cap	110	350
Muon	No. of layers (barrel/end cap)		9/8	3
	cut-off momentum (MeV/c)		0.4	0.5
	Solenoid magnet Field (T)		1.0	0.4
	$\Delta\Omega/4\pi$		93%	80%

to reduce the vertical beam size and thereby further increase the achievable luminosity. This is realised by an arrangement of superconducting quadrupole magnets placed very closely to the interaction point (see figure 3.3). The two innermost of these magnets are installed 0.55 meters from the interaction point and feature a very compact design, including a vertical focussing quadrupole (SCQ), a horizontal bending dipole (SCB), a skew quadrupole (SKQ) and three anti-solenoid windings (AS1, 2 , 3). Additional focussing is provided by six pairs of quadrupole magnets further along the beamline, the whole setup is closed of with a pair of beam bending magnets (OWBL) 13.52 meters from the interaction point [137].

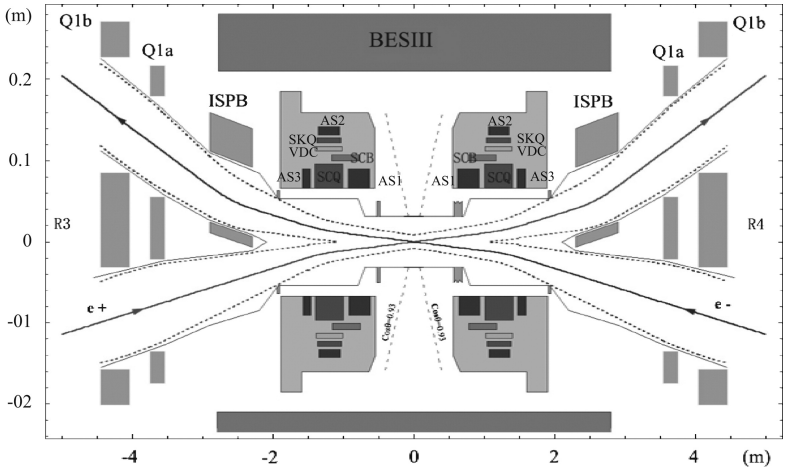

FIGURE 3.3: Arrangement of quadrupole magnets for beam focussing in the interaction region, taken from reference [137]

3.2.2 Beam pipe

The beam pipe must fulfil several requirements. To minimize the material between the interaction point and the detector, especially in the acceptance region, the material must have a low density and low atomic number, while being mechanically stable with a low wall strength. High amounts of material would lead to secondary interactions as well as multiple scattering of the reaction products, which is undesired. The walls must be able to maintain the high vacuum of 5×10^{-10} torr necessary to reduce beam-gas related background, while having a high resistance to differential pressure, a high thermal conductivity and a high electric conductivity to shield the beam bunches from the RF radiation.

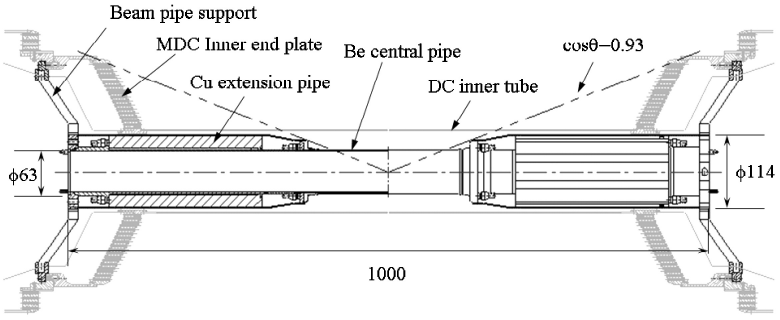

FIGURE 3.4: Schematic drawing of the beam pipe surrounding the interaction point, taken from reference [137].

To fulfil all these requirements, beryllium was chosen as the material for the 1 meter long beam pipe with an inner and outer diameter of 63 and 114 mm, respectively. The beam pipe consists of an 29.6 cm beryllium central pipe which is welded together with two copper extension pipes. The central pipe itself has 0.8 mm strong inner wall and an 0.6 mm strong outer wall. The schematic composition of the whole structure can be seen in figure 3.4. Since the maximum heat load on the inner wall at full current is about 700 W, an active fluid cooling system using high purity mineral oil is installed between the outer and inner beryllium wall.

3.2.3 Multilayer drift chamber

The tracking detector of the BESIII spectrometer is a multilayer drift chamber. The main tasks of this subdetector are the following:

- Three dimensional reconstruction of charged tracks
- Measurement of the momentum of charged particles

- Measurement of the specific energy loss (dE/dx) of charged particles, used for particle identification (PID)
- Reconstruction of long lifetime hadrons decaying in the MDC volume (e.g. K_S^0 and λ)
- Providing a level 1 trigger through reconstructed tracks and reject background tracks

The design of the chamber is optimised for the tracking of the relatively low momentum particles in the τ-charm energy region. It focusses on a high momentum resolution and precise measurement of dE/dx. A multilayer small cell design was chosen for this purpose, using a helium based gas mixture (60% He, 40% C_3H_8). This mixture minimises the effect of multiple scattering while maintaining a reasonable resolution of the dE/dx measurement of $\frac{\sigma(dE/dx)}{dE/dx} \approx 6\%$ due to its specific ionisation.

The MDC is divided into a total of 43 cylindrical layers of drift cells, which are units of one sense wire (gold-plated tungsten) surrounded by 8 field wires (gold-plated aluminium), both of which are coaxial with the beam pipe. The average single wire position resolution is about 130 μm in the R_{xy} - ϕ plane, limited by electron diffusion and uncertainties in the time measurement due to electronics. In z direction, the position is measured using stereo wires, which are not exactly axial, but tilted by an angle of -3.4° to +3.9° to the axis. All of the 8 layers of the inner chamber are stereo layers, while the outer chamber features 16 stereo layers and 19 axial layers. The achieved resolution with the chosen stereo angles is about 3-4 mm.

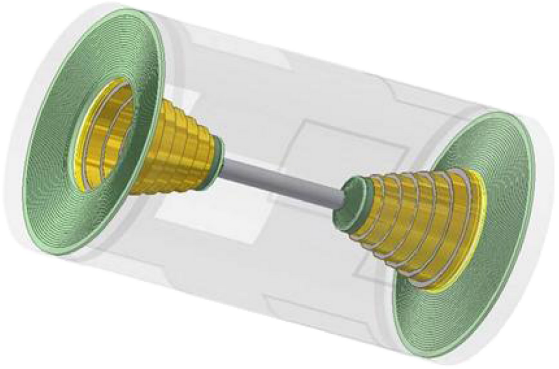

FIGURE 3.5: 3D model of the Multilayer Drift Chamber of BESIII, taken from reference [144].

Since the detector operates in a 1 tesla magnetic field provided by the superconducting solenoid magnet, any charged tracks in the detector assume a helix shape with a radius depending on the momentum of the particle. A precise measurement of the curvature of these helices therefore allows to deduce the momentum of charged particles passing

through the MDC. The resolution of the measured momentum depends on the position resolution of the drift chamber, in the case of the BESIII MDC a relative transverse momentum resolution of 0.5% for particles with 1 GeV momentum can be achieved.

Track reconstruction at BESIII uses an iterative tracking algorithm. In a first step, hits in the MDC are combined to track segments using pre-calculated patterns. These segments are then combined to circular tracks using a fit with the least-square method, followed by an iterative helix fit procedure [145]. Additional hits close to the found track candidate are added in a last step, before the track is refitted using the Kalman-filter technique. A GEANT4 [146] based algorithm is used to extrapolate the found tracks and provide the precise position and momentum to the outer subdetectors, considering the magnetic deflection and ionisation loss of the particles. The expected tracking efficiency for particles with transverse momentum larger than 150 MeV/c from Monte Carlo simulations is above 98% [147].

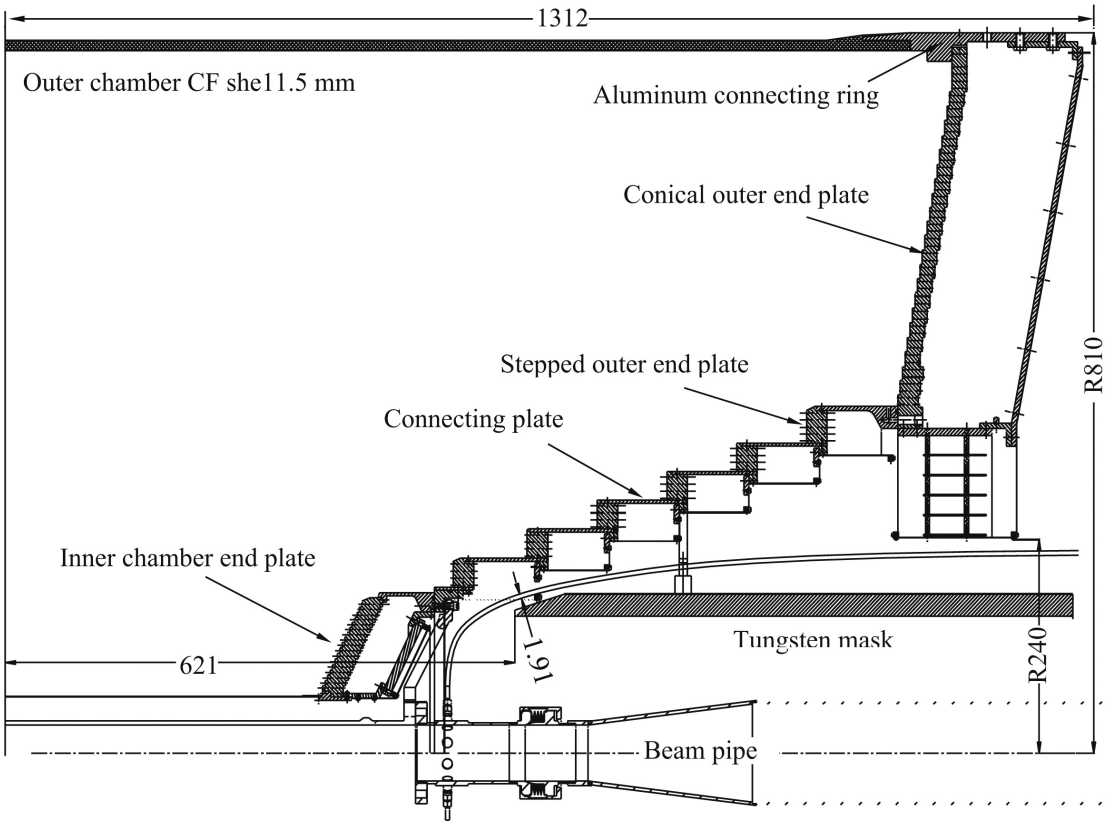

FIGURE 3.6: Schematic drawing of the mechanical design of the MDC, taken from reference [137].

Figure 3.6 shows the mechanical design of the MDC. It consists of an outer and an inner chamber which share a common gas volume, without a dividing wall to avoid an additional source of multiple scattering. The inner radius of the inner chamber is 59 mm with a 2 mm gap to the beam pipe, the outer radius of the outer chamber is 810 mm.

To be able to place the final focussing quadrupole as close as possible to the interaction point, the end plates of the inner chamber have a stepped conical design. The maximum length of the outer chamber is 2.582 m. The polar angle acceptance of the detector ranges from $\cos(\theta) \leq 0.83$ for the innermost and $\cos(\theta) \leq 0.93$ for the outermost layer.

Since the inner chamber of the MDC is showing ageing effects due to the high intensity of radiation close to the interaction point, there is an ongoing effort to replace it with a Cylindrical Gas Electron Multiplier (CGEM) detector. This state of the art detector design is expected to improve the spatial resolution of the inner detector in z direction to below 1 mm, while keeping a similar spatial resolution in the R_{xy} - ϕ plane as well as momentum resolution. The new detector is planed to be operated for about 5 years, foreseeably until the end of the BESIII experiment.

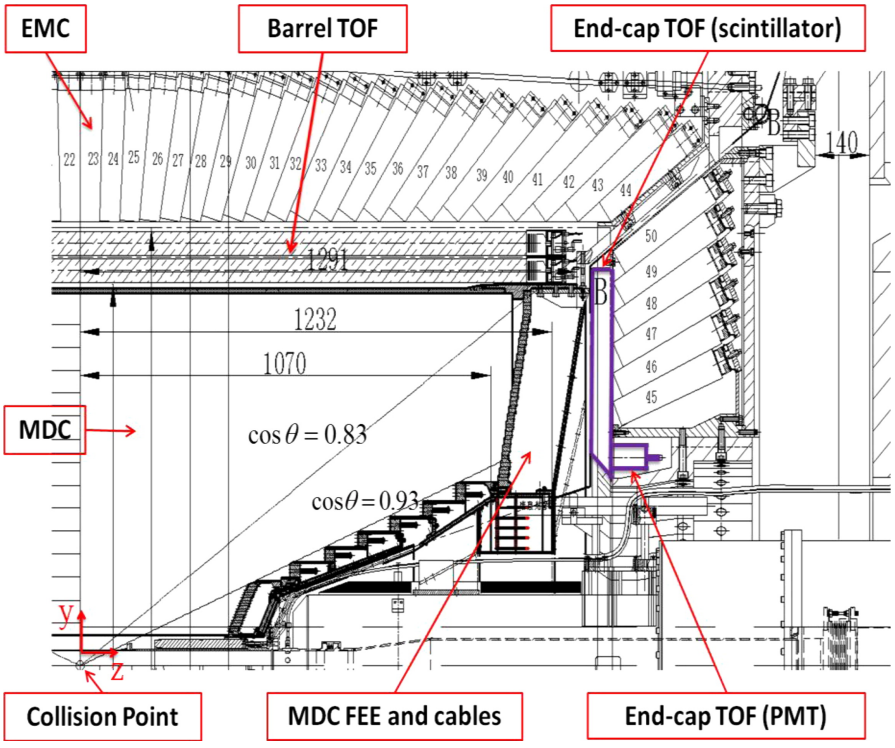

FIGURE 3.7: Schematic overview of the TOF barrel and endcap detectors within the BESIII spectrometer, taken from reference [148]

3.2.4 Time-of-flight system

The TOF system is used, together with the dE/dx measurement of the drift chamber, as the main means of BESIII to identify charged particles. In addition, the TOF can provide a fast trigger signal and help to reject cosmic background events. The decision to use a TOF based particle identification system for BESIII as opposed to for example

a Ring Imaging Cherenkov (RICH) detector was based on considerations of the available space, solid angle coverage as well as cost and technical complexities of such alternatives.

The TOF system is placed between the MDC and the EMC detector and consists of a double layer barrel and two single layer endcap parts with a small gap between them (see figure 3.7). The barrel part covers a solid angle of $|\cos(\theta)| < 0.83$, the two endcap parts on either side of the detector cover a solid angle of $0.85 < |\cos(\theta)| < 0.95$.
Each layer of the barrel TOF consists of 88 trapezoidal plastic scintillation counters of 2.3 m length and 5 cm thickness. They are cylindrically arranged around the beam axis within a radial space between 0.81 m and 0.93 m from the beam pipe. Each counter is read out at both ends by two fine-mesh Photomultiplier Tubes (PMT).
The endcaps are each built of 48 trapezoidal scintillation counters arranged in a single circular layer. They are 48 cm long and have the same thickness as their barrel counterparts, with a width of 10.9 cm at the top and 6.2 cm at the bottom. The inner end of each scintillator is cut at an angle of 45° to reflect light to the single fine-mesh PMT attached to the outside of the bar (see figure 3.8).

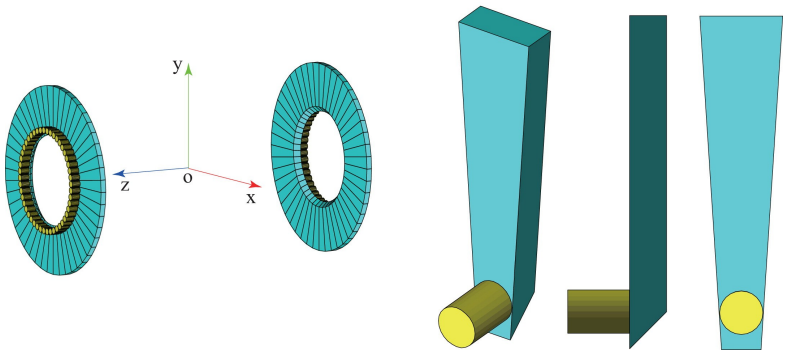

FIGURE 3.8: (left) Setup of the endcap TOF system, (right) schematic of a single plastic scintillation counter with attached PMT , taken from reference [149]

The ability of the TOF system to separate different particle species is mainly determined by its time resolution. The time resolution in turn depends for the largest part on the intrinsic time resolution of the scintillation counters and is further limited by several effects: the time resolution and jitter of the readout electronics, the uncertainty from the determination of the interaction vertices due to bunch length, uncertainty from bunch timing, from the hit position along the scintillation bar, registration of the global timing marker from the accelerator RF clock, momentum measurement and time-walk effects. This leads to a total time resolution of 110 ps for the endcaps and 80 ps for the barrel, assuming both layers can be used to improve the intrinsic time resolution as well as the uncertainty from time-walk. If this is not possible, the barrel resolution drops to about 100-110 ps.

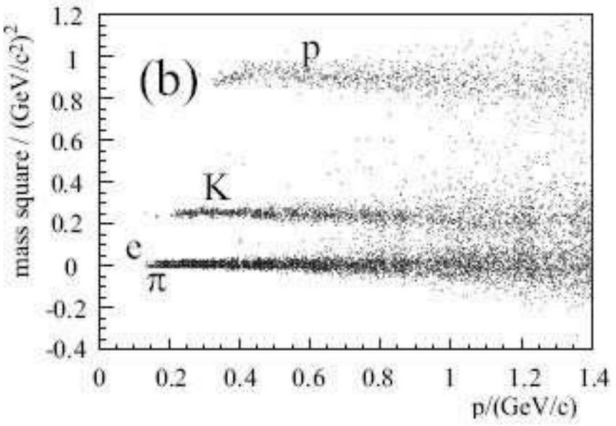

FIGURE 3.9: Mass square distributions for different particles calculated from their measured TOF for particle identification purposes, taken from reference [147]

The measured TOF allows to deduce the velocity (β·c) of the particle, which can be used together with the measured momentum to calculate the mass m of the particle:

$$\beta = \frac{L}{c \times t_{meas}}, \quad m^2 = p^2 \times \frac{1-\beta^2}{\beta^2} \tag{3.1}$$

where t_{meas} is the measured TOF, L is the flight path length, p is the momentum of the charged particle measured by the MDC, and c is the speed of light in vacuum.

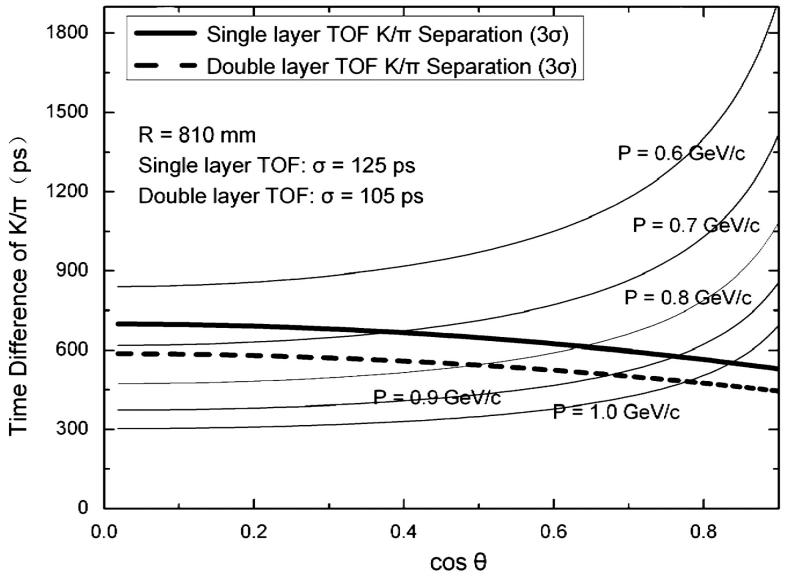

FIGURE 3.10: Kaon/pion separation using the measured TOF as a function of cos(θ), assuming a single (solid line) or double (dashed line) layer usage in the barrel part of the TOF system, taken from reference [137].

As figure 3.9 shows, the calculated mass square with the achieved time resolution allows

for a good separation of particles up to around 0.8 GeV, especially between electrons and protons, which is the most relevant separation for this work. At higher momenta, the separation power becomes worse due to the lower time of flight of particles and the corresponding higher relative uncertainty of the time measurement.
The achievable kaon and pion separation as a function of $\cos(\theta)$ from simulation can be seen in figure 3.10. The thick solid line and the thick dashed line represent the threshold above which a 3 σ separation between kaon and pion is possible using a single or both layers of the TOF system, respectively. In the simulation, a conservative time resolution of 125 ps for the single and 105 ps for the double layers TOF system was assumed. For the endcaps, the 3 σ separation limit is about 0.9 to 1 GeV due to the worse time resolution of the single layer system and increased electronic noise.

3.2.5 Electromagnetic calorimeter

Calorimetry is done at BESIII using a CsI(Tl) electromagnetic calorimeter. The main purpose of this detector is the measurement of the deposited energy of neutral and charged particles with high energy resolution and adequate position resolution. Additionally, the characteristics of electromagnetic showers of electrons, muons and hadrons can be used to distinguish these particles, making the EMC another PID tool especially for the separation of muons and electrons.

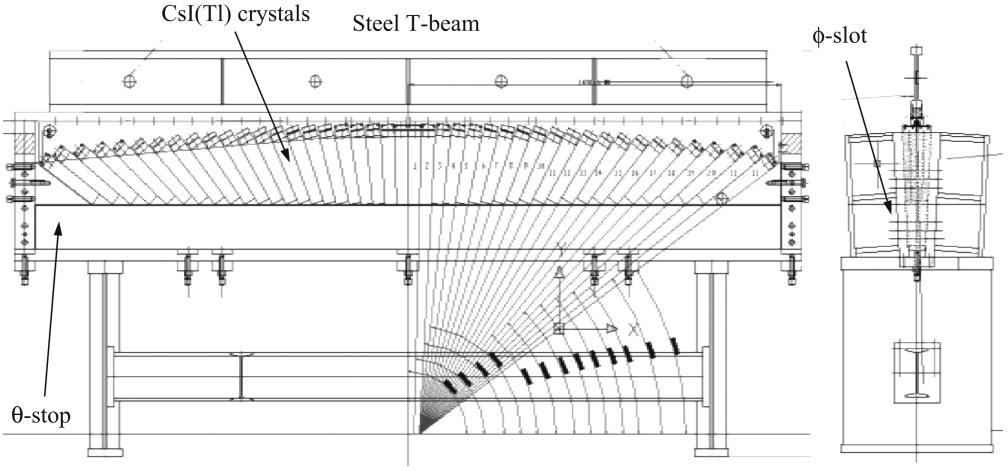

FIGURE 3.11: Schematic design of the EMC of BESIII, taken from reference [137].

Precise measurement of the energy and hit coordinates of photons is crucial for many processes of interest proposed by the BESIII physics program, e.g. to separate direct photons from π_0 and η decays from those produced in radiative decay processes such as $J/\psi \to \gamma\pi\pi$, $J/\psi \to \gamma KK$ or similar processes from Ψ' or Ψ''. Since the energy of most photons produced in these reactions is quite low, the calorimeter must have a

good detection efficiency and energy resolution for particles down to about 20 MeV. In addition, the EMC, similar to the MDC, provides another source for a level 1 trigger signal.

The EMC, like the TOF system, consists of a barrel part and two endcaps. There is a small gap between them, leading to a solid angle coverage of $|\cos(\theta)| < 0.83$ for the barrel and $0.85 < |\cos(\theta)| < 0.95$ for the endcaps with a total coverage of 93% of 4π. The barrel has an inner radius of 94 cm and a length of 2.75 m, the endcaps are each placed 1.38 m from the interaction point and have an inner radius of 88 cm and an outer radius of 110 cm. The total weight of the calorimeter is 25.6 tons.
In total, the BESIII EMC features 6240 CsI(Tl) scintillating crystals, of which 5280 are installed in the barrel and 960 in the endcap parts. The use of the EMC for particle identification requires a fine segmentation of the crystals to distinguish hadron showers from electron showers with pattern recognition and reduce shower overlap. The material of the crystals, along with a readout consisting of silicon photodiodes, was chosen to provide a good energy resolution and detection efficiency for low energy photons. Additional factors include a high light yield and density. The crystals of the barrel part are divided into 44 rings with each crystal pointing towards the interaction point at a small angle of about 1.5° to 3°, which prevents photons from the interaction point from escaping through gaps in the arrangement. The endcaps are each divided into 6 rings which are split into two tapered half-cylinders with varying numbers of crystals per ring. The length of each individual crystal is 28 cm or about 15 times the radiation length X_0, the front surface is 5.2 cm × 5.2 cm. A schematic drawing of the whole setup is shown in figure 3.11.
The design of the EMC allows a detection of photons and electrons from about 20 MeV up to 2 GeV with an energy resolution of $\frac{\sigma_E}{E} \leq 2.5\%$ at 1 GeV. The resolution is mainly limited by shower energy leakage at the back of the crystals, photodiode and amplifier noise, non-uniformity of light production and dead material between the crystals. The position resolution of the subdetector for an electromagnetic shower is $\sigma_{x,y} \leq 6mm/\sqrt{E(GeV)}$.

3.2.6 Muon identifier

The muon system of BESIII is installed in the magnet yoke of the superconducting magnet. It is designed to separate muons mainly from pions and other hadrons by their characteristic hit patterns when they penetrate the magnet yoke and the Muon System. A good identification of muons is important for a wide range of reactions relevant to the BESIII physics program. Examples are the studies of leptonic decay branching fractions, semileptonic decays of $c\bar{c}$ resonances, rare charmed meson decays and τ decays.

Analysing these reactions requires a high efficiency of muon identification and a good

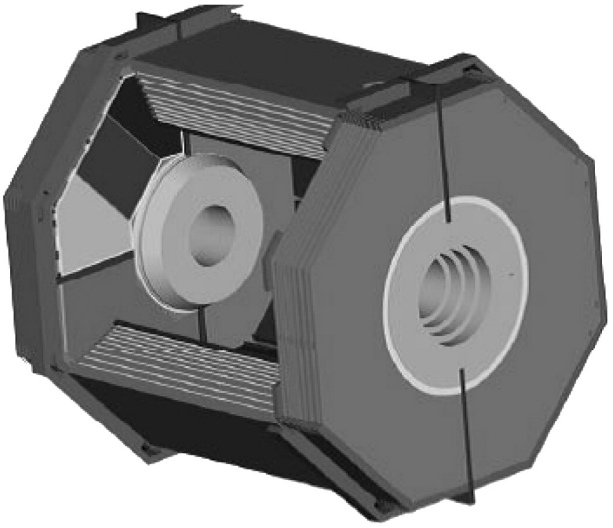

FIGURE 3.12: Three dimensional model of the Muon Identifier of BESIII, taken from reference [137].

separation from punch through pions or other hadrons from muons with a momentum cutoff as low as possible.
For this task, BESIII uses a Muon Identifier subdetector consisting of Resistive Plate Counters (RPC) interleaved with iron absorbers. Like the EMC and the TOF system, the Muon Identifier has a barrel and two endcap parts. The barrel part consists of nine layers of RPCs which are inserted into the steel plates of the magnetic flux return, with the first RPC layer placed in front of the first steel plate layer followed by an alternating pattern. The endcaps only contain eight RPC layers between the nine layers of steel plates due to space restrictions. The total thickness of the steel plates is 56 cm for the barrel part and 43 cm for each endcap.

The barrel part has an outer radius of 2.62 m and an inner radius of 1.7 meters and covers a polar angle of $\cos(\theta) \leq 0.75$. The endcaps are placed 2.05 m from the interaction point, the distance of the outer end of the detector to the interaction point is 2.8 m. Unlike the EMC and TOF system, the muon counter does not have a gap between endcap and barrel part, therefore the endcaps cover a polar angle of $0.75 \leq \cos(\theta) \leq 0.89$ giving the muon system a total coverage of 89% of 4π.

3.2.7 Trigger system and data acquisition

The trigger system of BESIII separates physics events of processes of interest from background events, e. g. from cosmic rays, electronic noise or machine background. An effective trigger system helps getting a high rate of data from desired physics processes

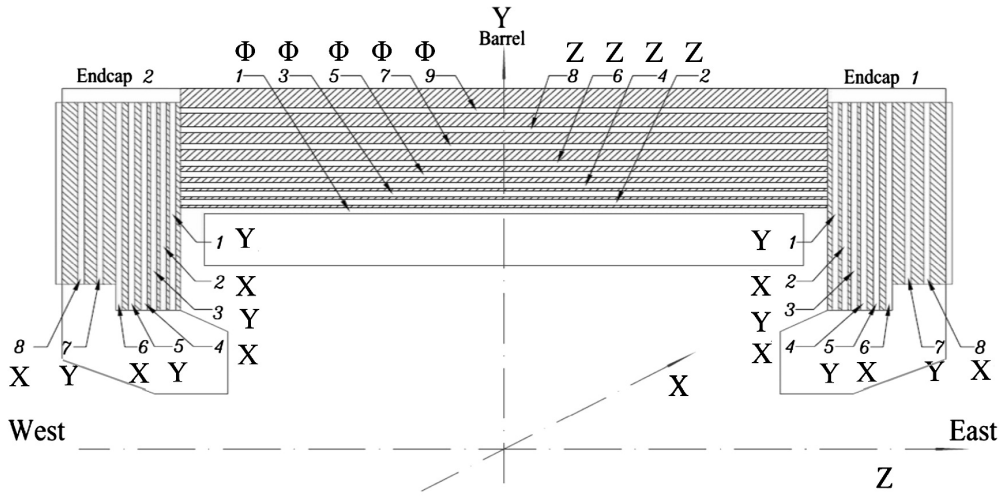

FIGURE 3.13: Schematic design of the Muon Identifier of BESIII, taken from reference [137].

TABLE 3.3: Parameters of the BESIII Muon Identifier, taken from reference [137].

Barrel	Value
Inner radius (m)	1.7
Outer radius (m)	2.62
Length (m)	3.94
Weight (tons)	300
Number of RPC layers	9
Polar angle coverage	$\cos(\theta) \leq 0.75$
Endcap	Value
Inner distance to IP (m)	2.05
Outer distance to IP (m)	2.8
Weight (tons)	208
Number of RPC layers	8
Polar angle coverage	$0.75 \leq \cos(\theta) \leq 0.89$

while keeping the event rate at a level the Data Acquisition (DAQ) system can handle, which is about 4 kHz in the case of the BESIII DAQ system. Since the rate of signal events can go as high as 2 kHz at the J/ψ peak, the trigger system must be able to suppress background events such as Bhabha scattering and beam related background to a rate below 2 kHz.

The Trigger System is a two level system, which consists of a Level-1 (L1) hardware trigger and a Level-3 (L3) software trigger operating on an online computing farm. The dataflow of the system is shown in figure 3.14. The L1 trigger receives signals from the MDC, TOF and EMC subdetectors and gives a readout signal to the front-end electronics buffers about 6.4 μs after a collision in case of an accepted event. The data

TABLE 3.4: Event rates of physics and background events before and after application of the L1 and L3 trigger, taken from [137]

Processes	Event rate [kHz]	After L1 [kHz]	After L3 [kHz]
Physics	2	2	2
Bhabha	0.8	Pre-scaled	Pre-scaled
Cosmic ray	<2	∼0.2	∼0.1
Beam background	$> 10^4$	<2	<1
Total	$> 10^4$	4	3

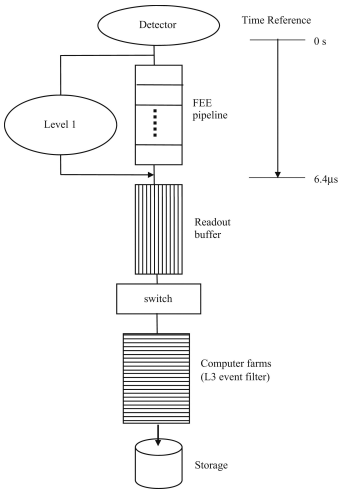

FIGURE 3.14: Dataflow of the BESIII Trigger System, taken from Ref. [137]

is then transmitted to the L3 event filter for further processing. An overview of the L1 trigger logic can be seen in figure 3.15.

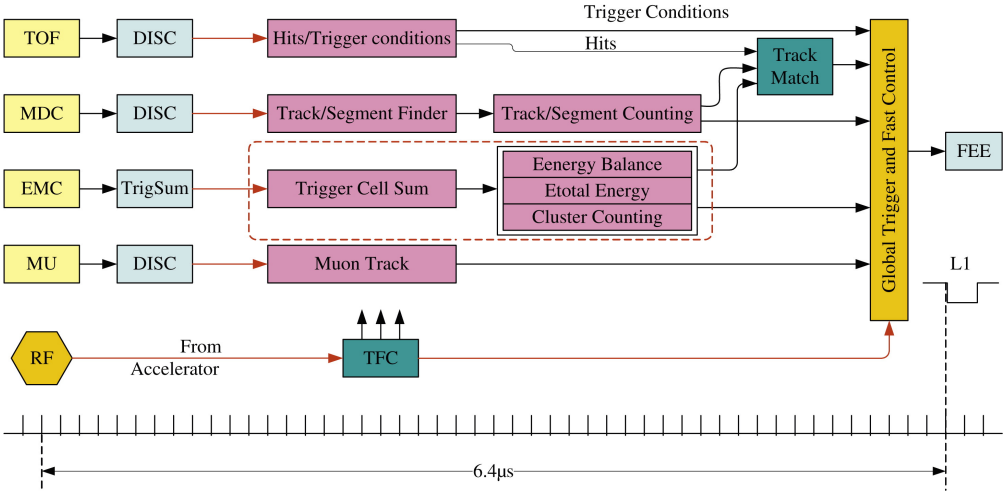

FIGURE 3.15: Block diagram of the L1 trigger system, taken from Ref. [150]

At the J/ψ peak, the L1 trigger already removes the largest part of the expected 800 Hz of Bhabha scattering events as well as cosmic ray events (1.5 kHz), mostly through

trigger signals from the MDC and TOF subdetectors. The high rate of beam related background (dominated by lost electrons and positrons) of more than 10^4 Hz due to the high beam currents is reduced to below 2 kHz by the L1 trigger and then further to below 1 kHz by the L3 software trigger. The event rates of signal and background events before and after the L1 and L3 triggers are shown in table 3.4.

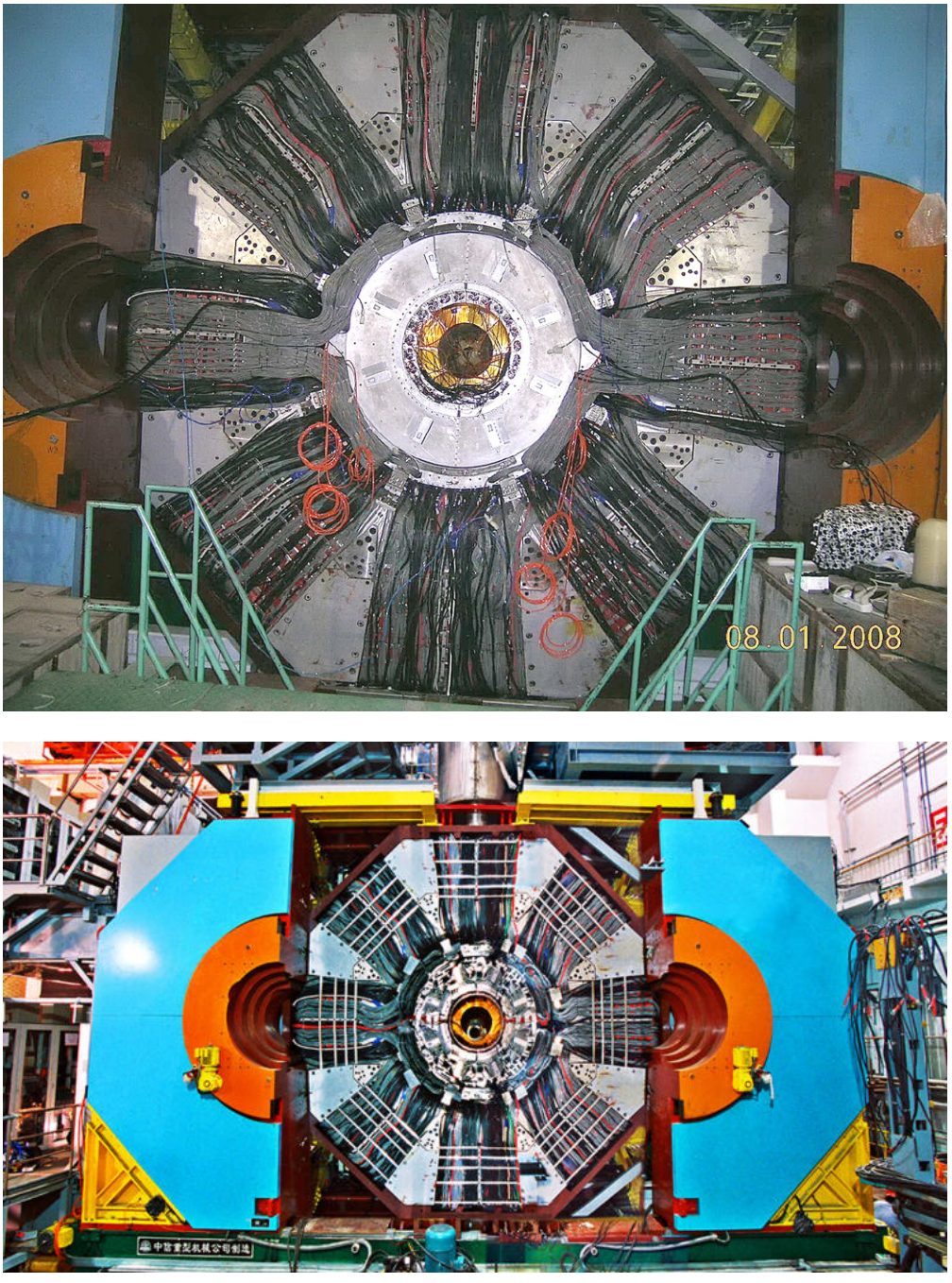

FIGURE 3.16: Photos of the open front of the BESIII detector

Chapter 4

Data Sets

The BESIII experiment was designed to collect data in the τ-charm energy region, an energy region above the production threshold of τ leptons characterised by the existence of many charmonion resonances. Over its more than 10 years operational history, it has collected some of the largest data sets available in the world for this energy range, especially at the J/ψ resonance.

The data taken at BESIII can be classified into two categories: the first is data taken at one specific energy at (or close to) a resonance, where usually a large amount of luminosity is collected. The second are dedicated scan data sets, where data is taken at many points over a large range of energy, with comparatively low amount of luminosity per data point. This second kind of data can be used for example to measure the $R_{had}=\frac{\sigma(e^+e^-\to hadrons}{e^+e^-\to\mu^+\mu^-}$ value, which is the ratio between the cross section of e^+e^- annihilation into hadrons and that into muons, or baryon FFs as done in this work (note: R_{had} as described above is not to be confused with the R value used throughout this thesis, which is defined as the ratio of the electric and magnetic FF and will be introduced later).
EM FFs of the nucleon, specifically of the proton which is the main subject of this work, can in principle be extracted from both kinds of data. In the case of resonance data, two challenges can arise: firstly, there can be strong background from the resonance decaying into proton antiproton pairs. This background can be hard to separate from the direct production process of $e^+e^-\to p\bar{p}$, especially for higher energy resonances where the cross section of the signal process is quite low. Secondly, the goal is to measure nucleon form factors as a function of the momentum transfer q^2, whereas data at resonances usually has high luminosity, but only at one energy and therefore one value of q^2. The first challenge can be overcome by using data at resonances which do not decay into proton antiproton pairs or only do so with a very low branching fraction (for BESIII resonances

above 3.686 GeV). Concerning the second challenge, to extract form factors over a wide range of q^2 from resonance data one can analyse initial state radiation processes, where a photon emitted from an initial state particle reduces the center of mass energy before the collision, leading to a lower momentum transfer. Since this process is a second order correction to the Born process, the cross section is reduce by a factor of α/π, which is roughly 400. Despite the high amount of luminosity collected at resonances at BESIII, this fact limits the precision that is achievable with the initial state radiation technique. To reach higher precisions comparable to those in the SL region, dedicated data sets have to be taken where the different energies (and therefore q^2) are scanned through and the FFs are extracted from the Born process.
This chapter will first give a short overview over all the data sets available at BESIII, including the large sets gathered at resonance energies. The data on which the analysis presented in this work is based on is a scan data set taken in 2015, which will be described in more detail in the second part of the chapter.

4.1 Available data sets at BESIII

Data available at BESIII includes the largest available data sets in the world for the charmonium resonances J/ψ, $\psi^{'}$ and $\psi^{''}$. Additionally, large data samples were collected for the so called XYZ resonance states, which are at energies between 3.8 and 4.6 GeV.

TABLE 4.1: Overview of the available BESIII data sets at resonances

$\sqrt{s}$ (GeV)	Sample size	Year	Resonance
3.097	$\sim$1 $\times 10^{10}$ events [151, 152]	2009, 2012, 2018	J/ψ
3.686	0.45 $\times 10^{6}$ events [153]	2009, 2012	$\psi^{'}$
3.773	2916.94 pb^{-1} [154]	2010, 2011	$\psi^{''}$
4.009	481.96 pb^{-1} [155]	2011	$\psi(4040)$
4.180	3100 pb^{-1} [155]	2016	$\psi(4180)$
4.230	1047.34 pb^{-1} [155]	2013	Y(4260)
4.260	825.67 pb^{-1} [155]	2013	Y(4260)
4.360	539.84 pb^{-1} [155]	2013	Y(4360)
4.420	1028.89 pb^{-1} [155]	2014	Y(4420)
4.600	566.93 pb^{-1} [155]	2014	Y(4600)

An overview of the data sets with the largest luminosities taken at resonances is given in table 4.1. Note that for the J/ψ, $\psi^{'}$ resonances, the number of collected events is given instead of the luminosity. For the other resonances, the integrated luminosity is determined by using QED processes with well known theoretical cross sections, such as Bhabha scattering (large angle), di-muon and di-gamma processes. A first rough measurement with this method is done online during data taking for data quality monitoring,

using the EMC endcaps and Bhabha scattering events. Once the data is reconstructed, a more precise offline measurement is performed including background suppression as well as better corrections for detector efficiencies with Monte Carlo simulations. Main uncertainties in this measurement come from trigger efficiencies, radiative corrections and remaining background pollution, leading to an overall uncertainty of the luminosity measurement of about 1% [155].

TABLE 4.2: Overview of available scan data sets at BESIII. $\mathcal{L}_{int}$ (pb^{-1}) denotes the integrated luminosity of each data set.

$\sqrt{s}$	Scan points	$\mathcal{L}_{int}$ $[pb^{-1}]$	Year	Sample
2.232 - 3.671	12	156.94 [156]	2012	R_{had} and τ mass scan
3.800 - 4.600	104	800 [156]	2014	R_{had}-scan
2.000 - 3.080	21	651.09 [157]	2015	Energy scan
4.190 - 4.280	8	3800 [158]	2017	Scan of XYZ states
4.130 - 4.440	8	3860 [158]	2018	Scan of XYZ states

The available scan data sets at BESIII can be found in table 4.2. The scan data was taken for different purposes, such as the aforementioned measurement of R_{had}, baryon form factor measurements, τ mass scan measurement and line-shape scans of resonances. The analysis in this work is based on the scan data set marked in red, which will be discussed in more details in the next section.

4.2 Scan data set of 2015

The extraction of the EM FFs of the proton described in this work is mainly based on a data set taken at BESIII in the 2014/2015 running period with a total luminosity of 651.09 pb^{-1}. In addition, data taken during the R_{had} scan from 2012 (see table 4.2) is merged with the new data from 2015 for energy points which exist in both data sets (at 2.2324 GeV, 2.8 GeV and 3.08 GeV), leading to a total luminosity of analysed data of 688.5 pb^{-1}.

The data of 2015 was taken at 21 center of mass energies between 2.0 and 3.08 GeV. Additionally, a large data sample was taken close to 2.125 GeV to investigate the Y(2175) resonance with a total luminosity of 108.49 ± 0.85 pb^{-1} and an exact center of mass energy of 2126.55 ± 0.85 MeV. Since there is no known decay of that resonance to proton antiproton pairs, it was included in the analysis of $e^+e^- \to p\bar{p}$. The luminosity of both the data for the Y(2175) resonance and the main scan data set was determined via large angle Bhabha scattering (see section 4.1).

The scan data set is the largest existing data set in the world within this energy region. In addition to the analysis of proton form factors presented in this work, the data set has

been used for a number of other interesting analyses, for example the first measurement of the individual form factors of the neutron [159–161] as well as a precise measurement of the form factors of the Λ baryon [162].

During the same running period in which the scan data set was taken, two so called separated beam data samples have been collected at 2.2324 and 2.6444 GeV with a data taking time of about 40 hours each. As the name suggests, these sample were collected in a collider mode where the electron and positron beam were not brought to collision, therefore all events within these data samples are due to machine and beam related background only. The separated beam data samples can be used to estimate this kind of background and develop analysis strategies to reduce or eliminate it. The luminosity at each energy point and the data taking time of the data set is summarised in table 4.3.

TABLE 4.3: Overview of the 2015 high luminosity scan data set taken at BESIII between 2.0 GeV and 3.08 GeV.

$\sqrt{s}$ [GeV]	$\mathcal{L}_{int}$ [pb^{-1}] [157, 163]	Date (yy.mm.dd)	tot. time (h:m)	run number
2.0000	10.07 ± 0.07	15.04.18-15.04.27	123:01	41729-41909
2.0500	3.34 ± 0.03	15.04.27-15.04.29	42:26	41911-41958
2.1000	12.17 ± 0.09	15.04.11-15.04.17	104:54	41588-41727
2.1250	108.49 ± 0.85	15.05.01-15.06.18	∼ 21 days	41588-41727
2.1500	2.84 ± 0.02	15.04.09-15.04.11	28:23	41533-41570
2.1750	10.63 ± 0.09	15.04.03-15.04.09	102:12	41416-41532
2.2000	13.70 ± 0.09	15.03.12-15.03.19	113:50	40989-41121
2.2324	2.65 ± 0.02	12.06.15-12.06.16	-	28632-28648
	11.86 ± 0.09	15.03.20-15.03.25	111:27	41122-41239
2.3094	21.09 ± 0.14	15.03.26-15.04.02	137:28	41240-41411
2.3864	22.55 ± 0.18	15.03.02-15.03.07	89:44	40806-40951
2.3960	66.87 ± 0.48	15.02.14-15.02.28	222:29	40459-40769
2.5000	1.10 ± 0.01	15.02.28-15.02.28	5:04	40771-40776
2.6444	33.72 ± 0.22	15.01.31-15.02.07	115:25	40128-40296
2.6464	34.00 ± 0.28	15.02.07-15.02.12	112:05	40300-40435
2.7000	1.03 ± 0.01	15.02.13-15.02.13	3:45	40436-40439
2.8000	3.75 ± 0.03	12.06.09-12.06.10	-	28553-28575
	1.01 ± 0.01	15.02.13-15.02.13	3:57	40440-40443
2.9000	105.25 ± 0.91	15.01.16-15.01.29	214:01:57	39775-40069
2.9500	15.94 ± 0.14	15.01.11-15.01.12	25:35	39619-39650
2.9810	16.07 ± 0.10	15.01.12-15.01.13	22:25	39651-39679
3.0000	15.88 ± 0.11	15.01.13-15.01.14	20:54	39680-39710
3.0200	17.29 ± 0.12	15.01.14-15.01.15	22:22	39711-39738
3.0800	31.02 ± 0.20	12.04.08-12.04.08	-	27147-27233
		12.05.23-12.05.24		28241-28266
	126.19 ± 0.92	14.12.31-15.01.10	194:48	39355-39618
sep. beam				
2.2324	-	15.04.30-15.04.30	38:44	41959-41999
2.6444	-	15.02.28-15.03.02	39:40	40777-40804

Chapter 5

Software Framework for the Analysis and Monte Carlo Simulations

The first part of this chapter covers a brief description of the software frame work that was used for the analysis presented in this thesis. The second part gives an overview the software and generators used to generate Monte Carlo (MC) simulations of both the signal process $e^+e^- \to p\bar{p}$ as well as possible background contaminations, which can be estimated with the help of those samples. A summary of the generated samples is given at the end of the chapter in table 5.2.

5.1 The BESIII Offline Software System

The software system used by BESIII and in this work is called BESIII Offline Software System (BOSS) [164, 165]. It is based on the C++ programming language and uses object oriented techniques based on the operating system of Scientific Linux CERN (SLC6). CMT (Software Configuration Management Tool) [166] is used for its configuration and to manage dependencies between different packages, provide executables and libraries.

The software system consists of five parts: the software framework, reconstruction, calibration, simulation and analysis tools. The software architecture of the framework was built based on Gaudi [167], whose event data service is used to manage the raw data, reconstructed data and Data-Summary-Tape (DST) type of data used for analysis. Data reconstruction algorithms can retrieve information from the Geometry Design Markup Language (GDML) [168] files, which store information about the detector's material and

geometry. In addition, the framework can provide several services and utilities usable for data analysis, for example exact maps of the magnetic field strength at each point of the detector or matching of reconstructed tracks to the original simulated MC particles. An overview of the architecture of the framework is shown in figure 5.1.

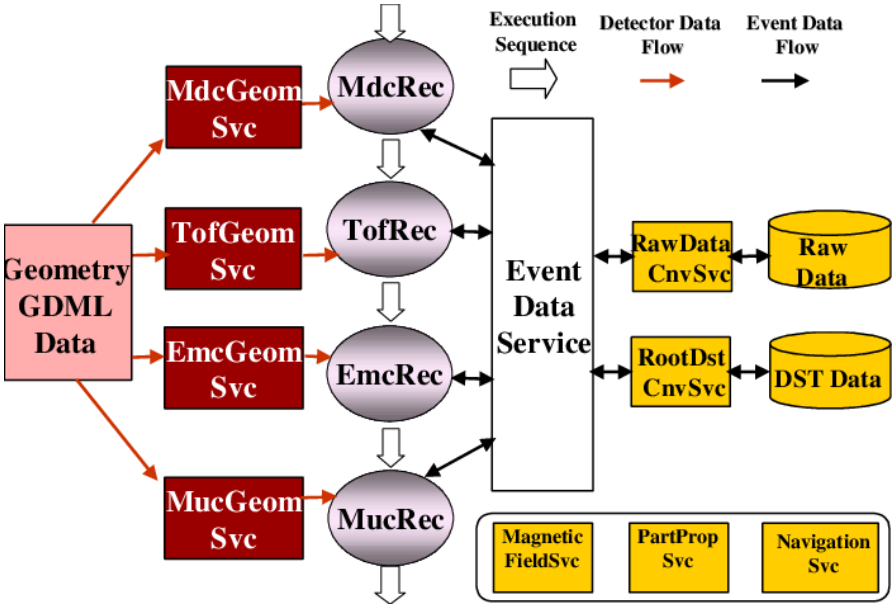

FIGURE 5.1: Overview of the architecture of the BOSS framework, taken from reference [165]

The reconstruction of events is handled by a chain of algorithms within the BOSS framework, for example those responsible for tracking in the MDC, dE/dx and TOF reconstruction, EMC clustering and shower making as well as muon track finding. The working principle of the MDC track finding algorithm is described in section 3.2.3. The dE/dx reconstruction provides precise values of the energy loss of particles through the MDC after applying corrections to the individual analog-to-digital converter (ADC) values of each MDC channel. In the TOF reconstruction, extrapolated tracks from the MDC tracking algorithm are used to calculate the exact time of flight of particles from the interaction point to the TOF system after applying corrections to the effective velocity, attenuation and others. Together with the dE/dx measurement, this TOF measurement provides the means to identify charged particles. The EMC reconstruction algorithm first performs an energy calibration by converting the ADC values of each crystal to an energy value by using EMC calibration constants. In a second and third step, clusters and then showers are formed with the calculated positions and energies, using the crystal with the highest local energy entry as a seed. Finally, the MUC reconstruction also uses the extrapolated tracks from the MDC to match them with collections of hits from the wires in the Muon System and thus form track candidates.

The calibration part of the BOSS software is based on GLAST (Ground Software Calibration Index) [169]. It consists of a framework and calibration algorithms which produce calibration constants for each subdetector. These are then stored in ROOT [170] files and a central database, along with informations about the individual runs, trigger conditions as well as software and hardware version numbers. From there they can be accessed by both simulation and reconstruction algorithms. The calibration constants are necessary to convert raw measured values in the subdetectors, for example measured drift time in the MDC to distance, which is needed to correct crosstalk effects or calculate the spatial resolution at a certain point of a detector cell. The structure of the calibration software of BOSS can be seen in figure 5.2

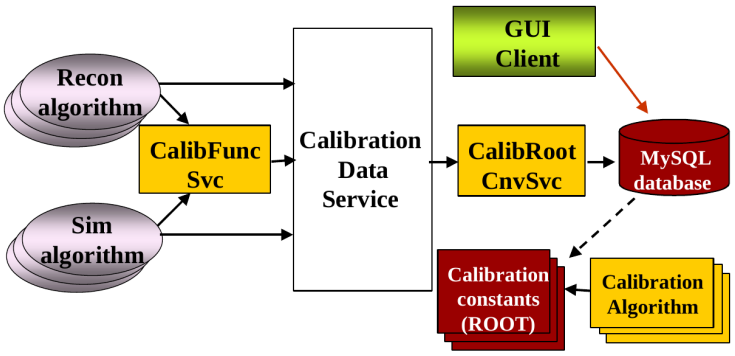

FIGURE 5.2: Structure of the BESIII calibration software, taken from reference [165].

For the simulation of the detector and data, BOSS uses a GEANTt4 [146] based software called BESIII Object Oriented Simulation Tool (BOOST). The simulation process consists of four parts: event generators, detector description, particle tracking and detector response. A large number of event generators is available within the framework, some of them inherited from the BESII experiment. A closer description of the generators relevant for this work will be given in section 5.2.
For the other three parts, BOOST is able to read in the geometrical and material description of the BESIII detector from the GDML files along with detector response and digitisation models as well as the running conditions of the detector. The tracking of particles is handled by the GEANT4 packgage. Gaudis event data service is again used to connect these different parts, as can be seen in the dataflow diagram of figure 5.3.

To further analyse the fully reconstructed data, BOSS provides a number of analysis tools. Events can undergo a vertex finding and fitting procedure of the primary and, depending on the kind of event, any possible secondary vertices. This improves not only the resolution of the common vertex of the tracks in an event, but also their momentum resolution. A particle identification service combines information from the TOF system, dE/dx measurements of the drift chamber, energy deposition in the EMC as well as

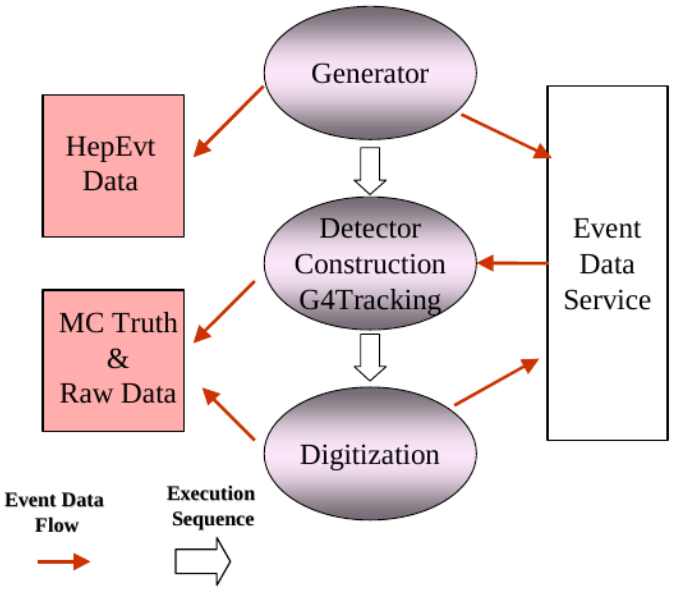

FIGURE 5.3: Diagram of the event data flow in MC simulation for BESIII, taken from [165].

Muon System information to assign each particle probabilities to belong to a certain particle species.

Tools for kinematic fitting can help to improve the mass and momentum resolution for both charged and neutral particles, and provide criteria for analysis strategies for the selection of events. To provide a graphical representation of events, an event display tool is also available within the framework. The structure of the different analysis tools can be seen in figure 5.4.

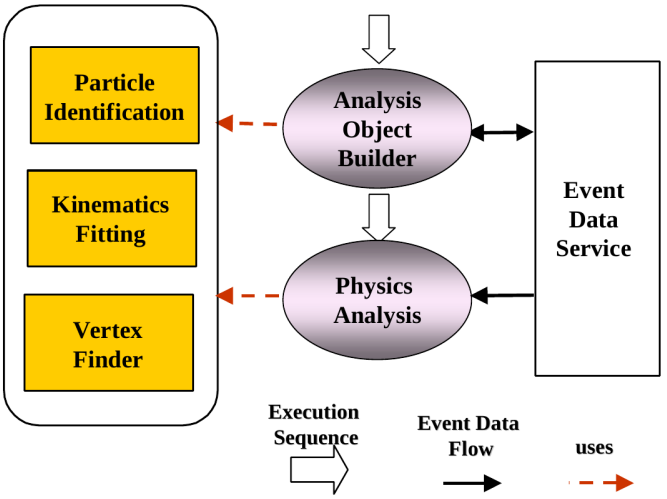

FIGURE 5.4: Structure of the analysis tools available within the BOSS framework, taken from reference [165].

5.2 Monte Carlo simulation

A number of event generators are available within the BOSS framework to simulate signal physics processes, for example to correct for detector efficiencies or radiative corrections, as well as background processes to estimate or correct for background contamination. In the following, the most important generators used within this thesis will be briefly introduced.

Charmonium decays are simulated by default with a combination of the KKMC [171] and BesEvtGen [172] generators. The simulation framework of this type of decay is illustrated in figure 5.5. The signal process of this work, $e^+e^- \to p\bar{p}$, was simulated using the Phokhara event generator, which will be covered in section 5.2. Background samples have been generated with the Babayaga generator for Bhabha scattering as well as $e^+e^- \to \mu^+\mu^-$ events, and BesEvtGen in the case of the inclusive hadronic background ($q\bar{q}$ samples). Additional exclusive hadronic channels such as $e^+e^- \to \pi^+\pi^-$ or $e^+e^- \to K^+K^-$ have also been generated with Phokhara.

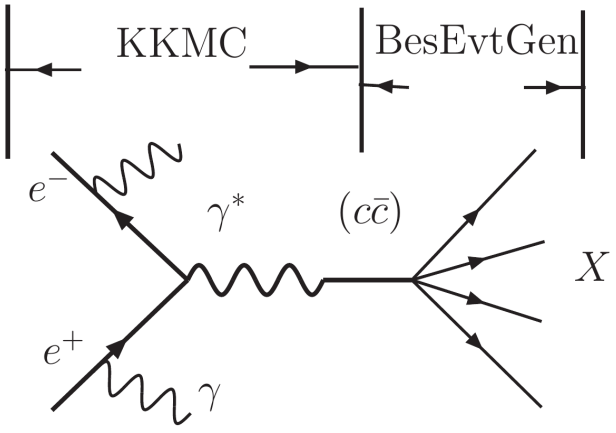

FIGURE 5.5: Illustration of the simulation framework of charmonium decays at BESIII, taken from reference [147].

KKMC

KKMC [171] is an event generator for the process $e^+e^- \to f\bar{f}+n\gamma$, with f = μ, τ, d, u, s, c, b and n = 1, 2..., for center of mass energies between the τ threshold up to 1 TeV. It uses precise calculations based on the electroweak standard model with radiative corrections up to the next-to-next-to leading order (NNLO), including interference effects between photon emission from the initial beams (initial state radiation, ISR) and the outgoing fermions (final state radiation, FSR). Elekroweak corrections are also included up to first order. The produced quarks are subsequently hadronised using a parton shower

model.
Within the BESIII framework, KKMC is used to generate charmonium states considering ISR effects as well as beam energy spread. The subsequent decays of these states, although also implemented in KKMC, is then handled by the BesEvtGen, which has better models and the possibility to consider FSR using the PHOTOS [173, 174] package.

BesEvtGen

BesEvtGen [172] is based on the EvtGen [175] generator, which was originally designed to study B-physics (physics involving hadrons which contain at least one bottom quark) and modified to be used for tau-charm physics in BESIII. BesEvtGen simulates the decays of the previously generated charmonium states through the use of an accept-reject algorithm based on the amplitude probability combined with forward and backward spin-density matrix information. The generator has 30 inbuilt models with amplitudes constructed from the helicity amplitude method and constrained by parity conservation. Additional decay models can be easily created by the user by providing the corresponding decay amplitudes. In addition, BesEvtGen allows for access to other generators such as PHOTOS [173, 174], PYTHIA [176] and Lund-charm inclusive generators, which can be used to generate unknown decays of a resonance.

Babayaga

Babayaga [177] is an exclusive event generator for the processes $e^+e^- \to e^+e^-, \mu^+\mu^-, \gamma\gamma$, and $\pi^+\pi^-$ with an energy below 12 GeV. It includes high precision QED calculations of the Bhabha scattering process and can therefore be used for precise luminosity determinations at e^+e^- colliders. These calculations are based on a matching of exact next-to-leading order (NLO) corrections with a QED parton shower algorithm. The theoretical precision of the generator, which is estimated by comparing it with existing independent calculations and a detailed analysis of the main components of theoretical uncertainty (two-loop corrections, hadronic vacuum polarisation, light pair contributions), is claimed to be 0.5% for Babayaga 3.5 (used in this work) [177] and 0.1% for its successor Babayaga@NLO [178, 179].

Phokhara

Phokhara [180] is a MC event generator that was mainly developed for simulating ISR for several exclusive hadronic final states, allowing a determination of the cross section of these states over a wide range of energies at high luminosity flavour facilities. Phokhara is able to generate this process up to NLO accuracy (with the ISR process as the base process), including virtual and soft photon corrections and the emission of two hard photons. The included processes are $e^+e^- \to p\bar{p}$, $n\bar{n}$, $\pi^+\pi^-$, K^+K^-, $K^0\bar{K}^0$, $\lambda(\to \pi^- p)\bar{\lambda}(\to \pi^+\bar{p})$, $\pi^+\pi^-\pi^0$, $2\pi^+2\pi^-$, $2\pi^0\pi^+\pi^-$, $\eta\pi^+\pi^-$, and $\mu^+\mu^-$. The theoretical precision of the generator is better than 0.5%.
In addition, Phokhara offers a scan mode, which simulates the processes above without the emission of an ISR photon. In this mode, Phokhara offers an accuracy up to NNLO (with the Born process as base process) for ISR and NLO for FSR. The signal MC samples for this work, which will be described in more details in section 5.3.1, have been generated using this scan mode of the Phokhara generator.

ConExc

ConExc [181] was developed as a hadronic event generator for R_{had} (see chapter 4) measurements at e^+e^- collider experiments that features precise calculations of ISR. It is able to generate a number of measured exclusive processes as well as unmeasured processes, which are generated according to the LUND Area Law Model. Radiative corrections are calculated using the total hadronic Born cross section and include ISR corrections up to NLO. The generator is embedded within the framework of BesEvtGen (see section 5.2) and provides the 4-momentum of the final state particles for detector simulation as well as the calculated ISR correction and vacuum polarisation factors.

5.3 Monte Carlo samples for the $e^+e^- \to p\bar{p}$ analysis

This section will give an overview over the MC samples generated for this analysis using the generators described above. This includes samples for background evaluation, which will be described in chapter 7, as well as MC for the signal process $e^+e^- \to p\bar{p}$ generated with Phokhara. The signal MC is used to optimise the event selection of the signal process, evaluate the efficiency of this selection as well as the detector efficiency, and determine the radiative correction factor $(1 + \delta)$. Since the characteristics of the generated signal MC sample, such as the angular distribution of events or the behaviour of the ISR, depend on the form factor model used by the generator, an iterative tuning procedure is necessary to ensure an unbiased measurement of the proton form factors.

This procedure requires the extraction of the EM FFs of the proton and will be therefore explained in detail in the corresponding chapter 9. In this section, only the generated amount and the properties of the signal MC will be discussed.

5.3.1 Signal Monte Carlo simulation

The main signal MC samples for this work have been generated with Phokhara and can be classified into two categories: samples containing only the born process and samples containing both radiative corrections (ISR up to NNLO, FSR up to NLO) as well as vacuum polarisation. The former are used to optimise selection criteria and determine efficiency corrections (see chapters 6 and 8), while the latter are necessary to determine the radiative and vacuum polarisation correction factors.

TABLE 5.1: Example input settings for a signal MC sample with full radiative corrections for the Phokhara event generator

Variable	Value	Notes
Phokhara.Channel	4	$p\bar{p}$ channel
Phokhara.ScanMode	1	Born as base process
Phokhara.NLO	1	ISR up to NNLO
Phokhara.FSR	1	FSR enabled
Phokhara.FSRNLO	0	FSR NLO disabled
Phokhara.VacuumPolarization	2	vacuum polarisation by Thomas Teubner
Phokhara.ProtonFormfactor	2	use FF model from iterative tuning procedure (see section 9.4)
Phokhara.SoftPhotonCutoff	0.0001	cutoff for soft radiative photons
Phokhara.MinPhotonEnergy	0.02	minimum energy for ISR photons
Phokhara.MinPhotonAngle	0	minimum angle for ISR photons
Phokhara.MaxPhotonAngle	180	maximum angle for ISR photons
Phokhara.MinHadronsAngle	0	minimum angle for final state hadrons
Phokhara.MaxHadronsAngle	180	maximum angle for final state hadrons

For each energy point, large samples of 1 million signal events with radiative corrections and 1 million pure Born events of the signal process have been created to minimise the contribution to the uncertainty of the results from radiative and efficiency corrections. An example of the input settings for Phokhara as used in this analysis is given in table 5.1 for a sample with full radiative corrections.

5.3.2 Background Monte Carlo samples

For an evaluation of potential background processes (details see chapter 7), MC samples of several background reactions have been generated according to the number of expected events at the given energy point of the data set:

$$N_{generated} = \mathcal{L}_{int}(s) \times \sigma_{background} \tag{5.1}$$

with the number of generated events $N_{generated}$, the integrated luminosity at each energy point $\mathcal{L}_{int}(s)$, and the cross section of the background channel $\sigma_{background}$.

TABLE 5.2: Overview of the generated MC samples for signal and background processes relevant to the analysis of this work

Final state	MC generator	$N_{generated}$ per energy point
$p\bar{p}$	Phokhara	1×10^6
e^+e^-	Babayaga	$> 1 \times 10^6$
$\mu^+\mu^-$	Phokhara	$> 8 \times 10^5$
$\pi^+\pi^-$	Phokhara	5×10^5
K^+K^-	ConExc	1×10^5
$q\bar{q}$	BesEvtGen	$(3.5 - 11.8) \times 10^6$
$\gamma\gamma$	Babayaga	$> 1 \times 10^6$
$p\bar{p}\pi^+\pi^-$	ConExc	$> 1.15 \times 10^6$
$p\bar{p}\pi^0$	BesEvtGen	6.5×10^5

The background samples include QED background channels (final states e^+e^-, $\mu^+\mu^-$, $\gamma\gamma$), inclusive hadronic background (final state $q\bar{q}$) and several exclusive hadronic channels (final states K^+K^-, $\pi^+\pi^-$, $p\bar{p}\pi_0$, $p\bar{p}\pi^+\pi^-$). For each background channel with a known cross section, at least the amount of events as calculated according to equation 5.1 or more have been generated. An exception is the Bhabha scattering reaction ($e^+e^- \to e^+e^-$), since this process has a very large cross section in the energy region of the 2015 scan data set, which makes it infeasible to generate the expected amount of events for all energy points. Instead, large samples of Bhabha scattering events with at least the amount of expected events have been generated at selected energy points. Table 5.2 gives an overview over the MC samples for the different background reactions as well as the size of both signal and background samples.

Chapter 6

Analysis of the Signal Process $e^+e^- \to p\bar{p}$

The first step in the analysis of the process of interest of this work, $e^+e^- \to p\bar{p}$, is selecting the signal events from the data samples taken in 2015 at BESIII (see section 4.2) among possible background processes. This chapter describes the requirements imposed on a number of variables in these samples, the so called event selection, and how they can reduce the most important background sources while keeping a good efficiency for the signal process. This is especially important for the extraction of the EM FFs of the proton later on (see chapter 9), which requires an angular analysis of the process and therefore a sufficiently high amount of selected events for as many energy points of the scan sample as possible. At the end of the chapter, a summary of the applied event selection criteria and the resulting amount of selected events at each energy point is given.

6.1 Event selection

The final state of the signal process is characterised by one positive and one negative particle. Neglecting processes of higher order (ISR, FSR), it is a two-body process, meaning that the two particles are expected to be emitted back-to-back from the vertex. These kinematical informations can be used to distinguish the signal process from several background processes, for example with more complex final states. In addition, information from various subdetectors of BESIII, mainly the MDC, EMC and TOF system, is used to rule out processes with different particle species in the final state. The following sections will describe which criteria have been applied and how they have been

chosen, first on the level of criteria for each charged track in section 6.1.1, and then for criteria concerning the whole event in section 6.1.2.

6.1.1 Selection criteria for charged tracks

In a first step, charged tracks found within the MDC are subjected to a number of preselection criteria. The tracks are required to have their point of closest approach (POA) to the interaction vertex within 10 cm in the direction of the beam ($|R_z| < 10$ cm) and within 1 cm in the plane perpendicular to the beam ($|R_{XY}| < 1$ cm). Tracks are also required to have a polar angle with respect to the positron beam direction of ($|cos(\theta)| < 0.93$) to ensure they are within the acceptance of the MDC.

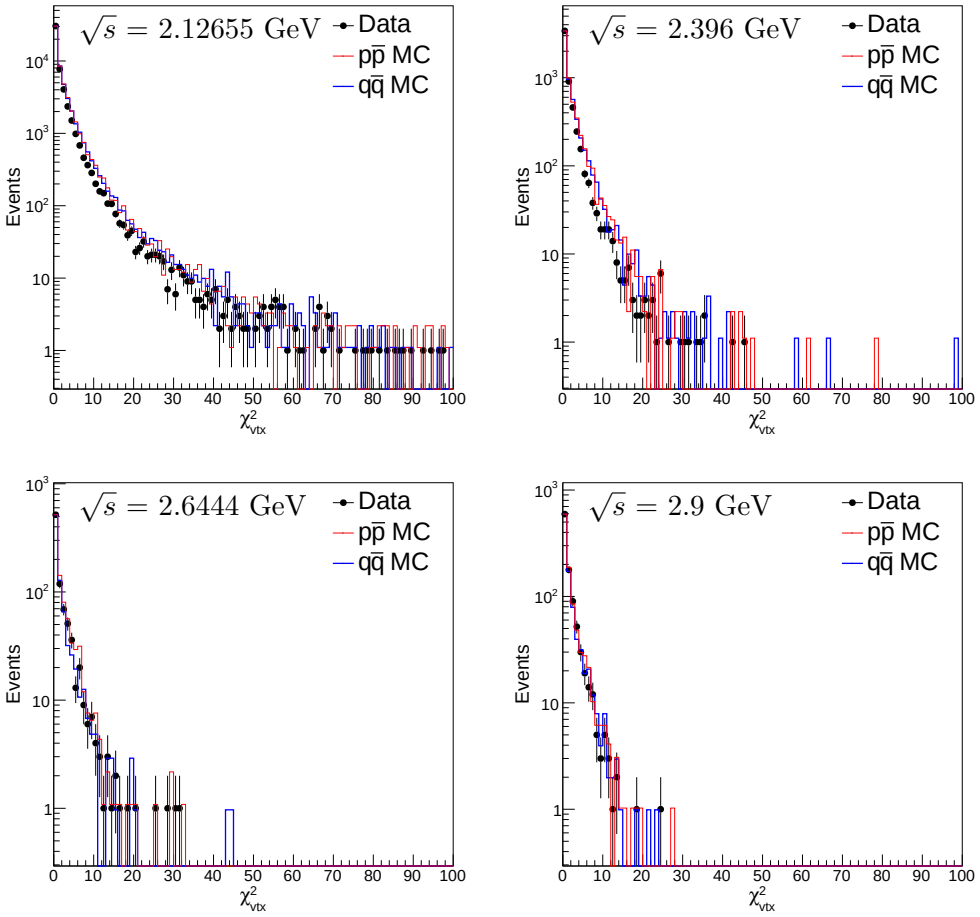

FIGURE 6.1: Distribution of the χ^2_{vtx} from the vertex fit performed on the positive and negative track of each event to constrain them to a common vertex. Shown are the distribution of data (black dots with error bars) on top of those for inclusive hadronic MC ($q\bar{q}$ including signal channel, blue histogram) and signal MC including ISR up to NNLO (red histogram) for example energy points of 2.12655, 2.396, 2.6444 and 2.9 GeV. All other requirements except the one for χ^2_{vtx} have been applied, and the distributions of signal and $q\bar{q}$ MC have been scaled to the bin with the highest amount of entries in data.

Tracks fulfilling these criteria are subsequently subjected to a vertex fit, which improves the resolution of the common vertex of the tracks and their momentum resolution. The fit is performed using a proton and antiproton hypothesis for positively and negatively charged tracks, respectively. A very loose constraint on the χ^2_{vtx} of the fit ($\chi^2_{vtx} < 100$) is used to remove gross outliers, for example cases where the fit did not converge, without losing a lot of signal events. The distribution of the χ^2_{vtx} can be seen in figure 6.1 for selected CM energies (2.12655, 2.396, 2.6444 and 2.9 GeV) for signal MC including ISR up to NNLO, inclusive hadronic ($q\bar{q}$) MC which includes the signal process, and data. Distributions for all other CM energies can be found in appendix A in figure A.1.

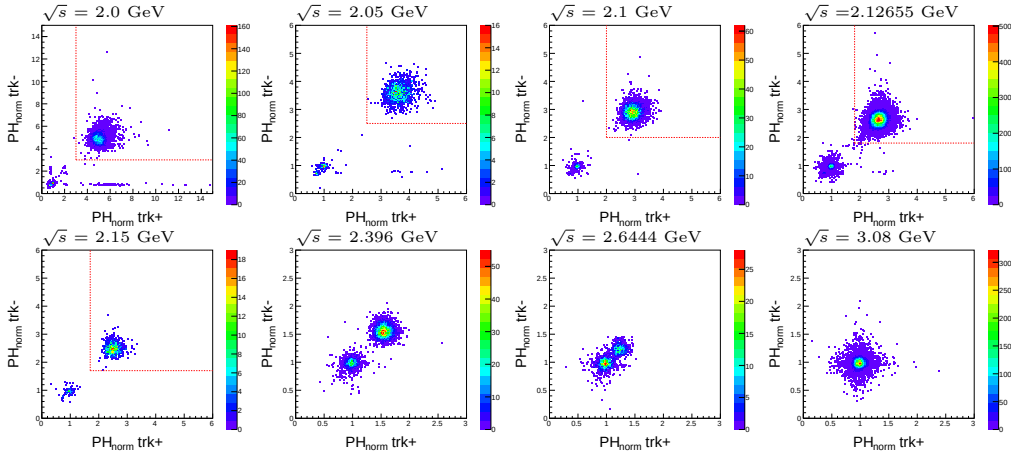

FIGURE 6.2: Distribution of the raw normalised pulse heights (PH_{norm}) of the dE/dx measurement from the MDC for the positive selected track versus the negative selected track. Shown are the distributions for data samples at energy points where a requirement is on this quantity is used instead of the PID system to identify particles (2.0 GeV, 2.05 GeV, 2.1 GeV, 2.12655 GeV, and 2.15 GeV) including the chosen cut values (red dashed lines), along with distributions for data samples at higher energies, where the PH_{norm} variable can not distinguish background from signal any more.

The particle species of each track is then identified using the PID system of BESIII implemented in the BOSS framework. The PID system can be configured to use the different subdetectors of BESIII to assign each track a probability (P_{PID}) to be of a certain particle type (electron, muon, proton, pion, kaon). For this analysis, the dE/dx measured in the MDC and the time-of-flight of the particles measured by the TOF system are used within the PID system. For the data samples above 2.15 GeV, this probability is then used to discriminate particles of background processes, mainly the radiative Bhabha scattering process ($e^+e^- \to e^+e^-\gamma$), from the protons of the signal process. A sufficient separation is achieved with the requirement that the probability assigned by the PID system to the positive (negative) track to be a proton (antiproton) must be higher than that of any other particle:

$$P_{PID}(proton) > P_{PID}(pion), P_{PID}(kaon), P_{PID}(electron) \tag{6.1}$$

For data sets with energies below 2.175 GeV, the proton and antiproton of the signal process have very low momentum, since the energy is fairly close to the production threshold of $e^+e^- \to p\bar{p}$. This causes some tracks to circle within the MDC, leading to an unexpected drop in efficiency for events with low polar angle θ. The effect is most apparent for the data sample at the lowest CM energy of 2.0 GeV, as can be seen in figure 6.3. To remedy this effect, tracks in samples below 2.175 GeV are identified by applying a requirement on the raw dE/dx information from the MDC, instead of using the PID system. While an efficiency drop is only visible by eye at 2.0 GeV, the method is also applied to the four data samples with 2.0 GeV$< E_{CM} <$ 2.175 GeV to rule out any non-visible effects to the data quality caused by the phenomenon. Not using the PID system at these low CM energies is unproblematic, since the main background rejected by the PID requirement, radiative Bhabha scattering, is not very dominant here. The strong difference in momenta of the final state particles of the signal and Bhabha process at these energies makes it easy for other requirements to distinguish them. At higher CM energies however, the raw dE/dx requirement becomes less effective for separating the signal from Bhabha scattering events, as can be seen in figure 6.2. A clear separation of the signal, located in the lower left corner of the plots, from the Bhabha scattering background, located in the upper right corner of the plots, becomes increasingly difficult with rising energies, which makes using the PID system mandatory. In numbers, the requirement on the dE/dx normalised pulse height (PH_{norm}) are $PH_{norm} <$ (3.0, 2.5, 2.0, 1.8 and 1.7) at (2.0, 2.05, 2.1, 2.12655 and 2.15) GeV, respectively, in arbitrary units.

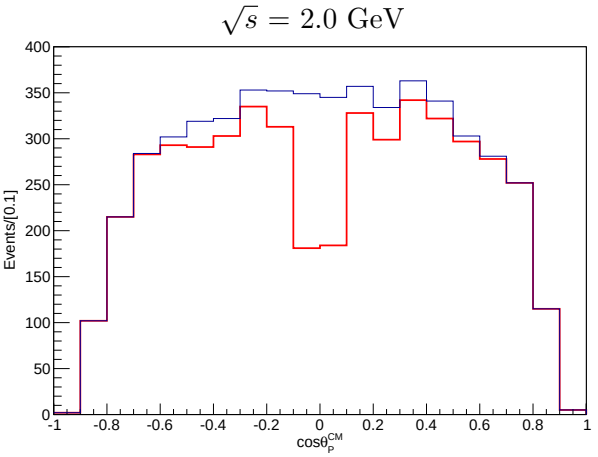

FIGURE 6.3: Comparison of the angular distribution of selected events at 2.0 GeV using the PID requirement of equation 6.1 (red histogram) and the direct requirement on the normalised dE/dx measurement of the MDC (blue histogram) after applying all other selection criteria. The clear dip in the former distribution is caused by circling low momentum tracks in the MDC causing problems for the PID system.

6.1.2 High level selection criteria for the signal process

Once the individual charged tracks have been preselected, a number of selection criteria are applied to the event as a whole to further reduce possible background.

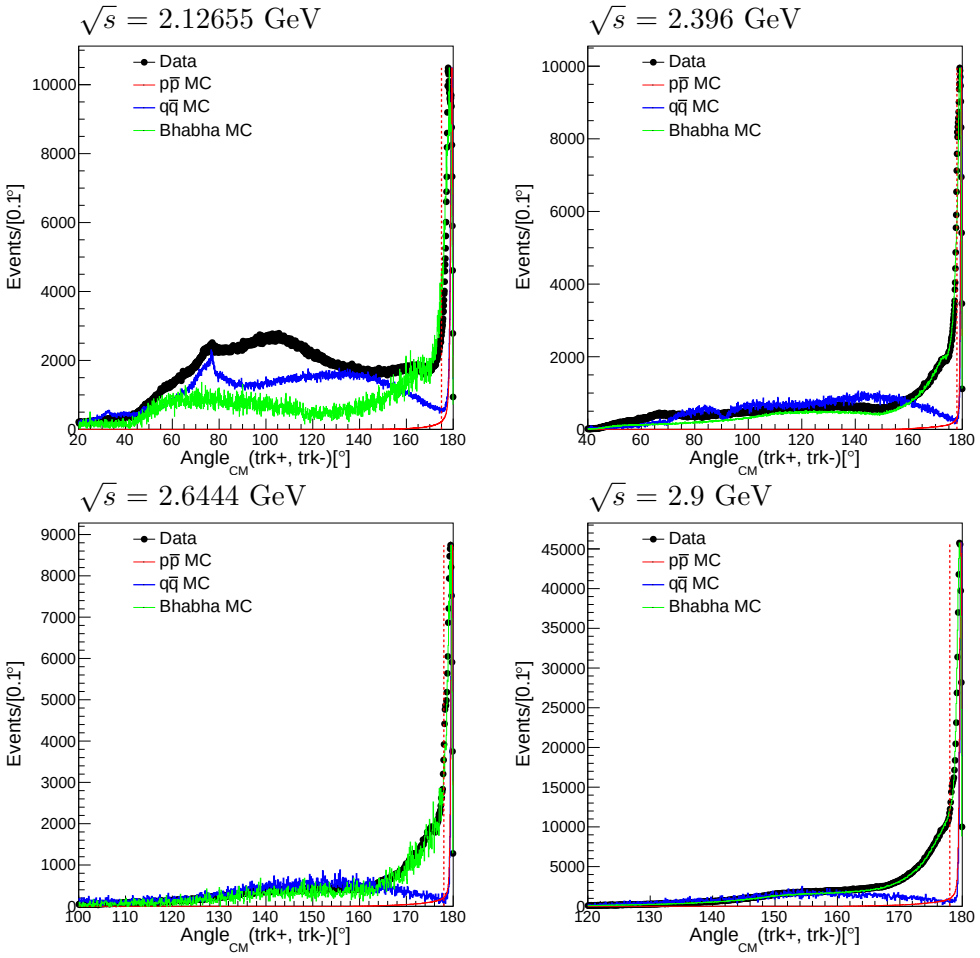

FIGURE 6.4: Distribution of the angle between the positive and the negative track for data (black dots with error bars), inclusive hadronic MC ($q\bar{q}$, blue histogram), signal MC including ISR up to NNLO (red histogram), and Bhabha scattering (e^+e^-) MC for example energy points of 2.12655, 2.396, 2.6444 and 2.9 GeV. The distributions of signal, Bhabha scattering and $q\bar{q}$ MC have been scaled to the bin with the highest amount of entries in data.

As a first step, each event is required to have exactly two charged tracks with opposite charge. These two tracks are then required to have a back-to-back signature, as expected from the two-body signal process. Both the positive and the negative track are boosted to the e^+e^- CM system beforehand to compensate for the small crossing angle between the two beams at BESIII. Since the detector does not have a perfect position resolution, the two tracks are not required to have an angle of exactly 180° between them, but rather a minimum angle of 170°, 175°, and 178° at (2.0-2.05, 2.1-2.3094 and 2.3864-3.08) GeV, respectively. The looser requirement for low CM energy samples are due to the

lower position resolution for low momentum tracks, with the aim to lose as few signal events as possible. Figure 6.4 shows the distribution of the angle between the two tracks without any other requirements imposed beforehand at example CM energies for data, signal MC, $q\bar{q}$ MC and Bhabha scattering MC. The same distributions, but with all other requirements of the final event selection except the one on the angle applied, can be seen in figure 6.5 for the same data and MC sets. Excluded is the Bhabha MC sample, which does not have any remaining events after the application of all other criteria described later in this chapter. Plots for all other energy points can be found in appendix A in figure A.2 and A.3 for distributions without and with all other requirements applied, respectively.

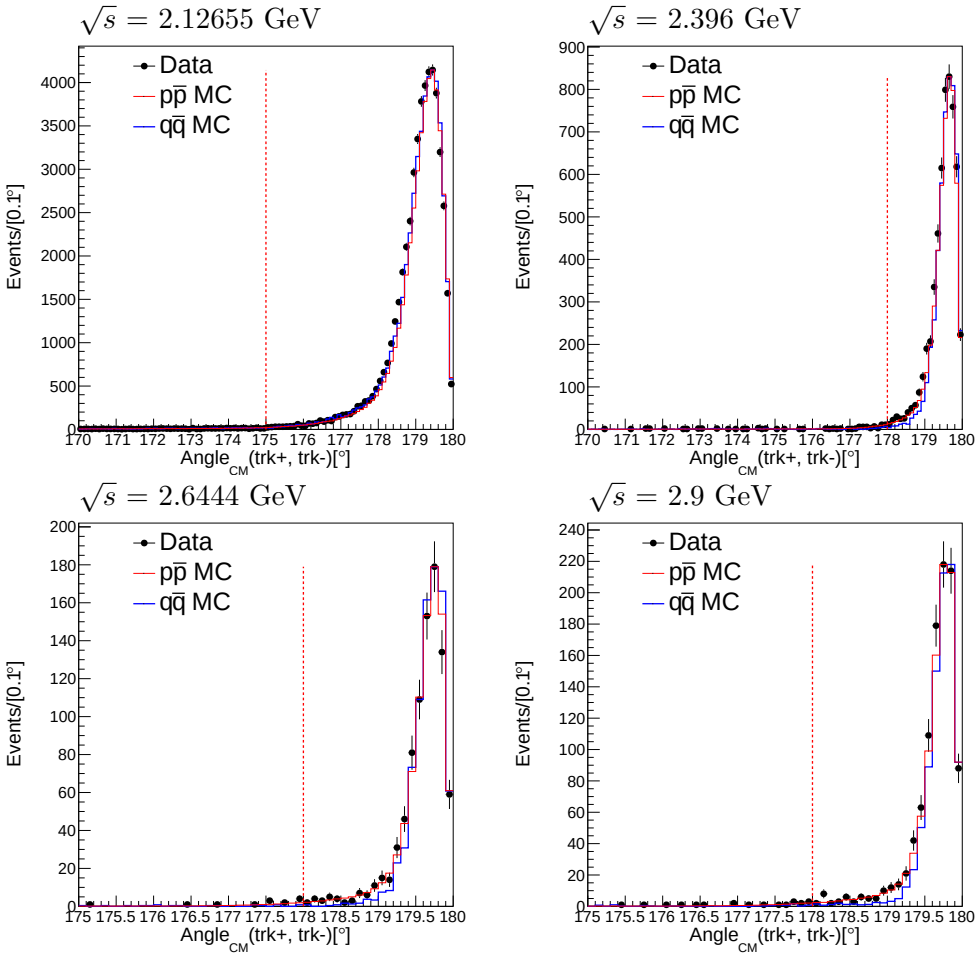

FIGURE 6.5: Distribution of the angle between the positive and the negative track for data (black dots with error bars), inclusive hadronic MC ($q\bar{q}$, blue histogram) and signal MC including ISR up to NNLO (red histogram) for example energy points of 2.12655, 2.396, 2.6444 and 2.9 GeV. All other requirements except the one for the angle between the tracks have been applied, and the distributions of signal and $q\bar{q}$ MC have been scaled to the bin with the highest amount of entries in data.

Since radiative Bhabha scattering events make up the main source of background to the signal process simply due to the very high cross section of that process (for details see

chapter 7), additional requirements to the ones imposed on the PID probabilities described in the last section are necessary to reduce events from this background channel. Especially at high energies, the dE/dx from the MDC can not be used to discriminate between protons and electrons any more (see fig. 6.6 a; as a reference, (anti)protons in the signal process reach 1 GeV/c momentum at about 2.75 GeV CM energy). In addition, the TOF of the particles becomes very small due to their large momentum, while the time resolution of the TOF system stays constant. Therefore, the relative uncertainty of the TOF measurements becomes large, leading to more miss-identifications by the PID system (see fig. 6.6 b)).

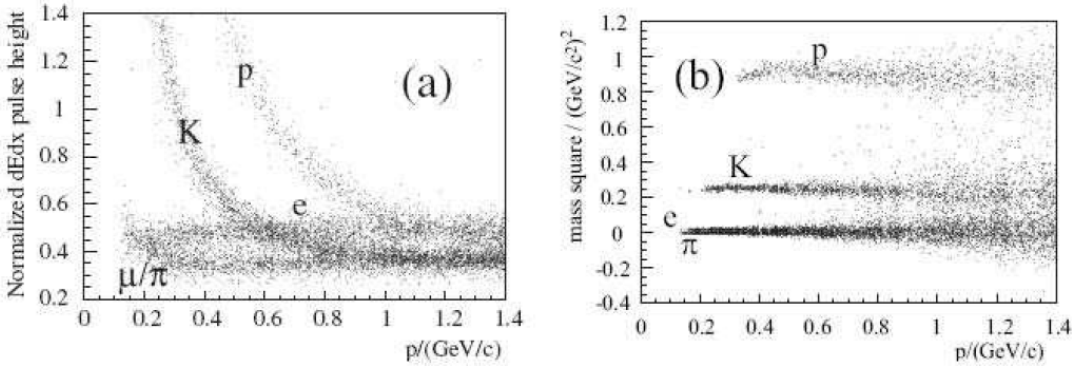

FIGURE 6.6: a) Comparison of the normalised pulse heights of dE/dx for different particles and b) comparisons of the mass square distributions calculated from the measured TOF for particle identification purposes, taken from reference [147]

Several approaches to further reduce this background have been tested, for example harder requirements on the PID probabilities ($P_{PID}(proton) > 10 \times P_{PID}(electron)$) or a cut on the polar angle of the tracks ($|cos(\theta)| < 0.8$), since radiative Bhabha scattering peaks at high values of $|cos(\theta)|$. After a thorough study, the simplest way which also proofed to have the best ratio of signal efficiency and background rejection was a requirement on the ratio of the momentum of the positive track, measured in the MDC, to the energy deposition in the EMC. Since electrons deposit most of their energy in the EMC and have a negligible rest mass compared to the CM energy, this E/p quantity has a value close to 1 for Bhabha scattering events. Protons as hadrons on the other hand mostly penetrate the EMC and only deposit a part of their energy within, leading to low E/p values. Requiring an E/p ratio of less than 0.5 only on the positive track (antiprotons can deposit larger amounts of energy in the EMC through annihilation) therefore effectively removes the remaining Bhabha scattering events without losing a significant amount of signal events. The requirement is applied for samples with CM energies at or above 2.150 GeV, since for lower CM energies the Bhabha process is not an issue as explained before. Additionally, for these lowest CM energies the E/p ratio can go above

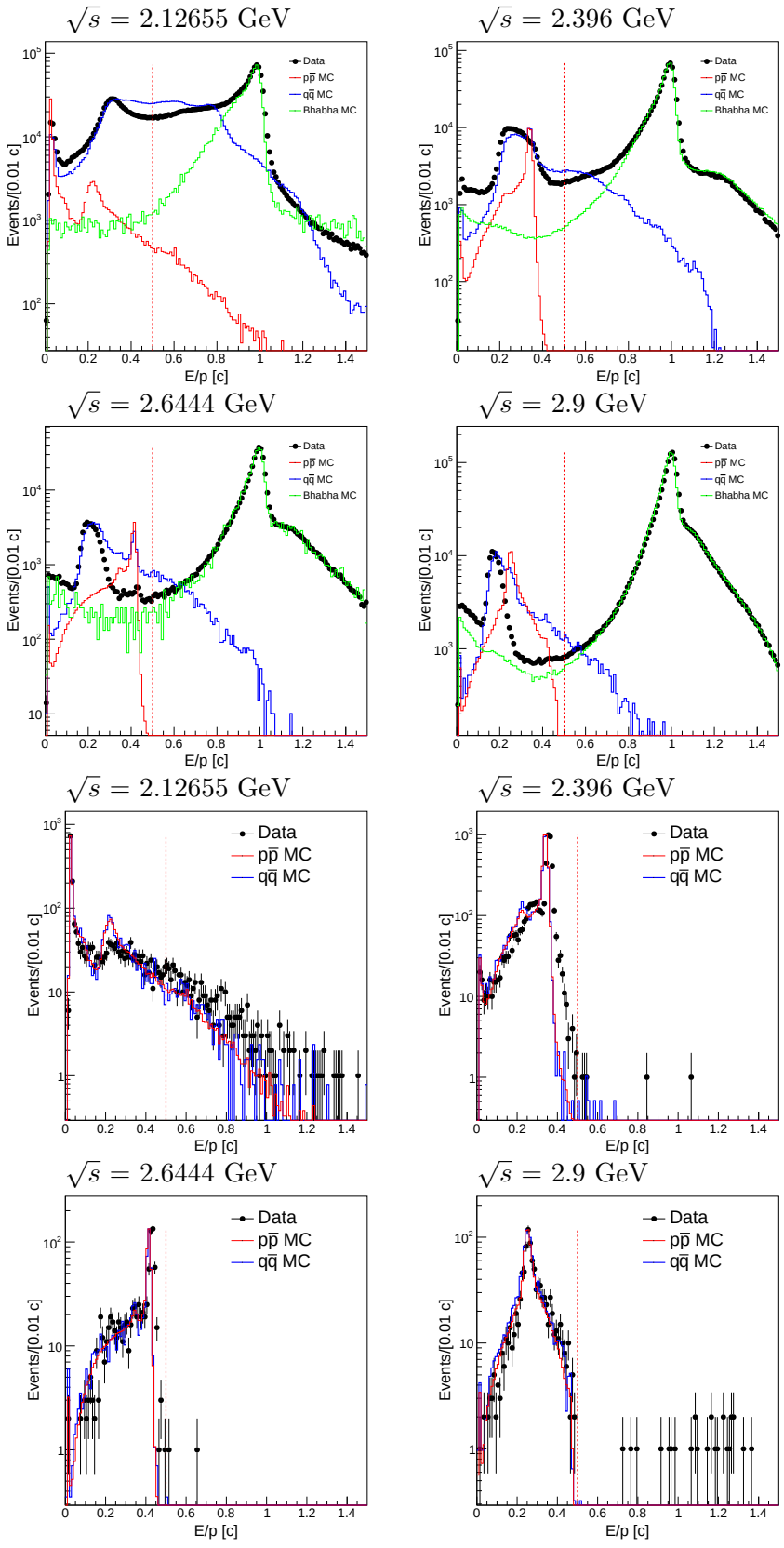

FIGURE 6.7: Distribution of the ratio of the energy measured in the EMC and the momentum measured in the MDC (E/p) for data (black dots with error bars), inclusive hadronic MC ($q\bar{q}$, blue histogram), signal MC including ISR up to NNLO (red histogram), and Bhabha scattering (e^+e^-) MC for example energy points of 2.12655, 2.396, 2.6444 and 2.9 GeV. The red dashed line marks the chosen limit for the requirement on this quantity, which is only applied for CM energies above 2.12655 GeV. The top four plots show the distributions without any other requirement applied, while in the bottom four all other requirements except the one for the E/p ratio have been applied. The distributions of signal, Bhabha scattering and $q\bar{q}$ MC have been scaled to the bin with the highest amount of entries in data.

0.5 due to the low momentum of the protons, which leads to a higher energy deposition in the EMC. While not strictly necessary for intermediate CM energies where the PID system can remove most Bhabha scattering events, the requirement is kept there to keep the analysis as consistent as possible over the whole energy range of the scan, since the loss in signal events is very small. In case there is no valid measurement of the energy deposition of the positive track in the EMC, the event is not rejected to avoid unnecessary loss of signal efficiency.

Figure 6.7 shows the distribution of E/p for example CM energies for data, signal MC, $q\bar{q}$ MC and Bhabha scattering MC. The top four plots are without any other requirements imposed, while the bottom four have all but the E/p selection criteria applied. Plots for all CM energies can be found in appendix A in figure A.4 and A.5 for distributions without and with all other requirements applied, respectively.

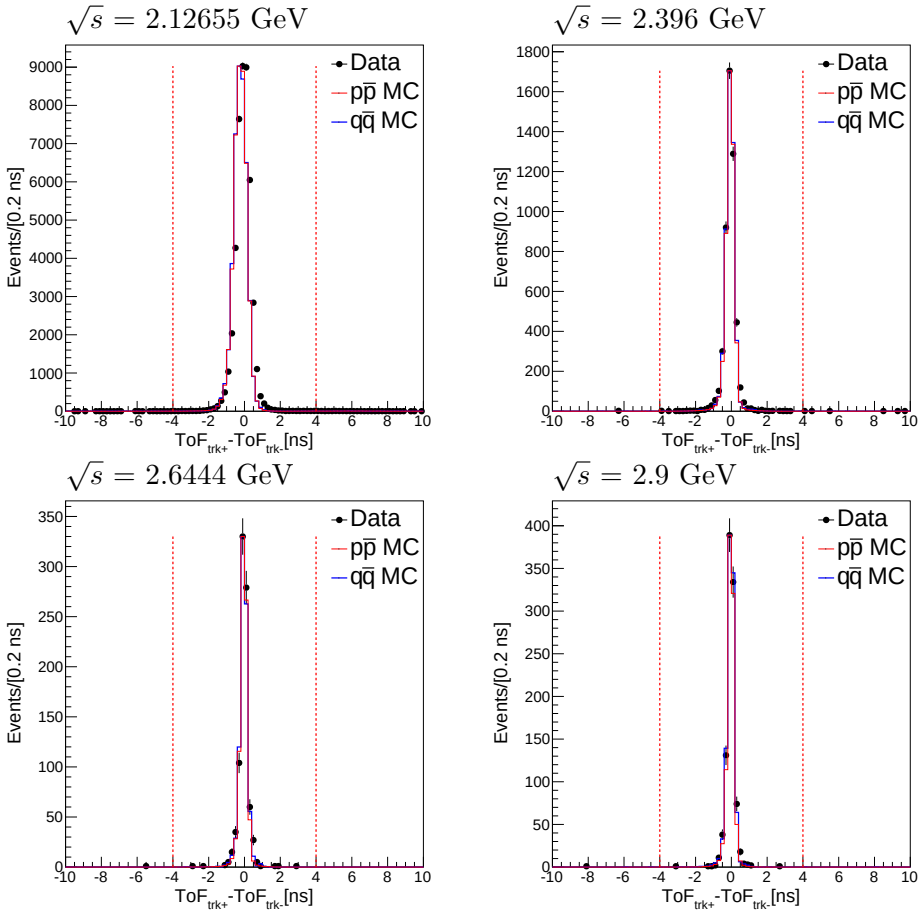

FIGURE 6.8: Distribution of the difference between the measured TOF of the positive and the negative track for data (black dots with error bars), inclusive hadronic MC ($q\bar{q}$, blue histogram) and signal MC (red histogram) for example energy points of 2.12655, 2.396, 2.6444 and 2.9 GeV. The two red dashed lines mark the chosen limits for the requirement on this quantity. All other requirements except the one for the TOF difference between the tracks have been applied, and the distributions of signal and $q\bar{q}$ MC have been scaled to the bin with the highest amount of entries in data.

To filter out cosmic events, a requirement is imposed on the difference between the time-of-flight measurements performed by the TOF system for the two charged tracks. A single cosmic particle crossing the detector through the interaction point can fake a symmetric two body event of a negatively and a positively charged particle coming from the interaction point. However, since tracks from cosmic rays enter the detector from outside rather than originating at the vertex of the e^+e^- collision, the TOF of one of these two fake charged tracks is delayed compared to the other. Therefore, a maximum TOF difference requirement of $|TOF_{track1} - TOF_{track2}| < 4$ ns can suppress these events. For CM energies below 2.5 GeV, the low momentum of the particles can prevent protons and antiprotons of the signal process from reaching the TOF system. For these energy points, events without a valid TOF measurement for one or both tracks are kept, although they can not fulfil the above requirement on the TOF difference. For energy points at or above 2.5 GeV, a valid TOF measurement is required for both tracks. The distribution of the TOF difference can be seen in figure 6.8 for data, signal MC and $q\bar{q}$ MC at selected CM energies along with the chosen requirement limits. Plots for all other CM energy points can be found in appendix A in figure A.6.

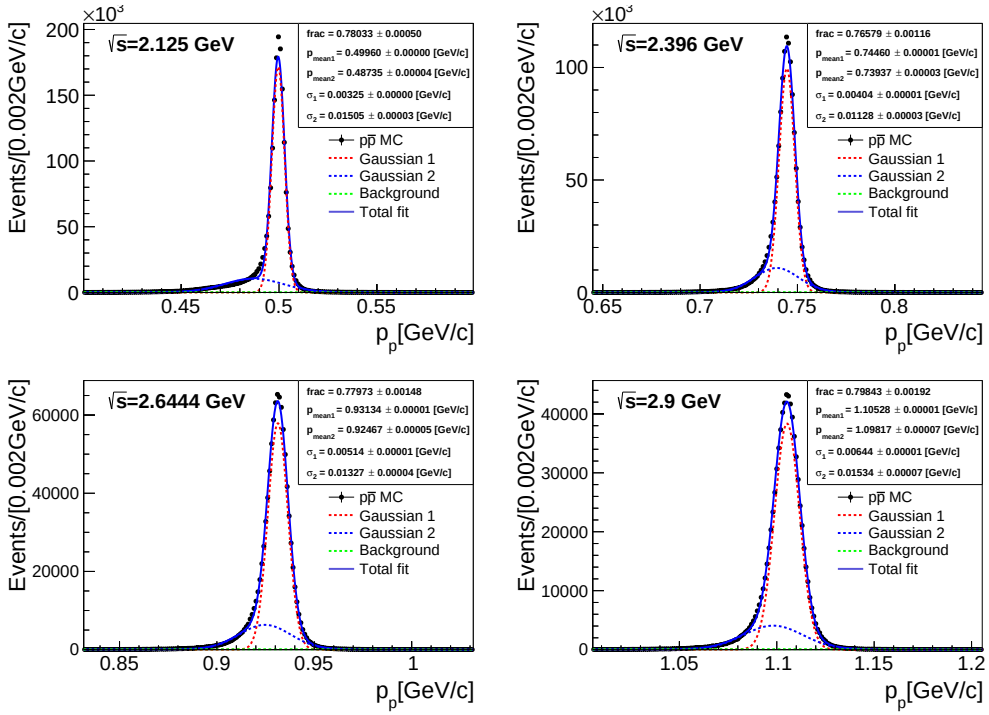

FIGURE 6.9: Momentum distribution of the positive track in signal MC ($e^+e^- \to p\bar{p}$ with NLO ISR radiative corrections) for selected CM energies. A fit with a double gaussian plus a polynomial is performed to extract the width of the distribution, which is used to define the momentum window in which tracks of accepted events have to be (see text). The red dashed line is the main gaussian, the blue dashed line is the secondary gaussian, and the green line is a polynomial function.

Finally, both the positive and the negative track of each event are required to be within a momentum window around the theoretical momentum of a proton (antiproton) determined by the two body kinematics at each CM energy.
The theoretical momentum can be calculated by:

$$p_{theo} = \sqrt{\left(\frac{E_{CM}}{2}\right)^2 - M_p^2} \tag{6.2}$$

with the center of mass energy E_{CM} and the mass of the proton M_p. A fit with a double gaussian plus a polynomial function is performed on the absolute momentum distribution of the positive and the negative track of a signal MC sample, which was generated including the ISR process up to NNLO. The fit is performed after boosting the two tracks to the CM system of e^+e^-, and can be seen in figure 6.9 for the positive track and figure 6.10 for the negative track for exemplary CM energies ((2.125, 2.396, 2.6444 and 2.9) GeV). Here, the red dashed line is the main gaussian, the blue dashed line is the secondary gaussian that describes the radiative tail, and the green line is a polynomial function.

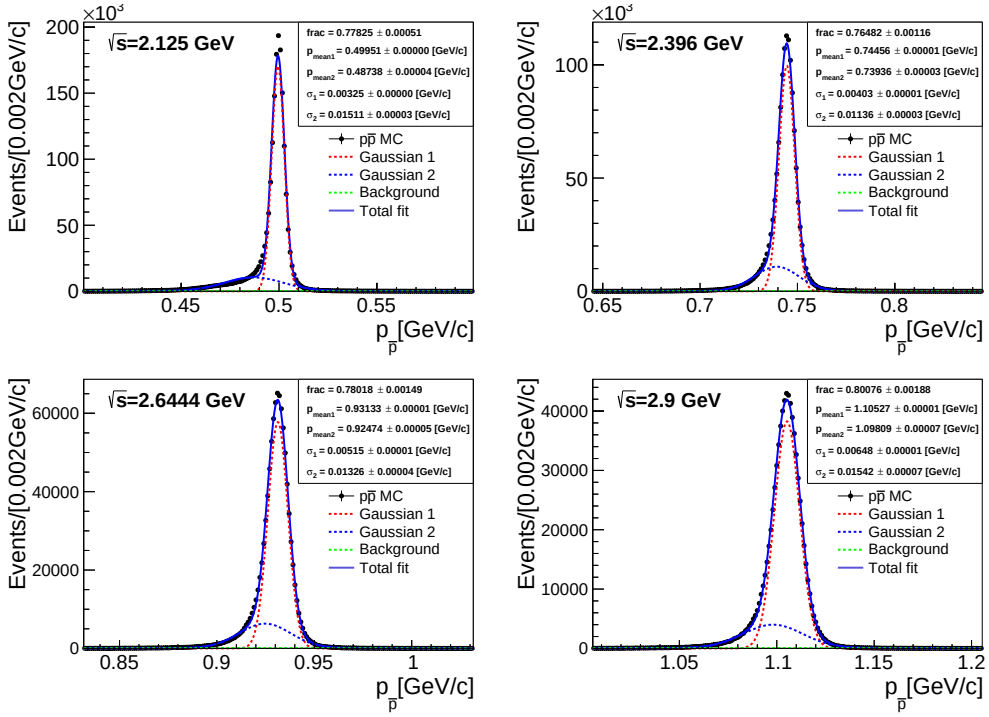

FIGURE 6.10: Momentum distribution of the negative track in signal MC ($e^+e^- \to p\bar{p}$ with NLO ISR radiative corrections) for selected CM energies. A fit with a double gaussian plus a polynomial is performed to extract the width of the distribution, which is used to define the momentum window in which tracks of accepted events have to be (see text). The red dashed line is the main gaussian, the blue dashed line is the secondary gaussian, and the green line is a polynomial function.

The width of the distribution is then calculated from the width of the two gaussians by:

$$\sigma_p = \sqrt{frac \times \sigma_1^2 + (1 - frac) \times \sigma_2^2 + f(1 - frac) \times (p_{mean1} - p_{mean2})^2} \tag{6.3}$$

with the width of the main gaussian σ_1, the width of the secondary gaussian σ_2, and the fraction of the main gaussian of the total fit "frac". For consistency reasons, the theoretical momentum is also extracted from that fit instead of equation 6.2 using

$$p_{theo,fit} = \sqrt{frac \times p_{mean1}^2 + (1 - frac) \times p_{mean2}^2} \tag{6.4}$$

with the same variables as in equation 6.3. The difference of the central value of the momentum extracted from equations 6.2 and 6.4 is well below 1% for most energy points, as can be seen in table 6.1.

TABLE 6.1: Theoretical momentum calculated from equation 6.2 (p_{theo}) and extracted from fit (see figures 6.9 and 6.10) with equation 6.4 ($p_{theo,fit}$. The last two columns show the width of the momentum distribution for the proton and the antiproton, also extracted from the fits using equation 6.3.

$\sqrt{s}$[GeV]	p_{theo}[GeV]	$p_{theo,fit}$[GeV]	σ_p [MeV]	
		proton and antiproton	proton	antiproton
2	0.346	0.342	9.83	9.97
2.05	0.413	0.409	9.91	9.89
2.1	0.471	0.468	8.97	8.97
2.12655	0.500	0.497	9.16	9.16
2.15	0.525	0.521	9.49	9.47
2.175	0.550	0.546	9.88	9.85
2.2	0.574	0.571	10.01	9.97
2.2324	0.605	0.601	10.38	10.41
2.3094	0.673	0.669	11.06	11.10
2.3864	0.737	0.736	6.86	6.87
2.396	0.745	0.743	6.88	6.88
2.5	0.826	0.824	7.39	7.43
2.6444	0.932	0.930	8.22	8.19
2.6464	0.933	0.931	8.22	8.18
2.7	0.971	0.969	8.39	8.46
2.8	1.039	1.037	8.85	8.89
2.9	1.106	1.104	9.58	9.56
2.95	1.138	1.136	9.49	10.05
2.981	1.158	1.156	10.24	10.28
3	1.170	1.168	10.41	10.48
3.02	1.183	1.181	10.46	10.49
3.08	1.221	1.220	10.23	10.22

Table 6.1 also summarises the fit results for the width and mean of the momentum distributions for all energy points. The momentum resolution is mostly stable throughout all energy points, the slow rise is due to an increased amount of ISR events with higher energies which broadens the distribution. The abrupt drops in σ_p at 2.1 and 2.3864 GeV are due to harder requirements on the back-to-back angle at these energy thresholds, which reduces the amount of ISR events and therefore the width of the momentum distribution.

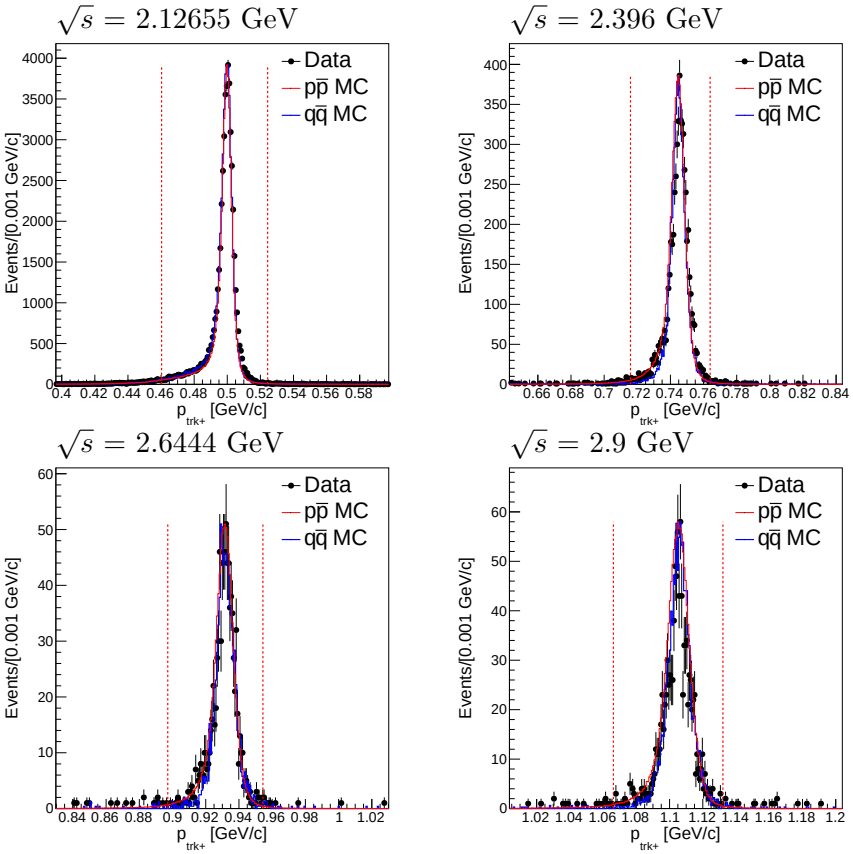

FIGURE 6.11: Distribution of the momentum of the positive track in the e^+e^- CM system for data (black dots with error bars), inclusive hadronic MC ($q\bar{q}$, blue histogram) and signal MC including ISR up to NNLO (red histogram) for example energy points of 2.12655, 2.396, 2.6444 and 2.9 GeV. The two red dashed lines mark the chosen momentum window requirement. All other requirements except the one for the momentum window have been applied, and the distributions of signal and $q\bar{q}$ MC have been scaled to the bin with the highest amount of entries in data.

The width of the momentum distribution calculated from equation 6.3 is now used to define the momentum window as $(p_{theo,fit} - 4\sigma_p) < p < (p_{theo,fit} + 3\sigma_p)$ for both the negative and the positive track, individually, with independently determined σ_p. The momentum window was chosen asymmetrically with a larger window towards lower momenta, seen from $p_{theo,fit}$, to include the radiative tail made up of ISR events ($e^+e^- \to p\bar{p}n\gamma$, $n = 1, 2, 3...$). Although these events are not signal events, the goal of the event

selection is not to filter out these events, which would be a hard task especially for events with very soft ISR photons which have a very similar signature as signal events. Instead, the ISR events will later be corrected for using the correction factor $1 + \delta$ determined by signal MC simulation (see sections 8.2 and 9.1.2).

The momentum distribution for data, signal MC and inclusive hadronic MC can be seen in figure 6.11 for the positive track and in figure 6.12 for the negative track at select CM energies, along with the chosen limits for the momentum window on both sides of the theoretical momentum. Plots for all other CM energy points can be found in appendix A in figures A.7 and A.8 for the positive and negative track, respectively.

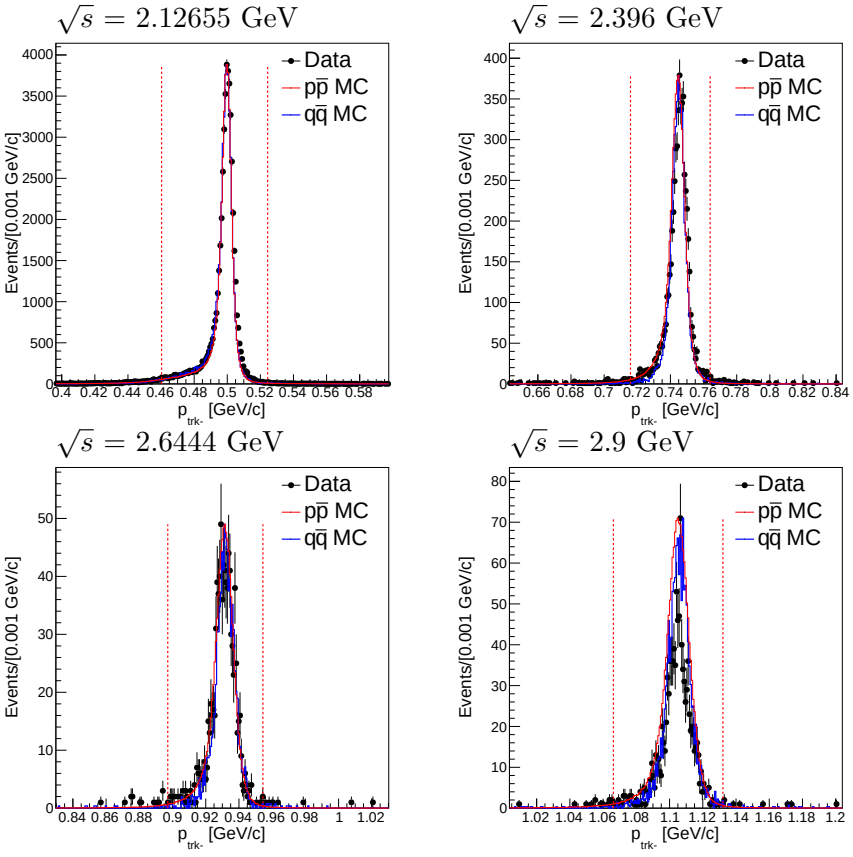

FIGURE 6.12: Distribution of the momentum of the negative track in the e^+e^- CM system for data (black dots with error bars), inclusive hadronic MC ($q\bar{q}$, blue histogram) and signal MC including ISR up to NNLO (red histogram) for example energy points of 2.12655, 2.396, 2.6444 and 2.9 GeV. The two red dashed lines mark the chosen momentum window requirement. All other requirements except the one for the momentum window have been applied, and the distributions of signal and $q\bar{q}$ MC have been scaled to the bin with the highest amount of entries in data.

As can be seen from these plots, the level of constant background outside the signal region (assuming no peak under the signal area) is very low after the application of the

event selection criteria discussed in this chapter. A thorough investigation of potential remaining background will be conducted in the next chapter.

6.1.3 Summary of event selection criteria

An overview over the event selection criteria discussed in detail in the last sections will be given here. In summary, charged tracks must first fulfil the following criteria:

- Point of closest approach of the track to the interaction vertex $|R_z| < 10$ cm and $R_{XY} < 1$ cm
- Polar angle of the track $|cos(\theta)| < 0.93$
- Vertex fit performed on the whole event, each track must have $\chi^2_{vertex} < 100$
- Particle identification depending on energy:
  - For E_{CM} = (2.0-2.15) GeV: Requirement on the normalised pulse height of the dE/dx measurement of the MDC, PH_{norm} <(3.0, 2.5, 2.0, 1.8 and 1.7) at (2.0, 2.05, 2.1, 2.12655 and 2.15) GeV
  - For E_{CM} = (2.15-3.08) GeV: Requirement on the particle probability given by the PID system: $P_{PID}(proton) > P_{PID}(pion), P_{PID}(kaon), P_{PID}(electron)$

The high level selection criteria applied to the event as a whole can be summarised as follows:

- Exactly two charged tracks fulfilling the above requirements with a total charge of 0 in each event
- Back-to-back signature of the two tracks with $\sphericalangle_{p,\bar{p}} > 170°$, 175°,178° at (2.0-2.05, 2.1-2.3094, 2.3864-3.08) GeV
- TOF difference between the two tracks: $|TOF_{track1} - TOF_{track2}| < 4$ ns
- Requirement on the ratio of momentum (from MDC) and energy deposition (from EMC) for the positive track: $E/p < 0.5$ for $E_{CM} \geq 2.150$ GeV
- Momentum window: both tracks required to fulfil $(p_{theo,fit} - 4\sigma_p) < p < (p_{theo,fit} + 3\sigma_p)$ with $p_{theo,fit}$ calculated from equation 6.4 and σ_p calculated from equation 6.3.

6.2 Number of selected signal events in data

The number of remaining events after applying all the selection criteria described in this chapter are shown in table 6.2 for all energy points of the data sample taken in 2015. After the aforementioned study of remaining background events in this selection in chapter 7, they will be used to extract the cross section of $e^+e^- \to p\bar{p}$ in chapter 8 and, after analysing their angular distribution, the EM FFs of the proton in chapter 9.

TABLE 6.2: Number of selected events (N_{sel}^{data}) after event selection in data for all energy points of the 2015 scan data set taken at BESIII.

E_{CM} [GeV]	$\mathcal{L}_{int}$ [pb^{-1}]	N_{sel}^{data}
2.00000	10.074	5296 ± 73
2.05000	3.343	1693 ± 41
2.10000	12.167	5988 ± 77
2.12655	108.49	50160 ± 224
2.15000	2.841	1186 ± 34
2.17500	10.625	3761 ± 61
2.20000	13.699	4089 ± 64
2.23240	14.501	3643 ± 60
2.30940	21.089	2322 ± 48
2.38640	22.549	1849 ± 43
2.39600	66.869	5512 ± 74
2.50000	1.098	54 ± 7
2.64440	33.722	868 ± 29
2.64640	34.003	838 ± 29
2.70000	1.034	20 ± 4
2.80000	4.761	53 ± 7
2.90000	105.253	1010 ± 32
2.95000	15.942	118 ± 11
2.98100	16.071	132 ± 11
3.00000	15.881	92 ± 10
3.02000	17.29	97 ± 10
3.08000	157.204	854 ± 29

Chapter 7

Evaluation of Background Processes

This chapter describes the investigation of the remaining background in data after the event selection whcih has been discussed in chapter 6. Two different methods are used for this investigation: First, a set of background MC samples is generated (see section 5.3.2) and subjected to the same event selection criteria as data to see if any events pass the selection. Depending on the results of this check, an estimation is then given either for the amount of remaining background events in data or, in case of no remaining events in the background MC samples, for an upper limit of the background contamination.
The second method uses two-dimensional sidebands in the momentum distribution of the proton and antiproton to estimate the remaining background in data after the event selection, which is then compared to the expected sideband distribution of a signal MC sample. It serves as a cross check, in case the MC based method is not accurate due to possible data-MC differences or an insufficient amount of generated events. The latter is especially problematic in case of the Bhabha scattering process due to the high cross section of this background channel, which would require huge amounts of generated MC events at all energy points.

7.1 Background evaluation with Monte Carlo simulation

The considered background channels include QED processes like $e^+e^- \to e^+e^-$, $\gamma\gamma$, $\mu^+\mu^-$, and hadronic processes. For the hadronic processes, one inclusive MC sample containing all possible hadronic final states has been produced, including also the signal process $e^+e^- \to p\bar{p}$. In addition, several hadronic background processes have been generated exclusively. In the following sections, these MC samples are investigated

regarding the amount of remaining events after the event selection described in chapter 6. In the case of no remaining events, an upper limit at 95% confidence level is estimated for the background contamination of that channel, for which the following formula has been used:

$$N_{estimated} = \frac{3\sigma_{bkg} L_{int}}{N_{generated}} \tag{7.1}$$

with the upper limit of estimated background events $N_{estimated}$, the cross section of the background process σ_{bkg}, the integrated luminosity at this energy point L_{int} and the amount of generated background MC events $N_{generated}$.

7.1.1 Hadronic background processes

The amount of generated and remaining events of the inclusive hadronic MC sample (final state $q\bar{q}$) can be seen in table 7.1. The amount of generated events is about as large as the expected events from the combined hadronic cross section, calculated with the ConExc event generator, and the luminosity of the data taken at each energy point. The remaining events in these samples have been investigated and found to be only events of the signal process or the signal process with radiative photons (ISR, FSR). After the exclusion of these events, no background events remain after the $e^+e^- \to p\bar{p}$ selection, resulting in an upper limit of remaining background of less than 2.54 events for all energies.

The first exclusive hadronic channel that was generated is $e^+e^- \to p\bar{p}\pi_0$. For low center of mass energies, this process can pass the event selection in cases where the π_0 has a very low momentum and decays undetected by the detector. In such cases, the kinematics of the remaining proton and antiproton (back-to-back signature, momentum of the particles) resembles that of the proton-antiproton pair of the signal process. An exemption is the energy point at 2.05 GeV, which is very close to the production threshold of the process (about 2.012 GeV). At this CM energy, the momentum of the proton-antiproton pair is so low that most events are sorted out due to the requirement on the POA of the charged tracks (details see section 6.1.1).
The cross section of the process is not known for center of mass energies below 4 GeV, therefore an estimate of the number of expected events using the luminosity and cross section is not possible. To be on the safe side, large samples have been generated at each CM energy of 5×10^5 events each, which is certainly an overestimation of the amount of events in data for this channel. Still, less then 23 events remain after the selection for data points at low CM energies, while at high CM energies, this background channel is irrelevant due to the different kinematics compared to the signal channel. In relation

TABLE 7.1: Background evaluation of the inclusive hadronic background sample $e^+e^- \to q\bar{q}$. For each center of mass energy E_{CM}, the number of generated events $N_{generated}$, the amount of remaining events after selection N_{obs}, the total cross section of all hadronic processes σ_{bkg} (calculated by the ConExc event generator), the integrated luminosity L_{int} and the estimated 95% confidence level upper limit for the background pollution $N_{estimated}$ is given. N_{obs} excludes events of the signal process.

E_{CM} [GeV]	$N_{generated}$	N_{obs}	σ_{bkg} [nb]	L_{int} [pb^{-1}]	$N_{estimated}$
2	6.6×10^6	0	57.867	$10.074 \pm 0.005 \pm 0.067$	< 0.26
2.05	4×10^6	0	56.455	$3.343 \pm 0.003 \pm 0.027$	< 0.14
2.1	4.06×10^6	0	55.111	$12.167 \pm 0.006 \pm 0.085$	< 0.50
2.12655	8.4×10^6	0	50.700	$108.49 \pm 0.02 \pm 0.94$	< 1.96
2.15	4×10^6	0	53.829	$2.841 \pm 0.003 \pm 0.024$	< 0.11
2.175	3.5×10^6	0	53.211	$10.625 \pm 0.006 \pm 0.091$	< 0.48
2.2	3.6×10^6	0	52.606	$13.699 \pm 0.007 \pm 0.092$	< 0.60
2.2324	4.5×10^6	0	51.843	$14.501 \pm 0.009 \pm 0.110$	< 0.50
2.3094	3.9×10^6	0	50.114	$21.089 \pm 0.009 \pm 0.143$	< 0.81
2.3864	5.545×10^6	0	48.4974	$22.549 \pm 0.010 \pm 0.176$	< 0.59
2.396	7.33×10^6	0	48.3027	$66.869 \pm 0.017 \pm 0.475$	< 1.32
2.5	6.77×10^6	0	46.2933	$1.098 \pm 0.002 \pm 0.009$	< 0.02
2.6444	11.18×10^6	0	43.7654	$33.722 \pm 0.013 \pm 0.216$	< 0.40
2.6464	11.18×10^6	0	43.7654	$34.003 \pm 0.013 \pm 0.282$	< 0.40
2.7	4.15×10^6	0	42.8642	$1.034 \pm 0.002 \pm 0.007$	< 0.03
2.8	5.25×10^6	0	41.3333	$4.761 \pm 0.008 \pm 0.031$	< 0.11
2.9	6.34×10^6	0	39.9080	$105.253 \pm 0.025 \pm 0.905$	< 1.99
2.95	3.95×10^6	0	39.2316	$15.942 \pm 0.010 \pm 0.143$	< 0.48
2.981	3.85×10^6	0	38.8237	$16.071 \pm 0.010 \pm 0.095$	< 0.49
3.0	3.85×10^6	0	38.5778	$15.881 \pm 0.010 \pm 0.110$	< 0.48
3.02	3.75×10^6	0	38.3223	$17.290 \pm 0.011 \pm 0.123$	< 0.53
3.08	6.99×10^6	0	37.5758	$157.204 \pm 0.066 \pm 1.148$	< 2.54

to the amount of signal events (see section 6.2), the remaining background events correspond to a background pollution of less than 0.5% despite the high amount of generated events. The summary of this background channel is shown in table 7.2, samples for center of mass energies below 2.05 GeV have not been generated since they are below the production threshold of the process.

Although the background pollution with events from this channel is likely very low as elaborated above, an estimation of an upper limit of remaining background events after event selection according to equation 7.1 is not possible due to the unknown cross section. Instead, an alternative method will be introduced in the following. For this method, the generated $e^+e^- \to p\bar{p}\pi_0$ MC samples as well as the data samples for the main analysis have been investigated using a selection algorithm to select $p\bar{p}\pi_0$ events. This selection algorithm is the same as the one used for background evaluation in reference [182].

The main selection criteria of the algorithm can be summarised as follows: the proton

TABLE 7.2: Background evaluation of the exclusive hadronic background samples for $e^+e^- \to p\bar{p}\pi_0$. For each center of mass energy E_{CM}, the number of generated events $N_{generated}$, the amount of remaining events after selection N_{obs}, the cross section of the process σ_{bkg} (not available for this process for $E_{CM} < 4$ GeV), the integrated luminosity L_{int} and the estimated 95% confidence level upper limit for the background pollution $N_{estimated}$ is given. For $E_{CM} < 2.05$ GeV, no samples have been generated since the energy is below the production threshold of the process.

E_{CM} [GeV]	$N_{generated}$	N_{obs}	σ_{bkg} [nb]	L_{int} [pb^{-1}]	$N_{estimated}$
2	-	-	-	$10.074 \pm 0.005 \pm 0.067$	–
2.05	5×10^5	0	-	$3.343 \pm 0.003 \pm 0.027$	–
2.1	5×10^5	23	-	$12.167 \pm 0.006 \pm 0.085$	–
2.12655	5×10^5	12	-	$108.49 \pm 0.02 \pm 0.94$	–
2.15	5×10^5	4	-	$2.841 \pm 0.003 \pm 0.024$	–
2.175	5×10^5	7	-	$10.625 \pm 0.006 \pm 0.091$	–
2.2	5×10^5	3	-	$13.699 \pm 0.007 \pm 0.092$	–
2.2324	5×10^5	5	-	$14.501 \pm 0.009 \pm 0.110$	–
2.3094	5×10^5	1	-	$21.089 \pm 0.009 \pm 0.143$	–
2.3864	5×10^5	0	-	$22.549 \pm 0.010 \pm 0.176$	–
2.396	5×10^5	0	-	$66.869 \pm 0.017 \pm 0.475$	–
2.5	5×10^5	0	-	$1.098 \pm 0.002 \pm 0.009$	–
2.6444	5×10^5	0	-	$33.722 \pm 0.013 \pm 0.216$	–
2.6464	5×10^5	0	-	$34.003 \pm 0.013 \pm 0.282$	–
2.7	5×10^5	0	-	$1.034 \pm 0.002 \pm 0.007$	–
2.8	5×10^5	0	-	$4.761 \pm 0.008 \pm 0.031$	–
2.9	5×10^5	0	-	$105.253 \pm 0.025 \pm 0.905$	–
2.95	5×10^5	0	-	$15.942 \pm 0.010 \pm 0.143$	–
2.981	5×10^5	0	-	$16.071 \pm 0.010 \pm 0.095$	–
3.0	5×10^5	0	-	$15.881 \pm 0.010 \pm 0.110$	–
3.02	5×10^5	0	-	$17.290 \pm 0.011 \pm 0.123$	–
3.08	5×10^5	0	-	$157.204 \pm 0.066 \pm 1.148$	–

and the antiproton are selected in a similar way as in the event selection of the signal process of this analysis (see chapter 6). Two charged tracks of opposite charge are required that have a POA to the interaction vertex of less than 1 cm in the XY plane and less than 10 cm in the Z plane. The PID system is used to identify them as proton and antiproton over pions, muons, kaons and electrons, and an E/p ratio of less than 0.5 is required to suppress Bhabha scattering events. In addition to these two good charged tracks, two good showers in the EMC are required. A good shower is defined by having a minimum energy of more than 25 (50) MeV if the shower is located in the barrel (endcap) part of the EMC to remove electronic noise. In addition, the timing information of the shower must be within 14 sampling periods (one sampling period corresponds to 50 ns) of the event start time to make sure the photons are from the same event. Finally, a five constraints kinematic fit is applied to the two charged tracks and the two neutral showers. The constraints of that fit are the four components of

the initial four momentum of the e^+e^- beam (four momentum conservation) and the mass of the π_0, which needs to be equal to the total energy of the two showers. The χ^2_{5C} of this fit is required to be lower than 60. In case more than two neutral showers exist, all possible combinations of showers are fitted and the one with the lowest χ^2_{5C} is selected. An additional four constraints kinematic fit on the two charged tracks as well as the shower with the highest energy, using only the four momentum of the beam as constraint, is used to veto $e^+e^- \to p\bar{p}\gamma$ background by requiring χ^2_{4C} of that fit to be larger than 25.

The algorithm described above can now be used to extract $p\bar{p}\pi_0$ events in the data samples of the main analysis as well as in the generated $p\bar{p}\pi_0$ MC samples. In combination with the amount of remaining events in the $p\bar{p}\pi_0$ MC samples after using the $p\bar{p}$ selection algorithm (see table 7.2), they can be used to estimate the $p\bar{p}\pi_0$ background pollution in data in the following way:

$$N_{p\bar{p}\pi_0,est} = N^{data}_{p\bar{p}\pi_0} \times \frac{N^{MC}_{p\bar{p}}}{N^{MC}_{p\bar{p}\pi_0}}. \tag{7.2}$$

On the right side of this equation, the upper indices of N indicate which sample is analysed and the lower indices which algorithm has been used: $N^{data}_{p\bar{p}\pi_0}$ is the amount of remaining events in data using the $p\bar{p}\pi_0$ selection, $N^{MC}_{p\bar{p}}$ is the amount of remaining events in the $p\bar{p}\pi_0$ MC sample using the $p\bar{p}$ selection, and $N^{MC}_{p\bar{p}\pi_0}$ is the amount of remaining events in the $p\bar{p}\pi_0$ MC sample using the $p\bar{p}\pi_0$ selection. On the left side, $N_{p\bar{p}\pi_0,est}$ stands for the estimated amount of remaining $p\bar{p}\pi_0$ events.

TABLE 7.3: Amount of remaining $p\bar{p}\pi_0$ background events in data estimated according to formula 7.2. $N_{p\bar{p}\pi_0,est}$ is the estimated amount of remaining $p\bar{p}\pi_0$ events, $N^{data}_{p\bar{p}\pi_0}$ is the amount of remaining events in data using the $p\bar{p}\pi_0$ selection, $N^{MC}_{p\bar{p}}$ is the amount of remaining events in the $p\bar{p}\pi_0$ MC sample using the $p\bar{p}$ selection, and $N^{MC}_{p\bar{p}\pi_0}$ is the amount of remaining events in the $p\bar{p}\pi_0$ MC sample using the $p\bar{p}\pi_0$ selection.

E_{CM} [GeV]	$N^{data}_{p\bar{p}\pi_0}$	$N^{MC}_{p\bar{p}}$	$N^{MC}_{p\bar{p}\pi_0}$	$N_{p\bar{p}\pi_0,est}$
2.1	7059	23	68387	2.37 ± 0.50
2.125	60974	12	120096	6.09 ± 1.76
2.150	1517	4	153257	0.04 ± 0.02
2.175	4676	7	188925	0.17 ± 0.07
2.200	5635	3	213659	0.08 ± 0.05
2.2324	4420	5	241751	0.09 ± 0.04
2.3094	7162	1	282680	0.03 ± 0.03

A summary of the estimated amount of remaining $p\bar{p}\pi_0$ events in data is given in table 7.3 for the energy points that have remaining events in the $p\bar{p}\pi_0$ MC sample after the $e^+e^- \to p\bar{p}$ selection. The error $N_{p\bar{p}\pi_0,est}$ was calculated using gaussian error propagation, by assuming an error of $\sqrt{N}$ for $N^{data}_{p\bar{p}\pi_0}$, $N^{MC}_{p\bar{p}}$ and $N^{MC}_{p\bar{p}\pi_0}$. This estimation confirms that the

background of this channel is negligible, with a maximum pollution of about 0.04% at 2.1 GeV.

TABLE 7.4: Background evaluation of the exclusive hadronic background samples $e^+e^- \to p\bar{p}\pi^+\pi^-$. For each center of mass energy E_{CM}, the number of generated events $N_{generated}$, the amount of remaining events after selection N_{obs}, the cross section this process σ_{bkg} (calculated by the Phokhara event generator), the integrated luminosity L_{int} and the estimated 95% confidence level upper limit for the background pollution $N_{estimated}$ is given. For $E_{CM} < 2.15$ GeV, no samples have been generated since the energy is below the production threshold of the process.

E_{CM} [GeV]	$N_{generated}$	N_{obs}	σ_{bkg} [nb]	L_{int} [pb^{-1}]	$N_{estimated}$
2	-	-	5.028 ± 0.018	$10.074 \pm 0.005 \pm 0.067$	-
2.05	-	-	4.657 ± 0.017	$3.343 \pm 0.003 \pm 0.027$	-
2.1	-	-	4.314 ± 0.016	$12.167 \pm 0.006 \pm 0.085$	-
2.12655	-	-	4.153 ± 0.015	$108.49 \pm 0.02 \pm 0.94$	-
2.15	5×10^5	0	4.020 ± 0.015	$2.841 \pm 0.003 \pm 0.024$	< 0.07
2.175	5×10^5	0	3.886 ± 0.014	$10.625 \pm 0.006 \pm 0.091$	< 0.25
2.2	5×10^5	0	3.767 ± 0.014	$13.699 \pm 0.007 \pm 0.092$	< 0.31
2.2324	5×10^5	0	3.627 ± 0.014	$14.501 \pm 0.007 \pm 0.087$	< 0.32
2.3094	5×10^5	0	3.335 ± 0.013	$21.089 \pm 0.009 \pm 0.143$	< 0.42
2.3864	5×10^5	0	3.087 ± 0.012	$22.549 \pm 0.010 \pm 0.176$	< 0.42
2.396	5×10^5	0	3.058 ± 0.012	$66.869 \pm 0.017 \pm 0.475$	< 1.23
2.5	5×10^5	0	2.781 ± 0.011	$1.098 \pm 0.002 \pm 0.009$	< 0.02
2.6444	5×10^5	0	2.464 ± 0.010	$33.722 \pm 0.013 \pm 0.216$	< 0.50
2.6464	5×10^5	0	2.460 ± 0.010	$34.003 \pm 0.013 \pm 0.282$	< 0.50
2.7	5×10^5	0	2.360 ± 0.009	$1.034 \pm 0.002 \pm 0.007$	< 0.01
2.8	5×10^5	0	2.187 ± 0.008	$4.761 \pm 0.008 \pm 0.031$	< 0.06
2.9	5×10^5	0	2.035 ± 0.008	$105.253 \pm 0.025 \pm 0.905$	< 1.29
2.95	5×10^5	0	1.964 ± 0.008	$15.942 \pm 0.010 \pm 0.143$	< 0.19
2.981	5×10^5	0	1.922 ± 0.008	$16.071 \pm 0.010 \pm 0.095$	< 0.19
3.0	5×10^5	0	1.899 ± 0.007	$15.881 \pm 0.010 \pm 0.110$	< 0.18
3.02	5×10^5	0	1.872 ± 0.007	$17.290 \pm 0.011 \pm 0.123$	< 0.19
3.08	5×10^5	0	1.798 ± 0.007	$157.204 \pm 0.066 \pm 1.148$	< 1.70

The exclusive channel $e^+e^- \to p\bar{p}\pi^+\pi^-$ was generated using the default model built into the Phokhara event generator. With 5×10^5 events per energy point, more than the amount of expected events has been generated at all CM energies and no events remain after the event selection. This results in a negligible estimated background pollution according to equation 7.1 by this process of less than 2 events for all energy points. Cross section numbers taken from the ConExc generator as well as the estimated upper limits for all energy points of this background channel can be seen in table 7.4.

The channel $e^+e^- \to K\bar{K}$ was generated using the ConExc event generator. The cross section of this process was measured by BESIII (see reference [183]) using the same data set as in the analysis presented in this work. With 1×10^5 events at each energy point, more events have been generated than expected, yet no events remain after the

TABLE 7.5: Background evaluation of the exclusive hadronic background samples for $e^+e^- \to K\bar{K}$. For each center of mass energy E_{CM}, the number of generated events $N_{generated}$, the amount of remaining events after selection N_{obs}, the cross section of this process σ_{bkg} (measured by reference [183]), the integrated luminosity L_{int} and the estimated 95% confidence level upper limit for the background pollution $N_{estimated}$ is given.

E_{CM} [GeV]	$N_{generated}$	N_{obs}	σ_{bkg} [pb]	L_{int} [pb^{-1}]	$N_{estimated}$
2	1×10^5	0	$351.5 \pm 8.2 \pm 9.0$	$10.074 \pm 0.005 \pm 0.067$	< 0.11
2.05	1×10^5	0	$296.1 \pm 13.1 \pm 7.5$	$3.343 \pm 0.003 \pm 0.027$	< 0.03
2.1	1×10^5	0	$220.6 \pm 5.9 \pm 5.5$	$12.167 \pm 0.006 \pm 0.085$	< 0.08
2.12655	1×10^5	0	$192.0 \pm 1.8 \pm 4.7$	$108.49 \pm 0.02 \pm 0.94$	< 0.63
2.15	1×10^5	0	$171.7 \pm 10.7 \pm 4.2$	$2.841 \pm 0.003 \pm 0.024$	< 0.02
2.175	1×10^5	0	$184.2 \pm 5.7 \pm 4.6$	$10.625 \pm 0.006 \pm 0.091$	< 0.06
2.2	1×10^5	0	$231.4 \pm 5.7 \pm 6.0$	$13.699 \pm 0.007 \pm 0.092$	< 0.10
2.2324	1×10^5	0	$253.2 \pm 6.3 \pm 6.4$	$14.501 \pm 0.009 \pm 0.110$	< 0.11
2.3094	1×10^5	0	$184.0 \pm 4.0 \pm 4.8$	$21.089 \pm 0.009 \pm 0.143$	< 0.12
2.3864	1×10^5	0	$101.5 \pm 2.9 \pm 4.8$	$22.549 \pm 0.010 \pm 0.176$	< 0.07
2.396	1×10^5	0	$102.6 \pm 1.7 \pm 2.8$	$66.869 \pm 0.017 \pm 0.475$	< 0.21
2.5	1×10^5	0	$88.1 \pm 12.2 \pm 2.9$	$1.098 \pm 0.002 \pm 0.009$	< 0.01
2.6444	1×10^5	0	$56.6 \pm 1.8 \pm 2.3$	$33.722 \pm 0.013 \pm 0.216$	< 0.06
2.6464	1×10^5	0	$56.7 \pm 1.8 \pm 1.8$	$34.003 \pm 0.013 \pm 0.282$	< 0.06
2.7	1×10^5	0	$36.3 \pm 8.4 \pm 1.3$	$1.034 \pm 0.002 \pm 0.007$	< 0.01
2.8	1×10^5	0	$37.9 \pm 8.8 \pm 1.7$	$4.761 \pm 0.008 \pm 0.031$	< 0.01
2.9	1×10^5	0	$30.4 \pm 0.8 \pm 1.5$	$105.253 \pm 0.025 \pm 0.905$	< 0.10
2.95	1×10^5	0	$25.3 \pm 1.9 \pm 1.4$	$15.942 \pm 0.010 \pm 0.143$	< 0.01
2.981	1×10^5	0	$28.0 \pm 1.6 \pm 1.6$	$16.071 \pm 0.010 \pm 0.095$	< 0.01
3.0	1×10^5	0	$24.4 \pm 1.8 \pm 1.5$	$15.881 \pm 0.010 \pm 0.110$	< 0.01
3.02	1×10^5	0	$24.8 \pm 1.8 \pm 1.5$	$17.290 \pm 0.011 \pm 0.123$	< 0.01
3.08	1×10^5	0	$25.3 \pm 0.7 \pm 2.2$	$157.204 \pm 0.066 \pm 1.148$	< 0.10

event selection. The resulting estimated background pollution at 95% confidence level is therefore below 1 at all energies and can be neglected.

7.1.2 QED background processes

The main background QED process to the signal process of $e^+e^- \to p\bar{p}$ is radiative Bhabha scattering. The amount of generated and remaining events of this channel can be seen in table 7.6.

Since the cross section of the process is very large (about 2×10^3 times larger than the signal process at low energies up to almost 100×10^3 times larger at the highest energy points), the amount of expected background events at each CM energy would require the generation of huge Bhabha MC samples, which is not feasible. Instead, large samples according to (or larger than) the amount of expected events have been generated at selected energy points within the energy range of the analysis, mostly at higher CM

energies where the separation of Bhabha scattering events from signal is more difficult (see section 6.1.2). Since there is no qualitative change in either the selection criteria or the data samples for neighbouring energy points, and no events remain after the selection at any CM energy, the remaining background pollution can be neglected. The high number of $N_{estimated}$ at some energy points comes solely from the too small MC samples generated at these CM energies.

TABLE 7.6: Background evaluation of the radiative Bhabha scattering background samples $e^+e^- \to e^+e^-$. For each center of mass energy E_{CM}, the number of generated events $N_{generated}$, the amount of remaining events after selection N_{obs}, the cross section of the Bhabha scattering process σ_{bkg} (taken from the Babayaga event generator), the integrated luminosity L_{int} and the estimated 95% confidence level upper limit for the background pollution $N_{estimated}$ is given. For CM energies where at least the amount of expected background events have been generated, $N_{generated}$ is marked in red.

E_{CM} [GeV]	$N_{generated}$	N_{obs}	σ_{bkg} [nb]	L_{int} [pb^{-1}]	$N_{estimated}$
2	1.2×10^7	0	1838.9	$10.074 \pm 0.005 \pm 0.067$	< 4.63
2.05	2×10^6	0	1750.6	$3.343 \pm 0.003 \pm 0.027$	< 8.78
2.1	2×10^6	0	1669.9	$12.167 \pm 0.006 \pm 0.085$	< 30.48
2.12655	1×10^7	0	1628.1	$108.49 \pm 0.02 \pm 0.94$	< 52.99
2.15	2×10^6	0	1593.5	$2.841 \pm 0.003 \pm 0.024$	< 6.79
2.175	2×10^6	0	1557.2	$10.625 \pm 0.006 \pm 0.091$	< 24.82
2.2	2×10^6	0	1522.2	$13.699 \pm 0.007 \pm 0.092$	< 31.28
2.2324	7×10^6	0	1478.1	$14.501 \pm 0.009 \pm 0.110$	< 9.19
2.3094	1.195×10^7	0	1382.6	$21.089 \pm 0.009 \pm 0.143$	< 7.32
2.3864	2.7×10^7	0	1294.7	$22.549 \pm 0.010 \pm 0.176$	< 3.24
2.396	1.937×10^8	0	1285.7	$66.869 \pm 0.017 \pm 0.475$	< 1.33
2.5	7×10^6	0	1175.5	$1.098 \pm 0.002 \pm 0.009$	< 0.55
2.6444	2.095×10^7	0	1054.7	$33.722 \pm 0.013 \pm 0.216$	< 5.09
2.6464	1.932×10^8	0	1054.7	$34.003 \pm 0.013 \pm 0.282$	< 0.56
2.7	6.9×10^6	0	1009.3	$1.034 \pm 0.002 \pm 0.007$	< 0.45
2.8	1.205×10^7	0	943.4	$4.761 \pm 0.008 \pm 0.031$	< 1.12
2.9	1.034×10^8	0	878.5	$105.253 \pm 0.025 \pm 0.905$	< 2.68
2.95	1.02×10^8	0	848.2	$15.942 \pm 0.010 \pm 0.143$	< 0.40
2.981	1.02×10^8	0	831.6	$16.071 \pm 0.010 \pm 0.095$	< 0.39
3.0	1.02×10^8	0	820.3	$15.881 \pm 0.010 \pm 0.110$	< 0.38
3.02	1.02×10^8	0	810.4	$17.290 \pm 0.011 \pm 0.123$	< 0.41
3.08	1.144×10^8	0	780.2	$157.204 \pm 0.066 \pm 1.148$	< 3.22

For the channel $e^+e^- \to \gamma\gamma$, large MC samples have been generated by the BESIII collaboration at the energy points used in this analysis. This is due to the fact that the channel is a major background source for signal processes with pure neutral final states, e.g. $e^+e^- \to n\bar{n}$, which have also been analysed with the 2015 scan data set, a paper has been accepted by Nature Physics and is pending publication at the time of the completion of this thesis [159–161]. Although it is unlikely that background events of this channel remain after the event selection of $e^+e^- \to p\bar{p}$, which requires two charged

tracks with opposite charge, the samples have still been analysed and the results can be seen in table 7.7. No events remain after the selection, and the amount of estimated background events is negligible due to the large MC sample size.

The last QED background process that was investigated is $e^+e^- \to \mu^+\mu^-$. At least the amount of events expected in data has been generated using the Babayaga event generator, estimated by the cross section calculated by said generator. No events remain at any CM energy after the event selection, which makes the estimated background pollution at 95% confidence level negligible with less than 3 estimated remaining background events across all energies. The summary of this background channel can be seen in table 7.8.

TABLE 7.7: Background evaluation of the process $e^+e^- \to \gamma\gamma$. For each center of mass energy E_{CM}, the number of generated events $N_{generated}$, the amount of remaining events after selection N_{obs}, the cross section of the background process σ_{bkg} (taken from the Babayaga event generator), the integrated luminosity L_{int} and the estimated 95% confidence level upper limit for the background pollution $N_{estimated}$ is given.

E_{CM} [GeV]	$N_{generated}$	N_{obs}	σ_{bkg} [nb]	L_{int} [pb^{-1}]	$N_{estimated}$
2.0	1×10^6	0	87.36	$10.074 \pm 0.005 \pm 0.067$	< 0.0026
2.05	1×10^6	0	83.17	$3.343 \pm 0.003 \pm 0.027$	< 0.0008
2.1	1×10^6	0	79.32	$12.167 \pm 0.006 \pm 0.085$	< 0.0029
2.12655	1×10^6	0	77.86	$108.49 \pm 0.02 \pm 0.94$	< 0.025
2.15	1×10^6	0	75.67	$2.841 \pm 0.003 \pm 0.024$	< 0.0006
2.175	1×10^6	0	73.96	$10.625 \pm 0.006 \pm 0.091$	< 0.0024
2.2	1×10^6	0	72.34	$13.699 \pm 0.007 \pm 0.092$	< 0.003
2.2324	1×10^6	0	70.26	$14.501 \pm 0.009 \pm 0.110$	< 0.0031
2.3094	1.3×10^6	0	65.67	$21.089 \pm 0.009 \pm 0.143$	< 0.0032
2.3864	1.3×10^6	0	61.54	$22.549 \pm 0.010 \pm 0.176$	< 0.0032
2.396	4×10^6	0	61.06	$66.869 \pm 0.017 \pm 0.475$	< 0.0031
2.5	1×10^6	0	56.10	$1.098 \pm 0.002 \pm 0.009$	< 0.0002
2.6444	1.6×10^6	0	50.19	$33.722 \pm 0.013 \pm 0.216$	< 0.0032
2.6464	1.6×10^6	0	50.12	$34.003 \pm 0.013 \pm 0.282$	< 0.0032
2.7	1×10^6	0	48.17	$1.034 \pm 0.002 \pm 0.007$	< 0.0001
2.8	1×10^6	0	44.81	$4.761 \pm 0.008 \pm 0.031$	< 0.0006
2.9	4.33×10^6	0	41.77	$105.253 \pm 0.025 \pm 0.905$	< 0.0030
2.95	1×10^6	0	40.34	$15.942 \pm 0.010 \pm 0.143$	< 0.0019
2.981	1×10^6	0	39.52	$16.071 \pm 0.010 \pm 0.095$	< 0.0019
3.0	1×10^6	0	39.02	$15.881 \pm 0.010 \pm 0.110$	< 0.0019
3.02	1×10^6	0	38.51	$17.290 \pm 0.011 \pm 0.123$	< 0.0020
3.08	4.31×10^6	0	37.02	$157.204 \pm 0.066 \pm 1.148$	< 0.0041

Finally, beam or machine related background was evaluated using the available dedicated data samples taken at the same time as the regular data on which this analysis was based on. These so called separated beam data samples were taken without the two beams colliding and therefore contain any background that does not originate from reaction products produced in the interaction region of the collider, but rather from effects

TABLE 7.8: Background evaluation of the process $e^+e^- \to \mu^+\mu^-$. For each center of mass energy E_{CM}, the number of generated events $N_{generated}$, the amount of remaining events after selection N_{obs}, the cross section of the background process σ_{bkg} (taken from the Babayaga event generator), the integrated luminosity L_{int} and the estimated 95% confidence level upper limit for the background pollution $N_{estimated}$ is given.

E_{CM} [GeV]	$N_{generated}$	N_{obs}	σ_{bkg} [nb]	L_{int} [pb^{-1}]	$N_{estimated}$
2.0	8×10^5	0	22.4	$10.074 \pm 0.005 \pm 0.067$	< 0.85
2.05	8×10^5	0	21.3	$3.343 \pm 0.003 \pm 0.027$	< 0.27
2.1	8×10^5	0	20.3	$12.167 \pm 0.006 \pm 0.085$	< 0.93
2.12655	5×10^6	0	19.8	$108.49 \pm 0.02 \pm 0.94$	< 1.29
2.15	8×10^5	0	19.4	$2.841 \pm 0.003 \pm 0.024$	< 0.21
2.175	8×10^5	0	19.0	$10.625 \pm 0.006 \pm 0.091$	< 0.76
2.2	8×10^5	0	18.6	$13.699 \pm 0.007 \pm 0.092$	< 0.96
2.2324	1.8×10^6	0	18.0	$14.501 \pm 0.009 \pm 0.110$	< 0.44
2.3094	8×10^5	0	16.9	$21.089 \pm 0.009 \pm 0.143$	< 1.34
2.3864	8×10^5	0	15.8	$22.549 \pm 0.010 \pm 0.176$	< 1.34
2.396	1.37×10^6	0	15.7	$66.869 \pm 0.017 \pm 0.475$	< 2.30
2.5	8×10^5	0	14.4	$1.098 \pm 0.002 \pm 0.009$	< 0.06
2.6444	1.6×10^6	0	12.9	$33.722 \pm 0.013 \pm 0.216$	< 0.82
2.6464	1.6×10^6	0	12.9	$34.003 \pm 0.013 \pm 0.282$	< 0.82
2.7	8×10^5	0	12.4	$1.034 \pm 0.002 \pm 0.007$	< 0.05
2.8	6.8×10^6	0	11.6	$4.761 \pm 0.008 \pm 0.031$	< 0.02
2.9	2.93×10^6	0	10.8	$105.253 \pm 0.025 \pm 0.905$	< 1.16
2.95	1.8×10^6	0	10.4	$15.942 \pm 0.010 \pm 0.143$	< 0.28
2.981	1.8×10^6	0	10.2	$16.071 \pm 0.010 \pm 0.095$	< 0.27
3.0	1.8×10^6	0	10.0	$15.881 \pm 0.010 \pm 0.110$	< 0.26
3.02	1.8×10^6	0	9.8	$17.290 \pm 0.011 \pm 0.123$	< 0.28
3.08	8.96×10^6	0	8.9	$157.204 \pm 0.066 \pm 1.148$	< 0.47

related to the machine itself. Possible examples for such background are synchrotron radiation especially at high CM energies, Bremsstrahlung caused by beam-gas due to the imperfect vacuum in the beam pipe, elastic coulomb scattering of beam-electrons on beam-gas, and the Touschek effect, which describes the scattering of beam-electrons between particles of the same bunch. The first two effects produce photons as background particles, which makes them unlikely sources of background considering the event selection of this analysis, since they lack the required two charged tracks of opposite charge. The latter two could in principle imitate a signal event in the same way as radiative Bhabha scattering could. However, the analysis of the two available separated beam data sets at 2.2324 and 26444 GeV using the event selection for $e^+e^- \to p\bar{p}$ reveals no remaining events. Since there is no reason this should differ for machine or beam related background at other CM energies where no separated beam data samples are available, this background source is also considered to be negligible for the further analysis.

7.1.3 Summary of estimated total background contamination using the Monte Carlo method

In this subsection, an overview of the determined upper limits at 95% confidence level of the background pollution estimated from MC samples is given for the different background channels which have been discussed in detail in the previous sections. The summary can be seen in table 7.9, where also the total amount of estimated background events is given and compared to the extracted signal events of section 6.2. The total is simply the sum of the estimated upper limits for each channel according to equation 7.1 and, in case of the $p\bar{p}\pi_0$ background, the amount of estimated events according to equation 7.2.

TABLE 7.9: Summary of the background evaluation using the MC method for different background channels. Shown are the number of estimated remaining background events ($p\bar{p}\pi_0$ final state) or their upper limits at 95% confidence level (all other final states), as well as the maximum total background contamination $N_{tot}^{bkg,MC}$ as an absolute number and in relation to the amount of selected signal events in data N_{sel}^{data}

E_{cm} [GeV]	(Upper limits of) remaining events per background final state							$N_{tot}^{bkg,MC}$	$\frac{N_{tot}^{bkg,MC}}{N_{sel}^{data}}$ [%]
	$q\bar{q}$	$p\bar{p}\pi_0$	$p\bar{p}\pi^+\pi^-$	$K\bar{K}$	e^+e^-	$\gamma\gamma$	$\mu^+\mu^-$		
2	0.26	-	-	0.11	4.63	0.0026	0.85	5.9	0.1
2.05	0.14	-	-	0.03	8.78	0.0008	0.27	9.2	0.5
2.1	0.5	2.37	-	0.08	30.48	0.0029	0.93	34.4	0.6
2.12655	1.96	6.09	-	0.63	52.99	0.025	1.29	63.0	0.1
2.15	0.11	0.04	0.07	0.02	6.79	0.0006	0.21	7.2	0.6
2.175	0.48	0.17	0.25	0.06	24.82	0.0024	0.76	26.5	0.7
2.2	0.6	0.08	0.31	0.1	31.28	0.003	0.96	33.3	0.8
2.2324	0.5	0.09	0.32	0.11	9.19	0.0031	0.44	10.7	0.3
2.3094	0.81	0.03	0.42	0.12	7.32	0.0032	1.34	10.0	0.4
2.3864	0.59	-	0.42	0.07	3.24	0.0032	1.34	5.7	0.3
2.396	1.32	-	1.23	0.21	1.33	0.0031	2.3	6.4	0.1
2.5	0.02	-	0.02	0.01	0.55	0.0002	0.06	0.7	1.2
2.6444	0.4	-	0.5	0.06	5.09	0.0032	0.82	6.9	0.8
2.6464	0.4	-	0.5	0.06	0.56	0.0032	0.82	2.3	0.3
2.7	0.03	-	0.01	0.01	0.45	0.0001	0.05	0.6	2.8
2.8	0.11	-	0.06	0.01	1.12	0.0006	0.02	1.3	2.5
2.9	1.99	-	1.29	0.1	2.68	0.003	1.16	7.2	0.7
2.95	0.48	-	0.19	0.01	0.4	0.0019	0.28	1.4	1.2
2.981	0.49	-	0.19	0.01	0.39	0.0019	0.27	1.4	1.0
3	0.48	-	0.18	0.01	0.38	0.0019	0.26	1.3	1.4
3.02	0.53	-	0.19	0.01	0.41	0.002	0.28	1.4	1.5
3.08	2.54	-	1.7	0.1	3.22	0.0041	0.47	8.0	0.9

The upper limit total background contamination from the MC method is well below 1% for most CM energies and therefore negligible. The CM energies with a higher relative background pollution are the ones of the low luminosity data samples at (2.5, 2.7, 2.8, 2.95-3.02) GeV, which have a very low signal yield. In addition, the generated MC background samples are small here compared to other energy points, which increases

the estimated upper limits of background pollution estimated with equation 7.1. The most relevant background final state throughout most CM energies is e^+e^-. However, as already discussed, the high upper limits for this channel are mostly caused by the limited size of the MC samples.

7.2 Detailed event selection of the signal channel compared to exemplary background channels

Before the second method for the background evaluation will be introduced, this section will discuss the effect of the different event selection criteria on the number of events for the signal channel $e^+e^- \to p\bar{p}$ and the generated MC samples of various chosen background channels, which is shown in table 7.10 for 2.396 GeV as an example.

TABLE 7.10: Effect of the individual selection criteria at 2.396 GeV on data, a signal MC sample including NLO radiative corrections, $e^+e^- \to e^+e^-$ MC, Bhabha scattering ($e^+e^- \to q\bar{q}$) MC and $e^+e^- \to \gamma\gamma$ MC. The $q\bar{q}$ MC sample includes the signal process.

Selection criterium	Data	Signal MC	e^+e^-	$q\bar{q}$	$\gamma\gamma$
No selection	-	1×10^6	15.67×10^7	2.85×10^6	4×10^6
2 charged tracks	70188842	839567	120953104	984002	95518
total charge 0	68998528	834601	120848505	921625	95088
Momentum window	19731	528392	19224	12325	3
$\chi^2_{VertexFit}$ <100	19573	528242	18962	12300	3
$\sphericalangle_{p,\bar{p}}$ <178°	8938	513563	3333	10328	0
$\Delta ToF < 4$ ns	7205	512826	3329	10313	0
PID	5517	512308	0	10294	0
E/p <0.5	5512	512105	0	10287	0

For the Bhabha scattering background, one can see that most events are already rejected by the requirements on the momentum of the two particles, since the rest mass of the electron is much lower compared to the proton and the electrons therefore have a higher momentum. The emission of an ISR photon however can reduce the momentum of the e^+e^- pair to fit the requirement. At the shown energy, the PID system is sufficient to reduce the background events of this channel to 0, the reduced discrimination power of

the PID system at higher energies however requires the E/p cut (see section 6.1.2). The inclusive $q\bar{q}$ MC sample includes the signal channel and all of the final remaining events have been checked to be signal events. A large portion of the background channels contained in this MC sample already get suppressed by the requirement on the amount of charged tracks, since they contain more charged particles in the final state. The remaining two-body background events are mostly removed by the momentum window requirement, since the particles have different masses compared to the proton.

From the $\gamma\gamma$ MC sample, only a few percent of events fulfil the requirement to have two charged tracks of opposite charge. In most of these events, one of the photon undergoes pair production to produce a pair of charged leptons, mostly electrons. Since the energy distribution of these electrons (and therefore roughly their momentum distribution due to negligible rest mass) peaks at half the energy of the photon or a quarter of the CM energy, their momentum is too low to pass the momentum window requirement. Any statistical outliers can easily be removed by the PID system.

For the signal MC, the largest loss of efficiency already comes from the requirement to have 2 good charged tracks of opposite charge. Signal events can get removed by this requirement due to one or both of the final state particles being emitted outside the detector acceptance (93% of 4π for the MDC) or due to their charged tracks in the MDC not fulfilling the quality requirements for good charged tracks. While the momentum window requirement seems to remove a lot of signal events, most of them are ISR events. When analysing a sample with the Born process only, less than 3% of events are removed by this requirement. All other requirements only result in a minor loss of signal efficiency.

7.3 Background evaluation using the sideband method

The background evaluation using MC samples in section 7.1 revealed no major sources of background, the sum of the upper limits at 95% confidence level of the amount of remaining events for all background channels is below 1% of the selected signal events in data for all high luminosity data points (see section 7.1.3). However, this analysis alone may not be fully reliable, for example due to differences in the behaviour of selection criteria between MC samples and real data, or simply because not all possible background channels have been considered. Therefore, a second method is used as a cross-check to determine the background pollution in data.

The method uses the two-dimensional distribution of momentum of the positive versus momentum of the negative selected track. Three different kinds of background are

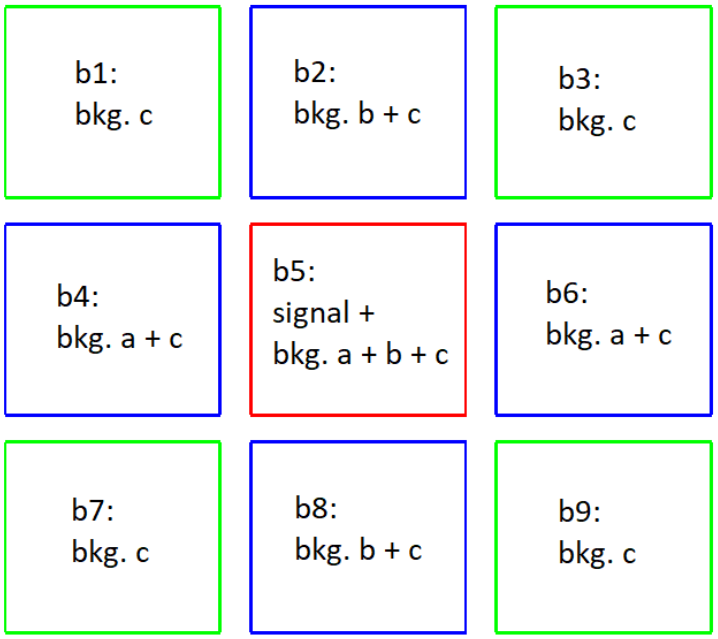

FIGURE 7.1: Illustration of the sideband method. The signal region is the red square, the sideband regions of background (bkg.) types a and b (see text) are the blue squares, and the sideband regions to determine the background type c are the green squares.

assumed: one uniformly distributed along the X direction (positive track) from the signal region (background a), one uniformly distributed along the Y direction (negative track) from the signal region (background b), and one uniformly distributed over the whole area independent of the axis X and Y (background c). By defining sideband regions next to the signal region using the width of the momentum distribution σ_p determined in section 6.1.2, one can estimate the total sum of background events from the background types a + b + c. In X and Y direction, the sideband areas are 1 σ_p away from the signal area and have the same size as the signal region. In addition, sideband regions in the "corners" are defined to determine background type c, which are again 1 sigma away from those for background types a and b and are also of the same size as the signal region. An illustration of the definition of the sidebands can be seen in figure 7.1.

An estimation of the total background can now be done by summing up the number of events in the boxes b1-b9 in the following way:

$$N_{tot}^{bkg} = 0.5 \times ((b_2 + b_8) + (b_4 + b_6) - 0.5 \times (b_1 + b_3 + b_7 + b_9)), \tag{7.3}$$

where N_{tot}^{bkg} is the total number of estimated background events and b_i is the number of events in box i, i=(1, 2, 3...9).

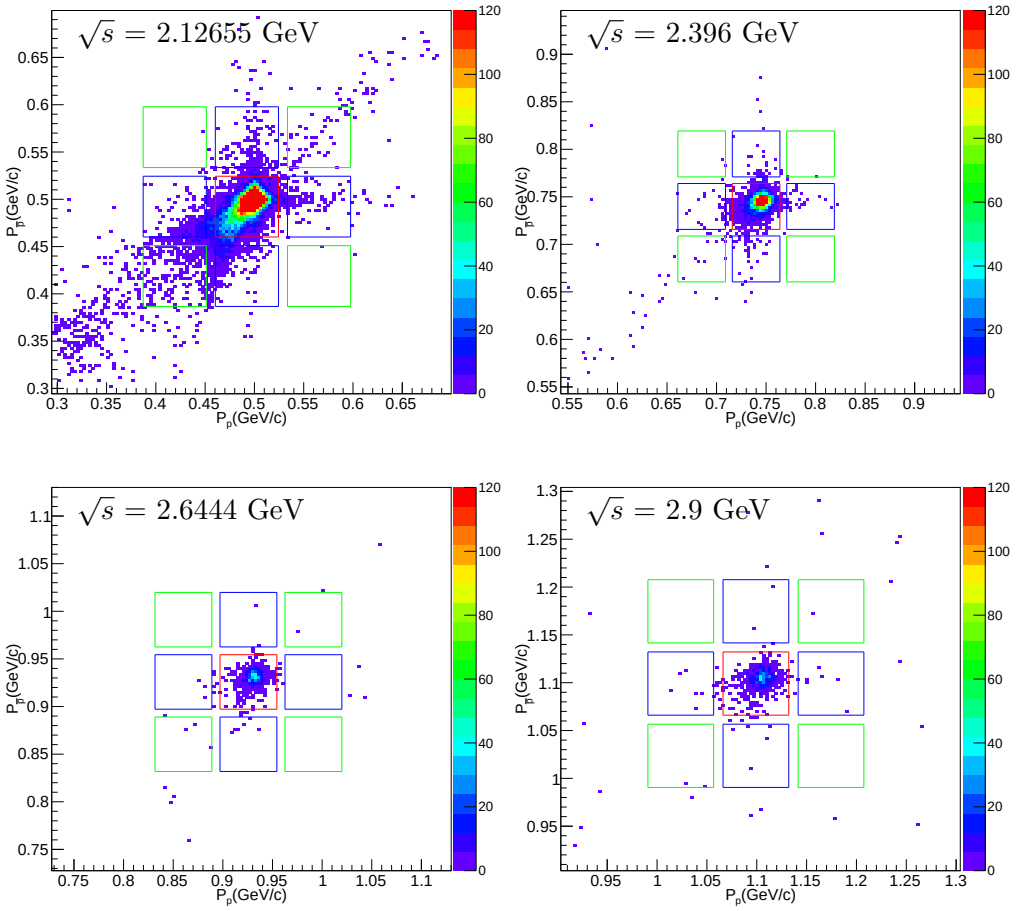

FIGURE 7.2: Two-dimensional histograms of the momentum of the proton versus the momentum of the antiproton for data samples at center of mass energies of 2.125 GeV, 2.396 GeV, 2.6444 GeV and 2.9 GeV. The different sideband regions (definition see text) are shown for background type a and b (blue squares) and background type c (green squares) along with the signal region (red square).

The two-dimensional distributions of momentum along with the defined sideband areas can be seen in figure 7.2 for data at selected CM energies of 2.12655 GeV, 2.396 GeV, 2.6444 GeV and 2.9 GeV, plots for all other CM energies can be found in appendix A in figure A.9. Especially for energy points with high luminosity, such as the one at 2.12655 GeV, one can see a large amount of events within the sideband areas, mostly along the X and Y axis and diagonally below the signal area towards lower momenta of both tracks. However, it can be expected that a part or even most of these events are not background events. The events along the X and Y axis can also be caused by outliers in the momentum measurement of signal events. Since the signal area is defined as 3 (4) σ_p for momenta above (below) the theoretical mean momentum, such outliers are unlikely, but possible with a sufficiently high amount of selected events, especially when considering not only statistical errors in the momentum measurement but also systematic ones. However, it is very unlikely that the momentum measurement of both

tracks of one event are far off the mean, which explains the distribution along the X and Y axis of these events. A possible explanation for the events diagonally below the signal area are ISR events, where the ISR photon takes a part of the available CM energy before the annihilation and therefore reduces the momentum of the formed proton and antiproton simultaneously.

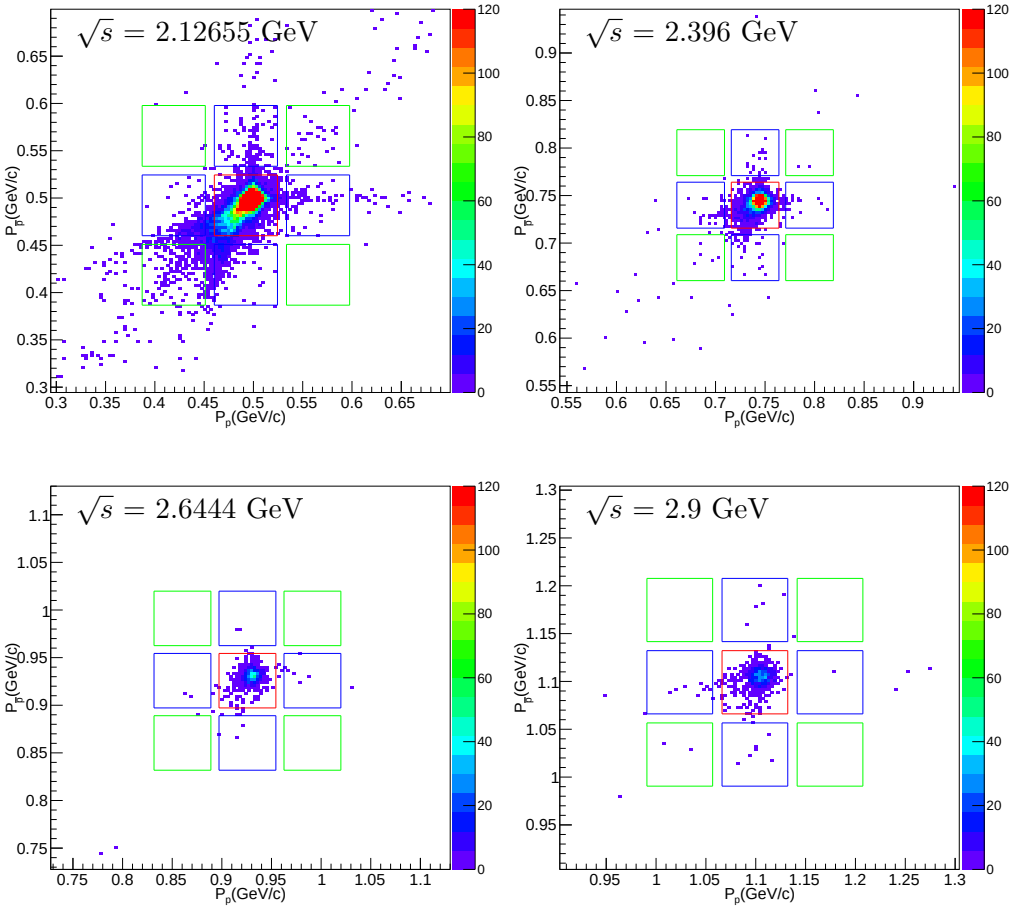

FIGURE 7.3: Two-dimensional histograms of the momentum of the proton versus the momentum of the antiproton of signal MC samples including ISR up to NNLO for center of mass energies of 2.125 GeV, 2.396 GeV, 2.6444 GeV and 2.9 GeV. The different sideband regions (definition see text) are shown for background type a and b (blue squares) and background type c (green squares) along with the signal region (red square). To compare to data, the same amount of events has been plotted as remain in data after the event selection.

To estimate how many of the background events found with this method are actually not background events, but outlier signal events or signal events with ISR photons, the method is also applied to a signal MC sample including ISR up to NNLO. To get a similar situation to the one in data, the remaining events after event selection of the MC sample are cut to the same number of events remaining in the data samples at each

CM energy. The results can be seen in figure 7.3 for the same CM energies as in figure 7.2 and in figure A.10 of Appendix A for all other CM energies.

TABLE 7.11: Background evaluation using the sideband method. Shown are the amount of background events extracted with equation 7.3 for data ($N_{tot}^{bkg,data}$), signal MC including ISR up to NNLO ($N_{tot}^{bkg,MC}$), the difference between the two, and the background pollution in data relative to the amount of selected events at all energy points.

E_{cm} [GeV]	$N_{tot}^{bkg,data}$	$N_{tot}^{bkg,MC}$	$N_{tot}^{bkg,data}$ - $N_{tot}^{bkg,MC}$	$\frac{N_{tot}^{bkg,data}}{N_{sel}^{data}}$ [%]
2	32.8 ± 5.9	15.3 ± 5.6	17.6 ± 8.2	0.6
2.05	4 ± 3.7	2.5 ± 3.1	1.5 ± 4.9	0.2
2.1	49.3 ± 5.6	36.8 ± 5	12.5 ± 7.5	0.8
2.12655	423 ± 16	394 ± 16	29 ± 22	0.8
2.15	9 ± 2.6	14.3 ± 2.8	-5.3 ± 3.8	0.8
2.175	30 ± 4.3	37.8 ± 4.7	-7.8 ± 6.3	0.8
2.2	46 ± 5.3	52.5 ± 5.4	-6.5 ± 7.6	1.1
2.2324	55.3 ± 5.5	43.5 ± 5	11.8 ± 7.4	1.5
2.3094	45.8 ± 5.1	42 ± 4.9	3.8 ± 7.1	2.0
2.3864	17 ± 3.2	13 ± 2.7	4 ± 4.2	0.9
2.396	53.5 ± 5.4	51 ± 5.2	2.5 ± 7.5	1.0
2.5	0.5 ± 0.5	0	0.5 ± 0.5	0.9
2.6444	4 ± 1.7	6 ± 1.7	-2 ± 2.4	0.5
2.6464	6.3 ± 1.8	2.8 ± 1.3	3.5 ± 2.2	0.7
2.7	0	0	0	0
2.8	2.3 ± 1.1	0	2.3 ± 1.1	4.2
2.9	10.3 ± 2.4	10.5 ± 2.4	-0.3 ± 3.4	1.0
2.95	0.25 ± 0.55	0.25 ± 0.55	0 ± 0.8	0.2
2.981	1.5 ± 0.86	0.25 ± 0.55	1.3 ± 1	1.1
3	0.5 ± 0.35	0.25 ± 0.55	0.25 ± 0.65	0.5
3.02	0 ± 0.61	0.25 ± 0.25	-0.25 ± 0.66	0.0
3.08	14.8 ± 2.8	4.3 ± 1.5	10.5 ± 3.2	1.7

Table 7.11 shows the resultant remaining background events estimated according to formula 7.3 for both data and signal MC samples with ISR up to NNLO at all energy points. At most CM energies, the signal MC samples show a similar amount of extracted background events as the data samples, indicating that the largest part of these events are not actual background events from physical background channels, but rather come from the effects described above. Even with these "fake" background events, the relative pollution in data samples, also shown in table 7.3, is below 2% for all energy points except 2.8 GeV, which is a data point with very low luminosity and therefore few remaining events after event selection. If the relative pollution is instead calculated using the difference of extracted background events in data and signal MC, the pollution drops to a level of less than 1% for all data points except 3.08 GeV, where it is 1.2%, possibly due to a higher contamination of Bhabha scattering events at high energies.

To summarise the results of this chapter, the level of background found by both the investigation with MC samples as well as the sideband method is on a level of a few percent at worst. Therefore, no background subtraction or similar methods to further reduce the background are deemed necessary, and the remaining background will be treated as negligible in the further analysis. Instead, any remaining background will be considered as a source of systematic uncertainty in chapter 10, discussed in detail in sections 10.1.5 and 10.3.3 for the cross section and the FF measurement, respectively.

Chapter 8

Determination of the Cross Section of the Signal Process $e^+e^- \to p\bar{p}$

The results of the previous chapters, the amount of extracted $e^+e^- \to p\bar{p}$ events and the negligible background pollution which makes a background subtraction unnecessary, allow for the extraction of the cross section of the signal process. To achieve this, the selected events need to first be corrected for detection and selection efficiency as well as for radiative corrections. These procedures are described in secion 8.1 and 8.2, after which a first round of results is presented in section 8.3. The extraction of the final results for the cross section requires an iterative tuning of the signal MC samples, described in section 9.4, which uses the proton EM FFs extracted in chapter 9 as input. The presentation of the final cross section results is therefore postponed until chapter 11.

8.1 Efficiency correction for the cross section measurement

The selection criteria necessary to eliminate background events and ensure data quality (see chapter 6) unavoidably also remove events of the the signal channel $e^+e^- \to p\bar{p}$. In addition, the BESIII detector covers only about 93% of the full solid angle, meaning that events where the final state proton and antiproton are emitted in a direction close to the beampipe are outside the detector acceptance and are therefore also lost. To estimate the actual amount of events from the signal channel contained in the data samples and correct for these effects, MC simulated samples of the signal channel (1 million events per CM energy point) are put through the GEANT4 detector simulation, which considers

the detector acceptance, and subsequently subjected to the same selection criteria as the samples of the scan data set. By comparing the amount of events generated (N_{gen}^{MC}) to those remaining after this procedure (N_{sel}^{MC}), one can extract the combined selection and detection efficiency ϵ_{MC} by

$$\epsilon_{MC} = \frac{N_{sel}^{MC}}{N_{gen}^{MC}}. \tag{8.1}$$

Together with the amount of selected data events taken from table 6.2 (N_{sel}), the integrated luminsity of each data sample taken from table 4.3 ($\mathcal{L}_{int}$), and the correction factor (1+δ) which will be discussed in section 8.2, the cross section of the process can be determined by:

$$\sigma_{p\bar{p}(s)} = \frac{4\pi\alpha^2\beta C}{3s}\left[|G_M(s)|^2 + \frac{2m_p^2}{s}|G_E(s)|^2\right] = \frac{N_{sel}}{\mathcal{L}_{int}\cdot\epsilon_{MC}\cdot(1+\delta)}, \tag{8.2}$$

where s is the squared center of mass energy, α is the fine-structure constant, C is the coulomb correction factor, G_E and G_M are the electric and magnetic FFs of the proton, and β is the velocity v of the proton and antiproton over the speed of light c.

With the large luminosity of the scan data set of 2015 this work is based on, the electric and magnetic FF can be extracted separately by doing an angular analysis, which will be covered in chapter 9. Previous experiments however did not have enough remaining events after event selection in their data sets to perform this angular analysis, and had to use an assumption to extract a FF quantitiy from their data. This quantity, the so called effective FF, can be derived from equation 8.2 by assuming the two form factors to be equal ($|G_E| = |G_M| = |G|$):

$$\sigma_{p\bar{p}(s)} = \frac{4\pi\alpha^2\beta C}{3s}\left(1 + \frac{2m_p^2}{s}\right)|G(s)|^2, \tag{8.3}$$

with the same variables as in equation 8.2. Solved for $|G(s)|$, this gives:

$$|G(s)| = \sqrt{\frac{\sigma_{p\bar{p}(s)}}{\frac{4\pi\alpha^2\beta C}{3s}\left(1 + \frac{2m_p^2}{s}\right)}} \tag{8.4}$$

Although this assumption is not necessary for the data set used in this work and also not correct over the whole energy range of the set (see final results in chapter 11), the effective FF is also extracted here to be able to compare to these older experiments.

8.2 Radiative corrections for the cross section measurement

The aim of the analysis described in this chapter is to extract the Born cross section of the process $e^+e^- \to p\bar{p}$. However, the data samples collected in 2015 at BESIII contain not only the Born process, but also processes of higher orders of α, such as $e^+e^- \to p\bar{p}n\gamma$, with n photons coming from either initial or final state radiation, or the signal process with vacuum polarisation. A part of these events is sorted out by the event selection, for example through the change in kinematics by the emission of an initial or final state photon compared to the two body final state process $e^+e^- \to p\bar{p}$, which causes the event to no longer fulfil the back-to-back angle or momentum window requirements (see section 6.1.2). However, events with low energetic photons which are not detected by the detector as well as events with vacuum polarisation (and other processes of higher order in α, e.g. box diagrams) can not be fully removed by any kind of selection criteria. Instead, they are corrected for with the radiative correction factor $(1+\delta)$, which is determined using MC event generators. Since these kinds of corrections become very small for high orders of α, the expected precision of the results of this work only requires NLO corrections. In the case of ISR, the NNLO was also included since it is available in the Phokhara event generator. NNLO precision for FSR radiation is not necessary for this work, since FSR is additionally suppressed by the high mass of the final state proton and antiproton.

To determine the correction factor $(1+\delta)$, the Phokhara generator is used to generate two different sets of MC samples. Each set consists of samples with 1 million events at each CM energy. The samples of the first set contain only the pure Born process of $e^+e^- \to p\bar{p}$, while the samples of the second set contain ISR up to NNLO, FSR up to NLO and vacuum polarisation corrections. Both the Born cross section σ^{MC}_{Born} as well as the cross section including radiative corrections, σ^{MC}_{rad}, are calculated by the event generator at each CM energy. With these two cross sections, the radiative correction factor can be determined by:

$$(1+\delta) = \frac{\sigma^{MC}_{rad}}{\sigma^{MC}_{Born}} \tag{8.5}$$

As explained in this and the previous section, both the signal efficiency and the radiative correction factor are estimated using MC simulation. The simulation of the signal process $e^+e^- \to p\bar{p}$ depends on the proton FF model used by the generator, for example for the angular distribution of events in the sample or the cross sections calculated by the generator which are used in equation 8.5. For a first round of results, the built in default

model of the Phokhara event generator is used, and the results for the cross section and effective FF using this model will be shown in the following section. However, to extract the final results of this work, an iterative MC tuning will be performed using the FFs obtained with the 2015 data set. This procedure is explained after the extraction of the FFs in chapter 9, and the final results using the FF model obtained from this tuning will be given in chapter 11.

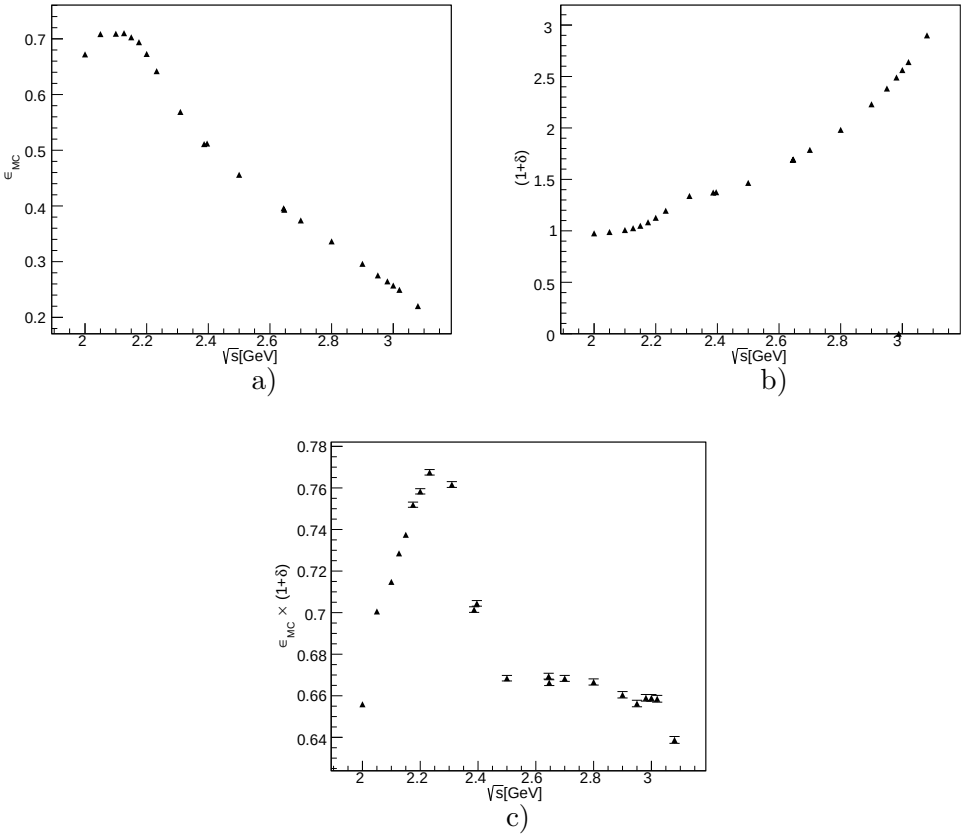

FIGURE 8.1: a) The total efficiency ϵ_{MC}, consisting of the selection efficiency and the detector efficiency, for all CM energy points of the 2015 scan data set. b) Radiative correction factor $(1+\delta)$ for ISR up to NNLO, FSR up to NLO and vacuum polarisation for all CM energy points of the 2015 scan data set. c) Product of the efficiency ϵ_{MC} and the radiative correction factor $(1+\delta)$ for all CM energy points of the 2015 scan data set.

The initial values for the efficiency, the radiative correction factor and their product obtained from the default model of Phokhara can be seen in figure 8.1. Due to the increasing amount of ISR events with rising energy, which are mostly filtered out by the event selection, the efficiency decreases for higher CM energies. Accordingly, the radiative correction factor also increases with rising energy, whereas the product of both remains mostly stable throughout the full energy range of the scan.

8.3 First results for the cross section of the signal process $e^+e^- \to p\bar{p}$ and the proton effective FF

Using the selection and detector efficiency as well as the radiative correction factor $(1+\delta)$ determined in sections 8.1 and 8.2, equation 8.2 can be used to determine the Born cross section $\sigma_{p\bar{p}}$ of $e^+e^- \to p\bar{p}$ for all energy points of the 2015 data set. The extracted cross section in turn can be used to calculate the effective FF $|G|$ according to equation 8.4. A first set of results for these two quantities using the MC with the default FF model of Phokhara can be seen in table 8.1, while the final results using the FF model from MC tuning can be found in section 11.1.

TABLE 8.1: Results for the Born cross section $\sigma_{p\bar{p}}$ of $e^+e^- \to p\bar{p}$ and the effective FF $|G|$ using the MC determined efficiency ϵ_{MC} and the radiative correction factor $(1+\delta)$ for MC samples generated with the built in default model of Phokhara for all CM energies of the 2015 scan data set.

E_{cm} [GeV]	N_{sel}	ϵ_{MC}	$(1+\delta)$	$\mathcal{L}_{int}$ $[pb^{-1}]$	$\sigma_{p\bar{p}}$ $[pb]$	$\lvert G\rvert$ $[10^{-2}]$
2	5296 ± 73	0.6721 ± 0.0005	0.9759 ± 0.0006	10.074	801 ± 11	27.22 ± 0.19
2.05	1693 ± 41	0.7086 ± 0.0005	0.9887 ± 0.0006	3.343	723 ± 18	24.75 ± 0.3
2.1	5988 ± 77	0.7092 ± 0.0005	1.0079 ± 0.0006	12.167	688.5 ± 8.9	23.6 ± 0.15
2.12655	50160 ± 224	0.7102 ± 0.0005	1.0258 ± 0.0006	108.49	634.6 ± 2.8	22.488 ± 0.05
2.15	1186 ± 34	0.7028 ± 0.0005	1.0493 ± 0.0006	2.841	566 ± 16	21.15 ± 0.31
2.175	3761 ± 61	0.694 ± 0.0005	1.0835 ± 0.0006	10.625	470.8 ± 7.7	19.23 ± 0.16
2.2	4089 ± 64	0.6729 ± 0.0005	1.127 ± 0.0007	13.699	393.6 ± 6.2	17.56 ± 0.14
2.2324	3643 ± 60	0.642 ± 0.0005	1.1955 ± 0.0008	14.501	327.3 ± 5.4	16.01 ± 0.13
2.3094	2322 ± 48	0.5688 ± 0.0005	1.339 ± 0.001	21.089	144.6 ± 3	10.7 ± 0.11
2.3864	1849 ± 43	0.5111 ± 0.0005	1.3725 ± 0.0012	22.549	116.9 ± 2.7	9.74 ± 0.11
2.396	5512 ± 74	0.5121 ± 0.0005	1.3756 ± 0.0012	66.869	117 ± 1.6	9.758 ± 0.066
2.5	54 ± 7	0.456 ± 0.0005	1.466 ± 0.0013	1.098	74 ± 10	7.91 ± 0.54
2.6444	868 ± 29	0.3958 ± 0.0005	1.6912 ± 0.0016	33.722	38.5 ± 1.3	5.93 ± 0.1
2.6464	838 ± 29	0.3932 ± 0.0005	1.6946 ± 0.0016	34.003	37 ± 1.3	5.81 ± 0.1
2.7	20 ± 4	0.374 ± 0.0005	1.7869 ± 0.0017	1.034	28.9 ± 6.5	5.22 ± 0.58
2.8	53 ± 7	0.3364 ± 0.0006	1.9815 ± 0.002	4.761	16.7 ± 2.3	4.07 ± 0.28
2.9	1010 ± 32	0.2962 ± 0.0006	2.2301 ± 0.0023	105.253	14.53 ± 0.46	3.907 ± 0.061
2.95	118 ± 11	0.2754 ± 0.0004	2.3831 ± 0.0025	15.942	11.3 ± 1	3.49 ± 0.16
2.981	132 ± 11	0.2646 ± 0.0004	2.4902 ± 0.0026	16.071	12.5 ± 1.1	3.7 ± 0.16
3	92 ± 10	0.2572 ± 0.0004	2.5626 ± 0.0027	15.881	8.79 ± 0.92	3.13 ± 0.16
3.02	97 ± 10	0.2494 ± 0.0004	2.6405 ± 0.0028	17.29	8.52 ± 0.86	3.09 ± 0.16
3.08	854 ± 29	0.2203 ± 0.0004	2.8998 ± 0.0031	157.204	8.5 ± 0.29	3.144 ± 0.054

Chapter 9

Extraction of the Electric and Magnetic Form Factor of the Proton

While the previous chapter already described an extraction of the cross section of the process $e^+e^- \to p\bar{p}$ and of the corresponding quantity of the effective FF (the FF of the proton under the assumption of an equal electric $|G_E|$ and magnetic $|G_M|$ FF), the large luminosity of the newly taken data set of 2015 allows for a much more sophisticated extraction of the TL EM FFs of the proton. By analysing the angular distribution of the remaining events after the event selection described in chapter 6, a separate determination of the individual $|G_M|$ and $|G_E|$, or equivalently $|G_M|$ and the ratio of the electric and magnetic FF, $R = |\frac{G_E}{G_M}|$, is possible. This chapter first discusses the efficiency and radiative corrections to the extracted angular distributions of the proton and antiproton of the signal process from data, before describing two independent methods for the extraction of the EM FFs of the proton, the fit method and the method of moments. A first round of results extracted with signal MC samples generated using the default FF model of Phokhara is presented in section 9.3. These results are then used in an iterative MC tuning procedure, described in section 9.4, to extract the final results for the cross section of $e^+e^- \to p\bar{p}$, the effective FF $|G|$, the electric FF $|G_E|$, and the magnetic FF $|G_M|$ presented in chapter 11.

9.1 Angular analysis of the signal process $e^+e^- \to p\bar{p}$

The formula for the total cross section of $e^+e^- \to p\bar{p}$ in section 8.1 (equation 8.2) already contains the electromagnetic FFs of the proton $|G_E|$ and $|G_M|$, but the integral form of

the formula does not allow for a separate extraction of the two. For the extraction of the individual FFs, the differential cross section has to be used, which is given by:

$$\frac{d\sigma_{p\bar{p}(s)}}{d\cos\theta_p^{CM}} = \frac{\pi\alpha^2\beta C}{2s}\left[|G_M(s)|^2(1+\cos^2\theta_p^{CM}) + \frac{1}{\tau}|G_E(s)|^2(\sin^2\theta_p^{CM})\right], \tag{9.1}$$

where s is the squared center of mass energy, α is the fine-structure constant, C is the coulomb correction factor, $|G_E|$ and $|G_M|$ are the absolute values of the electric and magnetic FFs of the proton, and β is the velocity v of the proton and antiproton over the speed of light c. τ is defined as $\frac{s}{4m_p^2}$ with the mass of the proton m_p, and $\cos\theta_p^{CM}$ is the angle between the proton or antiproton momentum in the CM frame of the e^+e^- system and the z-axis of the BESIII detector, which points along the direction of the positron beam.

9.1.1 Efficiency correction

Similar to the extraction of the cross section described in chapter 8, the angular distributions of the proton and antiproton first have to be corrected for detector and selection efficiency as well as for radiative corrections. The emission of radiative photons, e.g. from ISR, is not uniformly distributed over $\cos\theta_p^{CM}$. Events containing ISR photons have on average higher values of $\cos\theta_p^{CM}$ for the proton and antiproton, which leads to lower efficiencies at high values of $\cos\theta_p^{CM}$, since most ISR events are removed by the selection criteria. This effect is especially prominent at high CM energies, where a lot of ISR events are produced. In addition, effects like a lowered detector efficiency at the edges of the different subdetectors (MDC, TOF) may also lead to a dependency of the efficiency on $\cos\theta_p^{CM}$. Therefore, the angular distributions of proton and antiproton must be corrected bin-by-bin with an efficiency curve depending on $\cos\theta_p^{CM}$. Analogous to the determination of the efficiency for the cross section extraction, MC samples of the signal process containing 1 million events for each CM energy are subjected to the GEANT4 detector simulation and the event selection criteria. The full range of $\cos\theta_p^{CM} \in [-1, 1]$ is divided into 20 bins, and the amount of events remaining after the detector simulation and event selection is compared to the total amount of generated events for each bin:

$$\frac{d\epsilon_{MC}}{d\cos\theta_p^{CM}} = \frac{N_{i,sel}^{MC}}{N_{i,gen}^{MC}}, \tag{9.2}$$

where $N_{i,sel}^{MC}$ is the amount of remaining events in bin i and $N_{i,gen}^{MC}$ is the amount of generated events in bin i with i=(1, 2, ... 20).

The distributions of the total efficiency in $\cos\theta_p^{CM}$ can be seen in figure 9.1 for exemplary CM energies. The large drop in efficiency in the outermost bins of $\cos\theta_p^{CM}$ is due to the detector acceptance. The MDC acceptance of $\cos\theta_p^{CM} \in [-0.93, 0.93]$ leads to a very low efficiency for the outermost bin, while the efficiency of the second bin from the left and right is reduced by the gap between barrel and endcap region of the EMC (E/p requirement) and the TOF detector (TOF difference requirement, see section 6.1). Distributions for all CM energies can be found in appendix A in figure A.11.

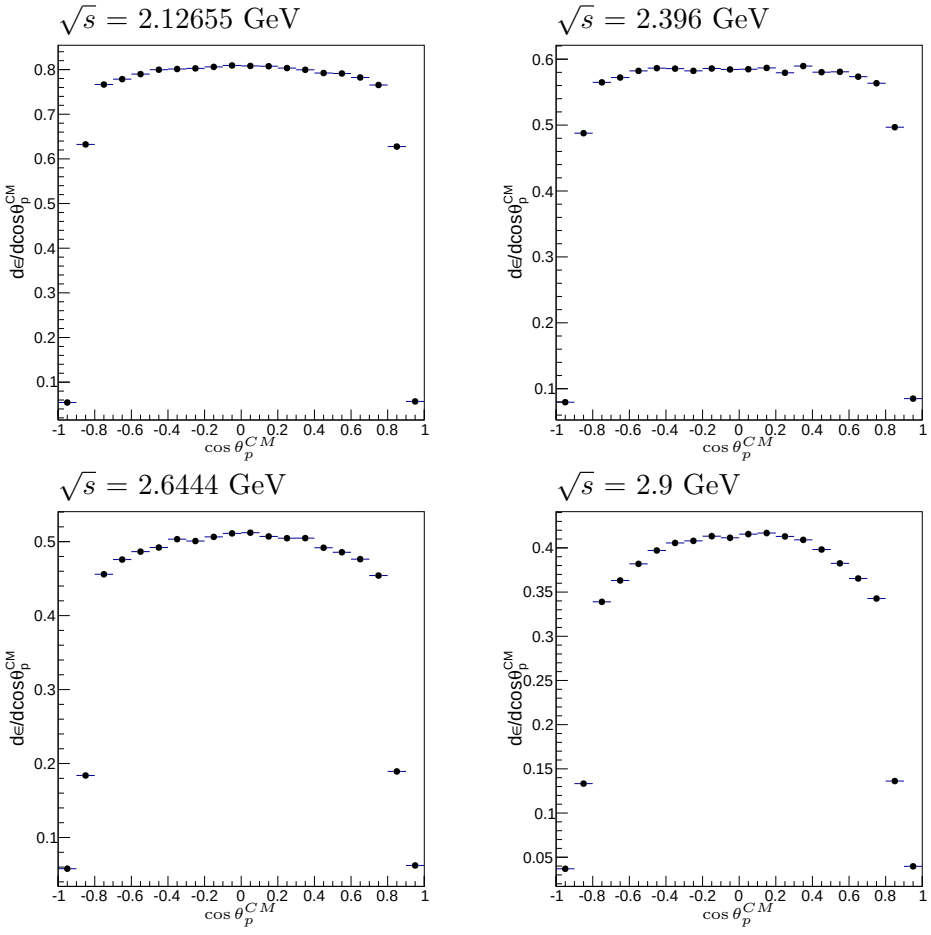

FIGURE 9.1: Distributions of detector and selection efficiency in $\cos\theta_p^{CM}$ for exemplary CM energies of 2.12655 GeV, 2.396 GeV, 2.6444 GeV and 2.9 GeV.

9.1.2 Radiative correction

The excess of ISR events at high values of $\cos\theta_p^{CM}$ of the proton and antiproton also leads to a dependency of the radiative correction factor $(1+\delta)$ on $\cos\theta_p^{CM}$. Similar to the efficiency correction, the angular distributions of proton and antiproton have to be corrected bin-by-bin using radiative correction curves depending on $\cos\theta_p^{CM}$. Analogous to the radiative correction for the extraction of the cross section (see section 8.2),

these curves are estimated using MC samples of the signal process generated with the Phokhara event generator. Two sets of MC samples with 1 million events per sample are generated at each energy point: the samples of the first set contain all radiative corrections (ISR up to NNLO, FSR up to NLO and vacuum polarisation), while the samples of the second set contain only the Born process of $e^+e^- \to p\bar{p}$. The $\cos\theta_p^{CM}$ distributions of proton and antiproton of each sample are then scaled by either the Born cross section of the signal process or the cross section containing all radiative corrections, which are both taken from the calculation of the Phokhara event generator. After that, the differential radiative correction curve can be determined by dividing the amount of events in the sample including radiative corrections ($N^{MC}_{gen,rad}$) by the amount of events in the Born sample ($N^{MC}_{gen,Born}$) for each bin of $\cos\theta_p^{CM}$:

$$\frac{d(1+\delta)}{d\cos\theta_p^{CM}} = \frac{N^{MC}_{gen,rad}}{N^{MC}_{gen,Born}} \tag{9.3}$$

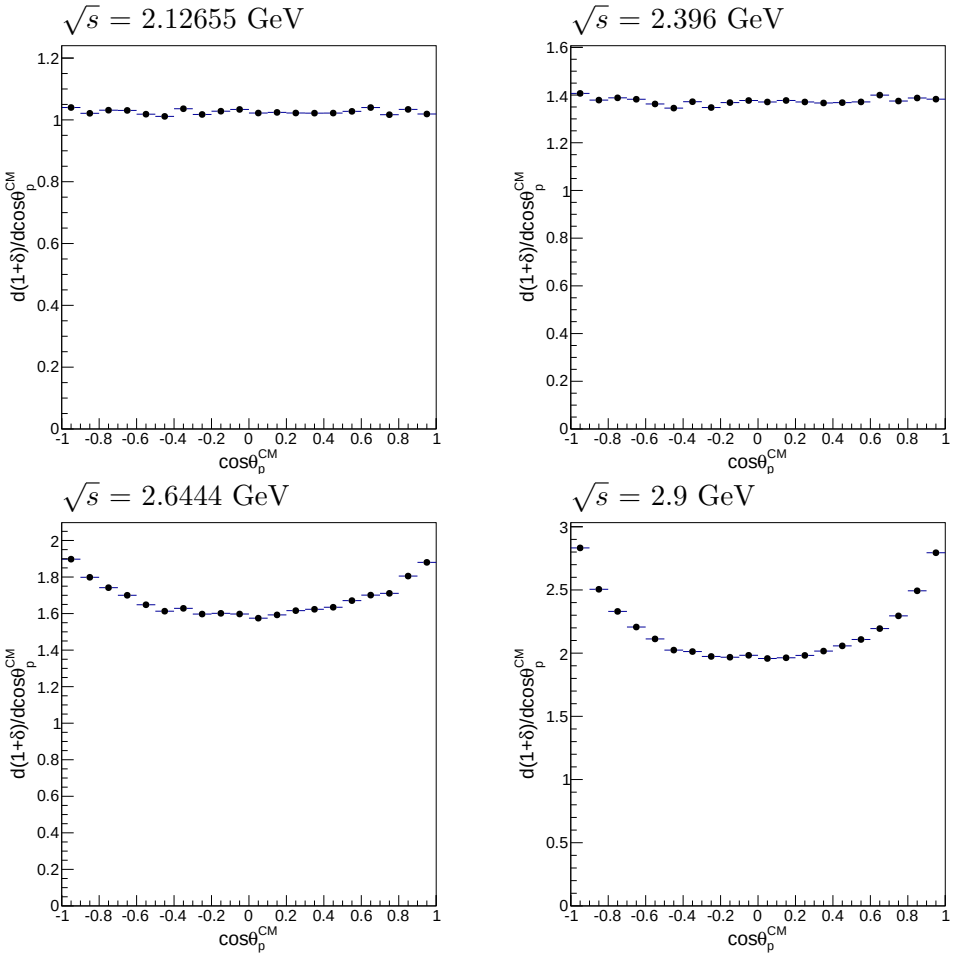

FIGURE 9.2: Distributions of the radiative correction factor $(1+\delta)$ in $\cos\theta_p^{CM}$ for exemplary CM energies of 2.12655 GeV, 2.396 GeV, 2.6444 GeV and 2.9 GeV. The radiative correction includes ISR up to NNlO, FSR up to NLO and vacuum polarisation.

The distributions of the radiative correction factor in $\cos\theta_p^{CM}$ can be seen in figure 9.2 for exemplary CM energies, those for all CM energies can be found in appendix A in figure A.12. The increase in radiative events with rising energy and especially at high values of $|\cos\theta_p^{CM}|$ at higher energies can be seen in these distributions.

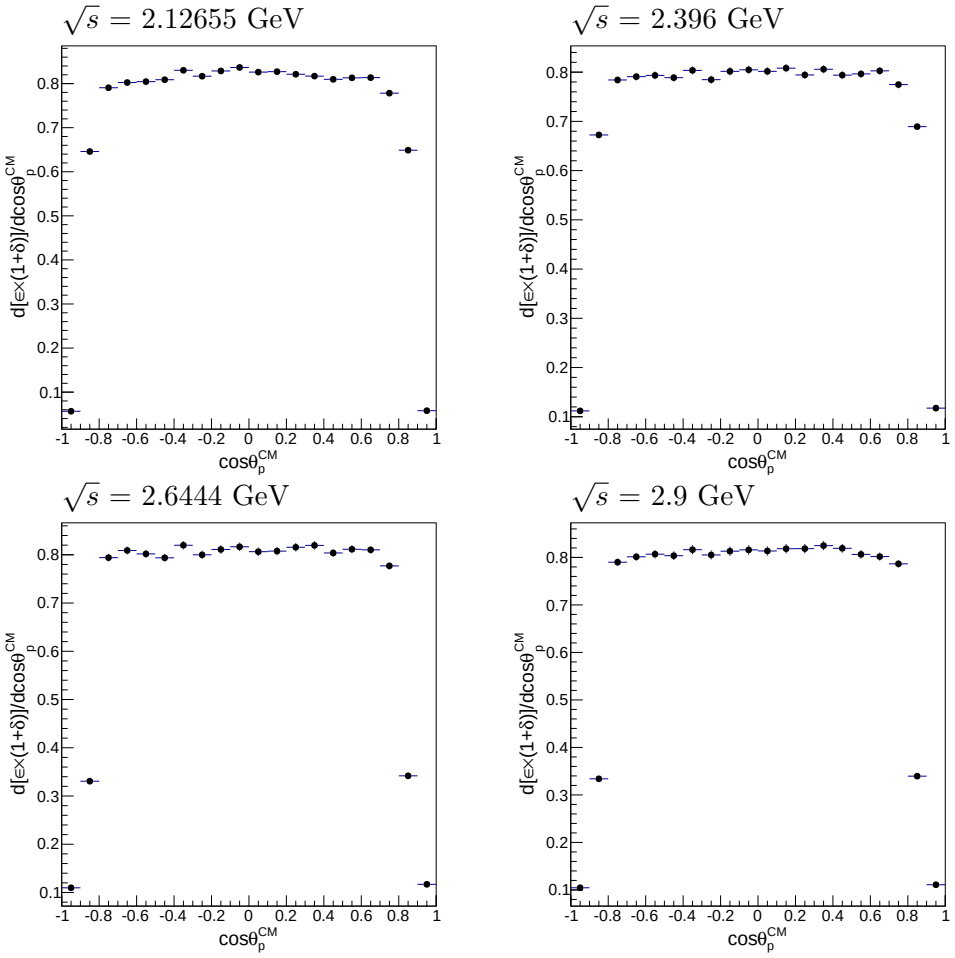

FIGURE 9.3: Distributions of the product of the radiative correction factor and the total efficiency in $\cos\theta_p^{CM}$ for exemplary CM energies of 2.12655 GeV, 2.396 GeV, 2.6444 GeV and 2.9 GeV.

Similar to the radiative and efficiency correction for the cross section extraction in chapter 8, the product of the efficiency and the $(1+\delta)$ distribution is expected to be more or less stable throughout the whole energy range of the scan data set. The distribution of this product should also be flat in $\cos\theta_p^{CM}$ for the region with full detector acceptance (barrel region of the EMC and TOF detector, $|\cos\theta_p^{CM}| \leq 0.8$). This can be seen in the distributions of $\epsilon\times(1+\delta)$ in figure 9.3 for exemplary CM energies, while the distributions for all center of mass energies can be found in appendix A in figure A.13.

9.2 Extraction of the electric and magnetic form factor of the Proton

In this section, two different methods will be introduced which can be used to extract the EM FFs of the proton: the fit method (section 9.2.1) and the method of moments (section 9.2.2), with a first comparison of the two methods presented in section 9.3.

9.2.1 Fit method

To extract the proton EM FFs from the angular distributions, a fit function can be derived from equation 9.1 after applying the efficiency and radiative corrections described in the previous sections:

$$\frac{dN}{\epsilon(1+\delta)d\cos\theta_p^{CM}} = \frac{\mathcal{L}_{int}\hbar c\pi\alpha^2\beta C}{2s}|G_M(s)|^2\left[(1+\cos^2\theta_p^{CM}) + \frac{1}{\tau}R(\sin^2\theta_p^{CM})\right] \quad (9.4)$$

with the magnetic FF $|G_M|$ and the FF ratio R=$|G_E/G_M|$ as the two independent fit parameters. Here, s is the center of mass energy, $\mathcal{L}_{int}$ is the integrated luminosity at the corresponding CM energy, $\hbar$ is the reduced Planck constant, c is the speed of light, α is the fine-structure constant, C is the coulomb correction factor, and β is the velocity v of the proton and antiproton over the speed of light c. τ is defined as $\frac{s}{4m_p^2}$ with the mass of the proton m_p, and $\cos\theta_p^{CM}$ is the angle between the proton or antiproton momentum in the CM frame of the e^+e^- system and the z-axis of the BESIII detector, which points along the direction of the positron beam.
Since the angular analysis of $e^+e^- \to p\bar{p}$ requires to divide the remaining events after event selection into bins of $\cos\theta_p^{CM}$, only samples at energy points with sufficiently high luminosity and therefore remaining events after selection can be analysed. All data points of the 2015 scan data set except the ones at 2.5 GeV, 2.7 GeV and 2.8 GeV as well as the four samples between 2.95 GeV and 3.02 GeV fulfil that requirement. In case of the latter four samples, the distribution of remaining events can be combined after each has been individually corrected for efficiency and radiative corrections. The resulting merged sample with a luminosity weighted average energy of 2.98839 GeV also has sufficiently high amounts of remaining events in each bin of $\cos\theta_p^{CM}$ to allow for an angular analysis.

Since the TOF detector and the EMC of BESIII have a small gap between their barrel and endcap part, the selection efficiency drops to zero for $0.83 < |\cos\theta_p^{CM}| < 0.85$. While the chosen binning for the $\cos\theta_p^{CM}$ distribution would still allow for an efficiency

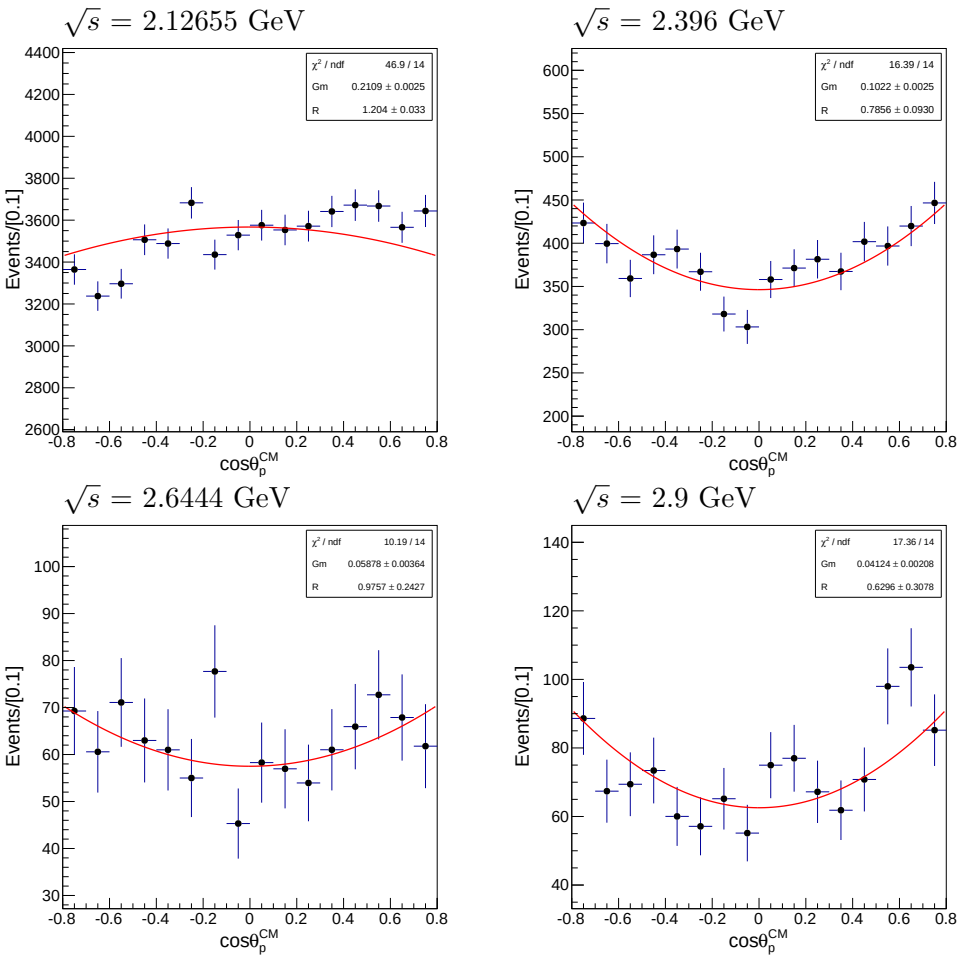

FIGURE 9.4: Distributions of the selected $e^+e^- \to p\bar{p}$ events in $\cos\theta_p^{CM}$ for exemplary CM energies of 2.12655 GeV, 2.396 GeV, 2.6444 GeV and 2.9 GeV. Shown is the data (black dots with error bars) after efficiency and radiative corrections along with a fit according to equation 9.4.

correction in the case of the fit method, the method of moments described in the next section requires an event-by-event efficiency correction, which is not possible with regions of 0 efficiency. Therefore, and to avoid undesired effects at the edges of the detector (e.g. partial shower loss in the EMC), the range of the angular analysis has been limited to $|\cos\theta_p^{CM}| < 0.8$. Figure 9.4 shows the distributions of the selected events in $\cos\theta_p^{CM}$ for CM energies of 2.12655 GeV, 2.396 GeV, 2.6444 GeV and 2.9 GeV with a performed fit using equation 9.4, the distributions and fits for all CM energies can be found in appendix A in figure A.14.

The distributions of events in $\cos\theta_p^{CM}$ show a slight asymmetry of events with $\cos\theta_p^{CM} > 0$ compared to events with $\cos\theta_p^{CM} < 0$ for samples at CM energies with high amounts of remaining events. For the energy point at 2.12655 GeV, the CM energy with the highest amount of remaining events in the scan data set, this asymmetry can be easily spotted by eye (see figure 9.4) and also leads to a inadequate fit with equation 9.4 with

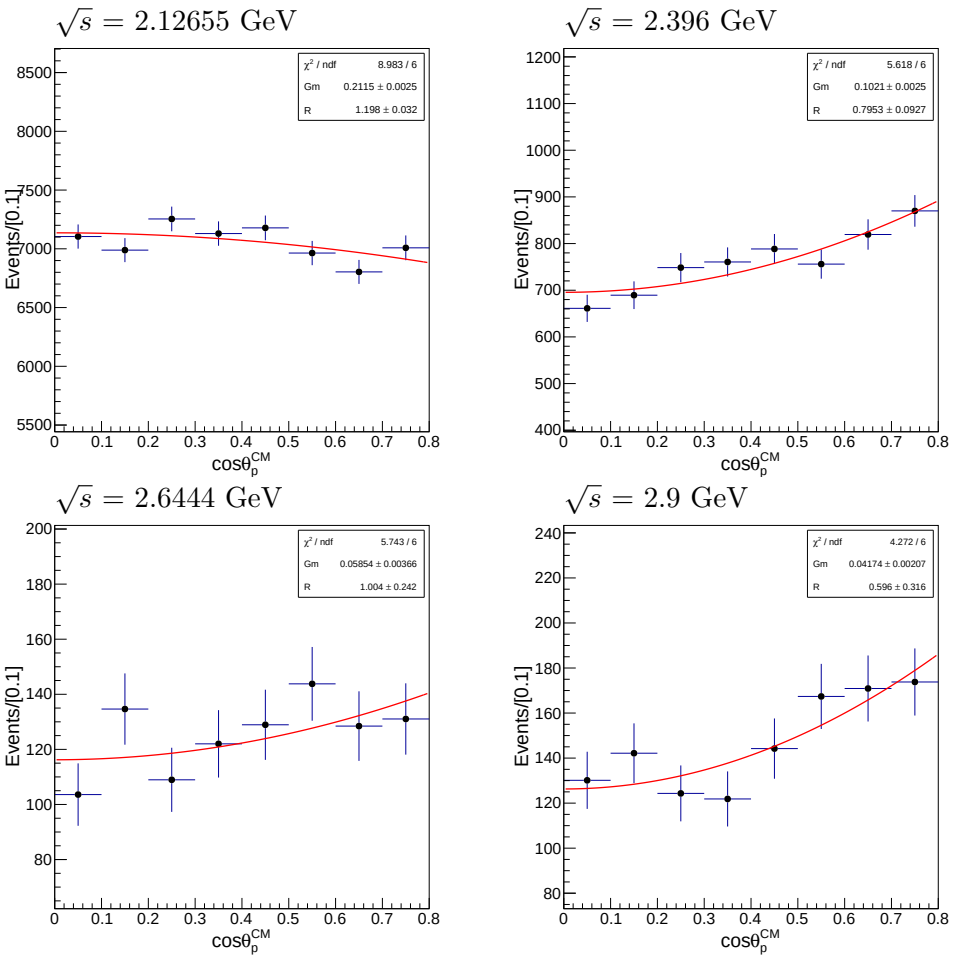

FIGURE 9.5: Distributions of the selected $e^+e^- \to p\bar{p}$ events in $|\cos\theta_p^{CM}|$ (instead of $\cos\theta_p^{CM}$ in figure 9.4) for exemplary CM energies of 2.12655 GeV, 2.396 GeV, 2.6444 GeV and 2.9 GeV. Shown is the data (black dots with error bars) after efficiency and radiative corrections along with a fit according to equation 9.4.

a reduced χ^2 value of 3.35.

To quantify the asymmetry, the following parameter can be defined:

$$A_P = \frac{N(\cos\theta_p^{CM}+) - N(\cos\theta_p^{CM}-)}{N(\cos\theta_p^{CM}+) + N(\cos\theta_p^{CM}-)} \tag{9.5}$$

Where A_P is the asymmetry parameter, $N(\cos\theta_p^{CM}+)$ is the amount of selected events with positive $\cos\theta_p^{CM}$ and $N(\cos\theta_p^{CM}-)$ the amount of events with negative $\cos\theta_p^{CM}$. Table 9.1 shows this parameter for all CM energies as well as the significance of its difference from an asymmetry of 0 in terms of the standard error of the asymmetry parameter. Apart from the over 5 σ_{A_P} significance of the 2.12655 GeV data sample, only the sample at 2.1 GeV shows an asymmetry that has a significant difference from 0 of more than 3 σ_{A_P}, and the significance at 2.9 GeV is close to 3 σ_{A_P}. However, another

TABLE 9.1: Values of the asymmetry parameter A_P according to equation 9.5 for all center of mass energy points of the scan data set of 2015 as well as the significance of the difference of the asymmetry from a value of 0 in units of σ_{A_P}.

E_{cm} [GeV]	A_P	A_P/σ_{A_P}
2	0.02 ± 0.014	1.43
2.05	0.019 ± 0.025	0.76
2.1	0.049 ± 0.013	3.77
2.12655	0.0239 ± 0.0047	5.09
2.15	-0.018 ± 0.03	0.60
2.175	0.034 ± 0.017	2.00
2.2	0.029 ± 0.016	1.81
2.2324	0.008 ± 0.018	0.44
2.3094	0.046 ± 0.022	2.09
2.3864	0.003 ± 0.025	0.12
2.396	0.032 ± 0.014	2.29
2.5	0 ± 0.14	0.00
2.6444	-0.004 ± 0.035	0.11
2.6464	0.051 ± 0.036	1.42
2.7	0.1 ± 0.22	0.45
2.8	0.11 ± 0.14	0.79
2.9	0.087 ± 0.032	2.72
2.95	0.1 ± 0.1	1.00
2.981	0.042 ± 0.092	0.46
3	-0.02 ± 0.11	0.18
3.02	0.04 ± 0.11	0.36
3.08	0.029 ± 0.035	0.83

strong hint at an asymmetry different from 0 is the fact that 19 of the 22 data samples of the scan have an asymmetry parameter larger than 0, while only 3 samples have a negative asymmetry parameter with very low significances.

Possible reasons for an asymmetry in $\cos\theta_p^{CM}$ for the process $e^+e^- \to p\bar{p}$ are correction terms of higher order of α to the Born process, which can contain terms that are uneven in $\cos\theta_p^{CM}$ such as two-photon-exchange instead of one-photon-exchange or the interference between ISR and FSR. To confirm this, additional work is necessary in the description of these processes with MC generators, while a thorough investigation into other possible, not physics related causes like detector related asymmetries must also be done. Such efforts are ongoing at BESIII, but are not subject of this thesis, which has the aim to perform a high precision extraction of the EM FFs of the proton. To avoid any bias for this measurement from the mentioned asymmetry, it is instead eliminated by fitting distributions of proton and antiproton in the absolute value $|\cos\theta_p^{CM}|$ instead of $\cos\theta_p^{CM}$, using the same formula of equation 9.4 with an adjusted normalisation. The new normalisation includes a factor of two to compensate the addition of events with negative values $\cos\theta_p^{CM}$ to those with positive values. As can be seen in figure 9.5 for

example CM energies and in the appendix A in figure A.15 for all other CM energies, the change in the fit results is small compared to the statistical uncertainty. To account for any systematic shift of the results due to this asymmetry effect, it was considered as a source of systematic uncertainty (see chapter 10).

9.2.2 Method of moments

To cross check the fit method for the extraction of the proton EM FFs described in the last section, another method called the method of moments can be used. Instead of a fit to histograms, this method is based on evaluating the expectation value of $\cos^2\theta_p^{CM}$ of the proton and antiproton. The expectation value of $\cos^2\theta_p^{CM}$ can be derived from formula 9.4 as (here and in all equations of this section, $\cos\theta_p^{CM} \equiv \cos\theta$):

$$\begin{aligned} < \cos^2\theta_p^{CM} > &= \frac{\int_{x_{min}}^{x_{max}} \cos^2\theta \frac{d\sigma}{d\cos\theta} d\cos\theta}{\int_{x_{min}}^{x_{max}} \frac{d\sigma}{d\cos\theta} d\cos\theta} \\ &= \frac{N_1}{N_{norm}} \int_{x_{min}}^{x_{max}} \cos^2\theta \left[\left(1+\cos^2\theta\right) |G_M|^2 + \frac{1}{\tau}\sin^2\theta |G_E|^2 \right] d\cos\theta, \end{aligned} \tag{9.6}$$

x_{max} (x_{min}) are the maximum (minimum) value of evaluated $\cos\theta_p^{CM}$, in case of this analysis $x_{max} = -x_{min} = 0.8$. N_1 and N_{norm} are normalisation factors, with $N_1 = \frac{\mathcal{L}_{int}\hbar c\pi\alpha^2\beta C}{2s}$ from equation 9.4 and

$$N_{norm} = \int_{x_{min}}^{x_{max}} \frac{d\sigma}{d\cos\theta} d\cos\theta. \tag{9.7}$$

All other variables are defined as in equation 9.4.

Equation 9.6 can be solved for the FF ratio $R = |\frac{G_E}{G_M}|$:

$$R = |\frac{G_E}{G_M}| = \sqrt{\tau \frac{y_4 - y_2 < \cos^2\theta >}{< \cos^2\theta > y_1 - y_3}}, \tag{9.8}$$

where y_i, i=1, 2, 3, 4, are the following integrals:

$$\begin{aligned} y_1 &= \int_{x_{min}}^{x_{max}} (1-x^2)dx, \quad y_2 = \int_{x_{min}}^{x_{max}} (1+x^2)dx, \\ y_3 &= \int_{x_{min}}^{x_{max}} (x^2-x^4)dx, \quad y_4 = \int_{x_{min}}^{x_{max}} (x^2+x^4)dx. \end{aligned} \tag{9.9}$$

The expectation value $< \cos^2\theta_p^{CM} >$ is evaluated event by event by weighting the $\cos^2\theta_p^{CM}$ value of each event by the corresponding efficiency $\epsilon(\cos\theta_p^{CM})$ and radiative correction factor $(1+\delta)(\cos\theta_p^{CM})$. The weighting factor can be determined by a fit with a polynomial function to a distribution of $\epsilon(\cos\theta_p^{CM}) \times (1+\delta)(\cos\theta_p^{CM})$ extracted from MC simulation with finer binning compared to the fit method. This fit can be seen in figure 9.6 for example CM energies and in appendix A in figure A.16 for all other CM energies.

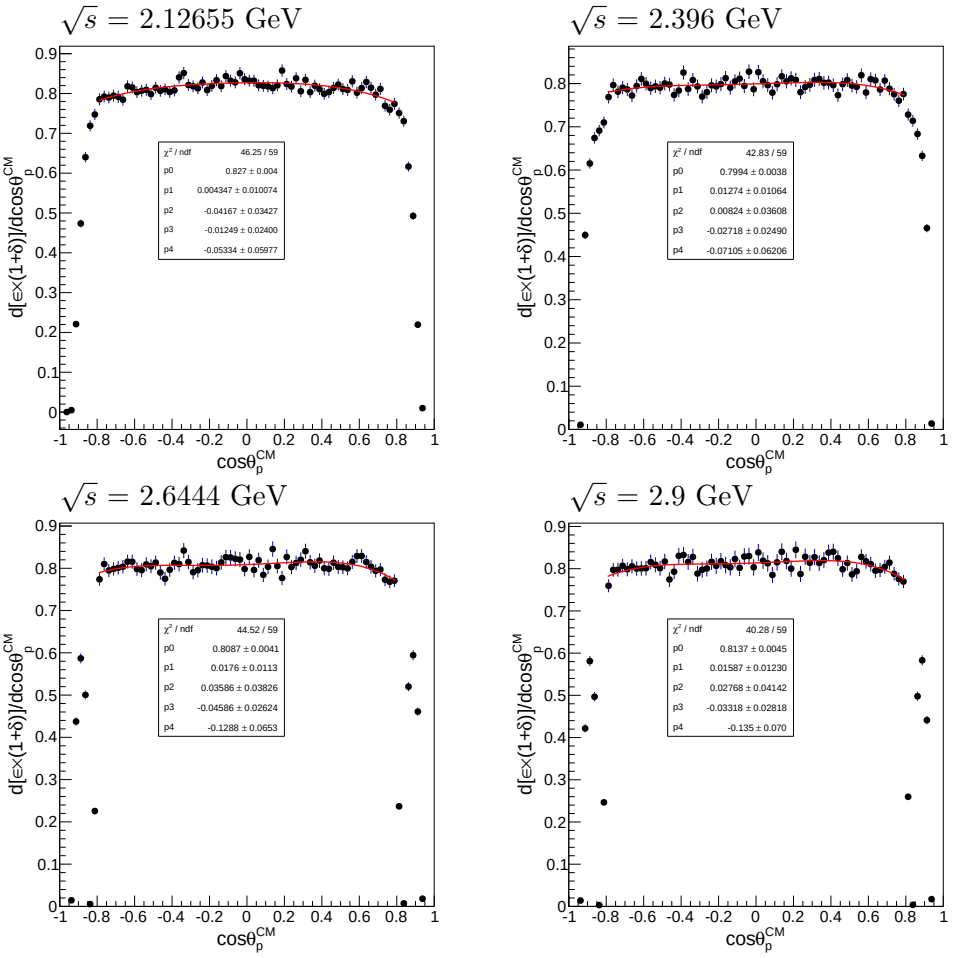

FIGURE 9.6: Distributions of the product of the radiative correction factor and the total efficiency in $\cos\theta_p^{CM}$ for exemplary CM energies of 2.12655 GeV, 2.396 GeV, 2.6444 GeV and 2.9 GeV. A fit with a polynomial function is applied to extract the value of $\epsilon(\cos\theta_p^{CM}) \times (1+\delta)(\cos\theta_p^{CM})$ for each $\cos\theta_p^{CM}$ value, necessary for an event-by-event correction in the method of moments.

The magnetic FF $|G_M|$ can be extracted using the normalisation factor N_{norm}, which, together with the FF ratio from equation 9.8, is equivalent to a separate extraction of the two EM FFs of the proton analogous to the fit method:

$$|G_M| = \sqrt{\frac{N_{norm}}{N_1(y_2 + \frac{1}{\tau}R^2 y_1)}} \tag{9.10}$$

The normalisation factor N_{norm} can be determined by integrating over the $\cos\theta_p^{CM}$ distributions corrected by efficiency and radiative correction, or equivalently by summing up $1/(\epsilon(\cos\theta_p^{CM})(1+\delta(\cos\theta_p^{CM})))$ event by event.

The error of R can be calculated from equation 9.8 by gaussian error propagation:

$$\begin{aligned} \Delta R &= \sqrt{(\Delta < \cos^2\theta >)^2 \left(\frac{\partial R}{\partial < \cos^2\theta >}\right)^2 + (\Delta\tau)^2 \left(\frac{\partial R}{\partial \tau}\right)^2} \\ &= \frac{\tau(y4 \cdot y1 - y2 \cdot y3)}{2R(y3 - y1 < \cos^2\theta >)^2} \Delta < \cos^2\theta > \end{aligned} \tag{9.11}$$

with the error of the expectation value of $\cos^2\theta_p^{CM}$:

$$\begin{aligned} \Delta < \cos^2\theta > &= \sqrt{< \cos^2\theta >^2 - \cos^4\theta} \\ &= \sqrt{\left(\frac{1}{N_{norm}} \sum_{i=0}^{N_{norm}} \cos^2\theta\right)^2 - \frac{1}{N_{norm}} \sum_{i=0}^{N_{norm}} \cos^4\theta} \end{aligned} \tag{9.12}$$

The error of $|G_M|$ can also be derived via gaussian error propagation from equation 9.10 and depends on the error of R from equation 9.11 and the error of N_{norm}:

$$\Delta|G_M| = \sqrt{\left(\frac{|G_M|}{2N_{norm}}(\Delta N_{norm})^2\right) + \left(\frac{N_1}{N_{norm}} R \cdot |G_M|^3 \frac{(y1 - y3)}{\tau}\right)(\Delta R)^2} \tag{9.13}$$

A comparison of a first round of results of the fit method and the method of moments for the proton EM FFs will be shown in the following section.

9.3 First results for the proton electromagnetic form factors

Analogously to the extraction of the cross section of $e^+e^- \to p\bar{p}$ (see chapter 8), the differential radiative and efficiency correction described in sections 9.1.2 and 9.1.1, respectively, depend on the FF model that is used in the generation of the signal MC samples. To be unbiased by this FF model, which is based on previous measurements like the ISR measurement done by BaBar in the case of the Phokhara event generator, an iterative MC tuning procedure will be performed (details see section 9.4).
To perform a first comparison of the two methods introduced in sections 9.2.1 and 9.2.2, the default model built into Phokhara was used to extract a first round of results, which will also be the starting point of the MC tuning procedure described in the next section. This comparison can be seen in table 9.2.

TABLE 9.2: Comparison of the results for the EM FF of the proton $|G_M|$ and the ratio of the two FFs $R = |G_E|/|G_M|$ from the fit method (see section 9.2.1) and the method of moments (MoM, see section 9.2.2). The results shown are not the final results of this work, but a first round based on the default FF model built in Phokhara. Final results are presented in chapter 11.

E_{cm}[GeV]	$R = \lvert G_E/G_M \rvert$			$\lvert G_M \rvert$ [10^{-2}]		
	Fit method	MoM	ΔR[%]	Fit method	MoM	$\Delta\lvert G_M \rvert$[%]
2	1.37±0.10	1.384±0.083	1.32	23.97±0.94	23.81±0.76	0.64
2.05	1.23±0.16	1.21±0.13	1.58	23.1±1.4	23.3±1.2	0.83
2.1	1.277±0.088	1.284±0.077	0.53	21.68±0.70	21.64±0.61	0.19
2.12655	1.198±0.032	1.199±0.026	0.09	21.15±0.25	21.15±0.20	0.001
2.15	1.65±0.25	1.59±0.22	3.17	17.0±1.5	17.4±1.3	2.18
2.175	1.21±0.11	1.21±0.10	0.31	18.14±0.70	18.14±0.62	0.01
2.2	1.10±0.10	1.125±0.091	2.07	17.15±0.59	17.03±0.53	0.68
2.2324	0.87±0.10	0.902±0.094	3.65	16.62±0.53	16.48±0.48	0.86
2.3094	0.58±0.15	0.58±0.14	0.96	11.84±0.42	11.87±0.38	0.29
2.3864	0.58±0.18	0.55±0.16	3.73	10.75±0.42	10.80±0.36	0.55
2.396	0.795±0.093	0.809±0.081	1.69	10.21±0.25	10.18±0.22	0.28
2.6444	1.00±0.24	1.05±0.22	4.87	5.85±0.37	5.80±0.33	0.86
2.6464	0.88±0.26	0.89±0.23	1.12	5.86±0.37	5.86±0.32	0.04
2.9	0.60±0.32	0.63±0.27	5.56	4.17±0.21	4.16±0.18	0.28
2.98839	1.05±0.39	1.09±0.35	3.56	3.24±0.28	3.23±0.25	0.24
3.08	0.54±0.41	0.45±0.41	15.60	3.34±0.18	3.38±0.15	1.14

The results of the two methods are in good agreement for both the FF ratio as well as the individual FFs, in this case $|G_M|$. For the R measurement, the results of most energy points only differ on a level of a few percent (relative to the fit result), larger deviations can only be observed for R values with high statistical uncertainty, such as the one at 3.08 GeV. In units of the standard deviation of the fit method σ^R_{fit}, the largest deviation is 0.23 σ^R_{fit} at 2.2 GeV. The situation for $|G_M|$ is similar, where the largest

deviation is 0.25 $\sigma_{fit}^{|G_M|}$ at 2.15 GeV.
The final results for the EM FFs of the proton after the MC tuning procedure can be found in chapter 11. A comparison between the fit method and the method of moments for the final results is presented section B.1 of appendix B.

9.4 Iterative tuning procedure of the form factor model for Monte Carlo generation

The properties of the generated signal MC of the process $e^+e^- \to p\bar{p}$, such as the amount and angular distribution of ISR events, the angular distribution of proton and antiproton or the cross section of the process calculated by the generator, all depend on the model of the EM FFs of the proton that is used in the generation.

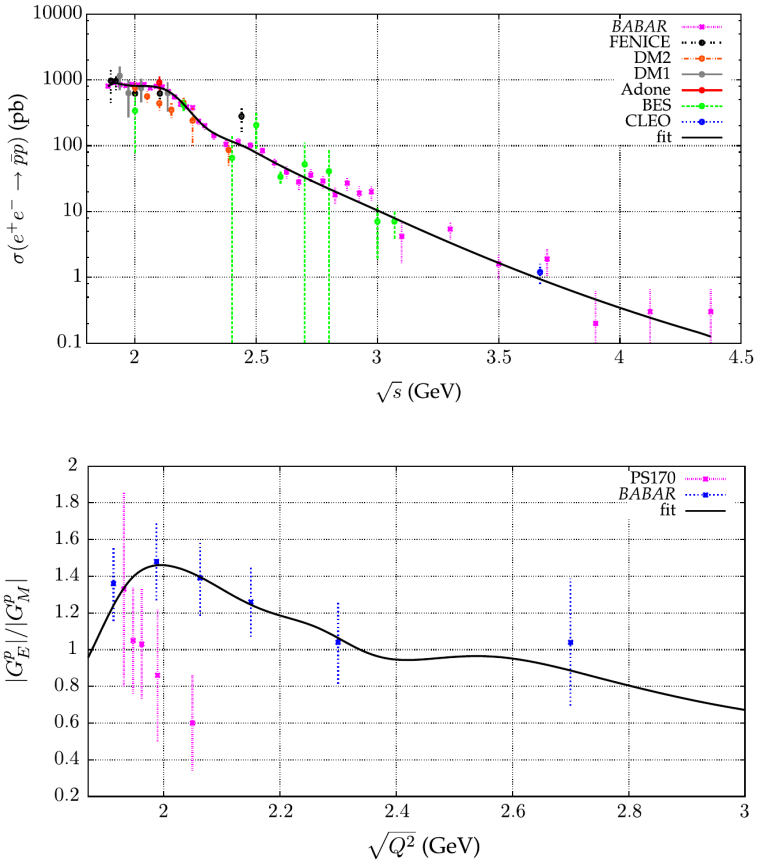

FIGURE 9.7: Data of the FF ratio R=$|G_E/G_M|$ and the cross section of the process $e^+e^- \to p\bar{p}$ from various experiments, together with the fit function (black line) of the Phokhara default model. The plot was taken from reference [184], where more detailed information can be found. References for the data shown are given in the text.

These properties in turn influence the extraction of the cross section of the process as well as the proton EM FFs described in this thesis. The cross section calculated by the

generator is for example used to perform the radiative corrections (see sections 8.2 and 9.1.2), while a change in the angular distribution of the proton in the signal MC may influence the efficiency correction (see sections 8.1 and 9.1.1).

The first round of results presented in the last section was extracted using the built in default model for the proton EM FFs of the Phokhara event generator. This model is based on a fit to the available data for the proton form factors from different experiments (BaBar [84], FENICE [70–72], DM1 [66], DM2 [67, 68], ADONE [69], BES [73], CLEO [74], PS170 [77–79]). Specifically, the ratio R of the electric and magnetic FF as well as the cross section of $e^+e^- \to p\bar{p}$ was fitted to obtain the model. In the case of the EM FF ratio, the model is mainly based on the data taken by BABAR and excludes the results from PS170, which are in strong disagreement with the BABAR data. The fit can be seen in figure 9.7 taken from reference [184]. A more detailed description of the built in Phokhara model can also be found in the same reference.

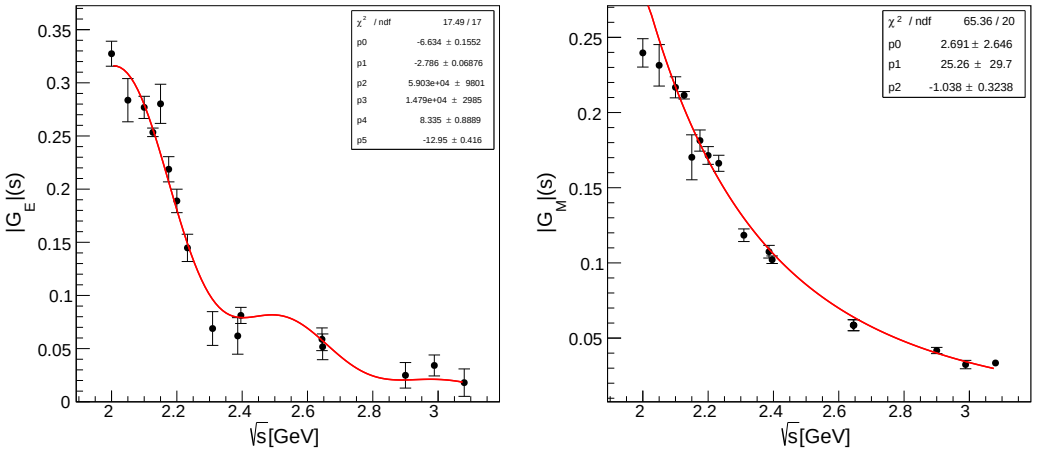

FIGURE 9.8: Results for the electric FF $|G_E|$ (left) and the magnetic FF $|G_M|$ (right) of the proton extracted with MC generated with the default FF model built into Phokhara. The red line represents the first iteration of the tuning model with a fit using equation 9.15 and 9.14 for the left and right plot, respectively.

To be unbiased by the previous measurements of the EM FFs of the proton used in the default Phokhara model, an iterative MC tuning procedure is performed using the first round of results (from the fit method) presented in the last section as the starting point. In a first step, the distribution of the first round individual FFs $|G_E|$ and $|G_M|$ are fitted with the following functions:

$$|G_M(q^2)| = \frac{p_0}{1 + q^2/p_1} \times \frac{1.0}{(1 + q^2/p_2)^2} \tag{9.14}$$

$$|G_E(q^2)| = e^{c_0 + c_1 q}(c_2 + c_3 cos(c_4 + c_5 q)), \tag{9.15}$$

where c_i and p_i are free parameters. Equation 9.14 represents a modified dipole function modelled after formula 2.44, while equation 9.15 is a purely empirical function consisting of an exponential decay modulated by a cosine function to better describe the oscillating behaviour of $|G_E|$.

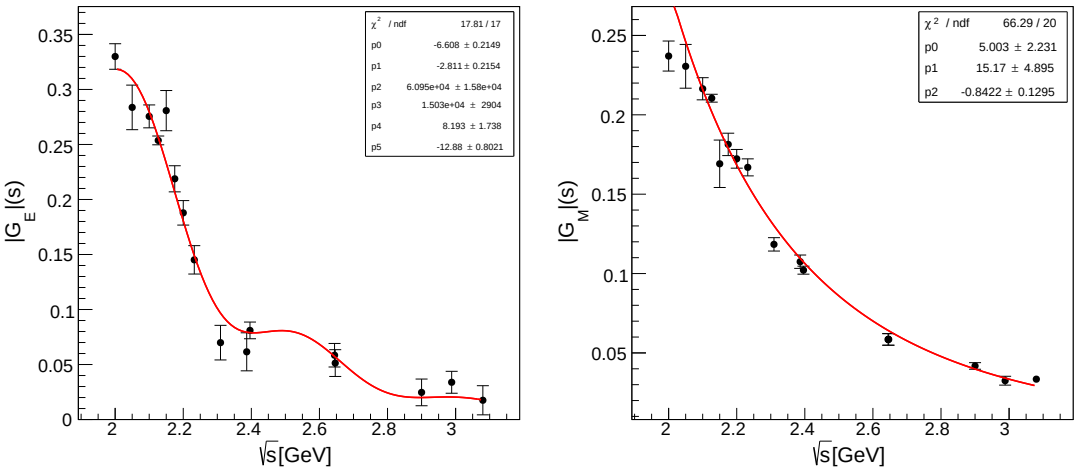

FIGURE 9.9: Results for the electric FF $|G_E|$ (left) and the magnetic FF $|G_M|$ (right) of the proton extracted with MC generated with the FF model of the first iteration of tuning. The red line represents the second iteration of the tuning model with a fit using equation 9.15 and 9.14 for the left and right plot, respectively.

TABLE 9.3: Comparison of the results for the magnetic FF $|G_M|$ and the electric FF $|G_E|$ of the proton extracted with MC using the default model of Phokhara, the first tuning model and the second tuning model.

E_{cm} [GeV]	$\|G_E\|[10^{-2}]$			$\|G_M\|[10^{-2}]$		
	Default model	Tuning 1	Tuning 2	Default model	Tuning 1	Tuning 2
2	32.7±1.2	33.0±1.2	32.8±1.2	23.97±0.94	23.70±0.95	23.93±0.94
2.05	28.4±2.0	28.4±2.0	28.4±2.0	23.1±1.4	23.1±1.4	23±1.4
2.1	27.7±1.0	27.6±1.0	27.5±1.0	21.68±0.70	21.64±0.70	21.68±0.70
2.12655	25.34±0.40	25.37±0.40	25.26±0.40	21.15±0.25	21.05±0.25	21.09±0.25
2.15	28.0±1.8	28.1±1.8	28.0±1.8	17.0±1.5	16.9±1.5	16.9±1.5
2.175	21.9±1.2	21.9±1.2	21.9±1.2	18.14±0.70	18.14±0.71	18.14±0.70
2.2	18.9±1.1	18.8±1.1	18.7±1.1	17.15±0.59	17.23±0.59	17.26±0.59
2.2324	14.5±1.3	14.5±1.3	14.4±1.3	16.62±0.53	16.69±0.54	16.73±0.54
2.3094	6.9±1.6	7.0±1.6	7.0±1.6	11.84±0.42	11.84±0.42	11.83±0.42
2.3864	6.2±1.7	6.2±1.7	6.2±1.7	10.75±0.42	10.75±0.42	10.74±0.42
2.396	8.12±0.76	8.10±0.76	8.10±0.76	10.21±0.25	10.21±0.25	10.21±0.25
2.6444	5.9±1.1	5.8±1.1	5.8±1.1	5.85±0.37	5.85±0.36	5.85±0.36
2.6464	5.2±1.2	5.1±1.2	5.2±1.2	5.86±0.37	5.85±0.36	5.84±0.36
2.9	2.5±1.2	2.5±1.2	2.5±1.2	4.17±0.21	4.18±0.21	4.17±0.21
2.98839	3.4±1.0	3.4±1.0	3.4±1.0	3.24±0.28	3.25±0.28	3.24±0.28
3.08	1.8±1.3	1.8±1.3	1.7±1.4	3.34±0.18	3.35±0.18	3.35±0.18

Figure 9.8 shows the fit of these functions on the initial FF results, which will be called the first iteration of MC tuning. The next step in this first iteration is feeding the fitcurves back into the Phokhara generator to generate a new set of MC samples.
The new MC samples are used again to extract $\sigma_{p\bar{p}}$, $|G_E|$ and $|G_M|$, which will be called the results of the first iteration of tuning. They are shown in figure 9.9.

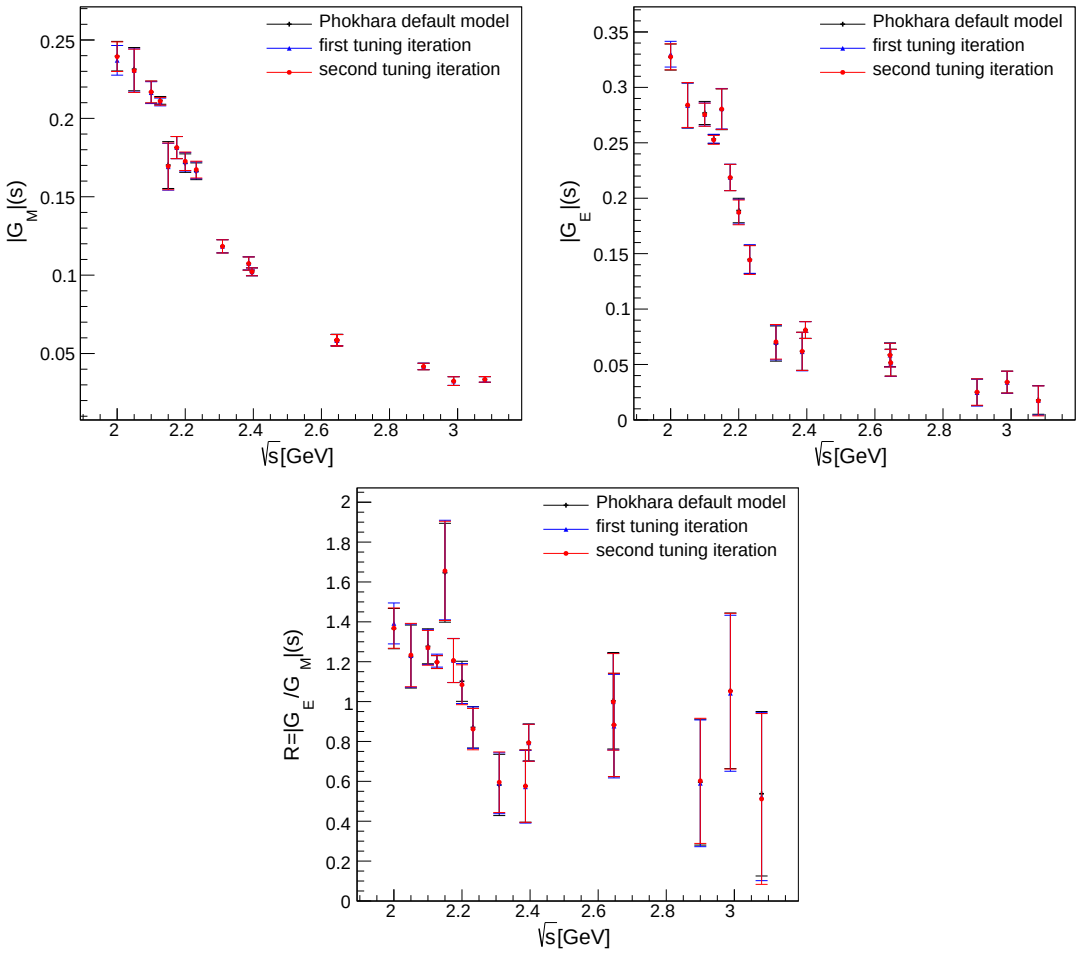

FIGURE 9.10: Comparison of the results for the magnetic FF $|G_M|$ (upper left) and the electric FF $|G_E|$ (upper right) of the proton as well as their ratio R (bottom) extracted with MC using the default model of Phokhara (black crosses with error bars), the first tuning model (blue triangles with error bars) and the second tuning model (red dots with error bars).

For the second iteration of tuning, these results are fitted again using the same functions as in the first iteration. The result of this fit can also be seen in figure 9.9. This procedure is repeated until the change in results is considered small enough at each CM energy compared to the statistical uncertainties of the FFs, which is the case after two iterations of tuning. Therefore, the results of the second tuning iteration are considered the final results of this work, which are presented and discussed in more detail in the final chapter 11 of this thesis.

A comparison between the results obtained with the default model as well as the different tuning iterations is shown in figure 9.10. As can be seen, the difference between the results obtained with the two tuning models and even to the results obtained with the default model of Phokhara are small compared to the statistical uncertainties.

Chapter 10

Determination of Systematic Uncertainties

In this chapter, potential sources of systematic uncertainties of the measurements presented in this work are investigated. That includes the measurement of the Born cross section of $e^+e^- \to p\bar{p}$, the effective FF and the EM FFs of the proton. The size of the uncertainty for each source is estimated based on methods described in sections 10.1, 10.2 and 10.3, after which an estimate of the total systematic uncertainty is given.

10.1 Systematic uncertainty in the Born cross section measurement

The sources of systematic uncertainty for the cross section include the uncertainty from tracking and PID efficiency, the selection criteria, remaining background pollution, luminosity measurement, tuning procedure and the FF model used in the MC simulations for efficiency and radiative corrections. An estimation of the magnitude of each of these contributions will be performed in the following sections. The total systematic uncertainty on the Born cross section is calculated as the sum of the quadratures of the individual contributions, assuming them to be uncorrelated:

$$\delta_{sys,\sigma} = \sqrt{\delta^2_{trk} + \delta^2_{PID} + \delta^2_{E/p} + \delta^2_{sel} + \delta^2_{bkg} + \delta^2_{lum} + \delta^2_{tun} + \delta^2_{mod}}, \tag{10.1}$$

with $\delta_{trk}, \delta_{PID}, \delta_{E/p}, \delta_{sel}, \delta_{bkg}, \delta_{lum}, \delta_{tun}, \delta_{mod}$ as the uncertainties from tracking efficiency, PID efficiency, E/p efficiency, selection criteria, background, luminosity, tuning and the FF model, respectively.

10.1.1 Tracking efficiency studies

The efficiency of the tracking of the BESIII detector is corrected for via the use of MC samples of the signal process (details see section 8.1 for the cross section measurement and section 9.1.1 for the FF measurement), which simulate the tracking as part of the GEANT4 detector simulation. A potential systematic uncertainty can arise from differences in the description of the detector in MC compared to real data. To ascertain these differences, a control channel is investigated using the same data samples as the main analysis at selected CM energy points ((2.3864, 2.396, 2.6444, 2.6464, 2.9, 2.95, 2.981, 3, 3.02, 3.08) GeV). The chosen control channel is $e^+e^- \to p\bar{p}\pi^+\pi^-$, where events can be identified using only the detector signatures of 3 of the 4 particles, the two pions and either the proton or antiproton. The remaining particle can be studied to determine its tracking efficiency in the data samples and compare it to that of MC samples generated for the process $e^+e^- \to p\bar{p}\pi^+\pi^-$. The difference between these two efficiencies is then be used to estimate the systematic uncertainty from the tracking efficiency.

The control channel is selected using the following event selection:

- At least 3 good charged tracks coming from the interaction vertex, with points of closest approach to the interaction vertex in the direction of the beam of 10 cm ($|R_Z| < 10cm$) and in the plane perpendicular to the beam of 1 cm ($|R_{XY}| < 10cm$). The polar angle of the tracks must be within the MDC acceptance, $|\cos\theta| < 0.93$
- PID requirement using dE/dx and TOF measurements to identify the two pions and either the proton or antiproton, depending on which particle is investigated:
  - $P_{PID}(pion) > P_{PID}(proton)$ and $P_{PID}(pion) > 0.001$ for both pion candidates
  - $P_{PID}(proton) > P_{PID}(pion), P_{PID}(kaon)$ and $P_{PID}(proton) > 0.001$ for the proton or antiproton
- Missing mass of proton (antiproton) M_p ($M_{\bar{p}}$) recoiling against the $\bar{p}(p)\pi^+\pi^-$ system must be within a window around the proton mass: $M_{p,\bar{p}} \in [0.838, 1.038]$ GeV/c^2

The total amount of events of the control sample (denoted as N) is then extracted by fitting the missing mass spectrum of events with at least 3 good charged tracks in bins of either $\cos\theta_p^{CM}$ or the transverse momentum p_t, which is the component of the

momentum perpendicular to the beam direction. The fit function used is a sum of a double gaussian for the signal and a polynomial function for the background. The amount of events where the proton (or antiproton in case of the antiproton efficiency study) has been tracked successfully in the MDC (denoted as n) is extracted by fitting the missing mass spectrum of events with exactly 4 charged tracks detected within the MDC, again in intervals of either $\cos\theta_p^{CM}$ or p_t depending on the study.

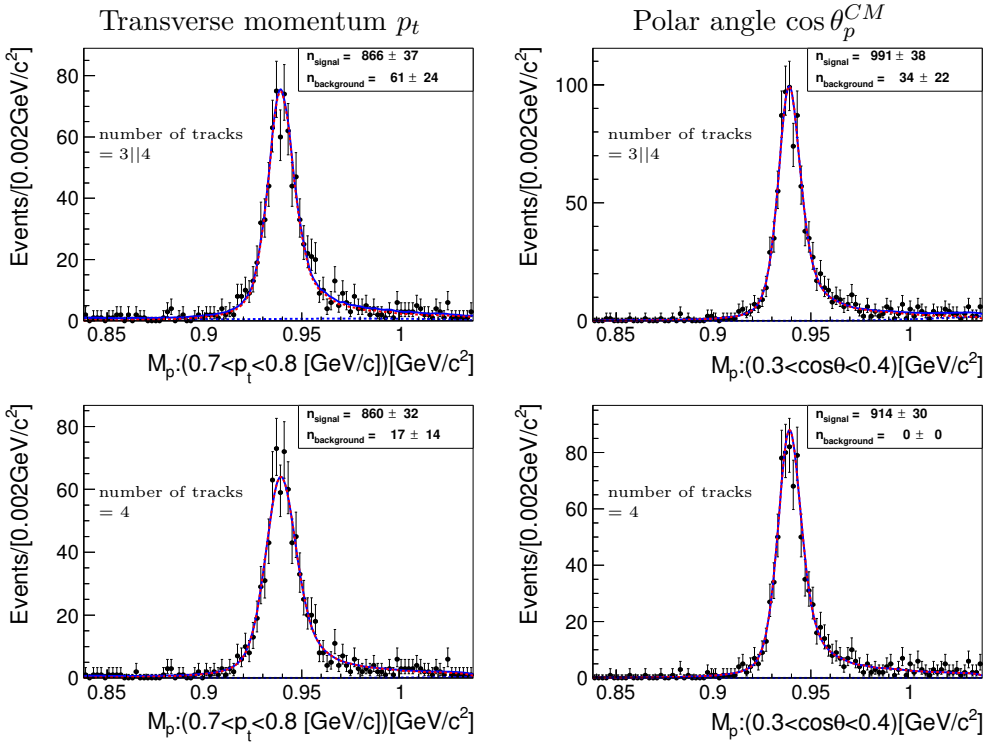

FIGURE 10.1: Missing mass of the proton recoiling against the $\pi^+\pi^-\bar{p}$ system. Upper row: distribution of events with with 3 or 4 good charged tracks in the MDC in an exemplary p_t interval of $p_t \in [0.7, 0.8]$ GeV (left) and an exemplary $\cos\theta_p^{CM}$ interval of $\cos\theta_p^{CM} \in [0.3, 0.4]$ (right), including a double gaussian fit plus a polynomial to extract the total number of events (N) for the control sample in this interval. Lower row: distribution of events with exactly 4 good charged tracks in the MDC in the same p_t and $\cos\theta_p^{CM}$ intervals as above, including a fit with the same fit function to extract the number of events with successful proton tracking (n) in the control sample.

The missing mass distributions including the fit to extract n and N can be seen in figure 10.1 for an exemplary p_t and $\cos\theta_p^{CM}$ interval for the proton. The distributions and fits for all other p_t and $\cos\theta_p^{CM}$ intervals for both the proton and the antiproton tracking efficiency study are shown in appendix C in section C.1.1.

The tracking efficiency can be calculated from the two numbers extracted from these fits as:

$$\epsilon_{trk} = \frac{n}{N}. \tag{10.2}$$

The uncertainty of the tracking efficiency is given by

$$\sigma_{\epsilon_{trk}} = \sqrt{(-\frac{\epsilon_{trk}}{N} \quad \frac{1}{N}) \begin{pmatrix} (\sigma_N)^2 & (\sigma_n)^2 \\ (\sigma_n)^2 & (\sigma_n)^2 \end{pmatrix} \begin{pmatrix} -\frac{\epsilon_{trk}}{N} \\ \frac{1}{N} \end{pmatrix}} \tag{10.3}$$

$$= \frac{1}{N}\sqrt{(1-2\epsilon_{trk})(\sigma_n)^2 + \epsilon_{trk}^2(\sigma_N)^2}. \tag{10.4}$$

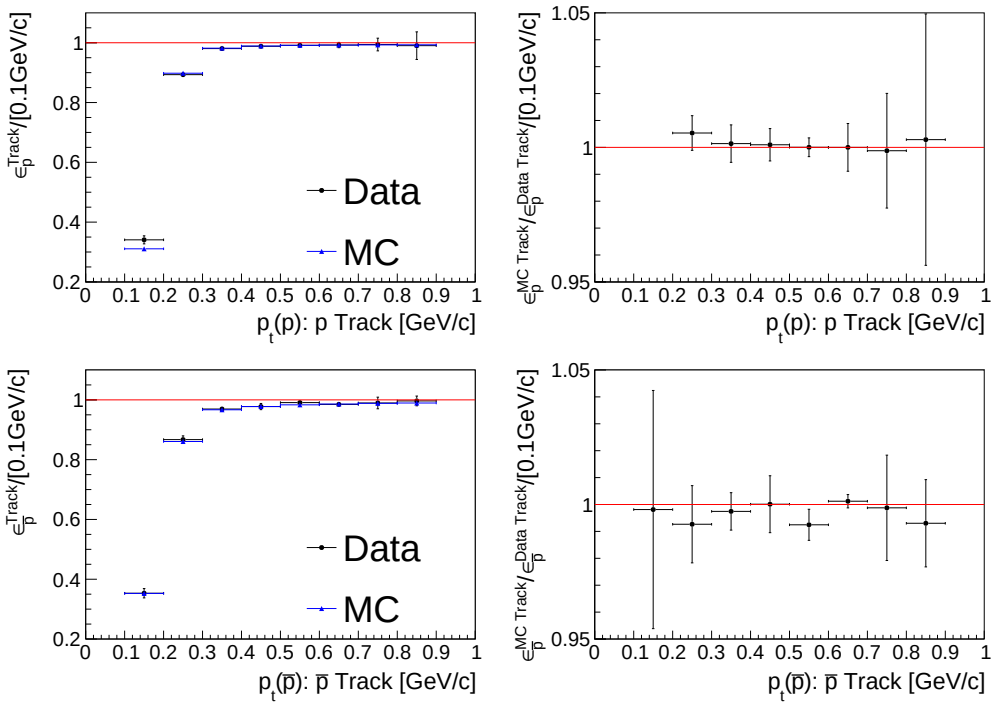

FIGURE 10.2: Left: Comparison of the tracking efficiency calculated by equation 10.2 in bins of the transverse momentum p_t for data (black points with error bars) and MC (blue triangles with error bars) of the control sample $e^+e^- \to \pi^+\pi^- p\bar{p}$. The top (bottom) row shows the comparison for the proton (antiproton) tracking efficiency study. Right: systematic uncertainty derived from the comparison according to equation 10.5 with its error calculated with equation 10.6.

Once the tracking efficiency has been determined according to equation 10.2 for both the data sample as well as a MC sample of the control channel $e^+e^- \to p\bar{p}\pi^+\pi^-$, the systematic uncertainty from the tracking efficiency can be estimated by comparing the two efficiencies:

$$\delta_{trk} = 1 - \frac{\epsilon_{trk}(MC)}{\epsilon_{trk}(data)}, \tag{10.5}$$

where $\epsilon_{trk}(MC)$ and $\epsilon_{trk}(data)$ are the tracking efficiencies from MC and data, respectively.
The standard error of the uncertainty can be calculated by

$$\sigma_{\delta_{trk}} = (1 - \Delta_{trk}) \cdot \sqrt{\frac{\sigma^2_{\epsilon_{trk}(MC)}}{\epsilon^2_{trk}(MC)} + \frac{\sigma^2_{\epsilon_{trk}(data)}}{\epsilon^2_{trk}(data)}} \tag{10.6}$$

The comparison between the data and MC tracking efficiencies can be seen on the left side of figure 10.2 for p_t intervals and on the left side of 10.3 for $\cos\theta_p^{CM}$ intervals. Large deviations between the two can only be observed for high values of $|\cos\theta_p^{CM}|$ and low values of p_t. The difference at high $|\cos\theta_p^{CM}|$ is possibly due to an incorrect description of effects at the edge of the MDC detector (detector acceptance: $|\cos\theta_p^{CM}| < 0.93$). For this analysis, only a very small amount of events falls in this $|\cos\theta_p^{CM}|$ bin ($\sim 3\%$), the impact of this effect is therefore negligible.

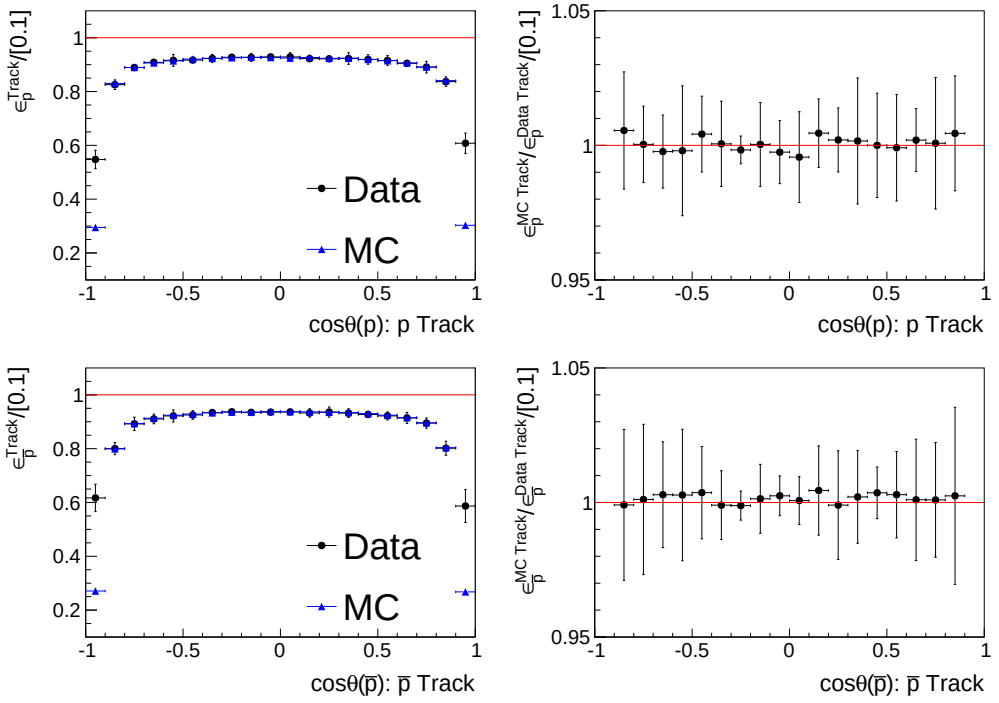

FIGURE 10.3: Left: Comparison of the tracking efficiency calculated by equation 10.2 in bins of the polar angle $\cos\theta_p^{CM}$ for data (black points with error bars) and MC (blue triangles with error bars) of the control sample $e^+e^- \to \pi^+\pi^- p\bar{p}$. The top (bottom) row shows the comparison for the proton (antiproton) tracking efficiency study. Right: systematic uncertainty derived from the comparison according to equation 10.5 with its error calculated with equation 10.6.

The deviation between data and MC at low p_t values is a lot smaller compared to that at high $|\cos\theta_p^{CM}|$. A larger discrepancy only exists only for the proton track at

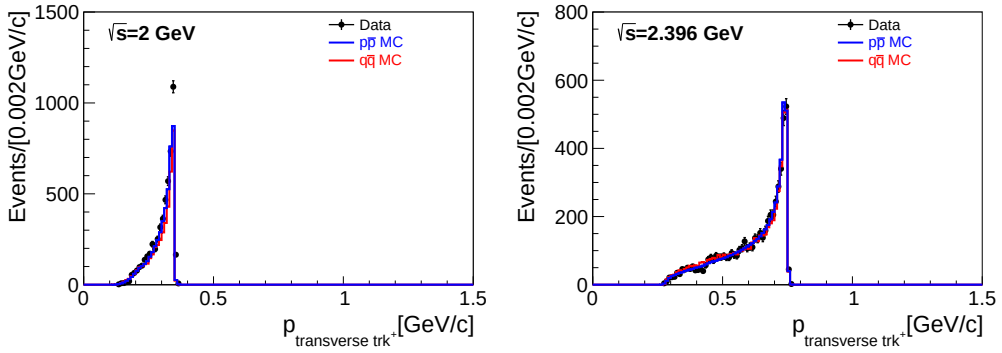

FIGURE 10.4: Distribution of the transverse momentum in data and signal MC of $e^+e^- \to p\bar{p}$ for CM energies of 2.0 GeV (left) and 2.396 GeV (right).

$p_t \in [0.1, 0.2]$ GeV. Figure 10.4 shows that even for the lowest CM energy 2.0 GeV, only a very small portion of $e^+e^- \to p\bar{p}$ events fall into this interval, while for higher CM energies (here 2.396 GeV), there are no events with such low p_t values.
The right side of figures 10.2 and 10.3 shows the systematic uncertainty and its error according to equations 10.5 and 10.6 for p_t and $\cos\theta_p^{CM}$ intervalls, respectively. For most p_t and $\cos\theta_p^{CM}$ values, the systematic tracking uncertainty is below 1%. Due to the large errors of the uncertainties however, especially for the $\cos\theta_p^{CM}$ study, a conservative assumption of 1% systematic uncertainty per track was assumed for the main analysis.

10.1.2 Uncertainty due to selection criteria

The choice of the selection criteria described in section 6.1 can introduce a bias due to differences in data and MC which might be sensitive to the chosen threshold values. To estimate this effect, the Born cross section has been extracted with a variation of the selection criteria for the TOF difference, the angle between the two tracks and the momentum window. The difference to the cross section extracted with the nominal threshold value for each selection criterion is taken as the estimate of this systematic uncertainty. The detailed changes for each selection criterion can be summarised as follows:

- TOF difference: the window for the TOF difference between the two tracks is changed from ± 4 ns to ± 3 ns and ± 5 ns. For both cases, the cross section is calculated and compared to the one obtained with the nominal cut after the last tuning iteration. The largest difference is taken as δ_{TOF}.
- Angle between tracks: the minimum angle between the two tracks is changed depending on the CM energy. For the CM energies of 2.0 GeV and 2.05 GeV,

it is changed from 170° to 172° and 168°. Between 2.1 GeV and 2.3094 Gev, it is changed from 175° to 176° and 174°. For the remaining energy points between 2.3864 GeV and 3.08 GeV, it is changed from 178° to 178.5° and 177.5°. Again, the cross section obtained with these threshold values is compared to that with the nominal threshold values after the last tuning iteration and the difference is taken as δ_{ang}

- Momentum window: the momentum window is changed by varying the upper and lower limit for the momentum simultaneously, first to produce a larger and then a smaller momentum window. These two cases have been investigated:
  - Case 1 (larger window): momentum window changed from $p_{p,\bar{p}} \in [p_{theo} - 4\sigma_p, p_{theo} + 3\sigma_p]$ to $p_{p,\bar{p}} \in [p_{theo} - 4.5\sigma_p, p_{theo} + 3.5\sigma_p]$
  - Case 2 (smaller window): momentum window changed from $p_{p,\bar{p}} \in [p_{theo} - 4\sigma_p, p_{theo} + 3\sigma_p]$ to $p_{p,\bar{p}} \in [p_{theo} - 3.5\sigma_p, p_{theo} + 2.5\sigma_p]$

  The largest difference of the Born cross section obtained with the requirement of those two cases to the nominal result after the second iteration of tuning is taken as δ_{mom}

TABLE 10.1: Systematic uncertainty of the cross section measurement for the TOF (δ^{σ}_{TOF}), the back-to-back angle (δ^{σ}_{ang}) and the momentum window (δ^{σ}_{mom}) selection criteria as well as the total systematic uncertainty from the selection (δ^{σ}_{sel}) for all CM energy points of the 2015 scan data set.

E_{cm} [GeV]	δ^{σ}_{TOF} [%]	δ^{σ}_{ang} [%]	δ^{σ}_{mom} [%]	δ^{σ}_{sel} [%]
2	0.12	0.19	0.17	0.28
2.05	0.01	0.10	0.77	0.77
2.1	0.06	0.23	0.11	0.27
2.12655	0.04	0.07	0.10	0.13
2.15	0.13	0.54	0.13	0.57
2.175	0.13	0.20	0.26	0.35
2.2	0.05	0.06	0.23	0.24
2.2324	0.02	0.04	0.13	0.14
2.3094	0.16	0.09	0.58	0.61
2.3864	0.07	0.30	0.14	0.34
2.396	0.06	0.19	0.47	0.51
2.5	0.05	2.09	1.41	2.53
2.6444	0.05	0.36	0.88	0.96
2.6464	0.20	0.55	1.11	1.26
2.7	0.04	4.10	1.52	4.37
2.8	0.03	1.62	1.53	2.23
2.9	0.07	0.49	0.47	0.68
2.95	0.03	0.79	1.93	2.09
2.981	0.03	1.38	2.41	2.78
3	0.02	1.61	1.40	2.13
3.02	0.02	0.39	0.37	0.54
3.08	0.02	0.07	0.97	0.97

The total uncertainty from the selection criteria is then calculated by assuming the three components described above to be uncorrelated:

$$\delta_{sel} = \sqrt{\delta_{TOF}^2 + \delta_{ang}^2 + \delta_{mom}^2}, \tag{10.7}$$

The value of the systematic uncertainty for each individual selection criterion as well as the total systematic uncertainty from the selection criteria can be seen in table 10.1 for all CM energies of the 2015 scan data set.

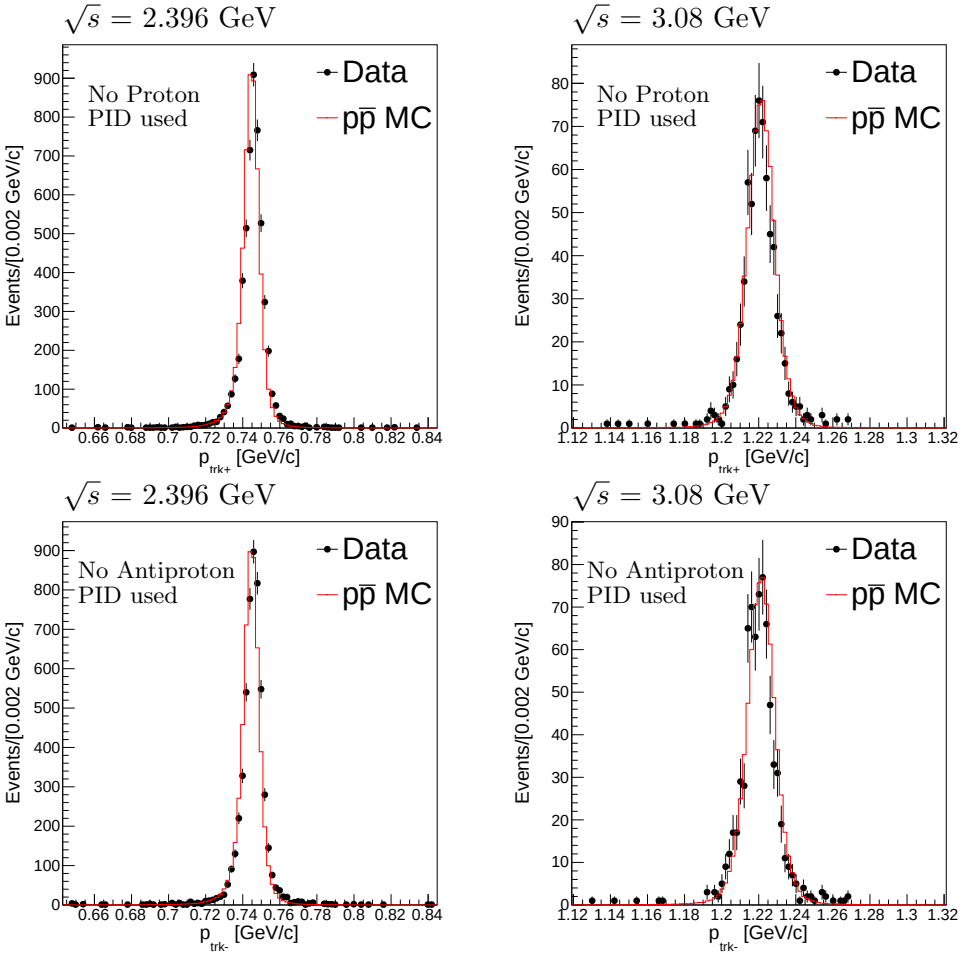

FIGURE 10.5: Momentum distribution of the proton (upper row) or antiproton (lower row) for two example CM energies of 2.396 GeV (left) and 3.08 GeV (right) for data (black points with error bars) compared with signal MC (red line) including radiative corrections up to NNLO. Compared to the main analysis, no PID requirements have been applied to the positive track (upper row) or negative track (lower row) to study the proton or antiproton PID efficiency, respectively, while a number of other requirements have been tightened (see text).

10.1.3 Particle identification efficiency studies

The systematic uncertainty from the efficiency of the PID criteria is studied using the same data samples and the same process as for the main analysis, $e^+e^- \to p\bar{p}$. In this study, the process is selected by only applying PID requirements to one of the two charged tracks; either the proton to study the antiproton PID efficiency, or the antiproton to study the proton PID efficiency. The other selection criteria are similar to the main analysis described in section 6.1, though some of them have to be chosen tighter to compensate for the missing PID requirement on one of the tracks. Compared to the selection criteria of the main analysis, this allows for a similarly low background level in data with a reduced signal efficiency, which still gives enough remaining events at high luminosity data points to perform this study.

Compared to the requirements of the main analysis, the tougher requirements can be summarised as follows:

- The requirement on the back to back angle of the two tracks is tightened: from
  $\sphericalangle_{p,\bar{p}} > 170°$, 175°,178° at (2.0-2.05, 2.1-2.3094, 2.3864-3.08) GeV
  $\to \sphericalangle_{p,\bar{p}} > 175°$, 176°, 177°, 178°, 179°, 179.5° at (2.0-2.05, 2.1-2.175, 2.2-23094, 2.3864, 2.396-3.02, 3.08) GeV
- A tighter PID requirement for the track that is not investigated for its PID efficiency is imposed for higher energies to ensure the removal of Bhabha scattering events. For CM energies above 2.5 GeV, the probability of the corresponding track to be a proton (antiproton) is required to be 10 times higher than that to be an electron: $P_{PID}(proton) > 10 \times P_{PID}(electron)$. PID requirements to distinguish protons from muons and kaons remain the same.

The resulting samples from these requirements consist mostly of $p\bar{p}$ events with low background pollution, as can be seen from the momentum distributions of the proton or antiproton in figure 10.5 for two CM energies, distributions for all other CM energies can be found in appendix C in figures C.5 and C.6 for the proton and antiproton, respectively.

Once the samples have been obtained, the PID efficiency can be determined in a similar way as the tracking efficiency described in section 10.1.1. The PID efficiency and its error can be calculated using formulas 10.2 and 10.3, respectively. Here, N is the total amount of events of each sample obtained with the above event selection, and n is the amount of events where the particle with previously unused PID information (proton or antiproton depending on the study) is correctly identified by the PID system. Both numbers can simply be obtained by counting due to the low level of remaining background. The PID

efficiency extracted for both data and $e^+e^- \to p\bar{p}$ signal MC allows to determine the systematic uncertainty due to the PID efficiency as well as the standard error on this uncertainty according to equations 10.5 and 10.6, respectively.

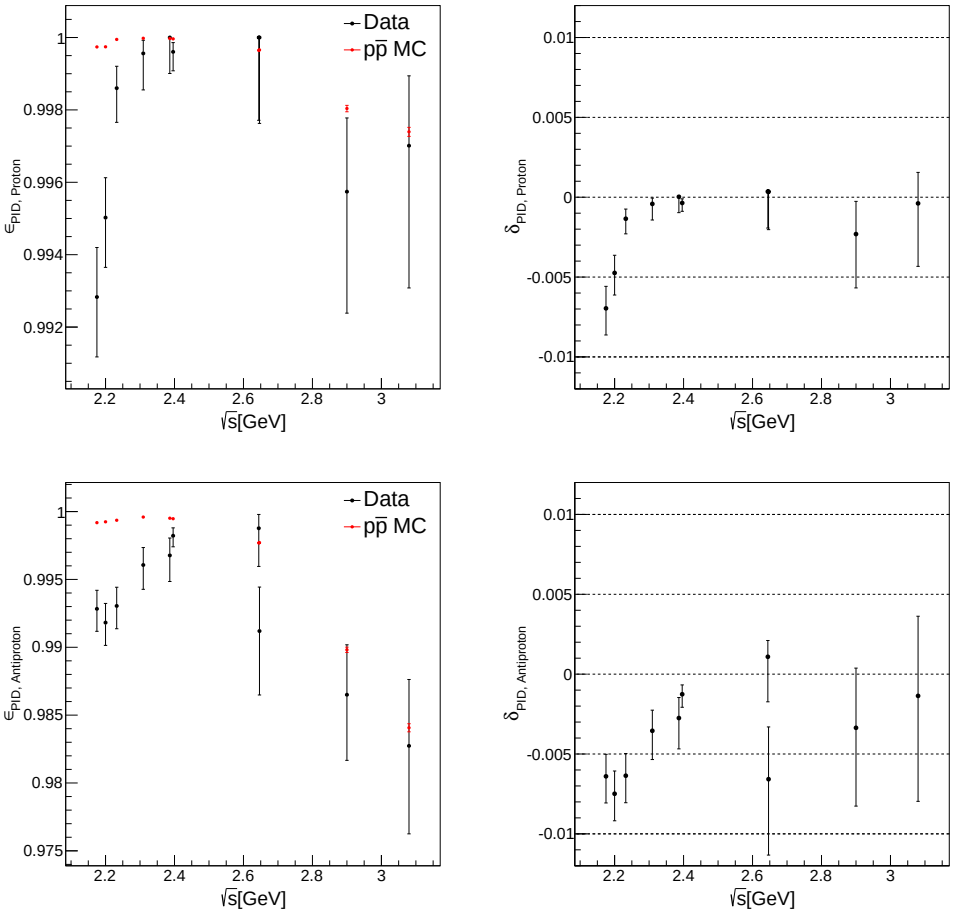

FIGURE 10.6: Left: comparison between the PID efficiency of data (black dots with error bars) and MC (red dots with error bars) calculated according to equation 10.2 for the proton (top) and antiproton (bottom) at CM energies of the 2015 scan data set with enough events remaining after the modified event selection (see text). Energy points below 2.175 are not shown since the PID system is not used there in the main analysis. Right: estimation of the systematic uncertainty due to the difference in efficiency in data and MC simulation calculated according to equation 10.5 for the same CM energy points.

The PID efficiency and the corresponding systematic uncertainty is studied for energy points where enough events remain after the requirements described above are imposed. This is the case for all energy points of the 2015 scan data set except for 2.5 GeV, 2.7 GeV, 2.8 GeV and the four energy points between 2.95 GeV and 3.02 GeV. For these seven points, the PID systematic uncertainty is assumed to be the same as at the closest CM energy where it can be determined. Energy points below 2.175 GeV are not shown since the PID system is not used at these energies in the main analysis, they will be treated separately later in this section.

The comparison between the PID efficiency of data and MC can be seen in figure 10.6 for all other CM energies, along with the resulting systematic uncertainty. Due to the large error on the systematic uncertainty that can be observed at some CM energies, the final uncertainty for the proton and antiproton is estimated conservatively at each CM energy as the absolute value calculated according to equation 10.5 plus one standard deviation of that value. The total systematic uncertainty due to the PID efficiency is then obtained by adding the uncertainty of proton and antiproton linearly, since it can not be assumed that they are uncorrelated.

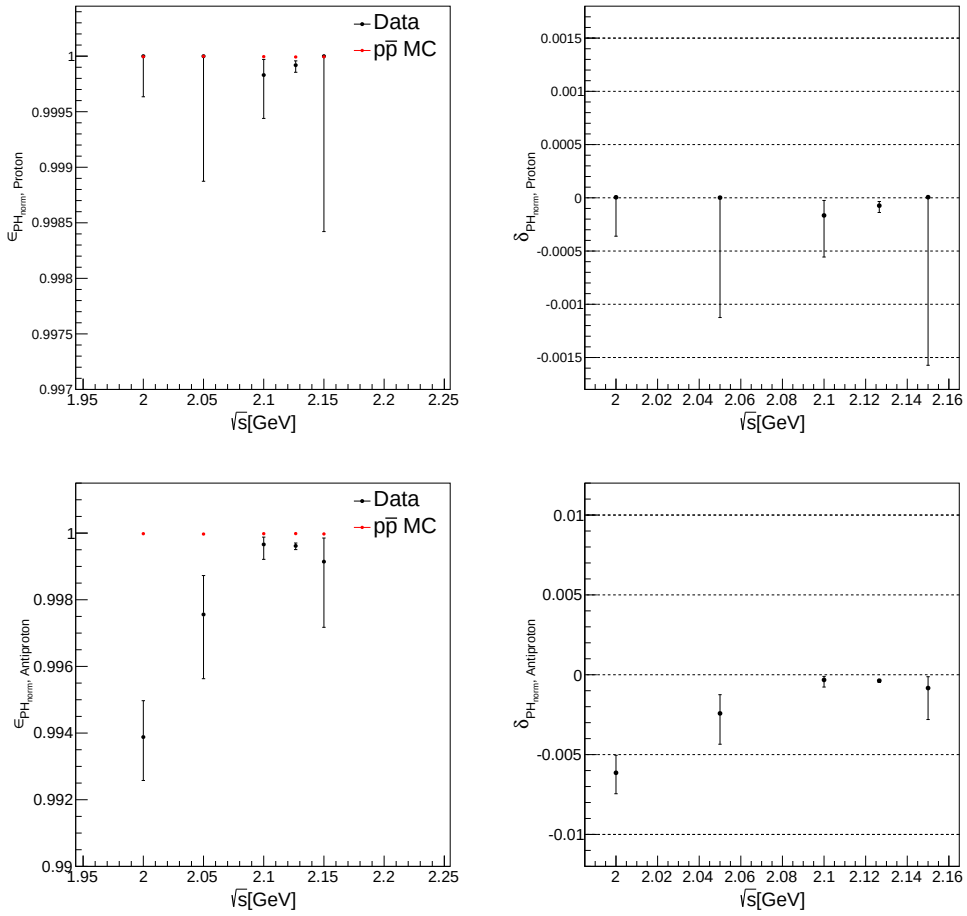

FIGURE 10.7: Left: comparison between the PH_{norm} efficiency of data (black dots with error bars) and MC (red dots with error bars) calculated according to equation 10.2 for the proton (top) and antiproton (bottom) at CM energies of the 2015 scan data set where the PH_{norm} requirement is used instead of the PID system. Right: estimation of the systematic uncertainty due to the difference in efficiency in data and MC simulation calculated according to equation 10.5 for the same CM energy points.

As mentioned above, the PID system is not used for CM energy points below 2.175 GeV in the main analysis, since the low momentum of the tracks at these energies can cause problems for the PID system. Instead, a direct requirement on the normalised pulse heights of the dE/dx measurement is imposed, a more detailed description can

be found in section 6.1.1. The systematic uncertainty due to the differences in data and MC in the efficiency of this requirement is investigated in the same way as for the PID requirement described above. The signal process $e^+e^- \to p\bar{p}$ is selected using the PH_{norm} requirement only on the negative (positive) track to study the systematic uncertainty from the requirement for the proton (antiproton), with the same tightened requirements as in the PID efficiency study. Similar to the PID study, the background level with these requirements is very low, as can be seen in the momentum distributions of proton and antiproton in figures C.5 and C.6 of appendix C, respectively. The PH_{norm} efficiency calculated according to equation 10.2 is then compared for data and a signal MC sample, which allows to calculate the corresponding systematic uncertainty using equation 10.5.

The comparison of the PH_{norm} efficiency between data and MC as well as the systematic uncertainty due to the differences between the two can be seen in figure 10.7 for the 5 CM energies below 2.175 GeV. Once again, the total uncertainty is calculated by linearly summing up the uncertainty for the proton and the antiproton, which are estimated as the individual uncertainties at each CM energy plus one standard deviation.

10.1.4 Uncertainty due to E/p requirement

The uncertainty due to data and MC differences in the efficiency of the E/p requirement is determined in the same way as described for the PID and PH_{norm} efficiency in the last section. The signal process $e^+e^- \to p\bar{p}$ is selected by applying the same stricter selection criteria as in the PID efficiency study, without applying the E/p requirement at first.

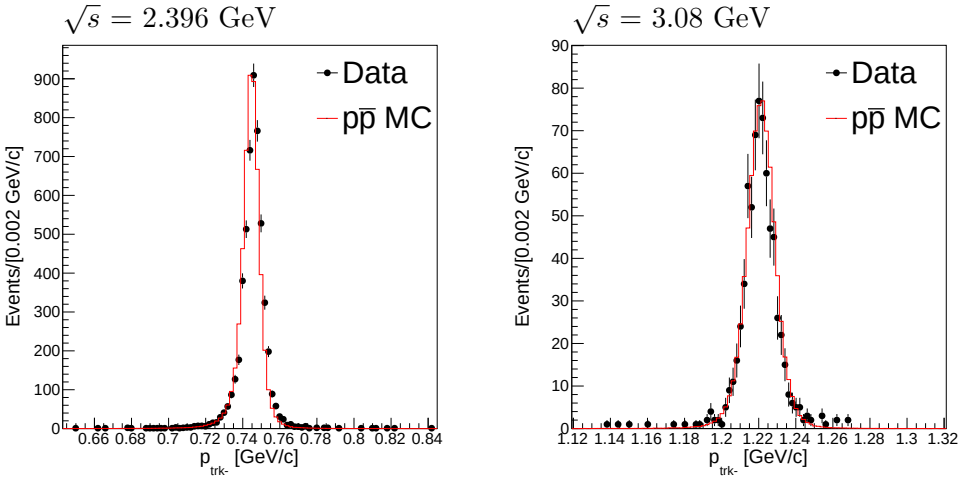

FIGURE 10.8: Momentum distribution of the proton for two exemplary CM energies of 2.396 GeV (left) and 3.08 GeV (right) of data (black points with error bars) compared with signal MC (red line). Compared to the main analysis, no E/p requirement has been applied while a number of other requirements have been tightened (see text).

Again, the tightened selection criteria result in a very low background pollution of the signal process even without the E/p requirement, although with a lower signal efficiency, as can be seen in figure 10.8 for two sample CM energies of 2.396 and 3.08 GeV and in appendix C in figure C.7 for all other CM energies. The E/p efficiency is then calculated according to equation 10.2 for data and a signal MC sample, the difference between the two allows an estimation of the corresponding systematic error according to equation 10.5.

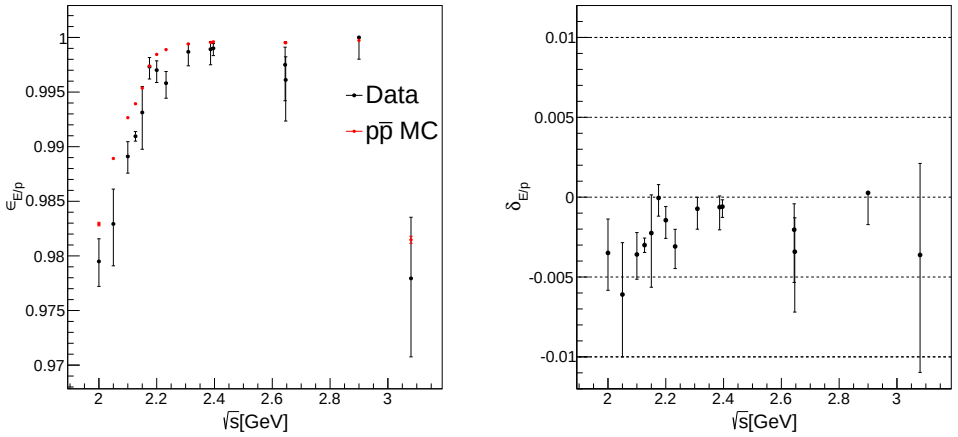

FIGURE 10.9: Left: comparison between the E/p efficiency of data (black dots with error bars) and MC (red dots with error bars) calculated according to equation 10.2 at CM energies of the 2015 scan data set with enough events remaining after the modified event selection. Note that the E/p requirement is only used for CM energies above 2.15 GeV, lower CM energies are still shown here for reference. Right: estimation of the systematic uncertainty due to the difference of efficiency in data and MC simulation calculated according to equation 10.5 for the same CM energy points.

The comparison is performed for all CM energy points of the 2015 scan data set with enough events surviving the selection, which is the case for all energy points except for 2.5 GeV, 2.7 GeV, 2.8 GeV and the four energy points between 2.95 GeV and 3.02 GeV. As in the case of the PID efficiency study, the uncertainty at these seven energy points is assumed to be the same as at the closest CM energy where it can be determined. At the five CM energies below 2.175 GeV, no E/p requirement is imposed in the main analysis, therefore no systematic uncertainty associated with the efficiency of the E/p cut is assigned to the Born cross section results in this energy range. The comparison between the data and MC E/p efficiency as well as the corresponding systematic uncertainty is still shown for all energy points (with sufficiently high amount of events) in figure 10.9 for reference. For CM energies above 2.15 GeV, the systematic uncertainty is once again estimated by adding one standard deviation to the value extracted according to equation 10.5.

10.1.5 Uncertainty due to remaining background

Although the background level in data after applying the event selection criteria of section 6.1 is very low, as is demonstrated in chapter 7, a small amount of background events may still remain and distort the result for the Born cross section with an increased event count. To estimate the systematic uncertainty associated with these background events, the two-dimensional sideband method is used once again, a detailed description of this method can be found in section 7.3. In short, the method estimates the background in a sample by investigating the two-dimensional distribution of the proton and antiproton momentum. A total of eight equally sized sideband regions are defined around the signal momentum window in this distribution. The total background in the signal region is then estimated by subtracting half of the sum of events in the boxes diagonally to the signal region (N_{corner}) from the sum of events in the boxes next to the signal region (N_{side}): $N_{bkg} = 0.5 \cdot (N_{side} - 0.5 \cdot N_{corner})$.

As shown in section 7.3, the amount of background events determined with the sideband method is similar for data samples and signal MC samples including radiative corrections up to NNLO at most CM energies of the 2015 scan data set. The reasons for this are discussed in detail section 7.3, mostly the overestimation of background comes from outlier signal events with a momentum measurement far from the theoretical momentum, or from ISR events, which both result in signal events within the sideband region. To avoid an overestimation of the systematic uncertainty from remaining background due to these effects, the following procedure is used to determine the uncertainty: first, the amount of background events is calculated with the sideband method for the data sample ($N_{bkg,data}$) as well as the signal MC sample ($N_{bkg,MC}$) that is used to determine the MC efficiency at each CM energy. $N_{bkg,data}$ is then subtracted from the selected events of each data sample. A "background" corrected MC efficiency is determined using a modified equation 8.1:

$$\epsilon_{MC,bkg} = \frac{N_{sel,MC} - N_{bkg,MC}}{N_{gen}^{MC}}. \tag{10.8}$$

After both the number of selected data events and the MC efficiency have been corrected for background, they are used to calculate the Born cross section of $e^+e^- \to p\bar{p}$ according to equation 8.2. The difference to the nominal Born cross section without background subtraction is then taken as the systematic uncertainty due to remaining background.

TABLE 10.2: Summary of the systematic uncertainties considered in the measurement of $\sigma(e^+e^- \to p\bar{p}$ from all sources as well as the total systematic uncertainty calculated according to equation 10.1 for all CM energy points of the 2015 scan data set.

E_{cm} [GeV]	δ^{σ}_{trk} [%]	δ^{σ}_{PID} [%]	$\delta^{\sigma}_{E/p}$ [%]	δ^{σ}_{sel} [%]	δ^{σ}_{bkg} [%]	δ^{σ}_{lum} [%]	δ^{σ}_{tun} [%]	δ^{σ}_{mod} [%]	$\delta^{\sigma}_{sys,tot}$ [%]
2	2	0.78	-	0.28	0.16	0.67	0.14	3.19	3.92
2.05	2	0.55	-	0.77	0.15	0.81	0.18	0.82	2.51
2.1	2	0.13	-	0.27	0.08	0.70	0.05	0.28	2.16
2.12655	2	0.06	-	0.13	0.03	0.89	0.11	0.51	2.25
2.15	2	0.44	-	0.57	0.23	0.85	0.05	0.19	2.31
2.175	2	1.67	0.12	0.35	0.25	0.86	0.03	0.53	2.83
2.2	2	1.53	0.26	0.24	0.02	0.67	0.08	1.10	2.85
2.2324	2	1.03	0.45	0.14	0.3	0.62	0.19	2.10	3.19
2.3094	2	0.68	0.2	0.61	0.53	0.68	0.23	2.29	3.31
2.3864	2	0.56	0.2	0.34	0	0.78	0.00	1.03	2.48
2.396	2	0.30	0.13	0.51	0.09	0.71	0.02	0.91	2.39
2.5	2	0.30	0.13	2.53	1.09	0.84	0.03	0.07	3.52
2.6444	2	0.40	0.53	0.96	0.32	0.64	0.02	0.14	2.43
2.6464	2	1.34	0.72	1.26	0.03	0.83	0.05	0.28	2.94
2.7	2	1.34	0.72	4.37	0.84	0.70	0.04	0.50	5.18
2.8	2	1.39	0.17	2.23	4.82	0.59	0.01	1.59	6.09
2.9	2	1.39	0.17	0.68	0.14	0.86	0.18	0.86	2.82
2.95	2	1.39	0.17	2.09	0.08	0.90	0.25	0.29	3.36
2.981	2	1.39	0.17	2.78	0.81	0.59	0.39	0.27	3.86
3	2	1.23	1.1	2.13	0.74	0.70	0.32	0.11	3.52
3.02	2	1.23	1.1	0.54	0.74	0.71	0.39	0.32	2.88
3.08	2	1.23	1.1	0.97	0.92	0.60	0.18	0.28	3.00

10.1.6 Uncertainty due to the form factor model in Monte Carlo Simulation

The characteristics of the signal MC samples that are used to determine efficiency and radiative corrections depend on the FF model used in the MC generator. Therefore, an iterative tuning procedure is used in this analysis (details see section 9.4) to extract results unbiased from previous measurements. However, the choice of model that is used during the tuning procedure to fit the FFs extracted in this work influences the results and can therefore introduce a systematic uncertainty. Since the default model built into Phokhara, which is based on a fit to previous results for the EM FFs of the proton, already describes the new FF results extracted in this work reasonably well, this uncertainty was simply estimated by comparing the Born cross section results extracted with MC samples of the last round of tuning with the cross section extracted with MC samples of the default Phokhara model. The difference between the two was taken as the systematic error due to the FF model.

10.1.7 Uncertainty from the luminosity measurement

The Luminosity of the 2015 scan data set is determined using large angle Bhabha scattering events, a well understood QED process where the cross section can be calculated exactly. The luminosity and its error is quoted from [157] for all data points except the one at 2.12655 GeV, which is quoted from [163]. The uncertainty quoted within these references is taken as the systematic uncertainty due to the luminosity measurement.

TABLE 10.3: Summary of the systematic uncertainties considered in the measurement of the effective FF $|G|$ from all sources as well as the total systematic uncertainty calculated according to equation 10.1 for all CM energy points of the 2015 scan data set.

E_{cm} [GeV]	$\delta^{\|G\|}_{trk}$ [%]	$\delta^{\|G\|}_{PID}$ [%]	$\delta^{\|G\|}_{E/p}$ [%]	$\delta^{\|G\|}_{sel}$ [%]	$\delta^{\|G\|}_{bkg}$ [%]	$\delta^{\|G\|}_{lum}$ [%]	$\delta^{\|G\|}_{tun}$ [%]	$\delta^{\|G\|}_{mod}$ [%]	$\delta^{\|G\|}_{sys,tot}$ [%]
2	1	0.39	-	0.14	0.08	0.34	0.07	1.60	1.96
2.05	1	0.27	-	0.39	0.08	0.41	0.09	0.41	1.25
2.1	1	0.07	-	0.13	0.04	0.35	0.02	0.14	1.08
2.12655	1	0.03	-	0.07	0.01	0.45	0.05	0.25	1.13
2.15	1	0.22	-	0.28	0.11	0.43	0.02	0.10	1.15
2.175	1	0.83	0.06	0.18	0.13	0.43	0.01	0.26	1.41
2.2	1	0.77	0.13	0.12	0.01	0.34	0.04	0.55	1.43
2.2324	1	0.52	0.22	0.07	0.15	0.31	0.10	1.05	1.60
2.3094	1	0.34	0.10	0.30	0.26	0.34	0.12	1.15	1.65
2.3864	1	0.28	0.10	0.17	0.00	0.39	0.00	0.52	1.24
2.396	1	0.15	0.06	0.25	0.05	0.36	0.01	0.46	1.19
2.5	1	0.15	0.06	1.26	0.55	0.42	0.02	0.03	1.76
2.6444	1	0.20	0.27	0.48	0.16	0.32	0.01	0.07	1.21
2.6464	1	0.67	0.36	0.63	0.01	0.42	0.03	0.14	1.47
2.7	1	0.67	0.36	2.18	0.42	0.35	0.02	0.25	2.59
2.8	1	0.70	0.09	1.12	2.41	0.30	0.00	0.80	3.04
2.9	1	0.70	0.09	0.34	0.07	0.43	0.09	0.43	1.41
2.95	1	0.70	0.09	1.04	0.04	0.45	0.13	0.14	1.68
2.981	1	0.70	0.09	1.39	0.40	0.30	0.19	0.14	1.93
3	1	0.61	0.55	1.07	0.37	0.35	0.16	0.06	1.76
3.02	1	0.61	0.55	0.27	0.37	0.36	0.19	0.16	1.44
3.08	1	0.61	0.55	0.48	0.46	0.30	0.09	0.14	1.50

10.1.8 Uncertainty from the Monte Carlo tuning procedure

To estimate the systematic uncertainty from the iterative tuning procedure for the Born cross section measurement, the extracted cross section using the MC from the last and the second last tuning iteration are compared. The difference in results is taken as a systematic uncertainty.

10.1.9 Summary of the systematic uncertainties in the cross section measurement

The size of the individual uncertainties from each source as well as the total systematic uncertainty of the cross section measurement is shown in table 10.2 for all CM energies of the 2015 scan data set.

10.2 Systematic uncertainty in the effective form factor measurement

The effective FF $|G|$ of the proton can be calculated from the Born cross section of the process $e^+e^- \to p\bar{p}$ using equation 8.4. None of the quantities in this equation except for the cross section is considered to have relevant systematic uncertainties associated with them. Therefore, the same sources of systematic uncertainty apply to both the cross section and the effective FF measurement, and the same methods as described in the sections above can be used to estimate them. The size of the individual uncertainties from each source as well as the total systematic uncertainty of the effective FF measurement is shown in table 10.3.

10.3 Systematic uncertainty in the form factor measurement

The considered systematic uncertainties for the measurement of the EM FFs of the proton include the uncertainty from efficiency differences between data and MC for tracking, PID or PH_{norm}, and the E/p selection criterion, from the other selection criteria, from remaining background pollution, from the asymmetry in the $\cos\theta_p^{CM}$ distributions, from the luminosity measurement, from the tuning procedure, and from the FF model used in the MC simulations for efficiency and radiative corrections. The uncertainty from the luminosity measurement only plays a role for the individual determination of $|G_E|$ and $|G_M|$, not for their ratio R. The individual contributions will be estimated based on methods described in the next sections, most of them similar to those described in section 10.1 for the cross section and effective FF measurement. The total uncertainty for the FFs $|G_E|$ and $|G_M|$ is calculated in the same way as for the cross section measurement, by assuming the individual contributions to be uncorrelated and summing them up in quadrature:

$$\delta_{sys,G_E,G_M} = \sqrt{\delta^2_{eff} + \delta^2_{sel} + \delta^2_{asym} + \delta^2_{bkg} + \delta^2_{lum} + \delta^2_{tun} + \delta^2_{mod}}, \tag{10.9}$$

with $\delta_{eff}, \delta_{sel}, \delta_{bkg}, \delta_{asym}, \delta_{lum}, \delta_{tun}, \delta_{mod}$ as the uncertainties from data and MC differences in the efficiency, selection criteria, background, asymmetry in the $\cos\theta_p^{CM}$ distributions, luminosity, tuning and the FF model, respectively. The uncertainty for the ratio R is calculated with the same formula, 10.9, except for the luminosity contribution which is cancelled out in the ratio.

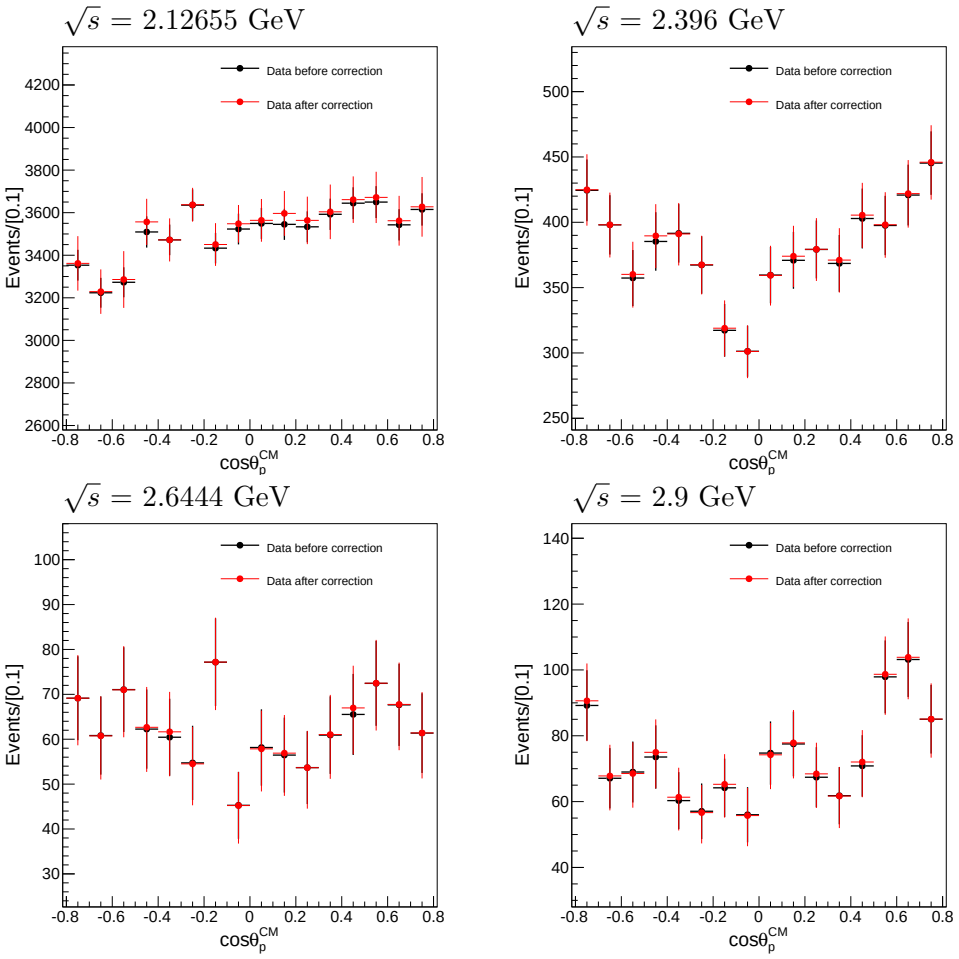

FIGURE 10.10: Efficiency corrected distributions of data in $\cos\theta_p^{CM}$ before (black dots with error bars) and after (red dots with error bars) correcting for efficiency differences in tracking, PID (or PH_{norm}) and E/p selection criteria between data and MC for exemplary CM energies of 2.12655 GeV, 2.396 GeV, 2.6444 GeV and 2.9 GeV.

10.3.1 Uncertainty due to efficiency differences between data and Monte Carlo simulation

The difference between data and MC in the efficiency of tracking, PID (or PH_{norm}) and E/p selection criteria described in sections 10.1.1, 10.1.3 and 10.1.4 also affects the

measurement of the proton EM FFs. The associated systematic uncertainty for the FF measurement estimated for all three sources (tracking, PID or PH_{norm}, and E/p) at once by applying additional correction histograms to the efficiency corrected $\cos\theta_p^{CM}$ distributions, before they are fit to extract the FFs. These histograms are obtained in the corresponding efficiency studies described in sections 10.1.1, 10.1.3 and 10.1.4 by comparing the differential efficiencies of data ($\epsilon_i^{Data}(\cos\theta_p^{CM})$) to those obtained from MC ($\epsilon_i^{MC}(\cos\theta_p^{CM})$) separately for proton and antiproton. The correction histograms for each of these 3 categories, H_i^{corr}, are then extracted by:

$$H_i^{corr} = \frac{\epsilon_i^{Data}(\cos\theta_p^{CM})}{\epsilon_i^{MC}(\cos\theta_p^{CM})}, \tag{10.10}$$

with i=PID, tracking, E/p. The total correction histogram for the proton and antiproton is obtained by multiplying the corresponding three individual histograms. A comparison of the data distributions in $\cos\theta_p^{CM}$ before and after the full correction histograms have been applied can be seen in figure 10.10 for exemplary CM energies. Comparisons of all other CM energies used in the extraction of the EM FFs as well as the comparison for the individual tracking, PID (or PH_{norm}) and E/p corrections are shown in section C.2.1 of appendix C.
Once these corrections have been applied, the EM FFs G_E and G_M as well as their ratio R are extracted as described in section 9.2.1. The difference to the nominal results is taken as the total systematic uncertainty due to data and MC differences in the efficiency.

10.3.2 Uncertainty due to selection criteria

The uncertainty due to the chosen thresholds for the selection criteria is estimated in the same way for the extraction of the FFs and the cross section. Details to the changed thresholds for each selection criterion can be found in the corresponding section for the systematic uncertainty of the cross section, section 10.1.2.

After the changed selection criterion has been applied, the corresponding systematic error for it is estimated by comparing the FFs $|G_E|$, $|G_M|$ and their ratio R extracted with the standard criteria and the modified criteria. The difference between the two is assigned as the systematic error, the total uncertainty due to the selection criteria is then calculated by summing up the contributions of each criterion in quadrature according to equation 10.7.
The extracted systematic uncertainties for the three evaluated selection criteria as well as the total uncertainty is summarised in table 10.4 for the $|G_E|$ and $|G_M|$ measurement and in table 10.5 for the measurement of their ratio R.

TABLE 10.4: Systematic uncertainty of $|G_M|$ and $|G_E|$ for the TOF ($\delta^{G_M}_{TOF}$, $\delta^{G_E}_{TOF}$), the back-to-back angle ($\delta^{G_M}_{ang}$, $\delta^{G_E}_{ang}$) and the momentum window ($\delta^{G_M}_{mom}$, $\delta^{G_E}_{mom}$) selection criteria as well as the total systematic uncertainty from the selection ($\delta^{G_M}_{sel}$, $\delta^{G_M}_{sel}$) for all CM energy points of the 2015 scan data set where the FFs are extracted.

E_{cm} [GeV]	$\delta^{G_M}_{TOF}$ [%]	$\delta^{G_M}_{ang}$ [%]	$\delta^{G_M}_{mom}$ [%]	$\delta^{G_M}_{sel}$ [%]	$\delta^{G_E}_{TOF}$ [%]	$\delta^{G_E}_{ang}$ [%]	$\delta^{G_E}_{mom}$ [%]	$\delta^{G_E}_{sel}$ [%]
2	0.31	0.43	0.23	0.58	0.17	0.29	0.44	0.55
2.05	0.31	0.07	0.95	1.00	0.34	0.13	0.87	0.94
2.1	0.15	0.16	0.57	0.61	0.15	0.39	0.68	0.80
2.12655	0.06	0.15	0.15	0.23	0.08	0.20	0.08	0.23
2.15	0.24	1.14	0.59	1.31	0.28	0.76	0.48	0.94
2.175	0.15	0.14	0.59	0.63	0.36	0.18	0.78	0.88
2.2	0.08	0.20	0.36	0.42	0.13	0.40	0.96	1.05
2.2324	0.02	0.50	0.44	0.67	0.05	1.50	0.83	1.72
2.3094	0.03	0.20	0.25	0.32	0.96	1.46	2.62	3.15
2.3864	0.27	0.52	0.76	0.96	1.56	3.12	6.65	7.51
2.396	0.05	0.19	0.32	0.38	0.30	0.70	0.47	0.89
2.6444	0.02	0.46	0.69	0.83	0.01	1.87	1.02	2.12
2.6464	0.40	0.55	1.80	1.93	1.30	1.92	5.42	5.90
2.9	0.30	0.93	0.70	1.20	2.45	6.57	7.97	10.61
2.98839	2.02	2.80	2.87	4.49	3.07	5.89	7.80	10.24
3.08	0.01	0.41	0.37	0.55	0.08	7.03	5.57	8.97

TABLE 10.5: Systematic uncertainty of the FF ratio R for the TOF (δ^{R}_{TOF}), the back-to-back angle (δ^{R}_{ang}) and the momentum window (δ^{R}_{mom}) selection criteria as well as the total systematic uncertainty from the selection (δ^{R}_{sel}) for all CM energy points of the 2015 scan data set where the FFs are extracted.

E_{cm} [GeV]	δ^{R}_{TOF} [%]	δ^{R}_{ang} [%]	δ^{R}_{mom} [%]	δ^{R}_{sel} [%]
2	0.47	0.72	0.66	1.09
2.05	0.64	0.20	1.83	1.95
2.1	0.30	0.55	1.26	1.41
2.12655	0.14	0.36	0.21	0.44
2.15	0.52	1.78	1.06	2.13
2.175	0.51	0.32	1.37	1.49
2.2	0.21	0.60	1.33	1.47
2.2324	0.07	2.02	1.27	2.38
2.3094	1.00	1.66	2.88	3.47
2.3864	1.82	3.49	7.36	8.35
2.396	0.34	0.88	0.80	1.24
2.6444	0.03	2.33	1.49	2.77
2.6464	1.69	2.33	7.36	7.90
2.9	2.77	7.57	8.59	11.78
2.98839	1.07	4.51	7.28	8.63
3.08	0.08	7.47	5.95	9.55

10.3.3 Uncertainty due to remaining background

To ascertain the systematic uncertainty due to remaining background events for the FF extraction, the two-dimensional sideband method is used again as described for the cross section measurement in section 10.1.5. In the case of the FF measurement, the remaining background is evaluated in bins of $\cos\theta_p^{CM}$ for both data and MC.

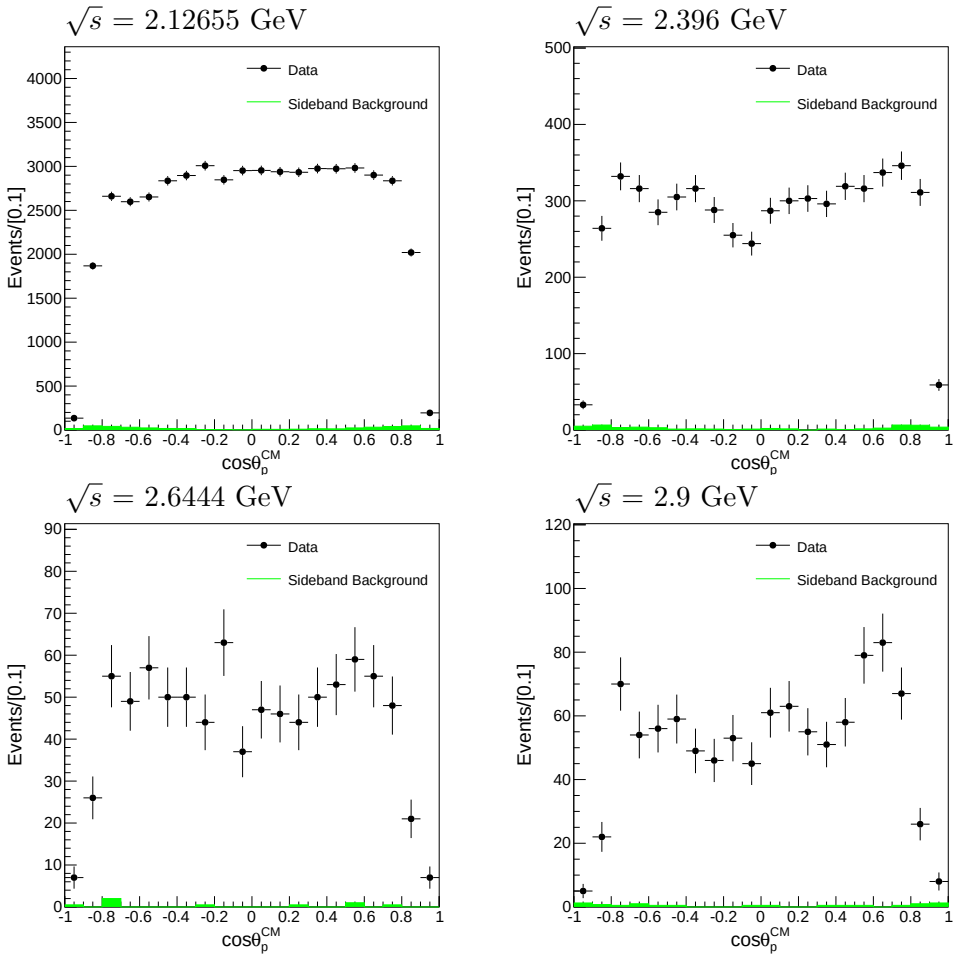

FIGURE 10.11: Distributions of data in $\cos\theta_p^{CM}$ before efficiency correction (black dots with error bars) with the distribution of remaining background events extracted with the two-dimensional sideband method in $\cos\theta_p^{CM}$ (green histogram) for example CM energies of 2.12655, 2.396, 2.6444 and 2.9 GeV.

A comparison between the $\cos\theta_p^{CM}$ distributions of selected data before efficiency correction and the background obtained from the two-dimensional sideband method can be seen in figure 10.11 for exemplary CM energies and in figure C.12 of appendix C for all other CM energies used for the FF extraction.

The background histograms obtained from data are then subtracted from the $\cos\theta_p^{CM}$ distribution of each data sample. Simultaneously, the "background" histogram obtained with the sideband method from signal MC is subtracted from each MC sample before the

MC efficiency is determined. After these corrections are applied, the EM FFs $|G_E|$ and $|G_M|$ as well as their ratio R are extracted as described in section 9.2.1. The difference in results between the FFs and their ratio before and after this background subtraction is taken as the systematic uncertainty due to remaining background.

10.3.4 Uncertainty due to the form factor model in Monte Carlo simulation

The systematic uncertainty due to the FF model used in the generation of the signal MC can be estimated in the same way as for the Born cross section measurement. The EM FFs and their ratio extracted with the MC samples of the final round of MC tuning are compared to those extracted using MC samples with the default built-in model of the Phokhara event generator. The difference between the two results is assigned as the systematic error due to the FF model.

TABLE 10.6: Summary of the systematic uncertainties considered in the measurement of the FF ratio R from all sources as well as the total systematic uncertainty calculated according to equation 10.9 for all CM energy points of the 2015 scan data set where an angular analysis can be performed, as well as the combined sample at 2.98839 GeV.

E_{cm} [GeV]	δ^R_{eff} [%]	δ^R_{sel} [%]	δ^R_{bkg} [%]	δ^R_{tun} [%]	δ^R_{mod} [%]	δ^R_{asym} [%]	$\delta^R_{sys,tot}$ [%]
2	0.17	1.09	0.05	1.71	0.19	0.77	2.19
2.05	2.18	1.95	0.18	0.23	0.61	1.28	3.26
2.1	1.01	1.41	0.54	0.27	0.60	0.53	2.00
2.12655	0.95	0.44	0.18	0.62	0.04	0.44	1.31
2.15	0.69	2.13	0.46	0.25	0.56	0.36	2.40
2.175	0.69	1.49	0.34	0.06	0.00	0.68	1.82
2.2	1.36	1.47	0.01	0.55	1.60	0.45	2.66
2.2324	0.37	2.38	1.89	0.90	1.02	0.32	3.37
2.3094	0.65	3.47	1.85	0.86	2.28	0.63	4.71
2.3864	3.71	8.35	0.33	0.57	0.05	2.97	9.63
2.396	0.53	1.24	0.38	0.01	0.25	1.39	1.99
2.6444	1.78	2.77	1.52	0.08	0.55	2.95	4.70
2.6464	6.71	7.90	0.00	0.70	0.05	3.43	10.94
2.9	5.43	11.78	1.84	2.04	1.06	5.87	14.54
2.98839	2.23	8.63	2.29	0.98	0.19	1.02	9.31
3.08	2.64	9.55	0.09	2.27	5.12	0.51	11.39

10.3.5 Uncertainty from the luminosity measurement

As already mentioned, the luminosity measurement and its uncertainty only plays a role in the individual measurements of $|G_E|$ and $|G_M|$, while it cancels out in the determination of their ratio. For the $|G_E|$ and $|G_M|$ measurements, the same source as for the

cross section measurement is quoted for 2.12655 GeV [163] and for all other CM energy points [157].

TABLE 10.7: Summary of the systematic uncertainties considered in the measurement of $|G_M|$ from all sources as well as the total systematic uncertainty calculated according to equation 10.9 for all CM energy points of the 2015 scan data set where an angular analysis can be performed, as well as the combined sample at 2.98839 GeV.

E_{cm} [GeV]	$\delta^{G_M}_{eff}$ [%]	$\delta^{G_M}_{sel}$ [%]	$\delta^{G_M}_{bkg}$ [%]	$\delta^{G_M}_{lum}$ [%]	$\delta^{G_M}_{tun}$ [%]	$\delta^{G_M}_{mod}$ [%]	$\delta^{G_M}_{asym}$ [%]	$\delta^{G_m}_{sys,tot}$ [%]
2	0.46	0.58	0.14	0.33	0.97	0.14	0.49	1.37
2.05	0.69	1.00	0.06	0.41	0.09	0.46	0.77	1.57
2.1	0.17	0.61	0.19	0.35	0.20	0.03	0.07	0.78
2.12655	0.14	0.23	0.07	0.45	0.20	0.28	0.24	0.67
2.15	0.35	1.31	0.36	0.43	0.14	0.50	0.47	1.62
2.175	0.27	0.63	0.20	0.43	0.01	0.01	0.07	0.83
2.2	0.64	0.42	0.01	0.34	0.21	0.69	0.00	1.10
2.2324	0.30	0.67	0.61	0.31	0.26	0.64	0.20	1.23
2.3094	0.22	0.32	0.51	0.34	0.05	0.06	0.22	0.76
2.3864	0.32	0.96	0.04	0.39	0.07	0.06	0.06	1.09
2.396	0.25	0.38	0.18	0.36	0.01	0.00	0.15	0.62
2.6444	0.19	0.83	0.40	0.32	0.01	0.07	0.42	1.08
2.6464	1.50	1.93	0.02	0.42	0.18	0.25	1.28	2.81
2.9	0.59	1.20	0.11	0.43	0.21	0.08	1.28	1.92
2.98839	0.84	1.71	0.59	0.73	0.30	0.03	1.11	2.42
3.08	0.01	0.55	0.23	0.30	0.14	0.23	0.36	0.80

10.3.6 Uncertainty from the Monte Carlo tuning procedure

To estimate the systematic uncertainty from the iterative tuning procedure for the FF measurement, the extracted FFs and their ratio using the MC from the last and the second last tuning iteration are compared. The difference in results is taken as a systematic uncertainty.

10.3.7 Uncertainty due to the asymmetry in the angular distributions

The distributions of the proton and antiproton events in $\cos\theta_p^{CM}$ show a slight asymmetry (details see section 9.2.1). In the main analysis, this asymmetry was eliminated by fitting distributions of the absolute value $|\cos\theta_p^{CM}|$ instead. To account for any bias from this procedure, the difference between the FF results extracted by fitting $\cos\theta_p^{CM}$ and $|\cos\theta_p^{CM}|$ is taken as a systematic uncertainty.

10.3.8 Summary of the systematic uncertainties in the form factor measurement

The size of the individual uncertainties from each source as well as the total systematic uncertainty for the measurement of the FF ratio R and the individual FFs $|G_M|$ and $|G_E|$ are shown in tables 10.6, 10.7 and 10.8, respectively.

TABLE 10.8: Summary of the systematic uncertainties considered in the measurement of $|G_E|$ from all sources as well as the total systematic uncertainty calculated according to equation 10.9 for all CM energy points of the 2015 scan data set where an angular analysis can be performed, as well as the combined sample at 2.98839 GeV.

E_{cm} [GeV]	$\delta^{G_E}_{eff}$ [%]	$\delta^{G_E}_{sel}$ [%]	$\delta^{G_E}_{bkg}$ [%]	$\delta^{G_E}_{lum}$ [%]	$\delta^{G_E}_{tun}$ [%]	$\delta^{G_E}_{mod}$ [%]	$\delta^{G_E}_{asym}$ [%]	$\delta^{G_E}_{sys,tot}$ [%]
2	0.63	0.55	0.19	0.33	0.73	0.06	0.28	1.20
2.05	1.47	0.94	0.11	0.41	0.14	0.15	0.51	1.88
2.1	0.84	0.80	0.35	0.35	0.07	0.57	0.46	1.46
2.12655	0.81	0.23	0.11	0.45	0.42	0.32	0.20	1.12
2.15	0.34	0.94	0.10	0.43	0.11	0.07	0.11	1.10
2.175	0.42	0.88	0.14	0.43	0.05	0.00	0.62	1.24
2.2	0.73	1.05	0.02	0.34	0.34	0.90	0.45	1.69
2.2324	0.07	1.72	1.27	0.31	0.64	0.37	0.13	2.28
2.3094	0.43	3.15	1.34	0.34	0.81	2.22	0.85	4.28
2.3864	3.38	7.51	0.29	0.39	0.48	0.13	2.82	8.73
2.396	0.29	0.89	0.20	0.36	0.00	0.25	1.22	1.62
2.6444	1.58	2.12	1.12	0.32	0.06	0.62	2.44	3.83
2.6464	5.31	5.90	0.01	0.42	0.51	0.20	2.23	8.27
2.9	4.86	10.61	1.73	0.43	1.83	0.98	4.85	12.93
2.98839	1.82	6.00	1.67	0.73	0.69	0.16	0.09	6.57
3.08	2.19	8.97	0.32	0.30	2.10	4.85	0.90	10.69

Chapter 11

Final Results

The final results for the cross section of $e^+e^- \to p\bar{p}$, the proton effective FF, as well as the individual proton Sachs FFs $|G_E|$ and $|G_M|$ are presented and discussed in this chapter, including statistical and the total systematic uncertainties discussed in the last chapter. All results are the ones obtained after the final round of MC tuning described in section 9.4, whereas the results presented earlier in this work for the cross section and the effective FF are preliminary results obtained before this procedure.

11.1 Final results for the $e^+e^- \to p\bar{p}$ cross section and proton effective form factor

A summary of the final results for the measurement of the cross section of $e^+e^- \to p\bar{p}$ as well as the effective FF of the proton calculated according to equation 8.4 is shown in table 11.1. Both the statistical and the total systematic uncertainty as discussed in the last chapter are given. For the data points with high luminosity at low to intermediate CM energy (up to $\sim$ 2.4 GeV), especially at 2.12655 GeV, the uncertainty of both the cross section and the effective FF is dominated by the systematic uncertainty. The total uncertainty is around 2-4% for all data points except for those with low luminosity at 2.5 GeV, 2.7 GeV, 2.8 GeV and the 4 points between 2.95 and 3.02 GeV.

A comparison of the results for the cross section measurement of $e^+e^- \to p\bar{p}$ of this work to results of previous experiments can be seen in figure 11.1. The most important previous measurements that cover a wide kinematic range come from the ISR analysis of the BaBar experiment (see section 2.3.2 for an explanation of the method) as well as the untagged ISR analysis of the BESIII experiment. The results of this work agree well with both measurements, but with an improved precision (excluding the low luminosity

points of this work): considering the same energy region, there are the aforementioned $\sim$ 2-4% for this work compared to $\sim$7% at low CM energies up to $\sim$30 % for higher CM energies of BaBar, and $\sim$8-26 % for the ISR analysis of BESIII.

TABLE 11.1: Final results of the cross section measurement of $e^+e^- \to p\bar{p}$ and the effective FF of the proton including statistical and systematic uncertainties, as well as the quantities of selected events (N_{sel}), MC efficiency (ϵ_{MC}), radiative correction factor (1+δ), and integrated luminosity ($\mathcal{L}_{int}$) necessary to calculate them. Note that the uncertainty of ϵ_{MC} and (1+δ) is omitted due to its small size, but is considered in the calculation, while the uncertainty of $\mathcal{L}_{int}$ is treated as a systematic uncertainty in section 10.1.7.

E_{cm} [GeV]	N_{sel}	ϵ_{MC}	(1+δ)	$\mathcal{L}_{int}$ [pb^{-1}]	$\sigma_{p\bar{p}}$ [pb]	$\lvert G\rvert$ [10^{-2}]
2	5296 ± 73	0.66	0.96	10.074	828± 11 ± 32	27.67 ± 0.19 ± 0.54
2.05	1693 ± 41	0.70	0.99	3.343	729 ± 18 ± 18	24.85 ± 0.30 ± 0.31
2.1	5988 ± 77	0.70	1.03	12.167	686.6 ± 8.9± 14.8	23.56 ± 0.15 ± 0.25
2.12655	50160 ± 224	0.69	1.06	108.49	631.4 ± 2.8 ± 14.2	22.43 ± 0.050± 0.25
2.15	1186 ± 34	0.68	1.08	2.841	565 ± 16 ± 13	21.13 ± 0.31 ± 0.24
2.175	3761 ± 61	0.67	1.11	10.625	473.2 ± 7.7 ± 13.4	19.28 ± 0.16 ± 0.27
2.2	4089 ± 64	0.66	1.14	13.699	398.0 ± 6.2 ± 11.3	17.65 ± 0.14 ± 0.25
2.2324	3643 ± 60	0.63	1.19	14.501	334.3 ± 5.5 ± 10.7	16.18 ± 0.13 ± 0.26
2.3094	2322 ± 48	0.58	1.27	21.089	148.0 ± 3.1 ± 4.9	10.83 ± 0.11 ± 0.18
2.3864	1849 ± 43	0.52	1.33	22.549	118.1 ± 2.7 ± 2.9	9.79 ± 0.11 ± 0.12
2.396	5512 ± 74	0.52	1.34	66.869	118.1 ± 1.6 ± 2.8	9.80 ± 0.07 ± 0.12
2.5	54 ± 7	0.48	1.40	1.098	73.5 ± 10.0 ± 2.6	7.91 ± 0.54 ± 0.14
2.6444	868 ± 29	0.40	1.66	33.722	38.40 ± 1.30 ± 0.93	5.92 ± 0.10 ± 0.07
2.6464	838 ± 29	0.40	1.66	34.003	36.9 ± 1.3 ± 1.1	5.81 ± 0.1 ± 0.09
2.7	20 ± 4	0.36	1.82	1.034	29.1 ± 6.5 ± 1.5	5.23 ± 0.58 ± 0.14
2.8	53 ± 7	0.31	2.12	4.761	17.0 ± 2.3 ±1.0	4.11 ± 0.28 ± 0.12
2.9	1010 ± 32	0.27	2.40	105.253	14.65 ± 0.46 ± 0.41	3.92 ± 0.06 ± 0.06
2.95	118 ± 11	0.26	2.55	15.942	11.31 ± 1.04 ± 0.38	3.50 ± 0.16 ± 0.06
2.981	132 ± 11	0.25	2.66	16.071	12.43 ± 1.08 ± 0.48	3.70 ± 0.16 ± 0.07
3	92 ± 10	0.24	2.73	15.881	8.78 ± 0.92 ± 0.31	3.12 ± 0.16 ± 0.05
3.02	97 ± 10	0.23	2.82	17.29	8.49 ± 0.86 ± 0.24	3.09 ± 0.16 ± 0.04
3.08	854 ± 29	0.20	3.15	157.204	8.48 ± 0.29 ± 0.25	3.14 ± 0.05 ± 0.05

While the ISR measurements have slightly more measurement points, the method leads to an uncertainty in the X ($\sqrt{s}$) direction due to the necessity to evaluate the cross section in intervals of the $p\bar{p}$ invariant mass in order to have enough statistics, whereas the energy uncertainty using the scan method is negligible in this work. Especially at high CM energies (see logarithmic plot, bottom of figure 11.1), this leads to a significantly higher uncertainty. However, due to the fewer measurement points of the scan data set, some possible structures seen in the ISR measurements, for example around 2.4 GeV as well as 2.7 GeV, can not be resolved well by the measurement presented in this work.

A comparison of the effective FF results to previous measurements is shown in figure 11.2, the results of this work are also summarised in table 11.1. Since the effective FF given in this work is directly calculated from the cross section according to the simple equation 8.4, the same discussion regarding the relative precision of this measurement

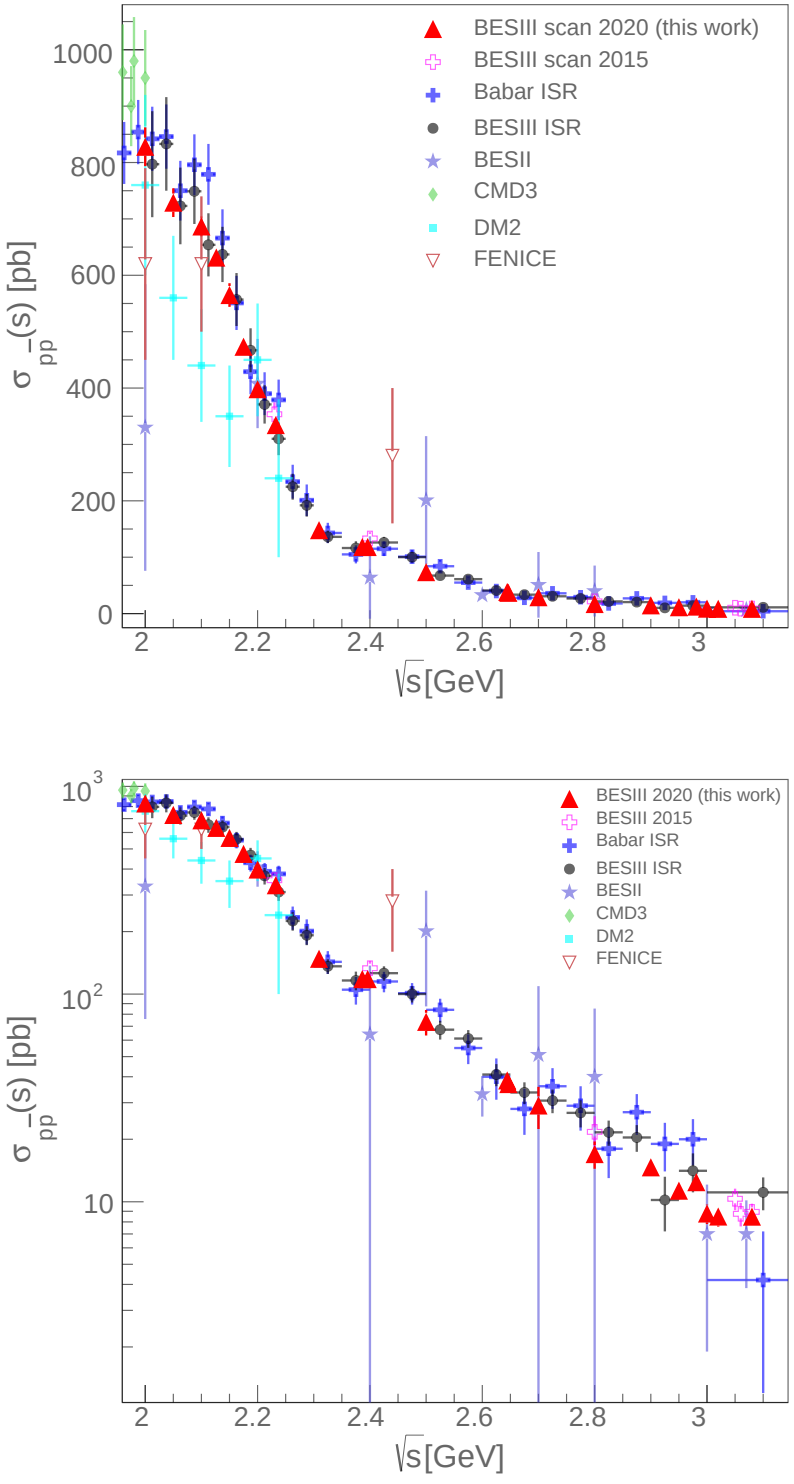

FIGURE 11.1: Comparison of the cross section of $e^+e^- \to p\bar{p}$ of this work to results from previous measurements, including statistical and systematic uncertainties added in quadrature, in linear (top) and logarithmic (bottom) scale. Shown are results from this work (red solid triangles), from previous BESIII scan (pink open crosses) [83] and ISR (black circles) [85] analysis, Babar (blue solid crosses) [84], BESII (purple stars) [73], CMD3 (green diamonds) [75], DM2 (turquoise squares) [67], and FENICE (brown open triangles) [72].

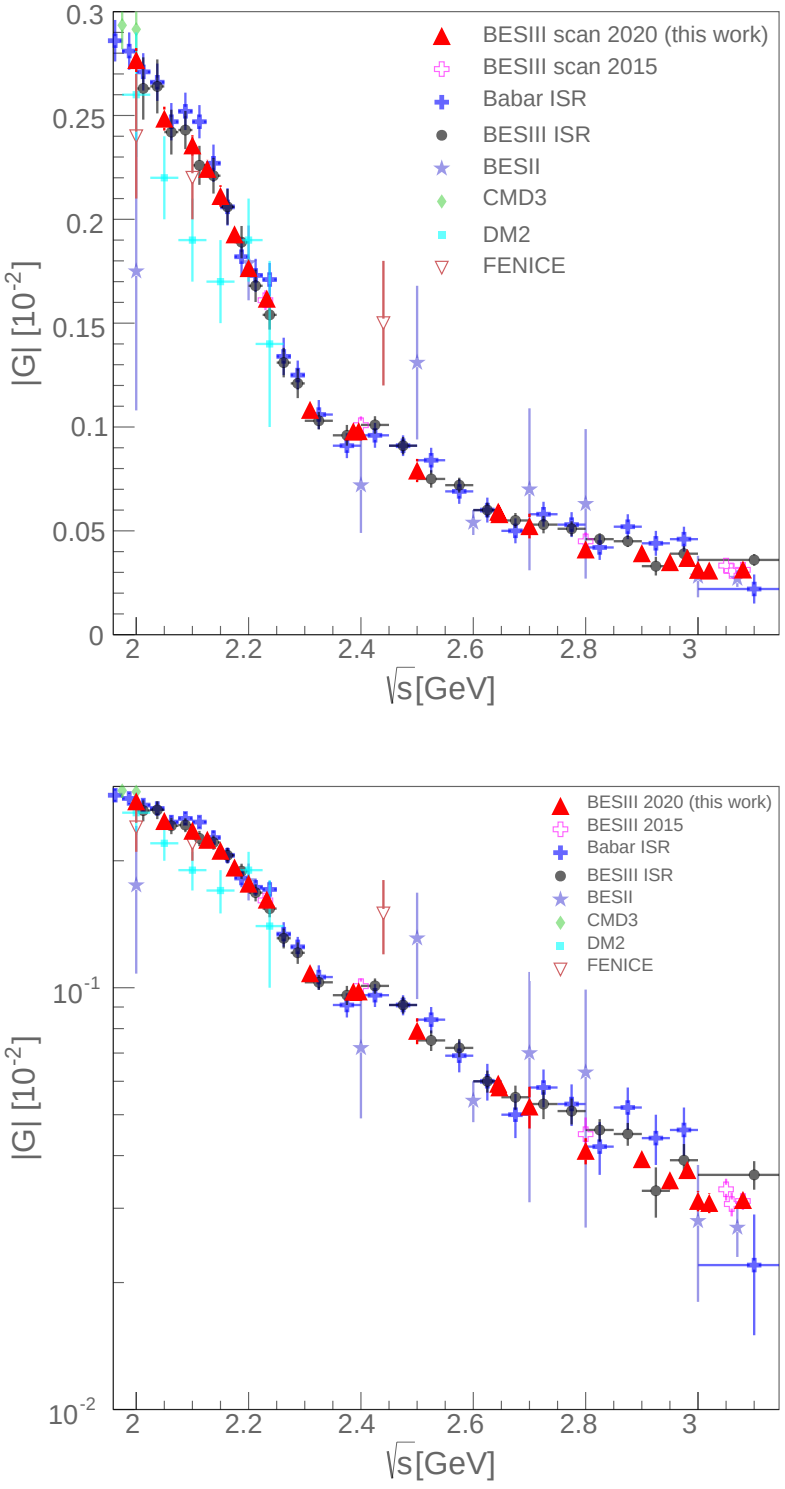

FIGURE 11.2: Comparison of the proton effective FF results calculated according to equation 8.4 of this work to results from previous measurements, including statistical and systematic uncertainties added in quadrature, in linear (top) and logarithmic (bottom) scale. Shown are results from this work (red solid triangles), from previous BESIII scan (pink open crosses) [83] and ISR (black circles) [85] analysis, Babar (blue solid crosses) [84], BESII (purple stars) [73], CMD3 (green diamonds) [75], DM2 (turquoise squares) [67], and FENICE (brown open triangles) [72]

.

compared to the previous measurements applies as given above for the cross section measurement.

11.2 Final results of the proton form factor measurement

The final results including statistical and systematic uncertainties for the electric and magnetic Sachs FFs, $|G_E|$ and $|G_M|$, as well as their ratio R, are summarised in table 11.2. The results are dominated by statistical uncertainty, the only exception being the electric FF measurement at the very high luminosity data point at 2.12655 GeV where they are of similar magnitude. The overall uncertainty (statistical and systematic uncertainty added in quadrature) ranges from 1.3% to 9.8% for the $|G_M|$ measurement, with most high luminosity energy points at an uncertainty of around 4%.

TABLE 11.2: Final results of this work for the electric and magnetic Sachs FFs $|G_E|$ and $|G_M|$, as well as their ratio R=$|G_E/G_M|$, including statistical and systematic uncertainties.

E_{cm} [GeV]	$\lvert G_E/G_M\rvert$	$\lvert G_M\rvert$ [10^{-2}]	$\lvert G_E\rvert$ [10^{-2}]
2	1.37 ± 0.10 ± 0.03	23.93 ± 0.94 ± 0.32	32.8 ± 1.2 ± 0.4
2.05	1.23 ± 0.16 ± 0.04	23.0 ± 1.4 ± 0.3	28.4 ± 2.0 ± 0.5
2.1	1.27 ± 0.087 ± 0.025	21.68 ± 0.70 ± 0.15	27.5 ± 1.0 ± 0.4
2.12655	1.198 ± 0.032 ± 0.016	21.09 ± 0.25 ± 0.11	25.26 ± 0.40 ± 0.26
2.15	1.66 ± 0.25 ± 0.04	16.9 ± 1.5 ± 0.3	28.0 ± 1.8 ± 0.3
2.175	1.21 ± 0.11 ± 0.02	18.14 ± 0.70 ± 0.13	21.9 ± 1.2 ± 0.3
2.2	1.08 ± 0.10 ± 0.03	17.26 ± 0.59 ± 0.18	18.7 ± 1.1 ± 0.3
2.2324	0.86 ± 0.10 ± 0.03	16.73 ± 0.54 ± 0.20	14.4 ± 1.3 ± 0.3
2.3094	0.60 ± 0.15 ± 0.03	11.83 ± 0.42 ± 0.08	7.0 ± 1.6 ± 0.3
2.3864	0.58 ± 0.18 ± 0.06	10.74 ± 0.42 ± 0.11	6.2 ± 1.7 ± 0.5
2.396	0.793 ± 0.093 ± 0.016	10.21 ± 0.25 ± 0.05	8.10 ± 0.76 ± 0.13
2.6444	1.00± 0.24 ± 0.05	5.85 ± 0.36 ± 0.06	5.8 ± 1.1 ± 0.2
2.6464	0.88 ± 0.26 ± 0.10	5.84 ± 0.36 ± 0.16	5.2 ± 1.2 ± 0.4
2.9	0.60 ± 0.31 ± 0.09	4.17 ± 0.21 ± 0.08	2.5 ± 1.2 ± 0.3
2.98839	1.05 ± 0.39 ± 0.10	3.24 ± 0.28 ± 0.15	3.4 ± 1.0 ± 0.4
3.08	0.51 ± 0.43 ± 0.06	3.35 ± 0.18 ± 0.02	1.7 ± 1.4 ± 0.2

For the $|G_E|$ measurement, the total uncertainty is between 1.9% and 83.2%, with rising uncertainties towards higher CM energies due to $|G_E|$ being suppressed by a factor of $1/\tau$ in equation 2.21. In addition, a low ratio $R = |G_E/G_M|$, as seen in the results of this work between 2.3 and 2.4 GeV as well as at 2.9 and 3.08 GeV, further reduces the achievable precision of $|G_E|$. The reason is the simultaneous extraction of $|G_E|$ and $|G_M|$ from one two-parameter fit, where a small R means a low contribution to

the overall shape of the angular distribution of events from $|G_E|$, which increases the relative uncertainty extracted from the fit.

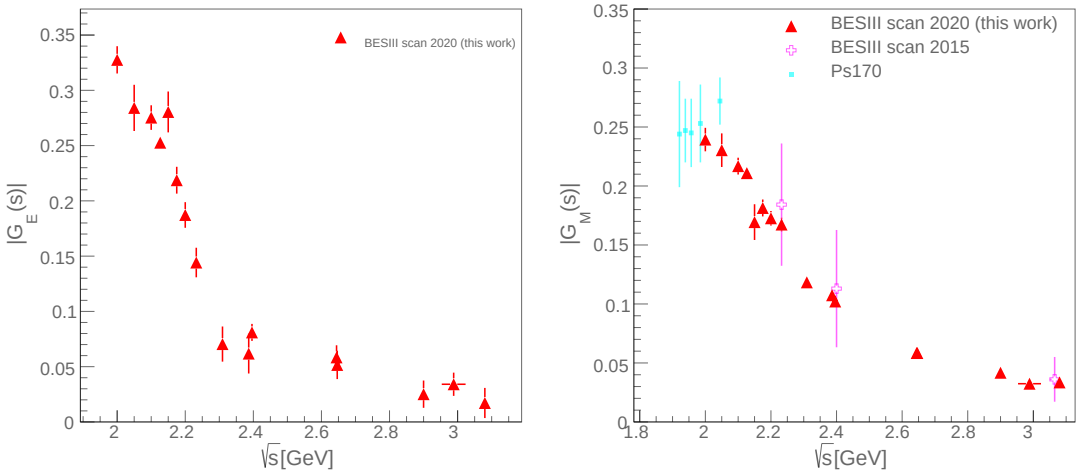

FIGURE 11.3: Left: Results of the electric FF $|G_E|$ of this work including statistical and systematic uncertainties added in quadrature. No previous measurements of $|G_E|$ are available for comparison. Right: Comparison of the magnetic FF $|G_M|$ of this work (red triangles) to results from the previous BESIII scan (pink open crosses) as well as the PS170 experiment (turquoise squares) including statistical and systematic uncertainties added in quadrature.

Finally, the precision of the measurement of the FF ratio $R = |G_E/G_M|$ lies between 3.0% and 85.1%, with the precision at higher CM energies and low values of R once again limited by the precision of $|G_E|$ for the reasons described above.

A comparison of the proton FF results of this work to previous measurements is shown in figure 11.3 for the individual FFs $|G_E|$ and $|G_M|$, as well as figure 11.4 for their ratio. In case of the individual FFs, few experiments have measured $|G_M|$ before this work, and none of them explicitly extracted $|G_E|$. Of course, the extraction of $|G_M|$ and simultaneously the ratio R, as done by PS170 and the previous BESIII scan, allows to calculate $|G_E|$ as well.

The magnetic FF measured by the previous BESIII scan agrees very well with the results of this work, albeit with only 3 measured points and significantly larger uncertainties. In addition, it is important to keep in mind that the previous BESIII scan measurement can only be seen as an independent measurement at 2.4 GeV, since the data at 2.2324 GeV and 3.08 GeV has been merged with the new scan data taken in 2015 to produce the results of this work (see section 4.2). Most of the data points of the PS170 measurement are at CM energies below those of the scan data set of this work. Of the two PS170 energy points in the same energy range, the one at lower energy agrees well with the measurement of this work, while the second disagrees on a level slightly outside of two standard deviations.

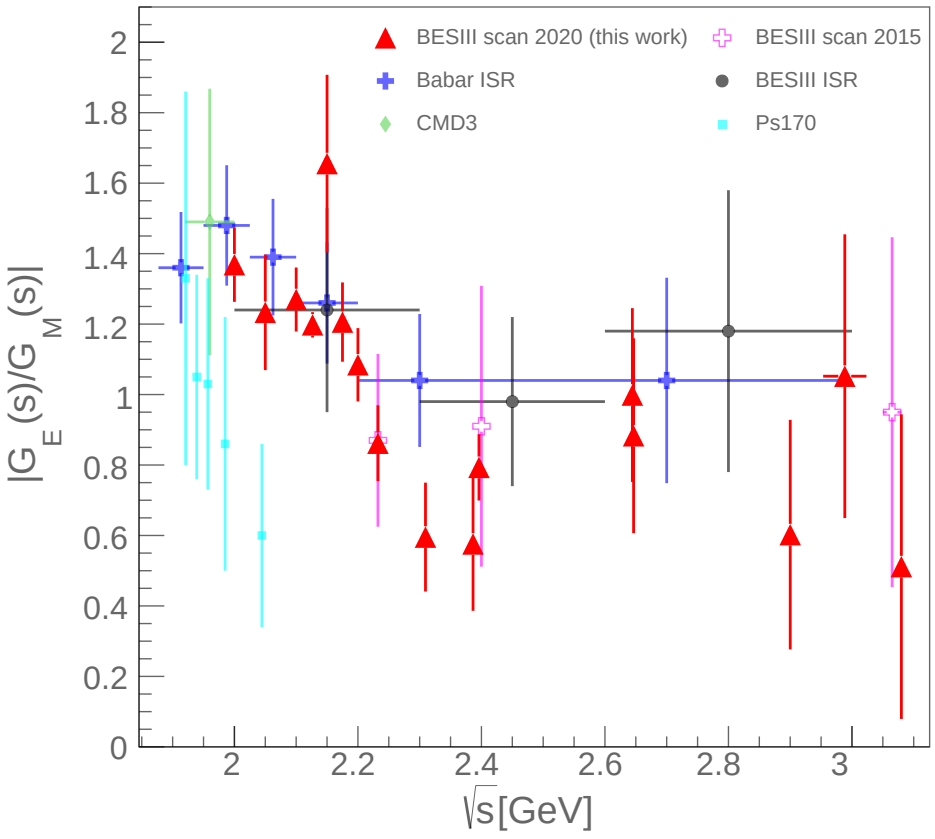

FIGURE 11.4: Comparison of the FF ratio $R = |G_E/G_M|$ of this work to results from previous measurements, including statistical and systematic uncertainties added in quadrature. Shown are results from this work (red solid triangles), previous BESIII scan (pink open crosses) and ISR (black circles) results, BaBar results (blue solid crosses), CMD3 results (green diamonds), and PS170 results (turquoise squares).

The comparison of the extracted FF ratio $R = |G_E/G_M|$ of this work to previous measurements in figure 11.4 shows a good agreement with the ISR measurements of BESIII and BaBar for low CM energies, clearly favouring them over the disagreeing PS170 measurement. The four scan points of this measurement between 2.2324 GeV and 2.396 GeV show a clear dip below a ratio of $R = 1$, which is not evident in the ISR measurements. However, due to the large uncertainties in both the ratio and the CM energy of the ISR measurements, no clear disagreement with the measurement of this work can be determined, all results lie within 2 standard deviations of the ISR measurements. At CM energies above 2.6 GeV, the R measurement of this work once again agrees with the ISR measurements within one standard deviation, although the uncertainties especially for CM energies above 2.9 GeV of these measurements are very large. The results of the previous BESIII scan agree well for all 3 measured energy points, again with the caveat that the data at 2.2324 GeV and 3.08 GeV were merged

with the data of this work.

Chapter 12

Summary and Conclusions

In the final chapter of this work, the final results presented in the last chapter are discussed and compared with some of the theoretical approaches to describe the proton EM FFs which have been introduced in section 2.4. Specific phenomena such as an observed oscillatory behaviour in the effective FF measurement are investigated closer and compared to similar observations from previous measurements. Finally, a summary of the results obtained in this work as well as a short conclusion is drawn in section 12.3.

12.1 Discussion of the effective form factor results

The general shape of the obtained results for the effective FF can be described by different parametrisations. As an example, the modified dipole parametrisation of the effective FF suggested in reference [185] (for an introduction of the parametrisation see section 2.4.1), is chosen as a comparison to the data. Within this approach, the effective FF is described by the following function:

$$|G(s)| = \frac{\mathcal{A}}{(1+\frac{s}{m_a^2})\left[1-\frac{s}{0.71(GeV/c)^2}\right]^2}, \tag{12.1}$$

where $\mathcal{A} = 9.61 \pm 0.42$ and $m_a^2 = 7.07 \pm 0.71$ are parameters obtained from fitting the data of this work. The corresponding fit for the results of this work can be seen in figure 11.2. Applying the same kind of fit on the effective FF results of BaBar, an interesting oscillating behaviour of the residuals of data compared to the fit is observed in reference [186]. A similar behaviour can be seen in the residuals of the effective FF results of this work compared to equation 12.1, as shown on the left side of figure 12.2.

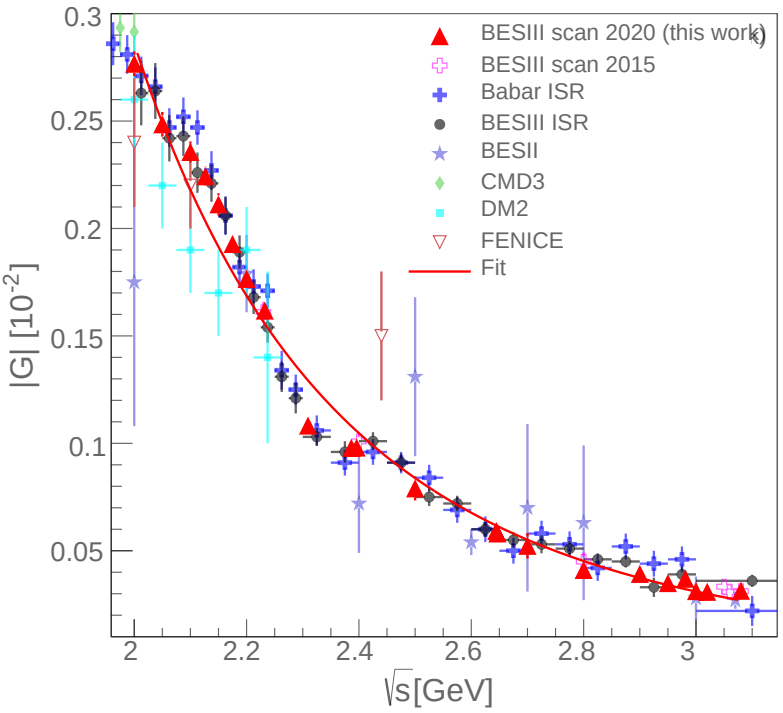

FIGURE 12.1: Fit of the effective FF results of this work according to equation 12.1. The data shown and the corresponding references are the same as in figure 11.2.

The right side of figure 12.2 shows the residuals as a function of the relative momentum between the proton and antiproton:

$$p(q^2) = \sqrt{E^2 - M^2}, \quad E = q^2/(2M) - M, \tag{12.2}$$

which is the form given in reference [186] for comparison. The same reference suggests to describe the overall behaviour of the effective FF as a composition of a monotonously falling term G_0, given by function 12.1, and an oscillating term G_{osc}:

$$|G(p)| = G_0(p) + G_{osc}(p). \tag{12.3}$$

For the oscillating part, the following function is suggested [186]:

$$G_{osc}(p) = b_0^{osc} e^{-b_1^{osc} p} \cos(b_2^{osc} p + b_3^{osc}). \tag{12.4}$$

A fit with function 12.4 to the results of this work is also shown on the right side of figure 12.2. The four parameters of equation 12.4 are extracted from the fit as $b_0^{osc} =$

0.076 ± 0.015, $b_1^{osc} = 1.06 \pm 0.13$, $b_2^{osc} = 5.14 \pm 0.16$, and $b_3^{osc} = 0.45 \pm 0.25$, with a reduced χ^2 of 4.8.

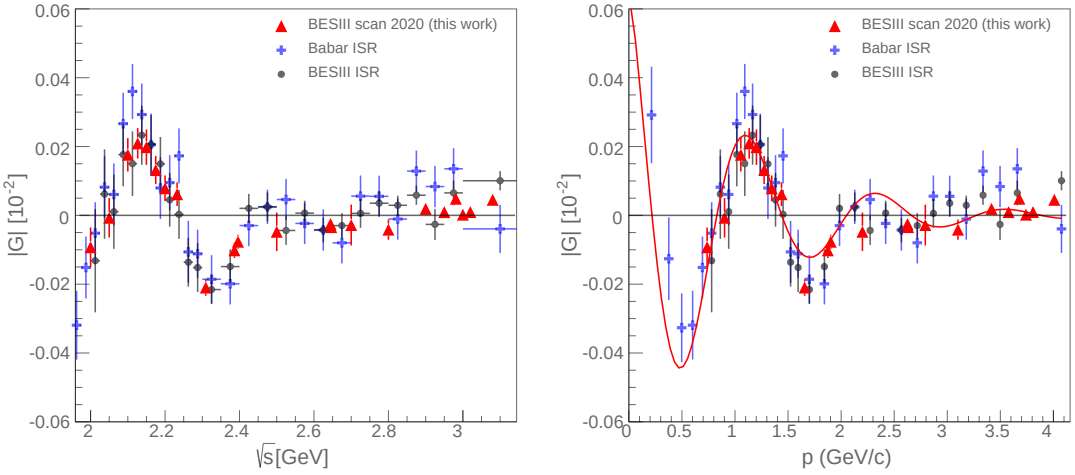

FIGURE 12.2: Comparison of the effective FF of this work to results from the BESIII and BaBar ISR analysis after subtraction of the fit function given in equation 12.1. The left side gives the residuals as a function of the CM energy, the right side as a function of the relative momentum defined in equation 12.2. A fit according to equation 12.4 as suggested in reference [186] has been applied to the data in the right plot.

The fit describes the oscillation of the residuals well for data points at low to intermediate CM energy, up to p∼2 GeV/c, and even provides a reasonable description of the BaBar data below p(q^2) ∼ 0.8 GeV/c, which was not considered in the fit. For data points with p(q^2) > 2 GeV/c however, no obvious oscillatory behaviour is visible any more in the data of this work, which, together with the small uncertainties, leads to a bad description of the data by equation 12.4 in this region as apparent in the high value of the reduced χ^2.

Several possible sources of the observed oscillation are in discussion, among them interference effects from a rescattering of the final state particles [187], or resonant structures [188]. The first explanation assumes a double layer imaginary optical potential, which is flux absorbing for CM distances of the formed proton and antiproton of $\gtrsim$ 1.7-1.8 and flux generating for $\lesssim$ 1.7-1.8. The second approach assumes the occurrence of an intermediate excited state after the formation of the proton antiproton pair during a rescattering of the final state particles. The positions of the "peaks" in the effective FF correspond to the thresholds of the $p\bar{\Lambda}$ and $\Lambda\bar{\Lambda}$ states, making the formation of these states a possible explanation for the enhancement of the effective FF in these regions. The occurring pion in the formation of the Λ resonance is absorbed by the other baryon, which is why it is not observed in the process. More detailed information about the proposed formalisms can be found in the corresponding references.

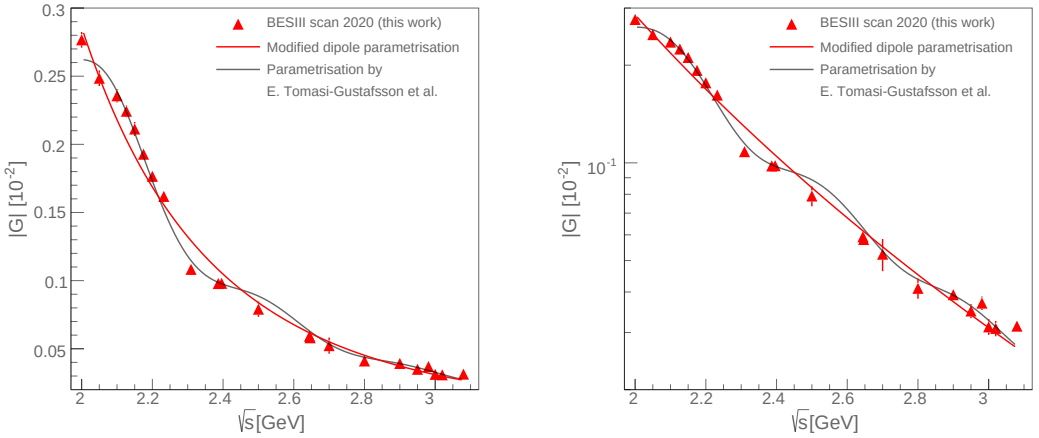

FIGURE 12.3: Results for the effective FF of this work in linear (left) and logarithmic (right) scale, compared to a modified dipole fit according to equation 12.1 (red) and the parametrisation suggested in reference [186] (black).

A fit with the full function from equation 12.3, combining the monotonously falling (equation 12.1) and the oscillating part (equation 12.4), is performed and shown in figure 12.3. In case of the monotonous part, the parameters of this combined fit differ from those of the separate fit with $\mathcal{A} = 8.42 \pm 0.36$, $m_a^2 = 9.55 \pm 1.09$, $b_0^{osc} = 0.098 \pm 0.021$, $b_1^{osc} = 1.18 \pm 0.14$, $b_2^{osc} = 5.06 \pm 0.15$, $b_3^{osc} = 0.63 \pm 0.22$, and a reduced χ^2 of 4.7. The parameters of the oscillating part agree within their uncertainties with those from the separate fit. Similarly to the separate fits, the combined fit describes the data at low to intermediate energies reasonably well, but the lack of oscillation for higher CM energies leads to a bad overall description as evidenced by the reduced χ^2. Limiting the fit to $E_{CM} < 2.9$ GeV leads to a reduced χ^2 of 1.8.

12.2 Discussion of the proton electromagnetic form factor results

In this section, the results of the individual FFs $|G_E|$ and $|G_M|$ from chapter 11 as well as their ratio R are compared to different theoretical predictions. Several approaches exist to describe the proton EM FFs, ranging from models based on first principles to purely phenomenological approaches. In the following, four of these approaches have been chosen as a comparison to the data in this work, however this selection is far from fully exhaustive.

The first approach covered is the same modified dipole parametrisation that was already used in the last section to describe the effective FF, equation 12.1, from reference [185]. The parameters of this function of $\mathcal{A} = 7.7$ and $m_a = 14.8$ have been taken from reference

[187]. The second approach is based on perturbative QCD considering counting rules (an introduction to this theoretical approach can be found in section 2.4.3), where the Sachs FFs can be expressed as [189]:

$$|G_{E,M}(q^2)| = \frac{\alpha_0}{q^4[ln(q^2/\Lambda^2_{QCD}) + \pi^2]}, \tag{12.5}$$

with the parameters Λ^2_{QCD}=0.3 and α_0=89.45.
The last two models are two different parametrisations based on VMD which have been analytically extended to the TL region by using the replacements described in equation 2.56. The first is a modified version of the IJL model described in section 2.4.2, where the FFs are expressed in terms of isoscalar and isovector components to F_1 and F_2:

$$F_1^S(q^2) = \frac{e}{2} g(q^2) \left[(1 - \beta_\omega - \beta_{phi}) + \beta_\omega \frac{M_\omega^2}{M_\omega^2 - q^2} + \beta_\phi \frac{M_\phi^2}{M_\phi^2 - q^2} \right] \tag{12.6}$$

$$F_1^V(q^2) = \frac{e}{2} g(q^2) \left[(1 - \beta_\rho) + \beta_\rho \frac{M_\rho^2}{M_\rho^2 - q^2} \right] \tag{12.7}$$

$$F_2^S(q^2) = \frac{e}{2} g(q^2) \left[(-0.120 - \alpha_\phi) \frac{M_\omega^2}{M_\omega^2 - q^2} + \alpha_\phi \frac{M_\phi^2}{M_\phi^2 - q^2} \right] \tag{12.8}$$

$$F_2^V(q^2) = \frac{e}{2} g(q^2) \left[3.706 \frac{M_\rho^2}{M_\rho^2 - q^2} \right]. \tag{12.9}$$

Here, the parameters $\beta_\omega = 1.102$, $\beta_\phi = 0.112$, $\beta_\rho = 0.672$ and $\alpha_\phi = -0.052$ [90] are extracted from a fit to proton SL FF data and M_ω, M_ϕ, and M_ρ are the masses of the corresponding mesons. The Dirac and Pauli FFs F_1 and F_2 are then given by $F_i = F_i^V + F_i^S$, $i = 1, 2$, and the Sachs FFs are derived from them in the usual way according to equation 2.11. The modifications to this parametrisation consist of the modification of the propagators of the vector mesons to account for their non-negligible width, details can be found in references [190, 191].

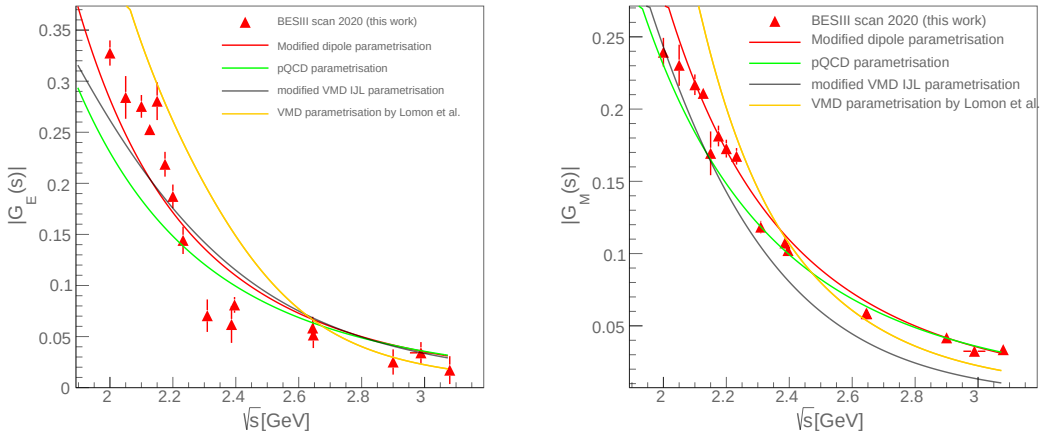

FIGURE 12.4: Comparison of the results for the proton EM FFs $|G_E|$ (left) and $|G_M|$ (right) of this work to different theoretical predictions. Shown are the modified dipole parametrisation from equation 12.1 [185], a pQCD based parametrisation from equation 12.5 [189], a model based on VMD by Iachello *et al.* [190, 191], and a VMD parametrisation by Lomon *et al.* [192].

The second chosen VMD model is based on reference [192] by Lomon *et al.* Here, the isoscalar and isovector components to F_1 and F_2 are given by:

$$F_1^S(q^2) = \left(\frac{g_\omega}{f_\omega}\frac{m_\omega^2}{m_\omega^2 - q^2} + \frac{g_{\omega'}}{f_{\omega'}}\frac{m_{\omega'}^2}{m_{\omega'}^2 - q^2}\right) F_1^\omega(q^2) + \frac{g_\phi}{f_\phi}\frac{m_\phi^2}{m_\phi^2 - q^2} F_1^\phi(q^2) + \left(1 - \frac{g_\omega}{f_\omega} - \frac{g_{\omega'}}{f_{\omega'}}\right) F_1^D(q^2) \tag{12.10}$$

$$F_1^V(q^2) = \frac{N}{2}\left[\frac{1.0317 + 0.0875(1 - q^2/0.3176)^{-2}}{1 - q^2/0.5496} + \frac{g_{\rho'}}{f_{\rho'}}\frac{m_{\rho'}^2}{m_{\rho'}^2 - q^2}\right] F_1^\rho(q^2) + \left(1 - 1.1192\frac{N}{2} - \frac{g_{\omega'}}{f_{\omega'}}\right) F_1^D(q^2) \tag{12.11}$$

$$F_2^S(q^2) = \left(\kappa_\omega \frac{g_\omega}{f_\omega}\frac{m_\omega^2}{m_\omega^2 - q^2} + \kappa_{\omega'}\frac{g_{\omega'}}{f_{\omega'}}\frac{m_{\omega'}^2}{m_{\omega'}^2 - q^2}\right) F_2^\omega(q^2) + \kappa_\phi \frac{g_\phi}{f_\phi}\frac{m_\phi^2}{m_\phi^2 - q^2} F_2^\phi(q^2) + \left(\kappa_s - \kappa_\omega\frac{g_\omega}{f_\omega} - \kappa_{\omega'}\frac{g_{\omega'}}{f_{\omega'}} - \kappa_\phi\frac{g_\phi}{f_\phi}\right) F_2^D(q^2) \tag{12.12}$$

$$F_2^V(q^2) = \frac{N}{2}\left[\frac{5.7824 + 0.3907(1 - q^2/0.1422)^{-1}}{1 - q^2/0.5362} + \kappa_{\rho'}\frac{g_{\rho'}}{f_{\rho'}}\frac{m_{\rho'}^2}{m_{\rho'}^2 - q^2}\right] F_2^\rho(q^2) + \left(\kappa_\nu - 6.1731\frac{N}{2} - \kappa_{\rho'}\frac{g_{\omega'}}{f_{\omega'}}\right) F_2^D(q^2), \tag{12.13}$$

with

$$F_1^{\alpha,D}(q^2) = \frac{\Lambda_{1,D}^2}{\Lambda_{1,D}^2 + \widetilde{q}} \frac{\Lambda_2^2}{\Lambda_2^2 + \widetilde{q}}, \quad F_2^{\alpha,D}(q^2) = \frac{\Lambda_{1,D}^2}{\Lambda_{1,D}^2 + \widetilde{q}} \left(\frac{\Lambda_2^2}{\Lambda_2^2 + \widetilde{q}} \right)^2, \tag{12.14}$$

$$F_1^{\phi}(q^2) = F_1^{\alpha} \left(\frac{-q^2}{\Lambda_1^2 - q^2} \right)^{1.5}, \quad F_2^{\phi}(q^2) = F_2^{\alpha} \left(\frac{\Lambda_1^2}{\mu_\phi^2} \frac{\mu_\phi^2 - q^2}{\Lambda_1^2 - q^2} \right)^{1.5} \tag{12.15}$$

$$\widetilde{q}^2 = -q^2 \frac{\ln\left[(\Lambda_D^2 - q^2)/\Lambda_{QCD}^2\right]}{\ln(\Lambda_D^2/\Lambda_{QCD}^2)}), \quad \alpha = \rho, \omega \text{ and } \Lambda_{1,D} = \Lambda_1 \text{ for } F_i^{\alpha}, \Lambda_{1,D} = \Lambda_D \text{ for } F_i^{D}. \tag{12.16}$$

The variables $g_{\rho'}/f_{\rho'} = 0.0608$, $g_\omega/f_\omega = 0.6896$, $g_\phi/f_\phi = -0.1852$, $g_{\omega'}/f_{\omega'} = 0.2346$ $\kappa_{\rho'} = 5.3038$, $\kappa_\omega = -2.8585$, $\kappa_\phi = 13.0037$, $\kappa_{\omega'} = 18.2284$, $\mu_\phi = 0.6848$, $\Lambda_1 = 0.9441$, $\Lambda_2 = 2.8268$, $\Lambda_D = 1.2350$, $\Lambda_{QCD} = 0.150$, N=1.0 have been determined in reference [192] by a fit to SL proton FF data.

A comparison of the parametrisations described above with the proton EM FF results of this work is shown in figure 12.4. In case of the $|G_M|$ measurement, the data is best described by the modified dipole function. While the parametrisation fits the measurement reasonably well by eye, the reduced χ^2 is still high with $\chi^2_{red} = 4.2$ due to the small uncertainties in the measurement.

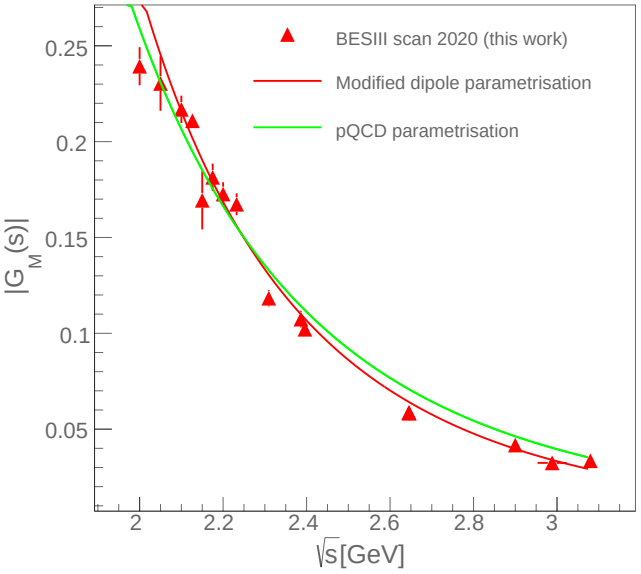

FIGURE 12.5: Comparison of the proton EM FF results of this work to the modified dipole parametrisation [185] and the pQCD based parametrisation [189]. Compared to figure 12.4, the parameters of these models have been fitted to the results of this work.

The parametrisation based on pQCD provides a good description of the measurement points at intermediate to high CM energies, but strongly underestimates the data at low CM energies, leading to a χ^2_{red} of 17.43. The two different chosen VMD based models both fail to describe the data, as is evident both by eye and in the reduced χ^2 of $\chi^2_{red} = 46.9$ and $\chi^2_{red} = 60.7$ for the IJL and the Lomon model, respectively.
An actual fit to the data of this work using the modified dipole and pQCD based parametrisations without predetermined parameters is shown in figure 12.5. While the reduced χ^2 of the first parametrisation stays the same with $\chi^2_{red} = 4.2$, the χ^2 of the second parametrisation improves to $\chi^2_{red} = 7.7$. The extracted parameters are $\mathcal{A} = 8.15 \pm 0.55$ and $m_a = 11.3 \pm 2.4$ for the modified dipole fit, and $\Lambda^2_{QCD} = 0.49 \pm 0.11$ and $\alpha_0 = 73 \pm 11$ for the pQCD based fit.
A comparison of the four parametrisations with the results of this work for the electric FF of the proton $|G_E|$ can be seen on the left side of figure 12.4. None of the chosen approaches is able to describe the data adequately, as shown by the reduced χ^2 values of 13.9, 32.5, 15.7, and 37.3 for the modified dipole, pQCD based, IJL VMD and Lomon VMD parametrisations, respectively. Similarly to the discussion of the effective FF, additional structures to the monotonously decrease of the FF are apparent which can not be described by any of the above functions. The same is true, to a lesser extent, for the results of the magnetic FF.

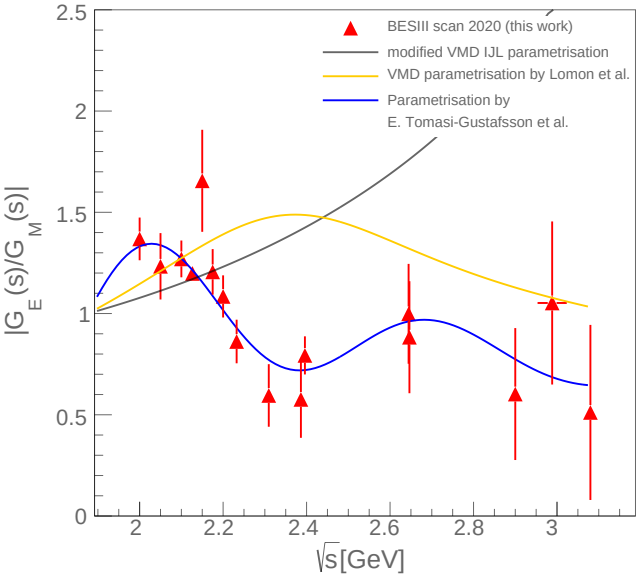

FIGURE 12.6: Comparison of the proton EM FF ratio R of this work to the parametrisation of equation 12.17 suggested in reference [193] (blue line), the IJL VMD model [190, 191], and the Lomon VMD model [192].

An approach describing these structures phenomenologically through an oscillatory behaviour of the FFs ratio $R = |G_E|/|G_M|$ can be found in reference [193]. Within this

approach, R is described by:

$$R(\omega(s)) = \frac{1}{1+\omega^2/r_0}\left[1 + r_1 e^{-r_2\omega}\sin(r_3\omega)\right], \quad \omega = \sqrt{s} - 2m_p \tag{12.17}$$

with the free parameters r_i, i=0, 1, 2, 3 and the proton mass m_p. A fit with equation 12.17 to the data of this work can be seen in figure 12.6, along with the two VMD based parametrisations introduced earlier in this section for reference. While neither of the VMD parametrisations can describe the R measurement of this work, the phenomenological function of equation 12.17 provides a good parametrisation of the data with a reduced χ^2 of $\chi^2_{red} = 0.86$ and parameters $r_0 = 3.6 \pm 2.8$, $r_1 = 0.43 \pm 0.14$, $r_2 = 1.3 \pm 1.1$, and $r_3 = 9.2 \pm 0.6$.

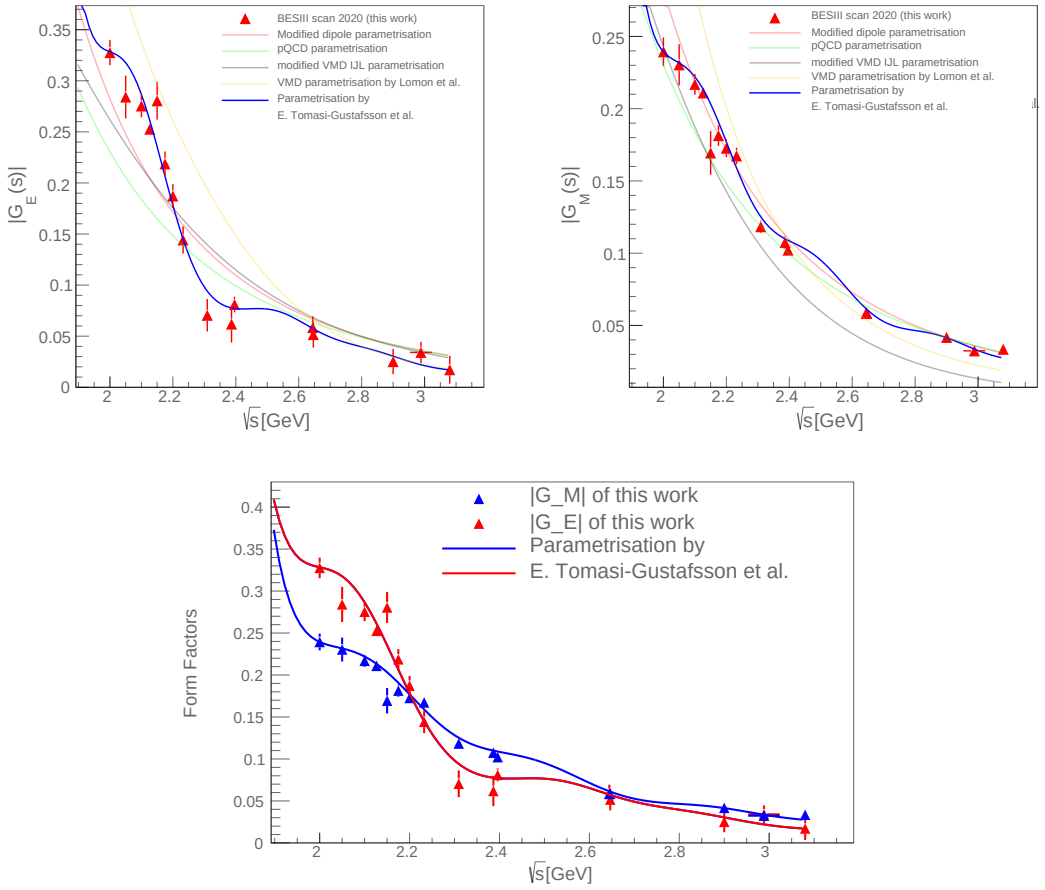

FIGURE 12.7: Comparison of the proton EM FF results of this work to the parametrisation of equation 12.18 suggested in reference [193] (top, blue line). The bottom shows $|G_E|$ and $|G_M|$ in a single plot, compared with the same parametrisation (red line for $|G_E|$, blue line for $|G_M|$).

The parametrisation of the effective FF $|G(s)|$ provided by equation 12.3 can be used together with the fit of the FF ratio from equation 12.17 to describe the individual FFs $|G_E|$ and $|G_M|$:

$$|G_E(s)| = |G(s)|\sqrt{\frac{1+2\tau}{1+2\tau/R^2(s)}}, \quad |G_M(s)| = |G(s)|\sqrt{\frac{1+2\tau}{R^2(s)+2\tau}}. \tag{12.18}$$

The resulting parametrisation is shown in figure 12.7 compared with the individual FF results of this work. A good description of the data is achieved with $\chi^2_{red} = 1.2$ for $|G_E|$ and $\chi^2_{red} = 1.4$ for $|G_M|$, as is expected since the functions for $|G(s)|$ and R(s) which make up equation 12.18 also fit well to their corresponding data.

In summary, none of the models based on first principles that have been chosen in this section for a comparison with the proton EM FF results of this work can provide a satisfying description of the data. While the general monotonously falling form is well replicated, the structures occurring especially in the electric FF $|G_E|$ are not considered in any of these approaches. Although the phenomenological parametrisation of reference [193] does replicate these structures, it does not provide any explanation of their origin. Further theoretical work will be necessary to explain the details of the q^2 dependence of the individual FFs with models based on first principles.

12.3 Summary and Conclusions

In the scope of this work, a scan data set with a total integrated luminosity of 651.09 pb^{-1}, taken at the BESIII detector in 2015 and dedicated to the determination of baryon FFs, has been analysed along with previously taken data for a total luminosity of 688.5 pb^{-1}. The measurement represents the first instance where the scan technique has been employed over a large kinematical range with high luminosity for the extraction of baryon, in case of this work specifically proton, EM FFs.
Within the analysis, the cross section of the process $e^+e^- \to p\bar{p}$ has been measured at all 22 CM energies of the data set between 2.0 GeV and 3.08 GeV. MC simulations using the Phokhara event generator have been performed for this signal process to correct for the detection and selection efficiency as well as radiative corrections, including ISR up to NNLO, FSR and vacuum polarisation. The achieved precision of the cross section measurement is unprecedented by any other experiment, with uncertainties of the order of a few percent, dominated by the systematic uncertainty for the first time. A thorough study of these uncertainties is described in chapter 10, the most important sources

include those from tracking and PID efficiency, selection criteria, remaining background, the luminosity measurement and the FF model used in the MC simulation, with the dominant contribution coming from either the tracking efficiency or the used FF model for high luminosity points. A comparison of the cross section to previous measurements has been performed in chapter 11, showing a good agreement while vastly improving the achieved precision, especially at high luminosity data points of the scan set such as 2.12655 GeV. Here, the previously most precise measurements, performed by the BaBar experiment and the BESIII untagged ISR measurement, have a total uncertainty which is higher by a factor of about 3.3.

The effective FF has been extracted from the cross section using formula 8.4 at all 22 energy points of the data set. Similarly to the cross section measurement, good agreement and simultaneously a huge improvement in precision has been achieved compared to previous results of the effective FF. The total uncertainty, again dominated by systematics for low to medium energy scan points, is between 2% and 4%, with the same sources for the systematic uncertainty as for the cross section measurement. The interesting oscillating structures observed in BaBar data by reference [186] could also be seen in the residuals of the effective FF of this work compared to a modified dipole fit function for low to intermediate data points of the scan data set, while no apparent oscillation is visible for CM energies above 2.4 GeV.

For 15 out of the 22 energy points of the 2015 scan data set with enough remaining events after event selection, an angular analysis has been performed to extract the individual Sachs FFs $|G_E|$ and $|G_M|$ of the proton in the TL region. In addition, four scan points with low luminosity between 2.95 and 3.08 GeV have been combined to a data set with a luminosity weighted average CM energy of ∼2.9884 GeV and a total luminosity of 65.184 pb^{-1}, which also allows an extraction of the FFs. After a differential efficiency and radiative correction, using MC samples including ISR up to NNLO, FSR and vacuum polarisation, the FFs have been extracted with two independent methods: the fit method (see section 9.2.1) and the method of moments (see section 9.2.2), both agreeing well within the statistical uncertainties.
The ratio $R = |G_E/G_M|$ of the two FFs has been extracted with total uncertainties of around 10% for data sets with low to intermediate CM energy, with the best achieved precision being ∼3% at 2.12655 GeV. Compared to the previously most precise measurements at a similar CM energy, e.g. by BaBar, this is an improvement by a factor of about 4.5 in the relative precision. While the uncertainty is still largely dominated by the statistical uncertainty, the measurement performed in this work raises the precision of the results for R in the TL region to a level comparable to results in the SL region, obtained from electron scattering experiments, for the first time. In terms of the long

standing discrepancy between R results of the BaBar and PS170 experiments, the extracted values of R from this work clearly favour the BaBar results.
The magnetic FF $|G_M|$ has been extracted for the first time with high precision over a large range of momentum transfer q^2, with uncertainties around 4% for most of the 16 data samples and a smallest uncertainty again at 2.12655 GeV of 1.3%. The few previous measurements agree well with those of this work within their limited precision. The extraction of the electric FF $|G_E|$ at the 16 CM energies is the first measurement of this quantity that has been performed in the TL region. Uncertainties for $|G_E|$ are below 10% for the data samples at CM energies below 2.3 GeV, but go up to ∼83% at the highest CM energies. A thorough investigation of the potential systematic uncertainty sources has been conducted in section 10.3 for the measurement of R, $|G_M|$ and $|G_E|$. The most important sources are the uncertainty from efficiency correction, selection criteria, remaining background, the tuning procedure, the FF model used in MC simulation, and the asymmetry in the angular distributions.
A comparison of the results for both the effective as well as the individual Sachs FFs to the predictions of several theoretical approaches has been performed in the earlier sections of this chapter. Additional structures have been observed especially in the electric FF $|G_E|$ and the effective FF. They can not be described by any of the models chosen for comparison, which only replicate the dipole like monotonous decrease of the FFs. A phenomenological model chosen for comparison [193] can describe the FF data well by assuming an oscillating behaviour of the FFs, but offers no deeper understanding of the underlying physics. The attempt to explain the origins of these structures has already sparked large interest from the theoretical side, and further investigations will provide interesting new insights into the proton structure in the next years.

Overall, the results of this work significantly improve our previously scarce knowledge about the TL electromagnetic FFs of the proton, especially the individual Sachs FFs as well as their ratio. A precise measurement of them is crucial as input for theoreticians to improve on existing models and develop new ones. For example, models like the IJL VMD model need the ratio of the two FFs as an input to adjust the parameters of their parametrisations [190]. In addition, the individual FFs and their ratio can be used to distinguish between existing models which make predictions for theses quantities. Analytic continuations of the functions for the proton FFs through logarithmic dispersion relations for example into the unphysical region below the production threshold of $p\bar{p}$ also require knowledge of the individual proton FFs over all of the included kinematical range [188]. A precise measurement of the proton EM FFs as performed in this work has therefore been eagerly awaited by theoreticians and constitutes a paradigm shift for the whole field.
The measurements of the cross section and effective FF have confirmed previous results

and significantly improved their precision, allowing to investigate phenomena such as the oscillating structures observed in the effective FF in more detail. The improved precision will allow future theoretical work to improve existing models of the proton FFs, deepening our understanding of the structure and internal dynamics of one of the most fundamental particles in nature.

Appendix A

Appendix A contains the plots of the different chapters of this work for all CM energies of the 2015 scan dataset instead of just the exemplary ones presented in the main text body. Additional plots for the systematic uncertainty study can be found in the separate appendix C.

A.1 Event selection plots for all CM energies of the 2015 dataset

In the following, plots which illustrate the choice of event selection criteria (detailed discussion see chapter 6) are shown for all CM energies, as opposed to the 4 selected CM energies in the corresponding chapter.

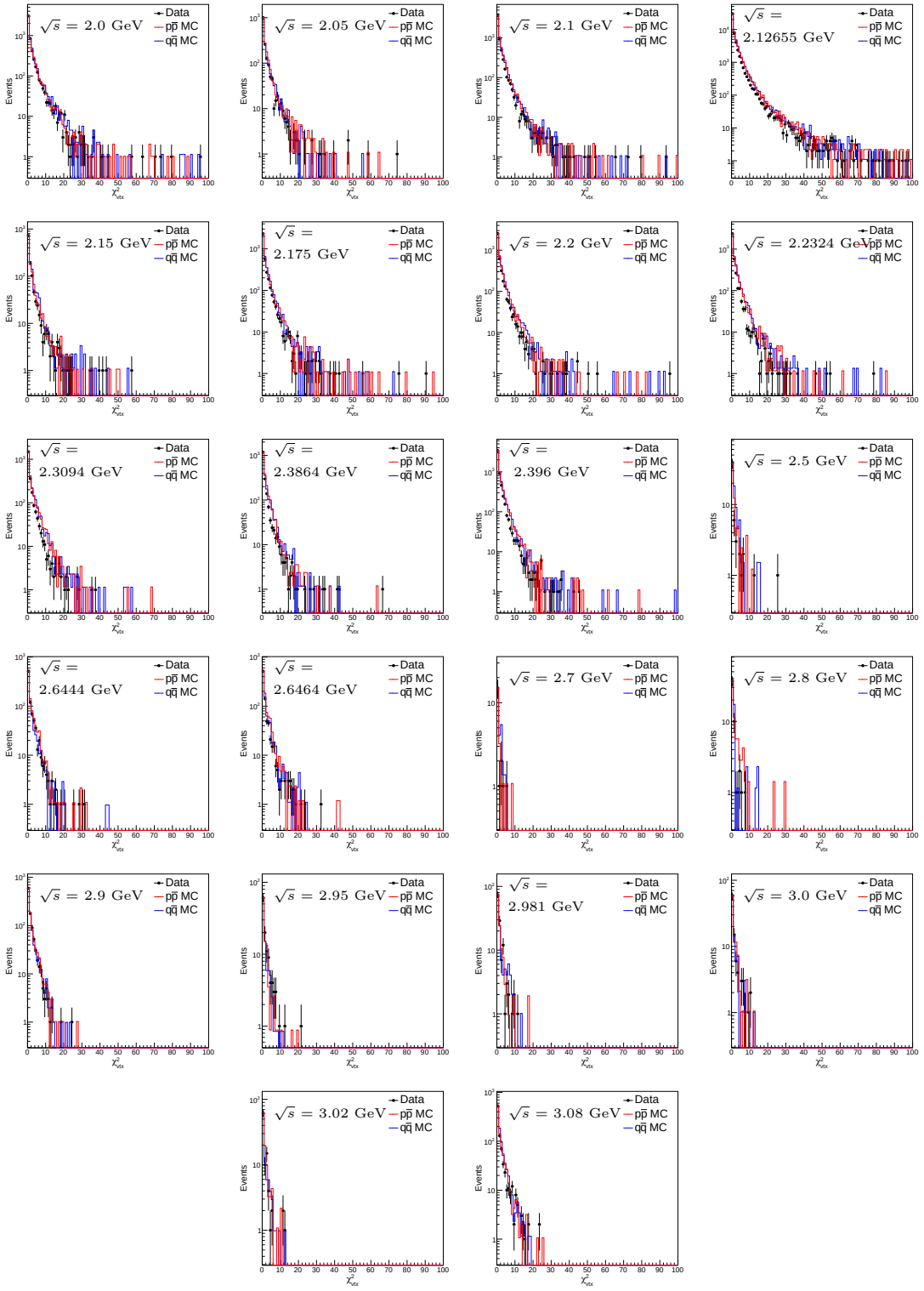

FIGURE A.1: Distribution of the χ^2_{vtx} from the vertex fit performed on the positive and negative track of each event to constrain them to a common vertex. Shown are the distribution of data (black dots with error bars) on top of those for inclusive hadronic MC ($q\bar{q}$, blue histogram) and signal MC including ISR up to NNLO (red histogram) for all energy points of the 2015 data set. All other requirements except the one for χ^2_{vtx} have been applied, and the distributions of signal and $q\bar{q}$ MC have been scaled to the bin with the highest amount of entries in data.

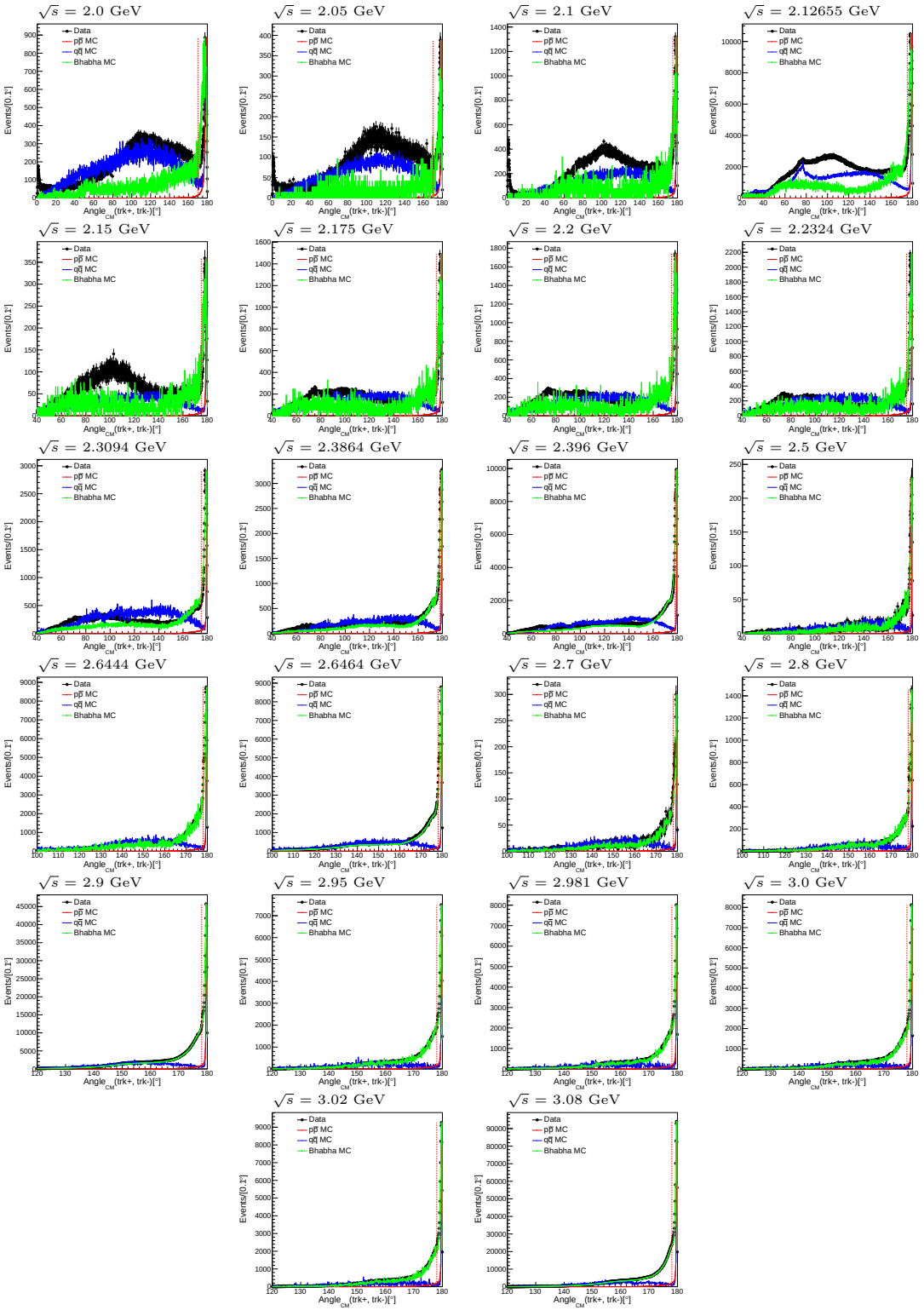

FIGURE A.2: Distribution of the angle between the positive and the negative track for data (black dots with error bars), inclusive hadronic MC ($q\bar{q}$, blue histogram) and signal MC including ISR up to NNLO (red histogram) for all energy points of the 2015 data set. The distributions of signal, Bhabha scattering and $q\bar{q}$ MC have been scaled to the bin with the highest amount of entries in data.

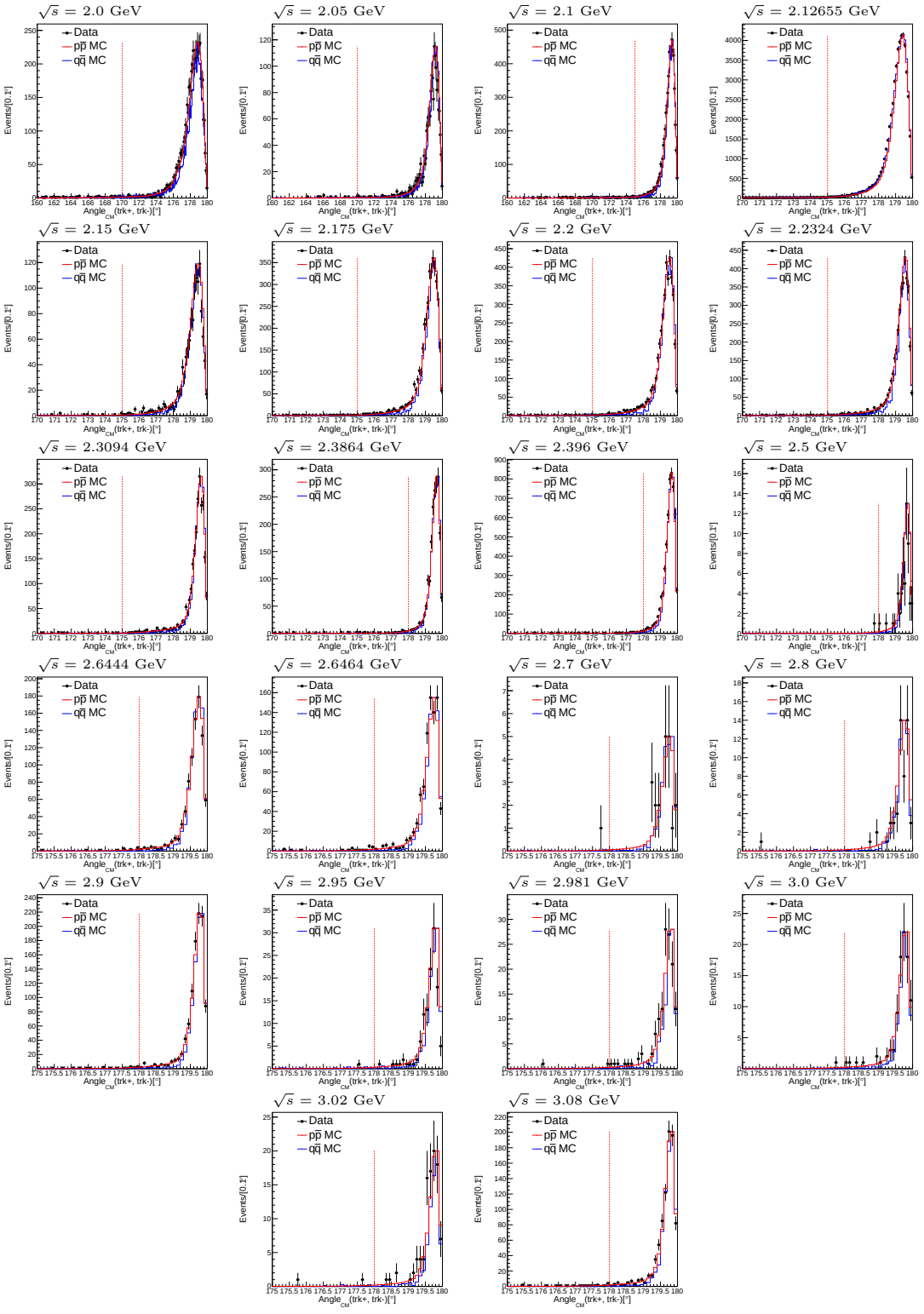

FIGURE A.3: Distribution of the angle between the positive and the negative track for data (black dots with error bars), inclusive hadronic MC ($q\bar{q}$, blue histogram) and signal MC including ISR up to NNLO (red histogram) for all energy points of the 2015 data set. All other requirements except the one for the angle between the tracks have been applied, and the distributions of signal and $q\bar{q}$ MC have been scaled to the bin with the highest amount of entries in data.

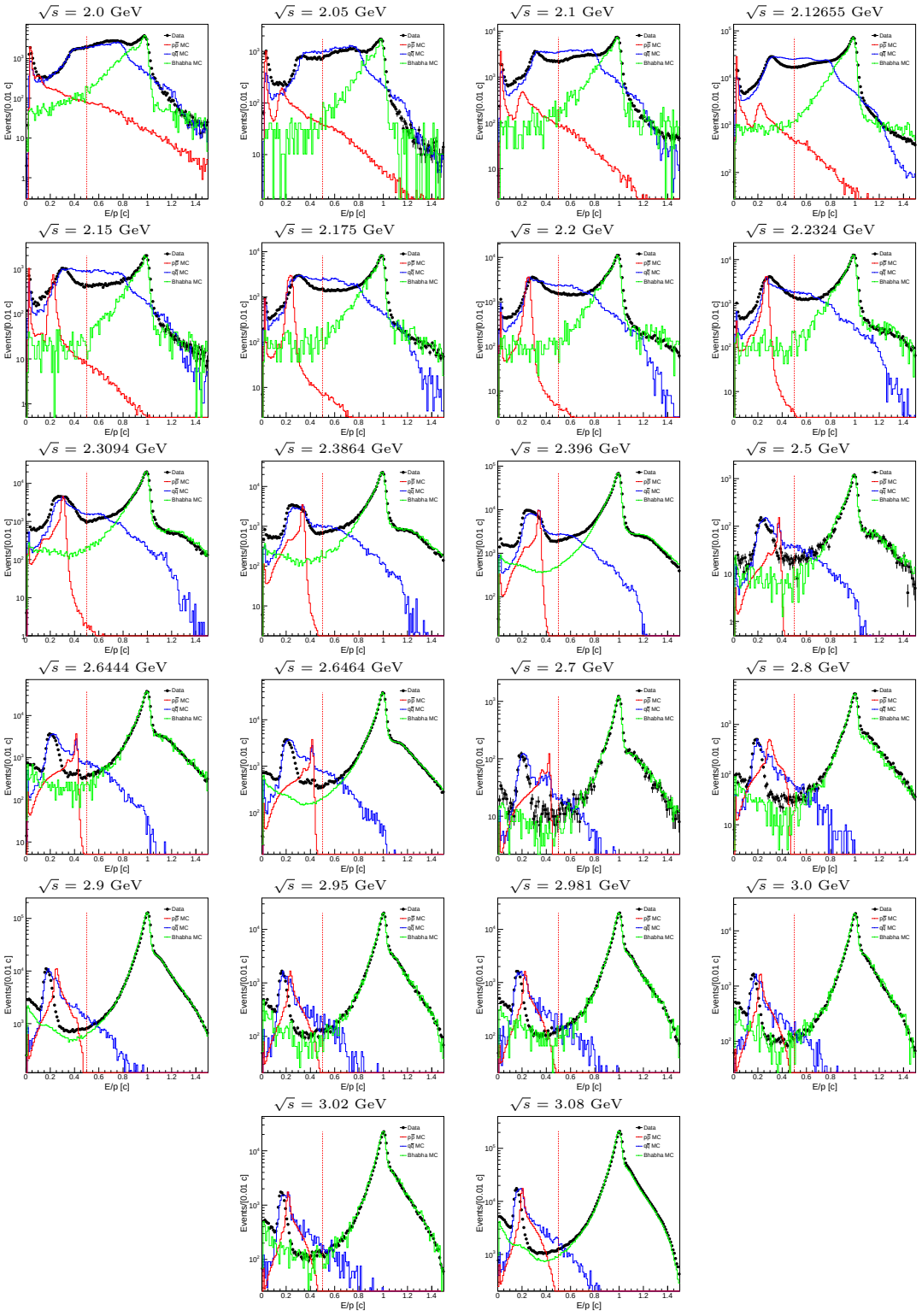

FIGURE A.4: Distribution of the ratio of the energy measured in the EMC and the momentum measured in the MDC (E/p) for data (black dots with error bars), inclusive hadronic MC ($q\bar{q}$, blue histogram), signal MC including ISR up to NNLO (red histogram), and Bhabha scattering (e^+e^-) MC for all energy points of the 2015 data set. The red dashed line marks the chosen limit for the requirement on this quantity, which is only applied for CM energies above 2.12655 GeV. All other requirements except the one for the E/p ratio have been applied, and the distributions of signal and $q\bar{q}$ MC have been scaled to the bin with the highest amount of entries in data.

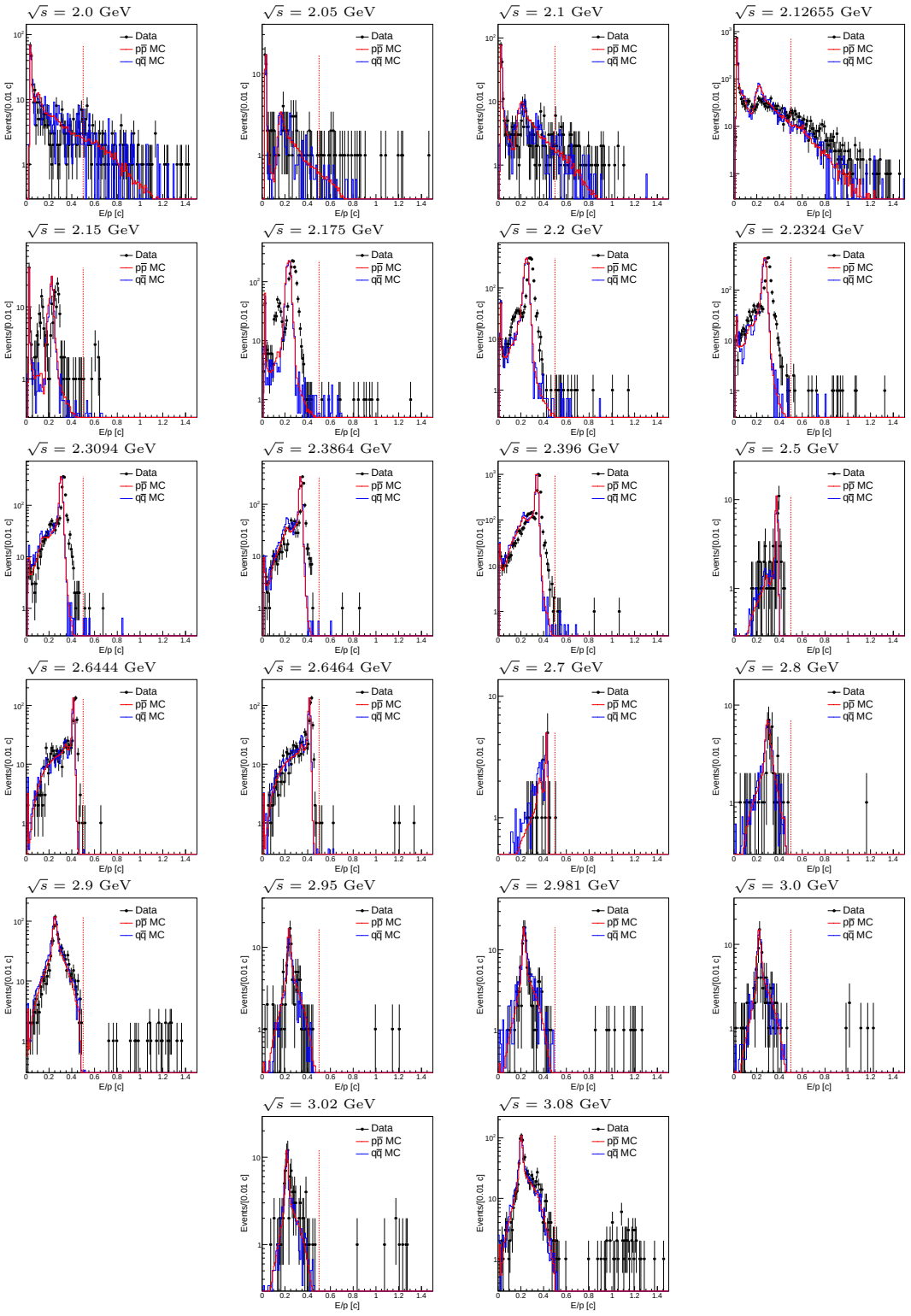

FIGURE A.5: Distribution of the ratio of the energy measured in the EMC and the momentum measured in the MDC (E/p) for data (black dots with error bars), inclusive hadronic MC ($q\bar{q}$, blue histogram), signal MC including ISR up to NNLO (red histogram), and Bhabha scattering (e^+e^-) MC for all energy points of the 2015 data set. The red dashed line marks the chosen limit for the requirement on this quantity, which is only applied for CM energies above 2.12655 GeV. The distributions of signal, Bhabha scattering and $q\bar{q}$ MC have been scaled to the bin with the highest amount of entries in data.

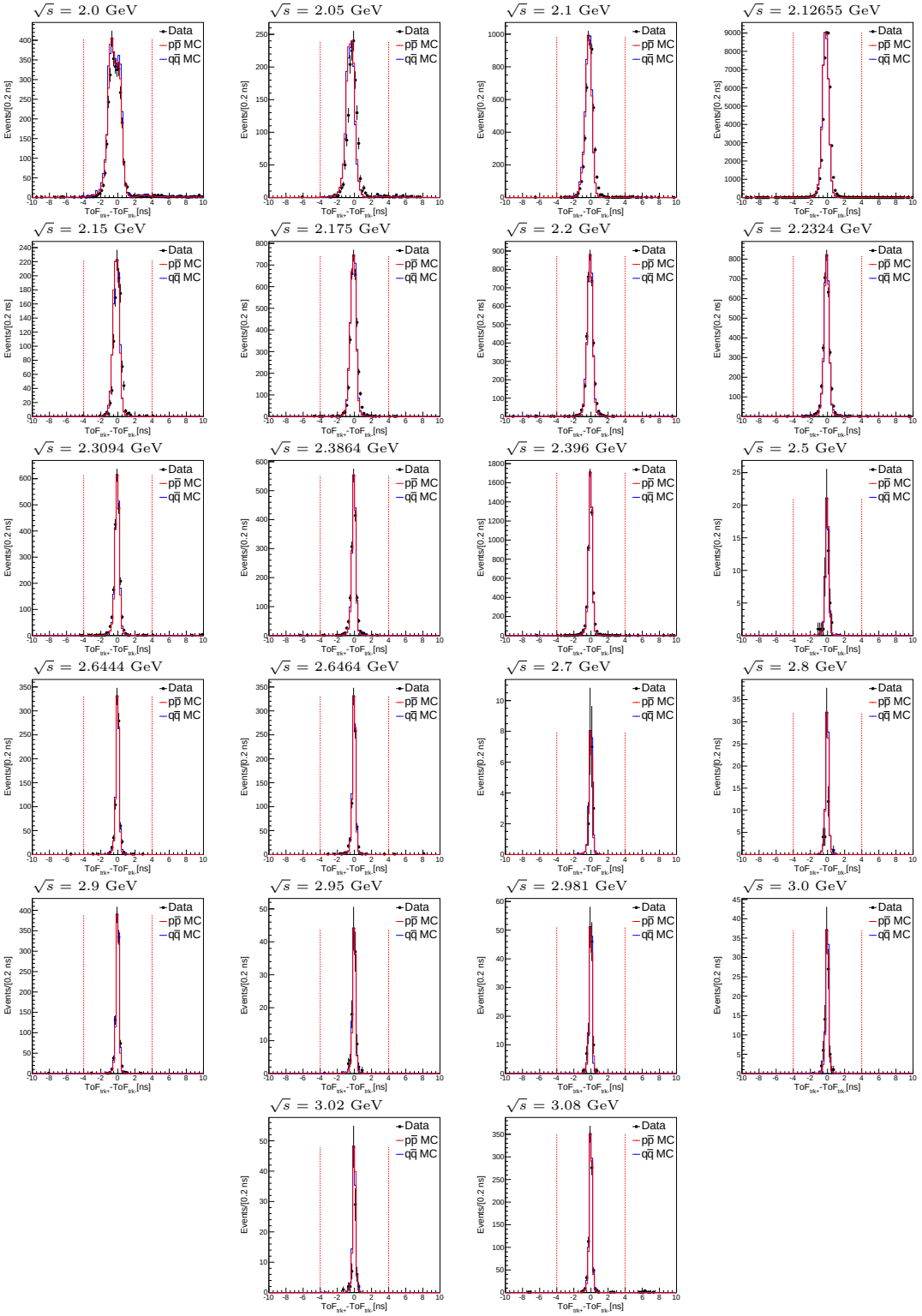

FIGURE A.6: Distribution of the difference between the measured TOF of the positive and the negative track for data (black dots with error bars), inclusive hadronic MC ($q\bar{q}$, blue histogram) and signal MC including ISR up to NNLO (red histogram) for all energy points of the 2015 data set. The two red dashed lines mark the chosen limits for the requirement on this quantity. All other requirements except the one for the TOF difference between the tracks have been applied, and the distributions of signal and $q\bar{q}$ MC have been scaled to the bin with the highest amount of entries in data.

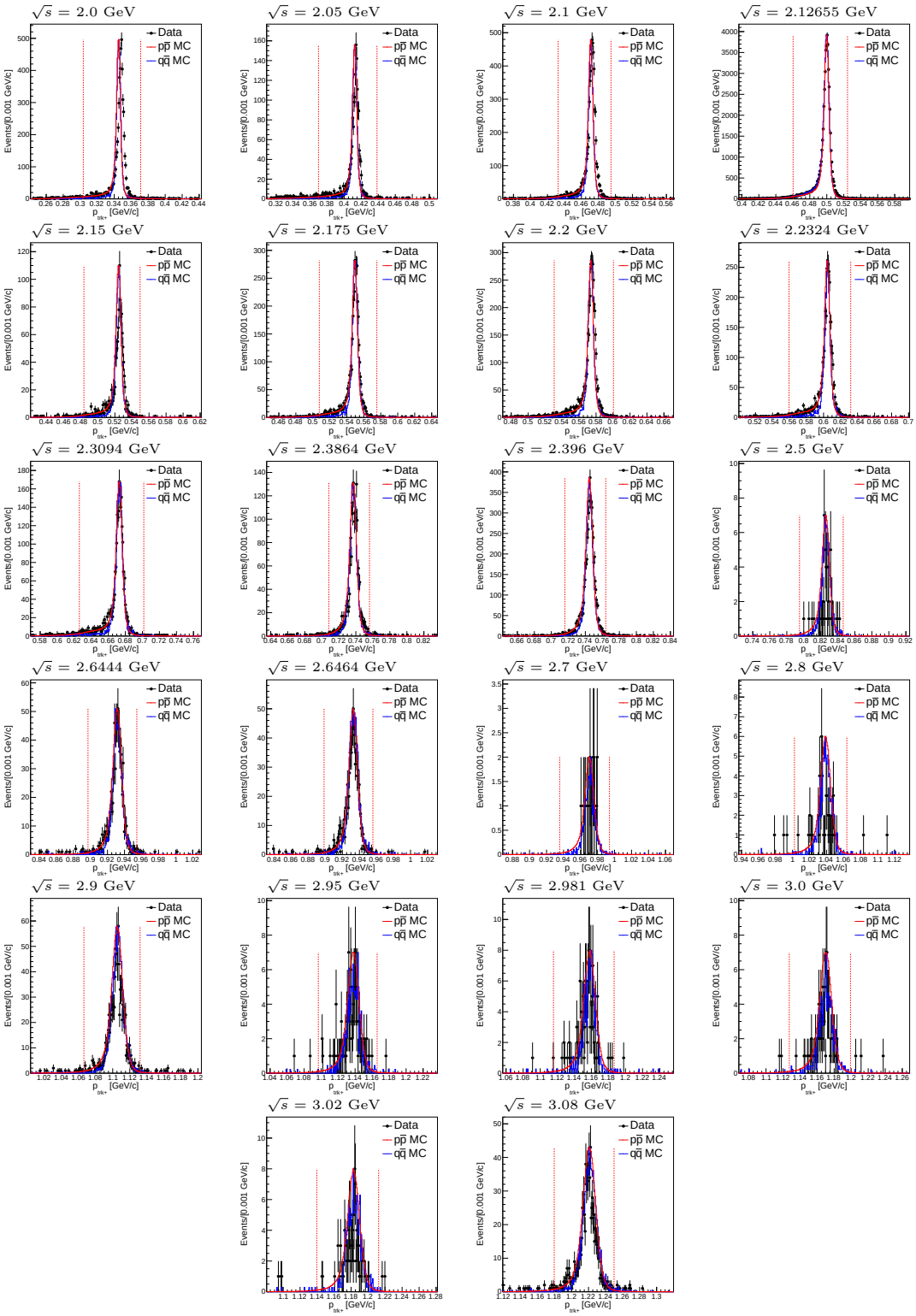

FIGURE A.7: Distribution of the momentum of the positive track in the e^+e^- CM system for data (black dots with error bars), inclusive hadronic MC ($q\bar{q}$, blue histogram) and signal MC including ISR up to NNLO (red histogram) for all energy points of the 2015 data set. The two red dashed lines mark the chosen momentum window requirement. All other requirements except the one for the momentum window have been applied, and the distributions of signal and $q\bar{q}$ MC have been scaled to the bin with the highest amount of entries in data.

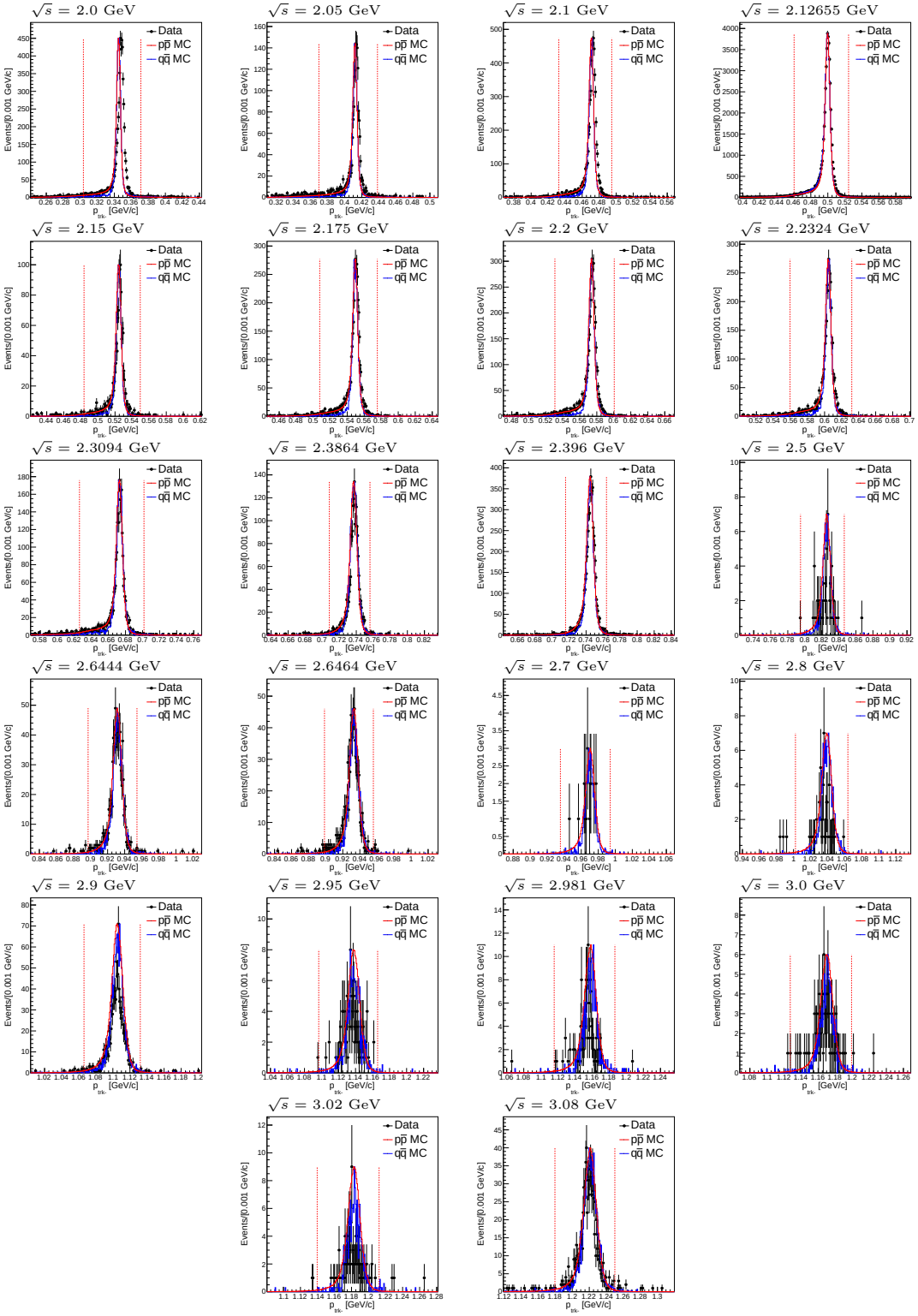

FIGURE A.8: Distribution of the momentum of the negative track in the e^+e^- CM system for data (black dots with error bars), inclusive hadronic MC ($q\bar{q}$, blue histogram) and signal MC including ISR up to NNLO (red histogram) for all energy points of the 2015 data set. The two red dashed lines mark the chosen momentum window requirement. All other requirements except the one for the momentum window have been applied, and the distributions of signal and $q\bar{q}$ MC have been scaled to the bin with the highest amount of entries in data.

A.2 Plots of the background evaluation with the sideband method for all CM energies

Here, additional plots illustrating the sideband method, explained in detail in section 7.3, are shown for all CM energies of the 2015 scan data set. They include the two dimensional momentum distributions with the defined sideband areas for data in figure A.9 as well as for the corresponding signal MC in figure A.10, which has been cut to contain the same amount of events for each CM energy as in the selected data samples.

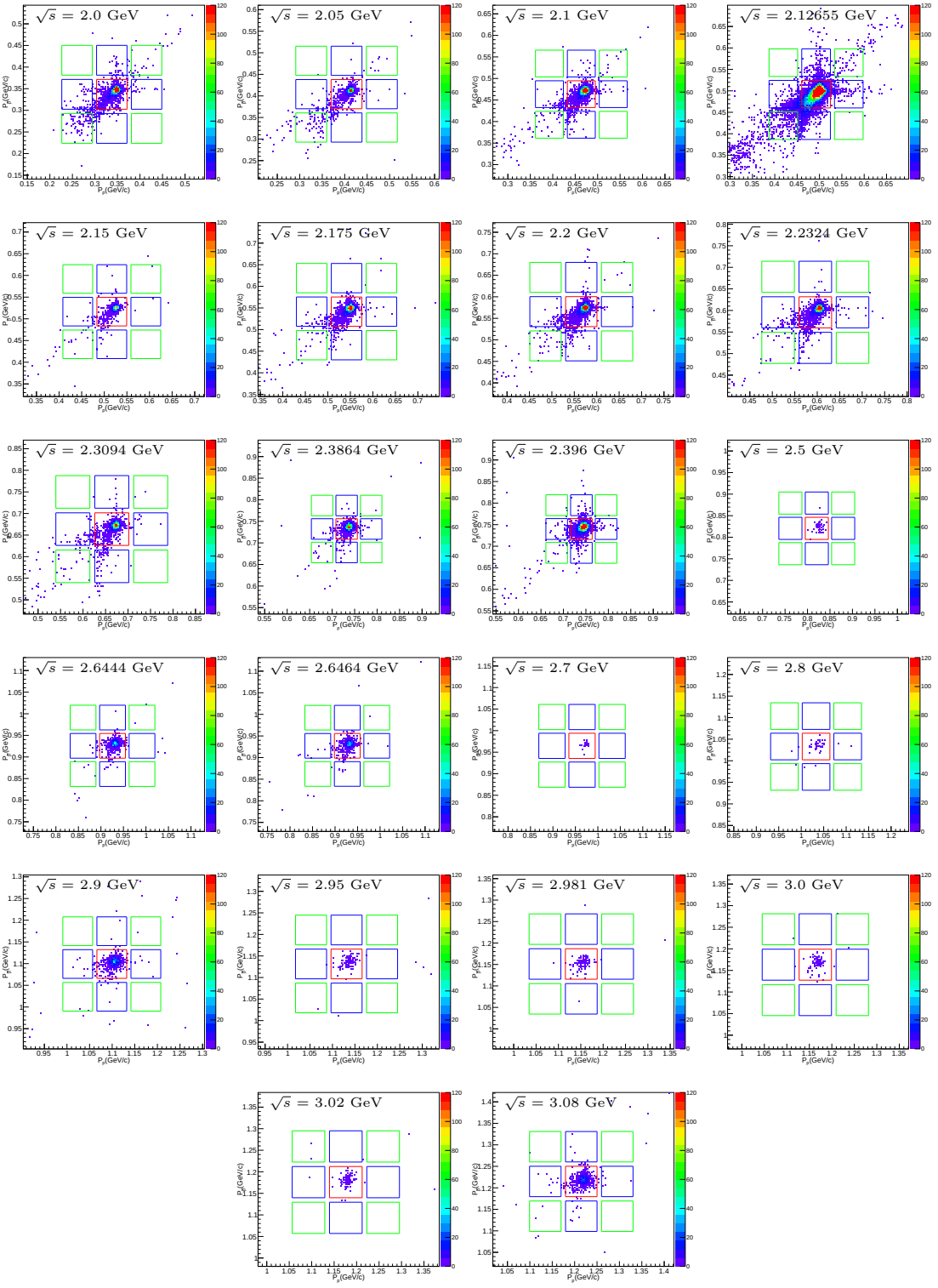

FIGURE A.9: Two dimensional histograms of the momentum of the proton versus the momentum of the antiproton of data samples for for all energy points of the 2015 data set. The different sideband regions (definition see section 7.3) are shown for background type a and b (blue squares) and background type c (green squares) along with the signal region (red square).

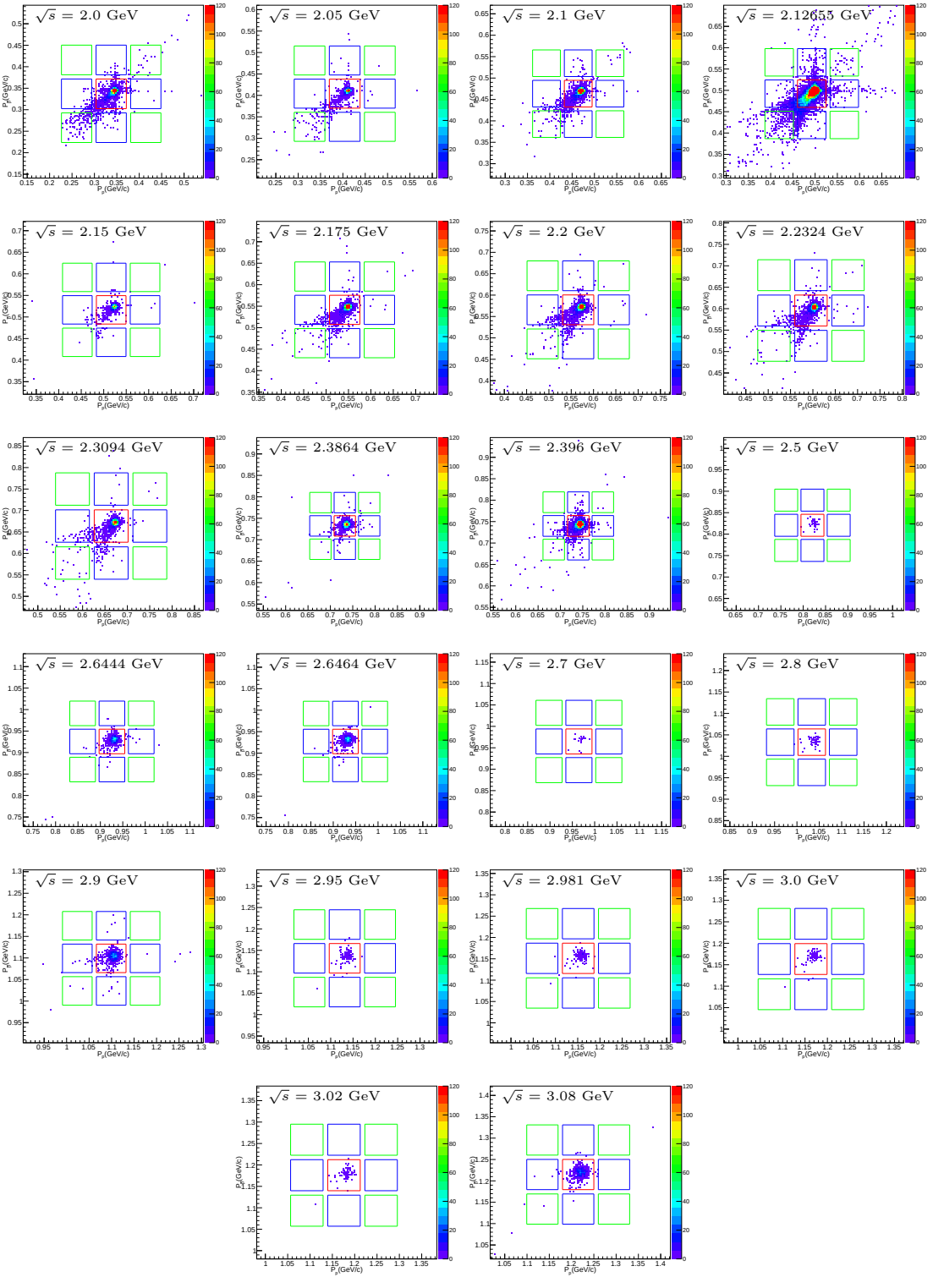

FIGURE A.10: Two dimensional histograms of the momentum of the proton versus the momentum of the antiproton of signal MC samples including ISR up to NNLO for all energy points of the 2015 data set. The different sideband regions (definition see section 7.3) are shown for background type a and b (blue squares) and background type c (green squares) along with the signal region (red square). To compare to data, the same amount of events has been plotted as remain in data after the event selection.

A.3 Plots of the angular analysis of $e^+e^- \to p\bar{p}$ for all CM energies

This section provides additional plots for all CM energies of the 2015 scan dataset concerning the angular analysis of the remaining $p\bar{p}$ events after the event selection to extract the proton EM FFs in the TL region, discussed in detail in chapter 9.

A.3.1 Plots of the differential efficiency and radiative correction

In the following, plots for all CM energies of the efficiency and radiative correction as well as their product are shown as a function of $\cos\theta_p^{CM}$. Detailed discussion about these distributions can be found in section 9.1.1 for the efficiency correction and in section 9.1.2 for the radiative correction.

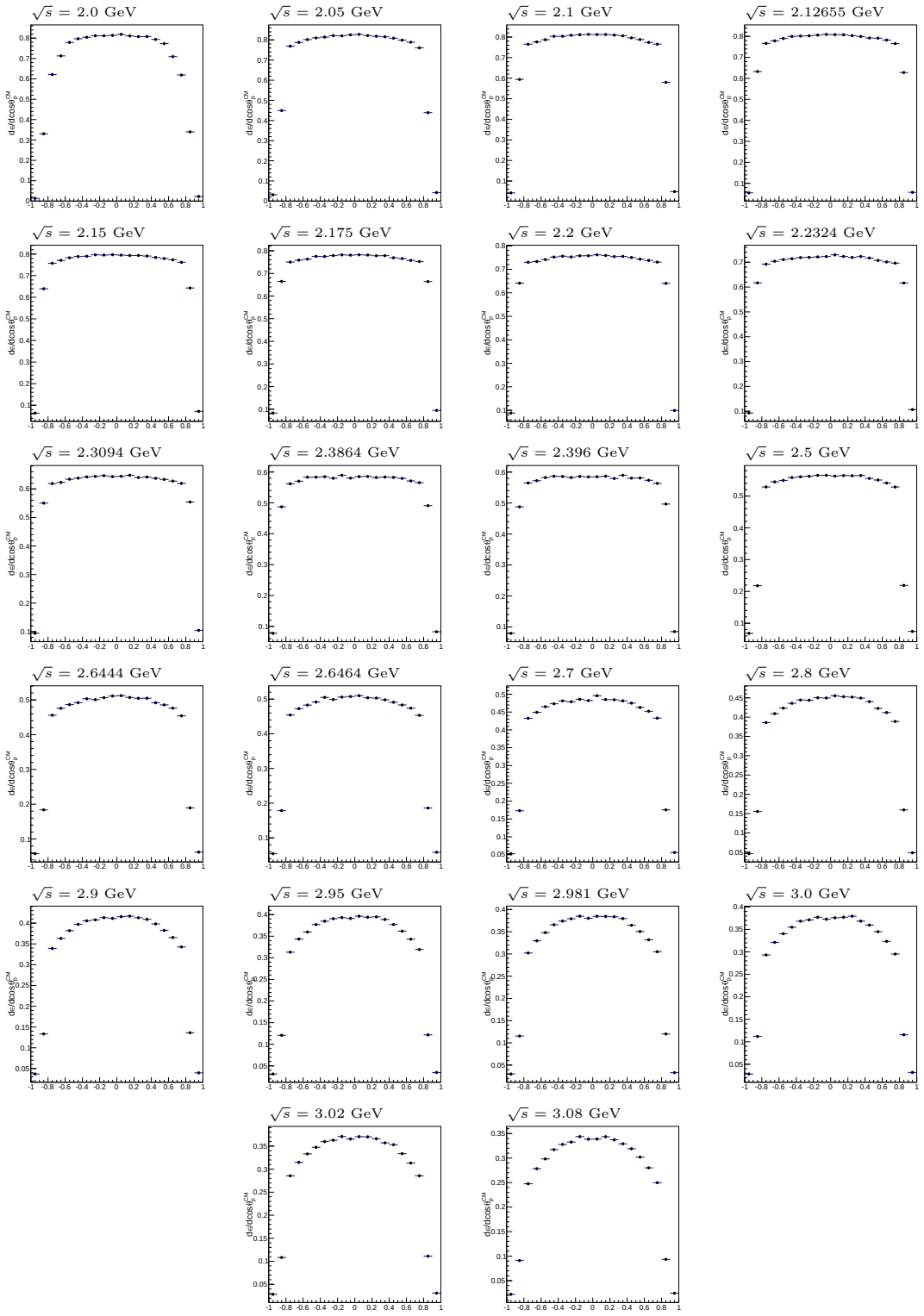

FIGURE A.11: Distributions of detector and selection efficiency in $\cos\theta_p^{CM}$ for all energy points of the 2015 data set.

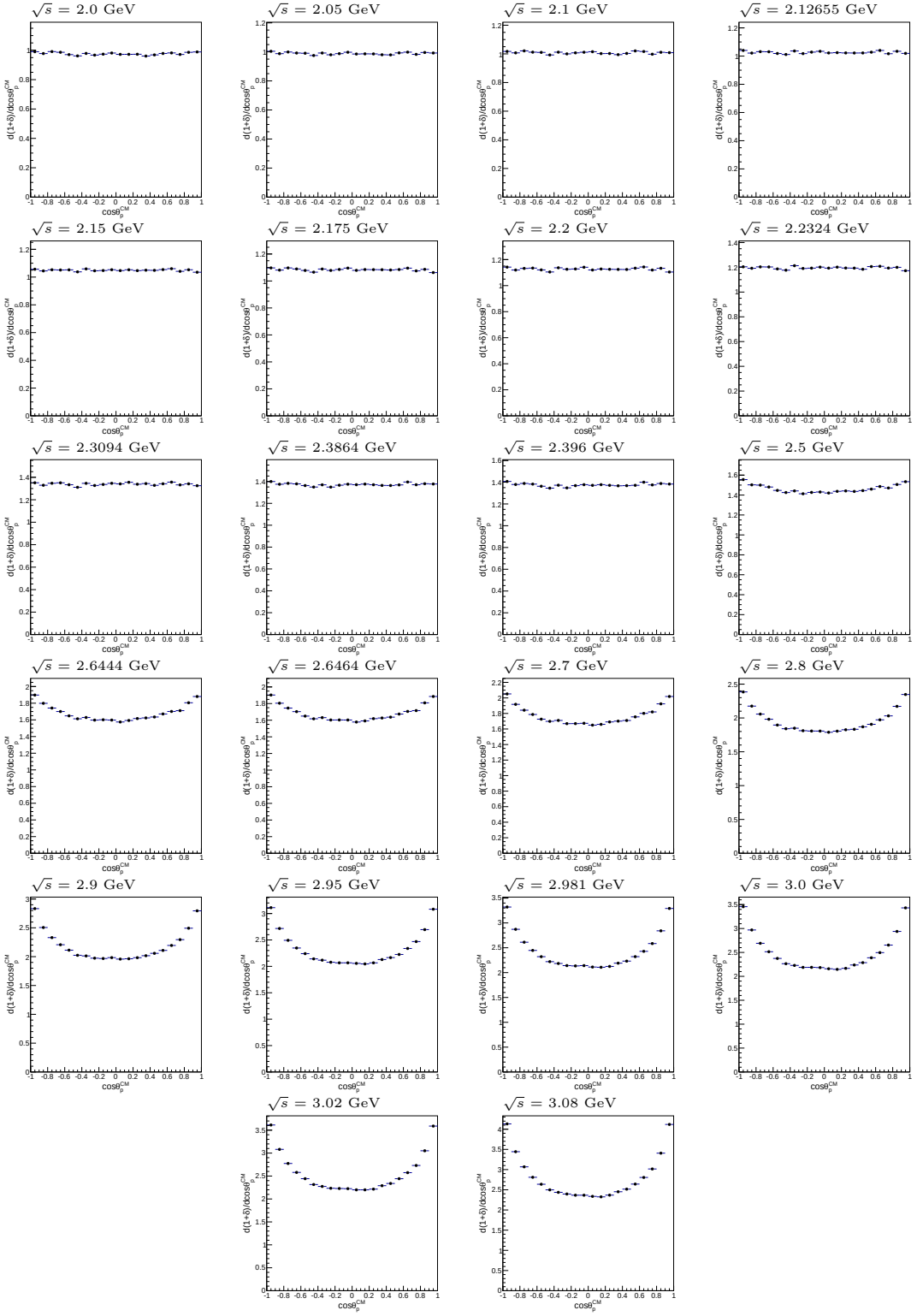

FIGURE A.12: Distributions of the radiative correction factor $(1+\delta)$ in $\cos\theta_p^{CM}$ for all energy points of the 2015 data set. The radiative correction includes ISR up to NNlO, FSR up to NLO and vacuum polarisation.

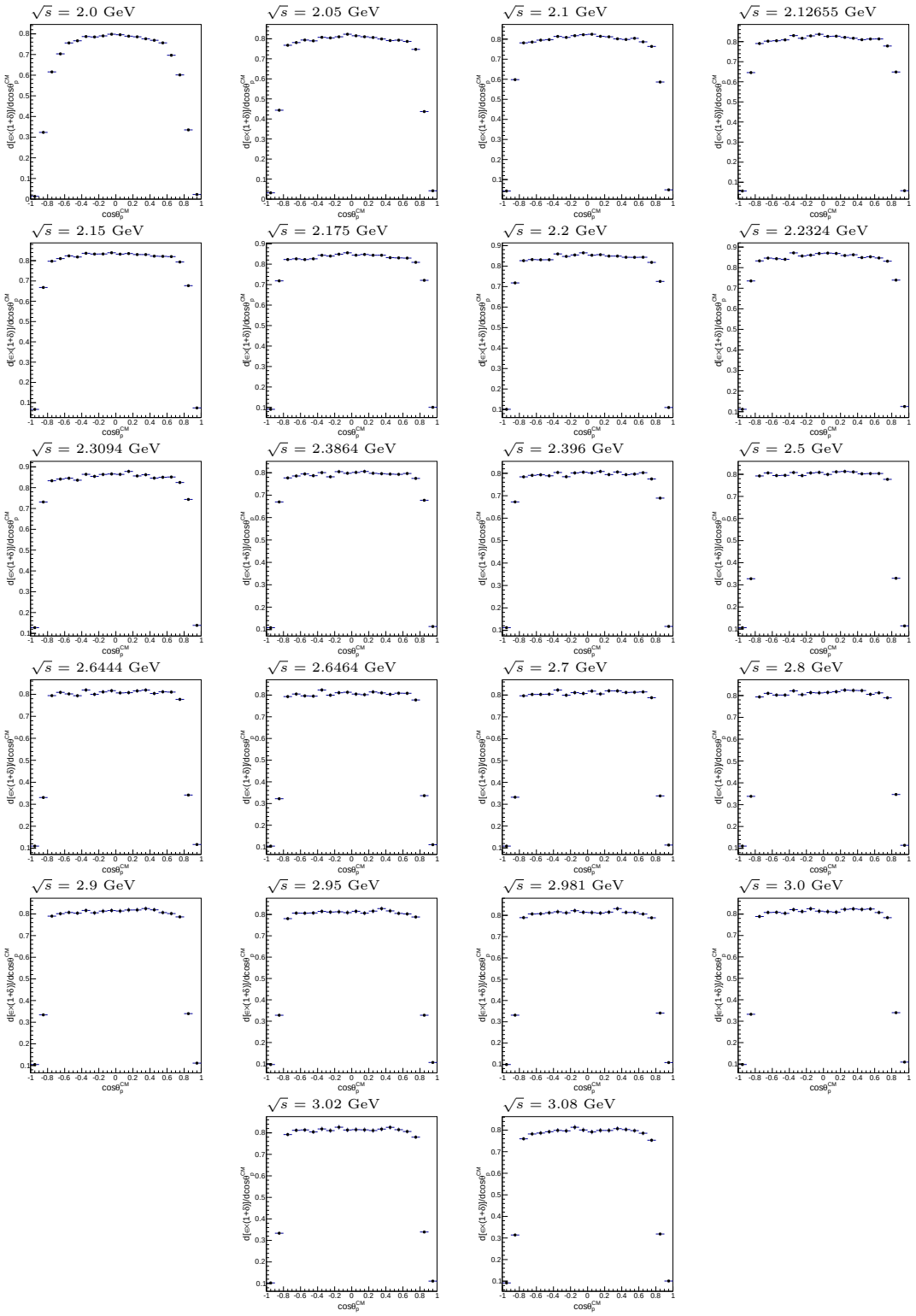

FIGURE A.13: Distributions of the product of the radiative correction factor and the total efficiency in $\cos\theta_p^{CM}$ for all energy points of the 2015 data set.

A.3.2 Plots for the proton EM FF extraction using the fit method

Here, additional plots for all CM energies of the angular distributions of selected $e^+e^- \to p\bar{p}$ events are shown after efficiency and radiative corrections, including a performed fit to extract the proton EM FFs. A detailed discussion about the fit method can be found in section 9.2.1.

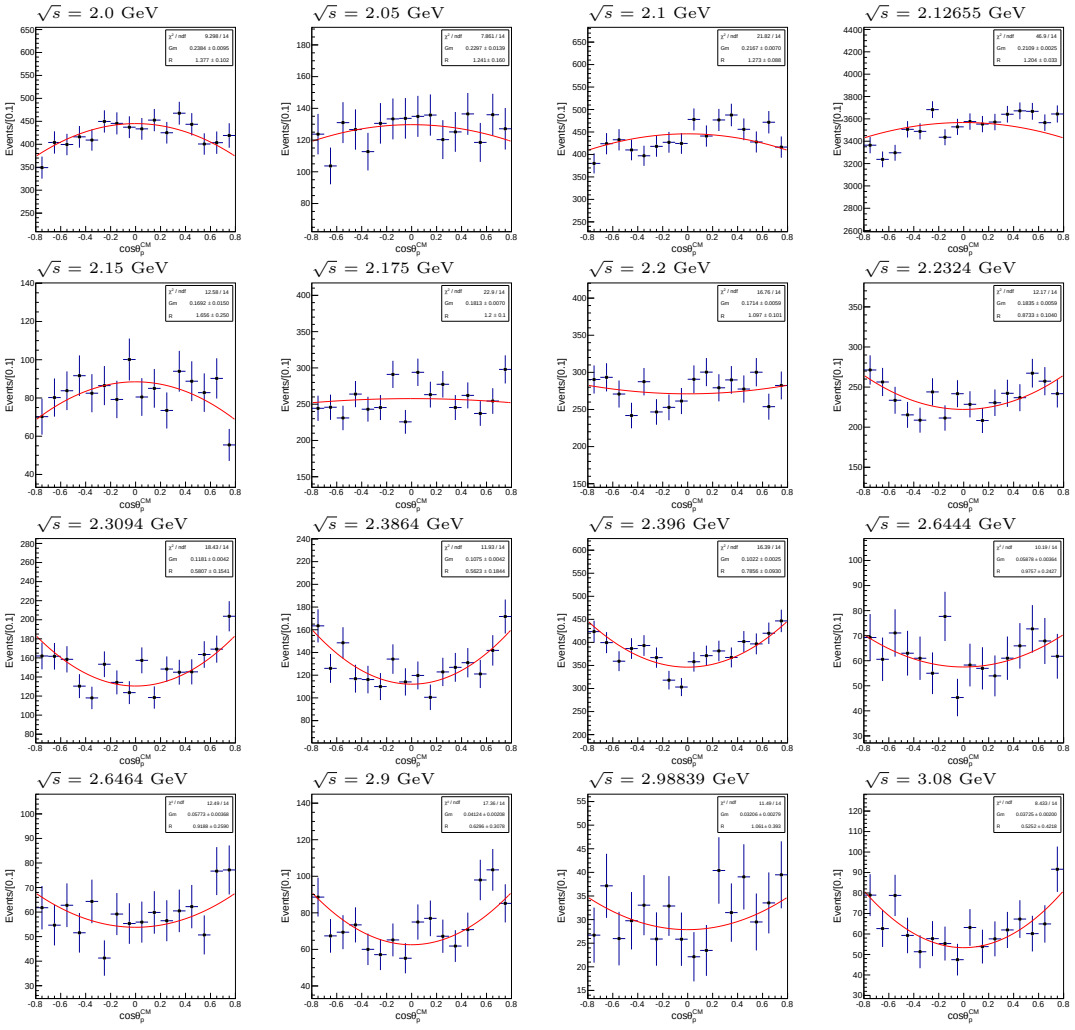

FIGURE A.14: Distributions of the selected $e^+e^- \to p\bar{p}$ events in $\cos\theta_p^{CM}$ for all energy points of the 2015 data set with enough remaining events after selection to allow for an angular analysis, as well as a merged sample of the data at 2.95-3.02 GeV with a luminosity weighted average CM energy of 2.98839 GeV. Shown is the data (black dots with error bars) after efficiency and radiative corrections along with a fit according to equation 9.4.

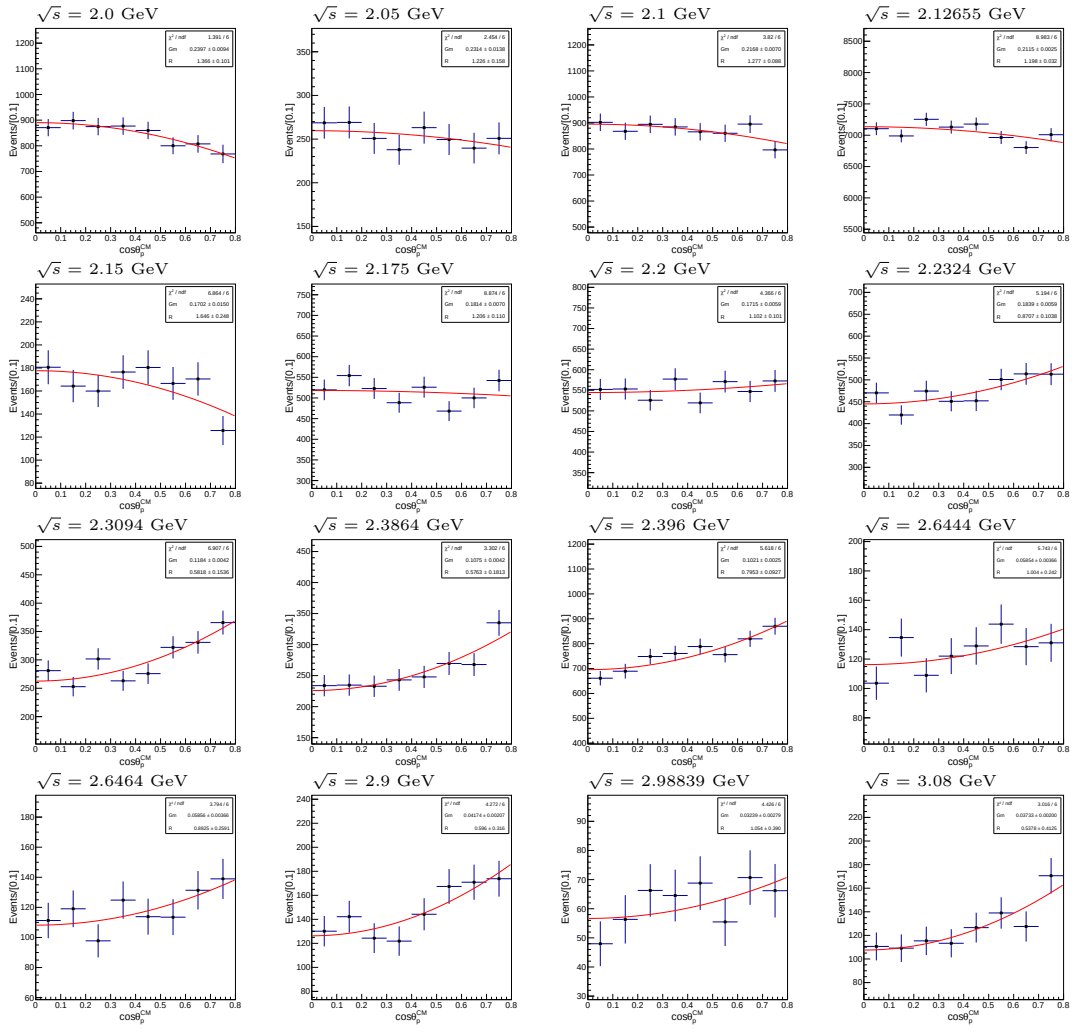

FIGURE A.15: Distributions of the selected $e^+e^- \to p\bar{p}$ events in $|\cos\theta_p^{CM}|$ (instead of $\cos\theta_p^{CM}$ in figure A.14) for all energy points of the 2015 data set with enough remaining events after selection to allow for an angular analysis, as well as a merged sample of the data at 2.95-3.02 GeV with a luminosity weighted average CM energy of 2.98839 GeV. Shown is the data (black dots with error bars) after efficiency and radiative corrections along with a fit according to equation 9.4.

A.3.3 Efficiency and radiative correction plots for the method of moments

In figure A.16, additional distributions for all CM energies are shown for the determination of $\epsilon(\cos\theta_p^{CM}) \times (1+\delta)(\cos\theta_p^{CM})$ through a polynomial fit function, which is necessary for an event-by-event correction of the data to prepare the extraction of the EM FFs of the proton with the method of moments. A detailed explanation of the method can be found in section 9.2.2.

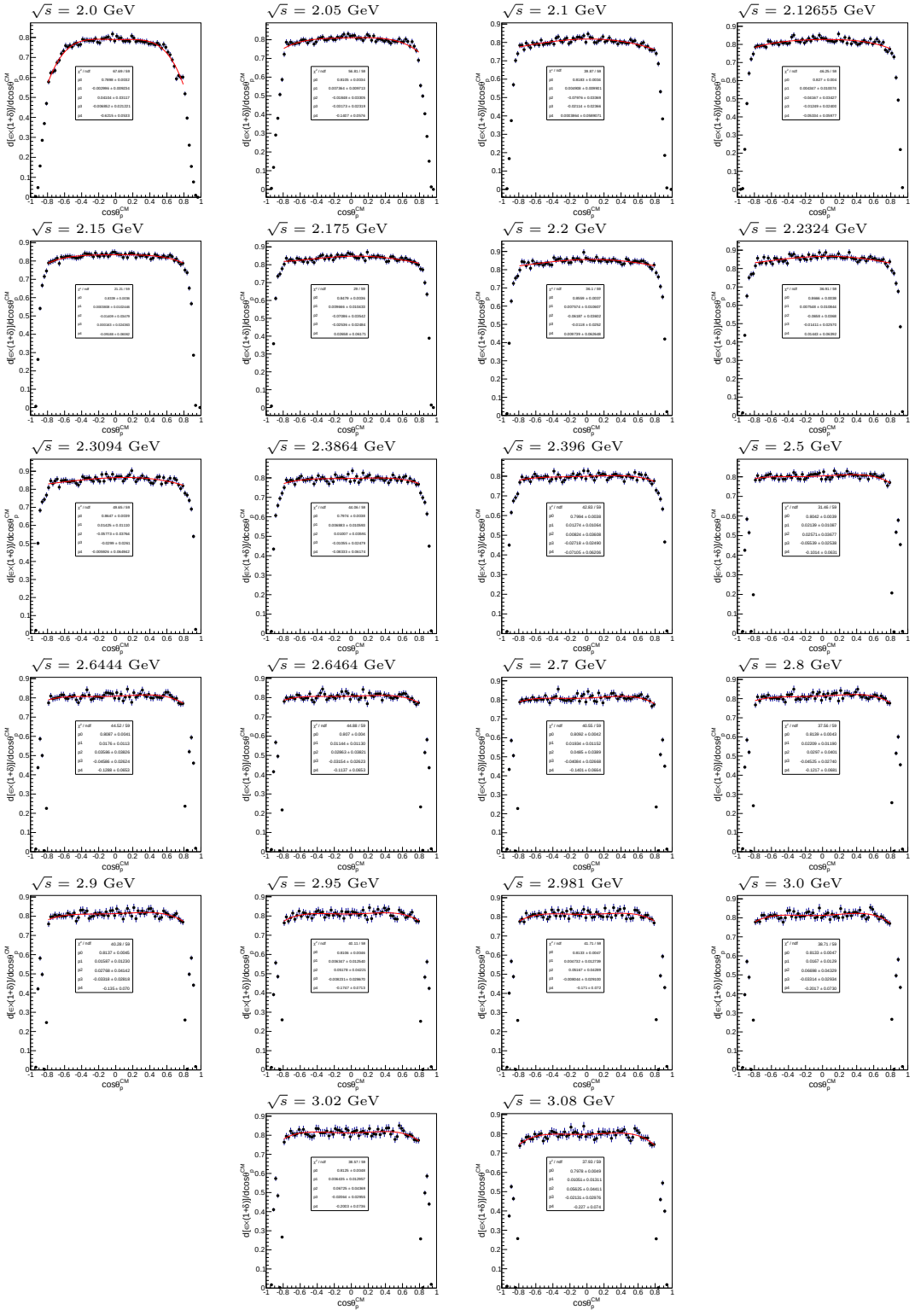

FIGURE A.16: Distributions of the product of the radiative correction factor and the total efficiency in $\cos\theta_p^{CM}$ for all energy points of the 2015 data set. A fit with a polynomial function is applied to extract the value of $\epsilon(\cos\theta_p^{CM}) \times (1+\delta)(\cos\theta_p^{CM})$ for each $\cos\theta_p^{CM}$ value, necessary for an event-by-event correction in the method of moments.

Appendix B

B.1 Comparison of the Fit method and the method of moments for the final results of the proton EM FFs

The two methods to extract the EM FFs of the proton are introduced in sections 9.2.1 and 9.2.2 for the fit and the method of moments, respectively. A comparison with a first round of results using MC with the default FF model of Phokhara is presented in section 9.3. Here, the same comparison is performed with the final results of this thesis, which are extracted after an iterative tuning procedure described in section 9.4.

TABLE B.1: Comparison of the results for the EM FF of the proton $|G_M|$ and the ratio of the two FFs $R = G_E/G_M$ from the fit method (see section 9.2.1) and the method of moments (MoM, see section 9.2.2). Shown are the final results of this work after the MC tuning procedure of section 9.4.

E_{cm}[GeV]	$R = \lvert G_E/G_M \rvert$			$\lvert G_M \rvert$ [10^{-2}]		
	Fit method	MoM	ΔR[%]	Fit method	MoM	ΔG_M[%]
2	1.37±0.10	1.387±0.083	1.36	23.93±0.94	23.77±0.76	0.67
2.05	1.23±0.16	1.21±0.14	1.57	23.0±1.4	23.2±1.2	0.84
2.1	1.270±0.087	1.277±0.077	0.61	21.68±0.70	21.63±0.61	0.23
2.12655	1.198±0.032	1.201±0.026	0.27	21.09±0.25	21.07±0.20	0.086
2.15	1.66±0.25	1.60±0.22	3.36	16.9±1.5	17.3±1.3	2.34
2.175	1.21±0.11	1.21±0.10	0.33	18.14±0.70	18.14±0.62	0.01
2.2	1.08±0.10	1.108±0.090	2.20	17.26±0.59	17.14±0.53	0.71
2.2324	0.86±0.10	0.893±0.093	3.62	16.73±0.54	16.59±0.48	0.84
2.3094	0.60±0.15	0.59±0.14	1.04	11.83±0.42	11.87±0.38	0.30
2.3864	0.58±0.18	0.55±0.16	4.27	10.74±0.42	10.81±0.36	0.62
2.396	0.793±0.093	0.806±0.081	1.64	10.21±0.25	10.18±0.22	0.27
2.6444	1.00±0.24	1.05±0.22	4.68	5.85±0.36	5.80±0.33	0.81
2.6464	0.88±0.26	0.89±0.23	0.75	5.84±0.36	5.85±0.32	0.11
2.9	0.60±0.31	0.64±0.27	5.96	4.17±0.21	4.16±0.18	0.34
2.98839	1.05±0.39	1.09±0.44	3.59	3.24±0.28	3.23±0.25	0.24
3.08	0.51±0.43	0.42±0.35	17.72	3.35±0.18	3.39±0.15	1.14

The comparison is shown in table B.1. Similar to the comparison of the first round of results, the two methods are in good agreement, with a maximum deviation in units of the standard deviation of the fit method σ_{fit} of 0.3 σ_{fit}^{R} for the R measurement at 2.2324 GeV and 0.27 $\sigma_{fit}^{|G_M|}$ for the $|G_M|$ measurement at 2.15 GeV.

Appendix C

In this appendix, additional information is shown for the studies of the systematic uncertainty of the cross section measurement of $e^+e^- \to p\bar{p}$ as well as the effective and individual EM FF measurement of the proton. The investigation of the systematic uncertainty can be found in chapter 10.

C.1 Additional plots for the cross section and effective FF measurement

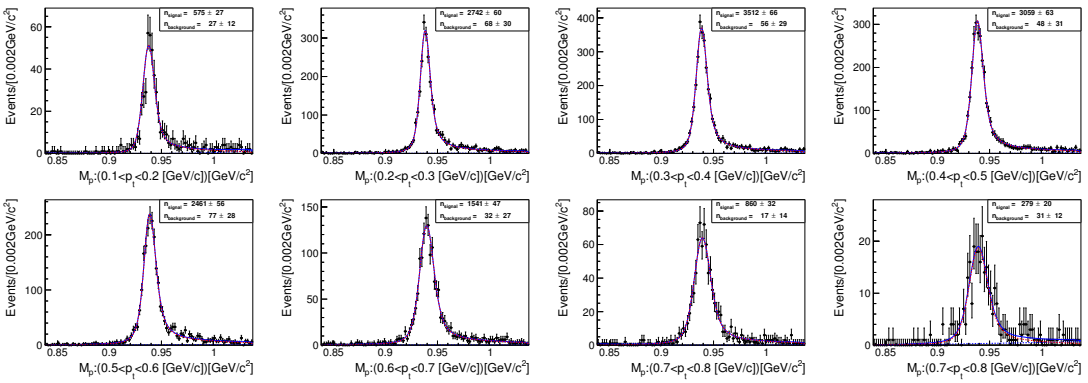

(1) number of tracks=4

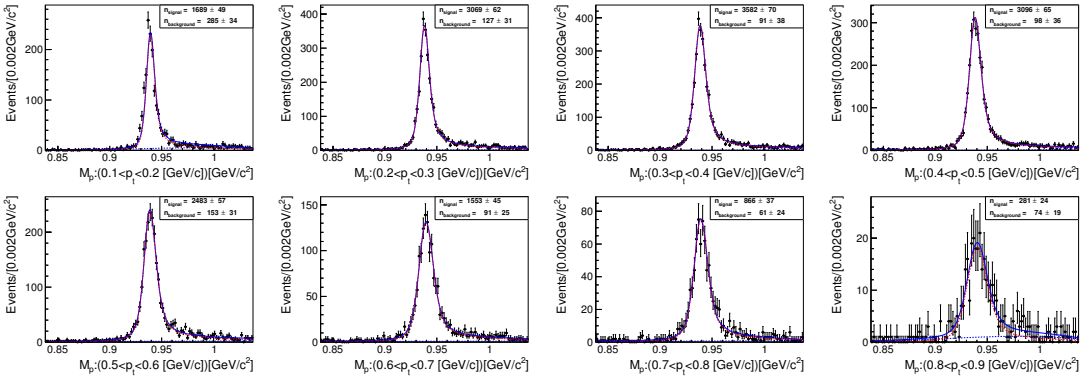

(2) number of tracks=3||4

FIGURE C.1: Proton mass distributions and fit results depending on the transverse momentum of the proton for number of tracks=4 or number of tracks=3||4 events.

C.1.1 Tracking efficiency study

Here, additional plots for the study of the tracking efficiency are shown. The shown plots are used to extract the number of total events in the control sample $e^+e^- \to p\bar{p}\pi^+\pi^-$ (plots with number of tracks =3||4) and the number of events where the fourth track has been reconstructed successfully (plots with number of tracks = 4), both of which allow to determine the uncertainty of the tracking efficiency in section 10.1.1. This is shown in bins of the transverse momentum in figure C.1 for the proton and figure C.2 for the antiproton. The same analysis in bins of $\cos\theta_p^{CM}$ is shown in figure C.3 for the proton and figure C.4 for the antiproton.

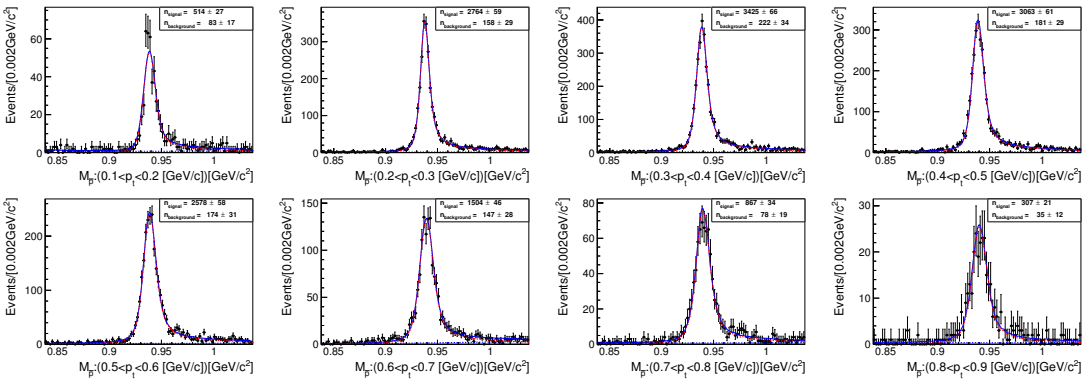

(1) number of tracks=4

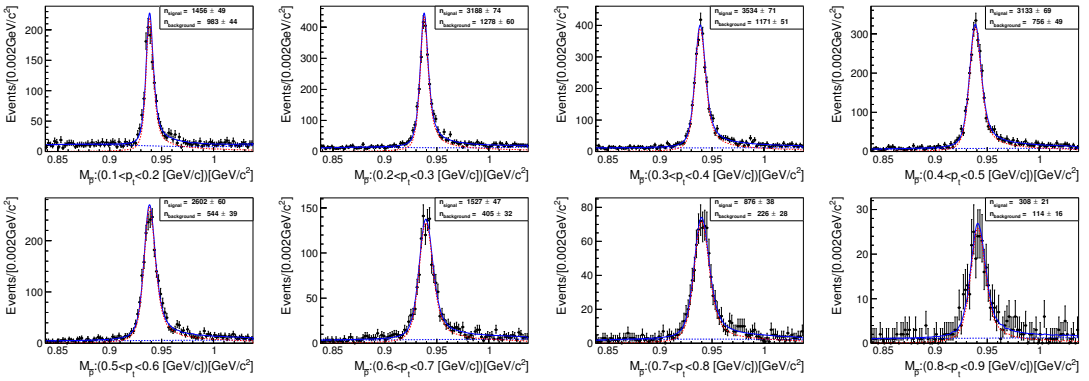

(2) number of tracks=3||4

FIGURE C.2: Antiproton mass distributions and fit results depending on the transverse momentum of the antiproton for number of tracks=4 or number of tracks=3||4 events.

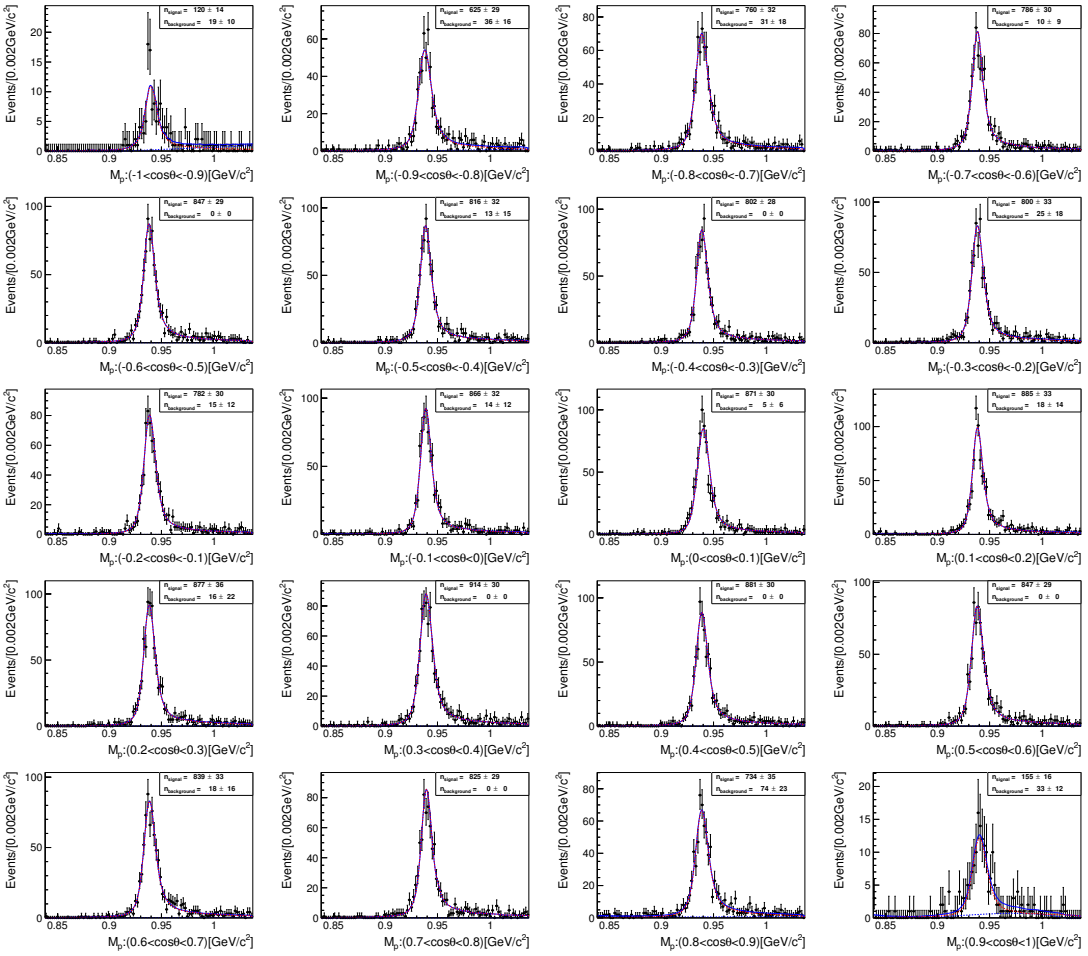

(1) number of tracks=4

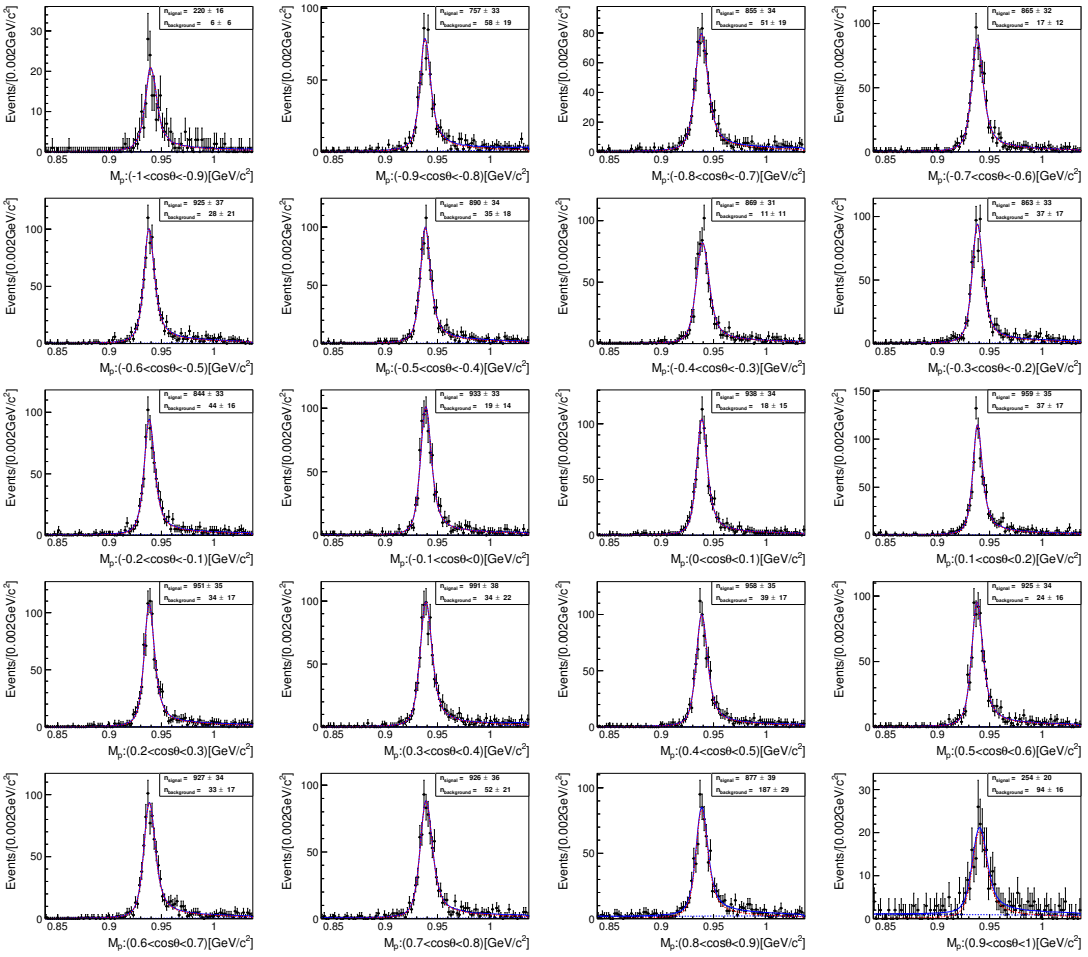

(2) number of tracks=3||4

FIGURE C.3: Proton mass distributions and fit results depending on the cosine of the polar angle of the proton for number of tracks=4 or number of tracks=3||4 events.

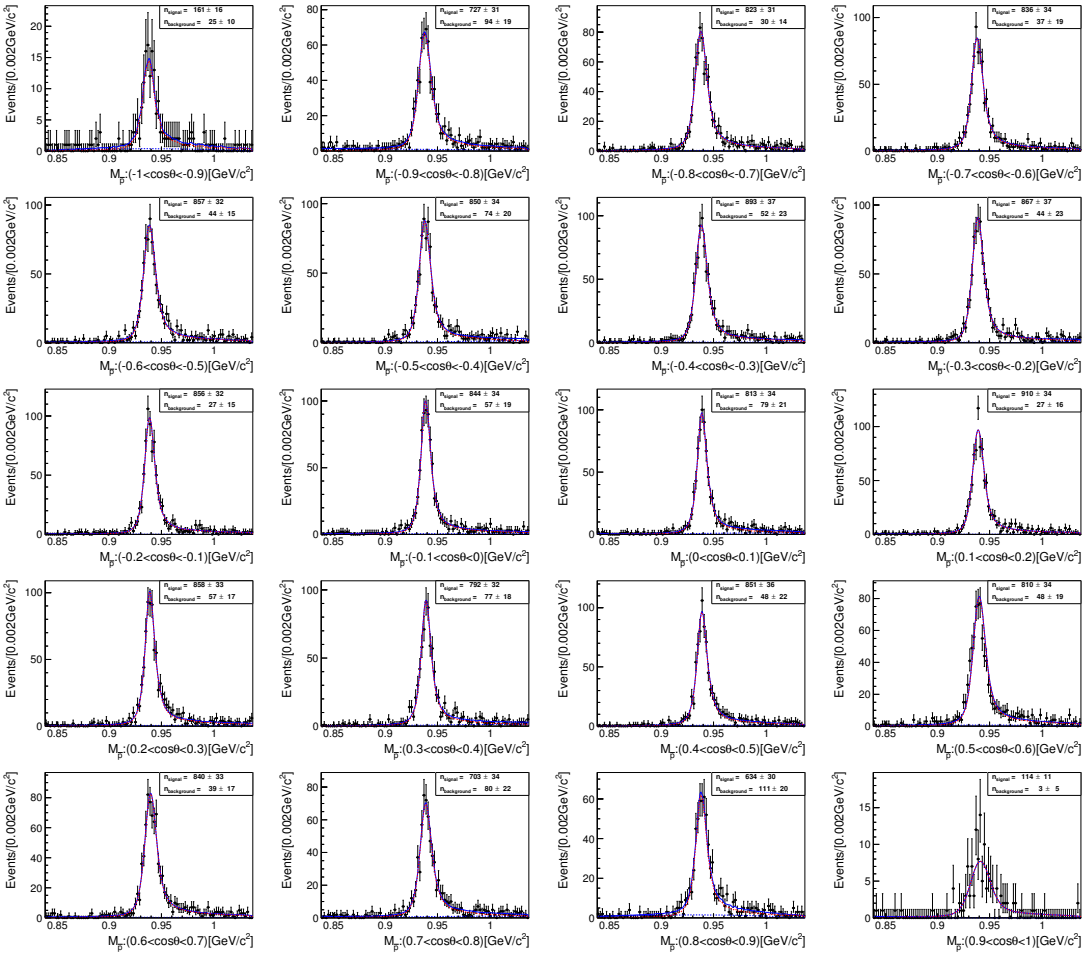

(1) number of tracks=4

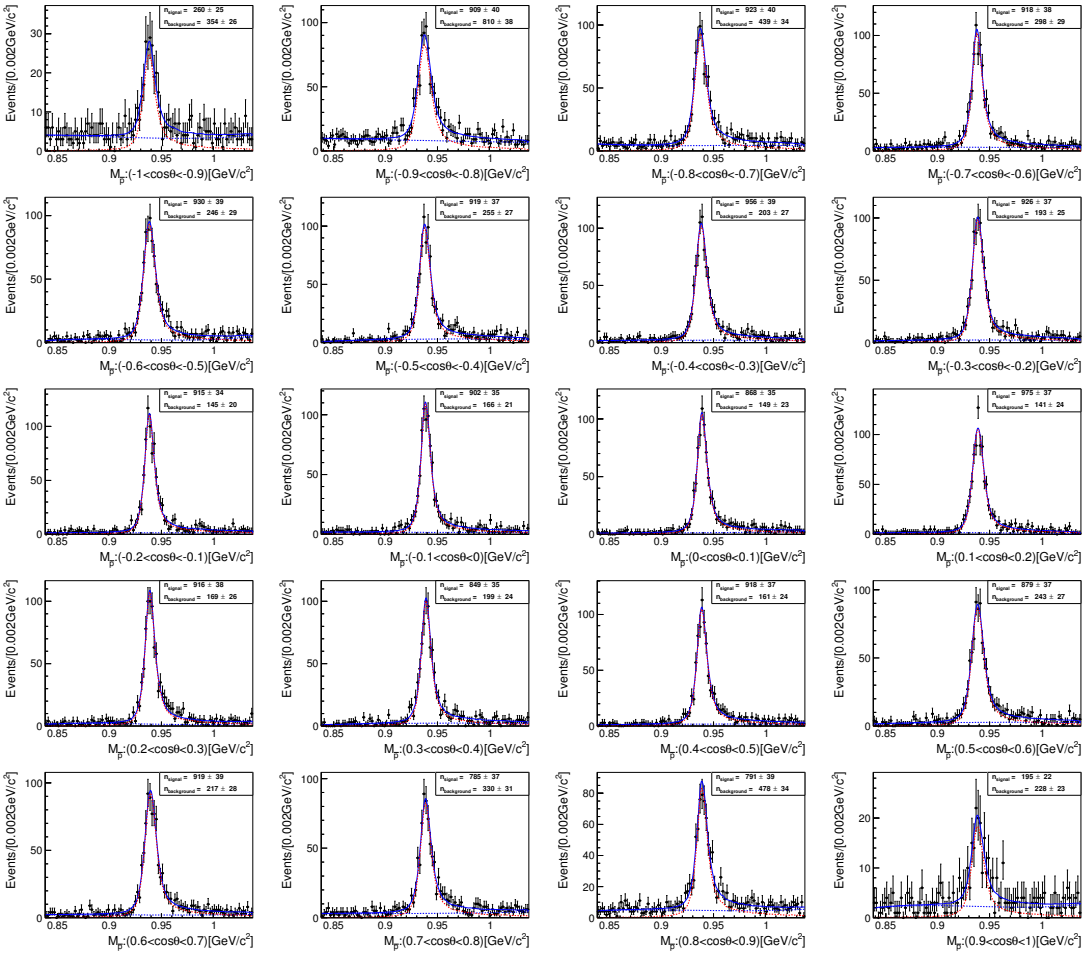

(2) number of tracks=3||4

FIGURE C.4: Antiproton mass distributions and fit results depending on the cosine of the polar angle of the antiproton for number of tracks=4 or number of tracks=3||4 events.

C.1.2 PID requirement efficiency study

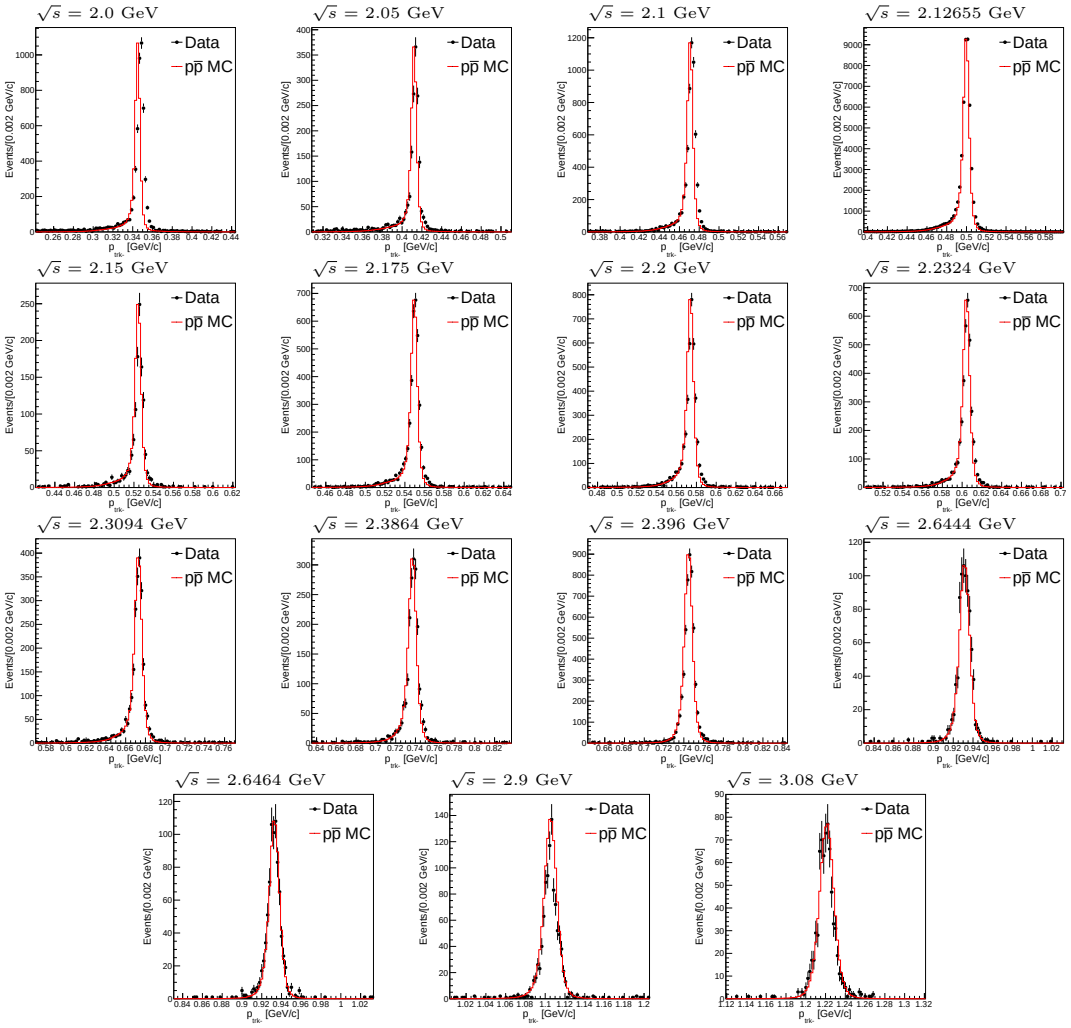

FIGURE C.5: Momentum distribution of the proton for all CM energies with enough remaining events for data (black points with error bars) compared with signal MC (red line) including radiative corrections up to NNLO. Compared to the main analysis, no PH_{norm} requirement ($\sqrt{s} \leq 2.15$ GeV) or PID requirement ($\sqrt{s} > 2.15$) has been applied to the negative track to study the proton PID or PH_{norm} efficiency, respectively, while a number of other requirements have been tightened.

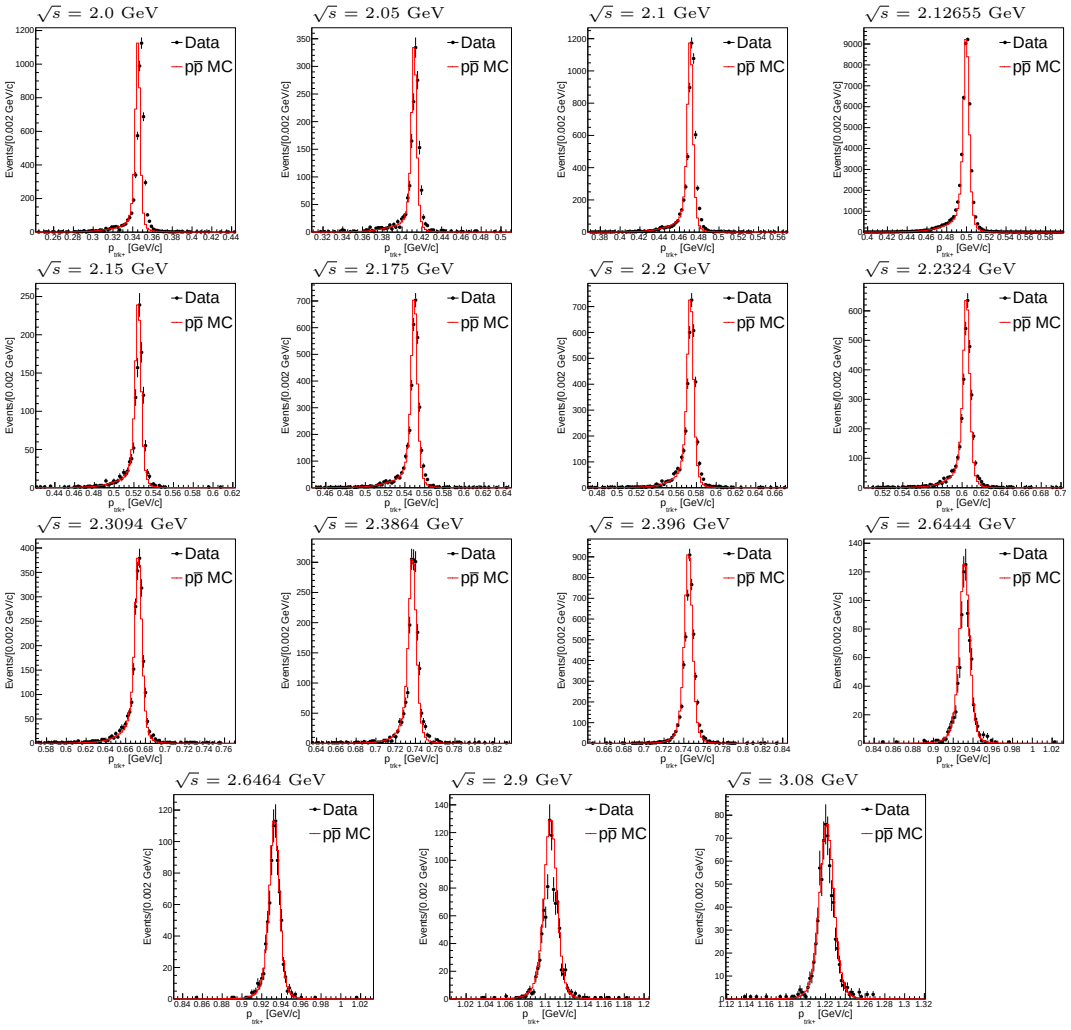

FIGURE C.6: Momentum distribution of the antiproton for all CM energies with enough remaining events for data (black points with error bars) compared with signal MC (red line) including radiative corrections up to NNLO. Compared to the main analysis, no PH_{norm} requirement ($\sqrt{s} \leq 2.15$ GeV) or PID requirement ($\sqrt{s} > 2.15$) has been applied to the positive track to study the antiproton PID or PH_{norm} efficiency, respectively, while a number of other requirements have been tightened.

C.1.3 E/p requirement efficiency study

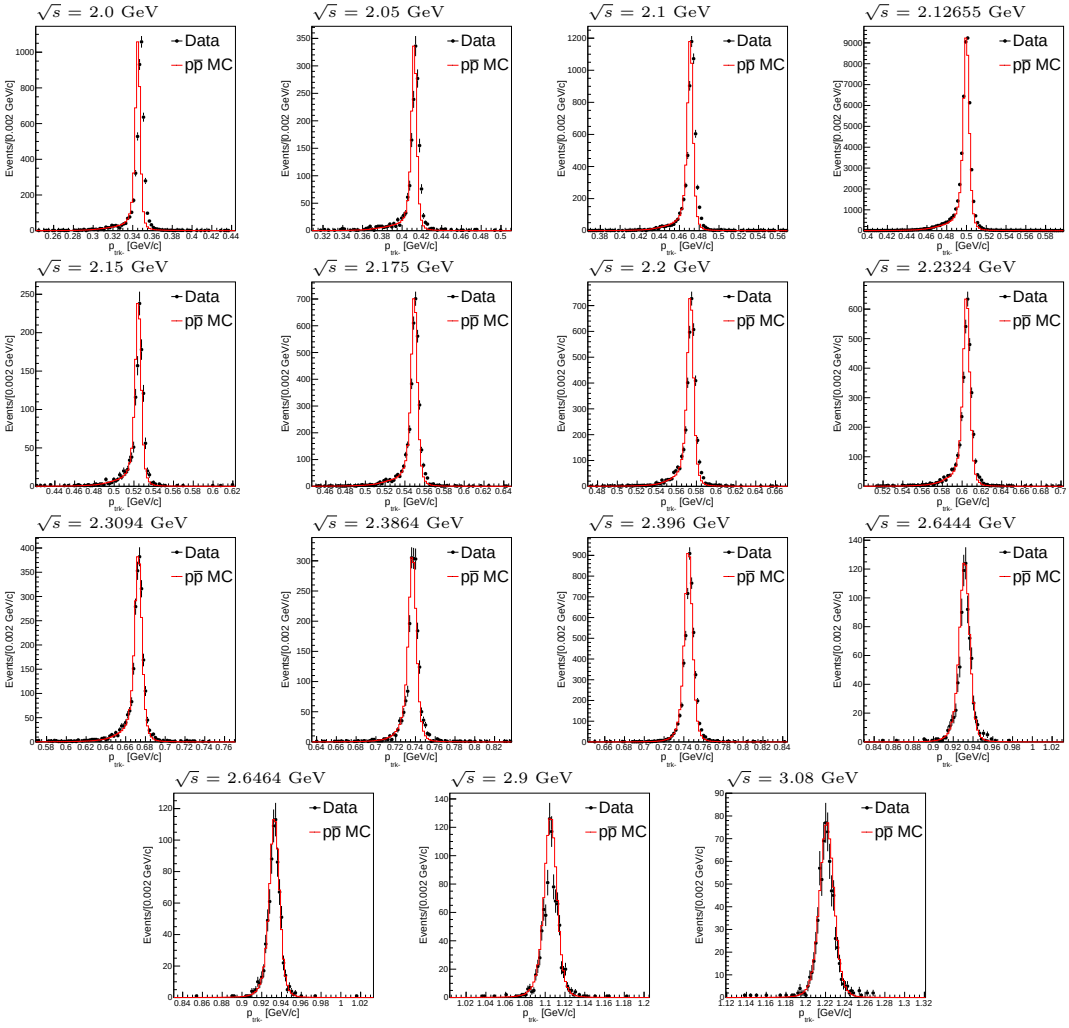

FIGURE C.7: Momentum distribution of the proton for all CM energies with enough remaining events of data (black points with error bars) compared with signal MC (red line). Compared to the main analysis, no E/p requirement has been applied while a number of other requirements have been tightened.

C.2 Additional plots for the form factor measurement

C.2.1 Uncertainty due to efficiency differences in data and MC

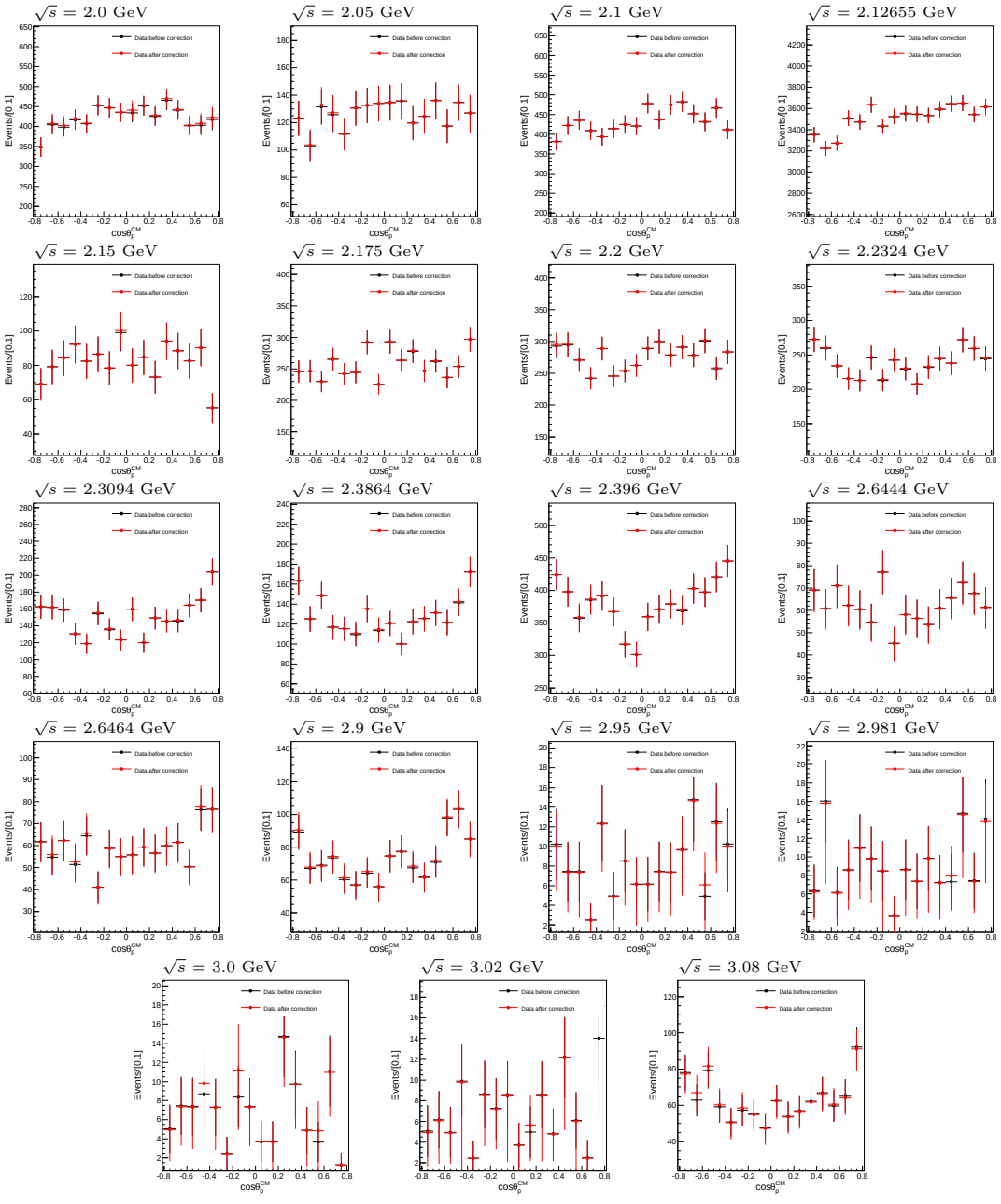

FIGURE C.8: Efficiency corrected distributions of data in $\cos\theta_p^{CM}$ before (black dots with error bars) and after (red dots with error bars) correcting for efficiency differences in PID (or PH_{norm}) selection criteria between data and MC for all CM energies of the 2015 scan data set.

C.2.2 Uncertainty due to remaining background

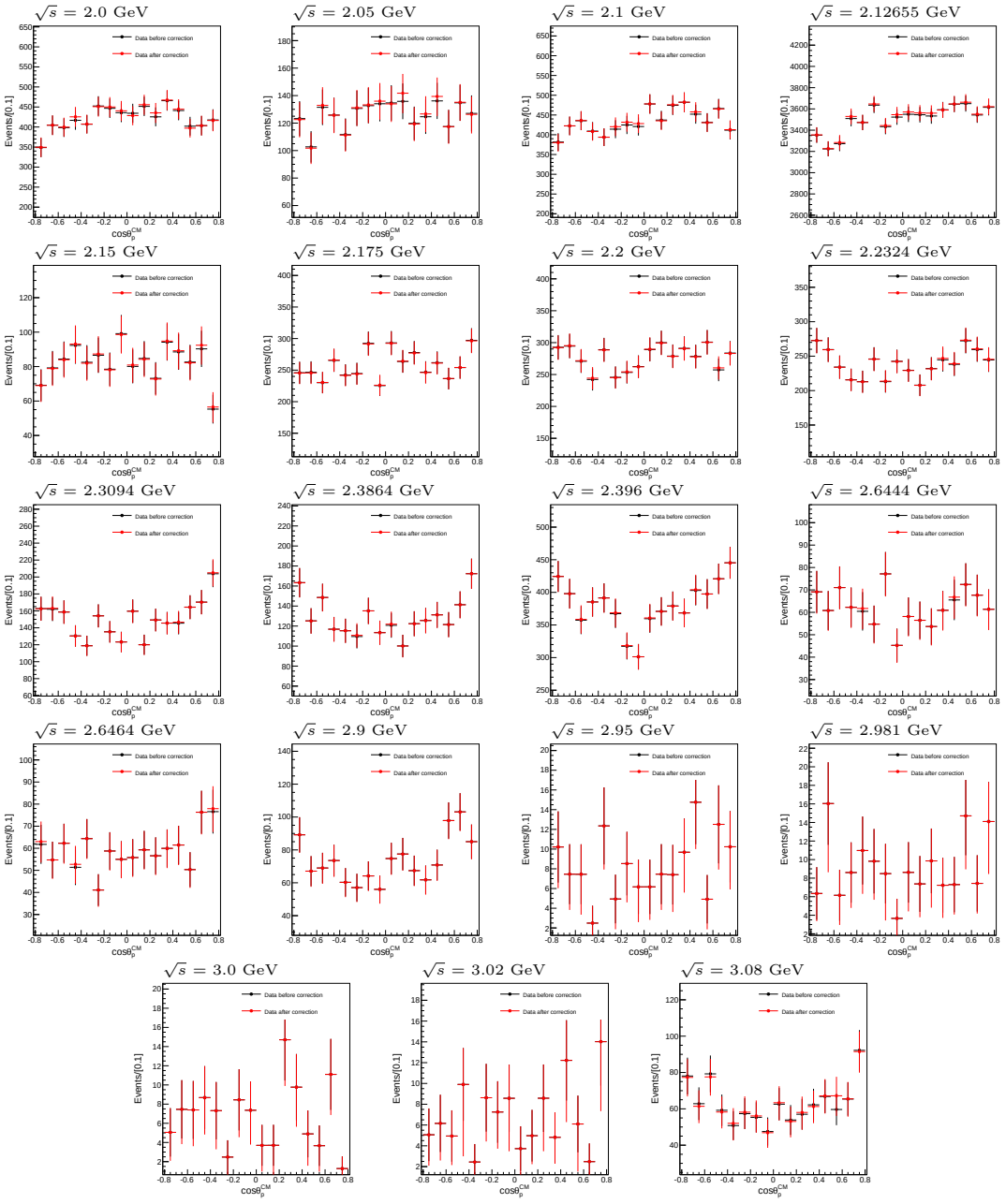

FIGURE C.9: Efficiency corrected distributions of data in $\cos\theta_p^{CM}$ before (black dots with error bars) and after (red dots with error bars) correcting for efficiency differences in the E/p selection criteria between data and MC for all CM energies of the 2015 scan data set.

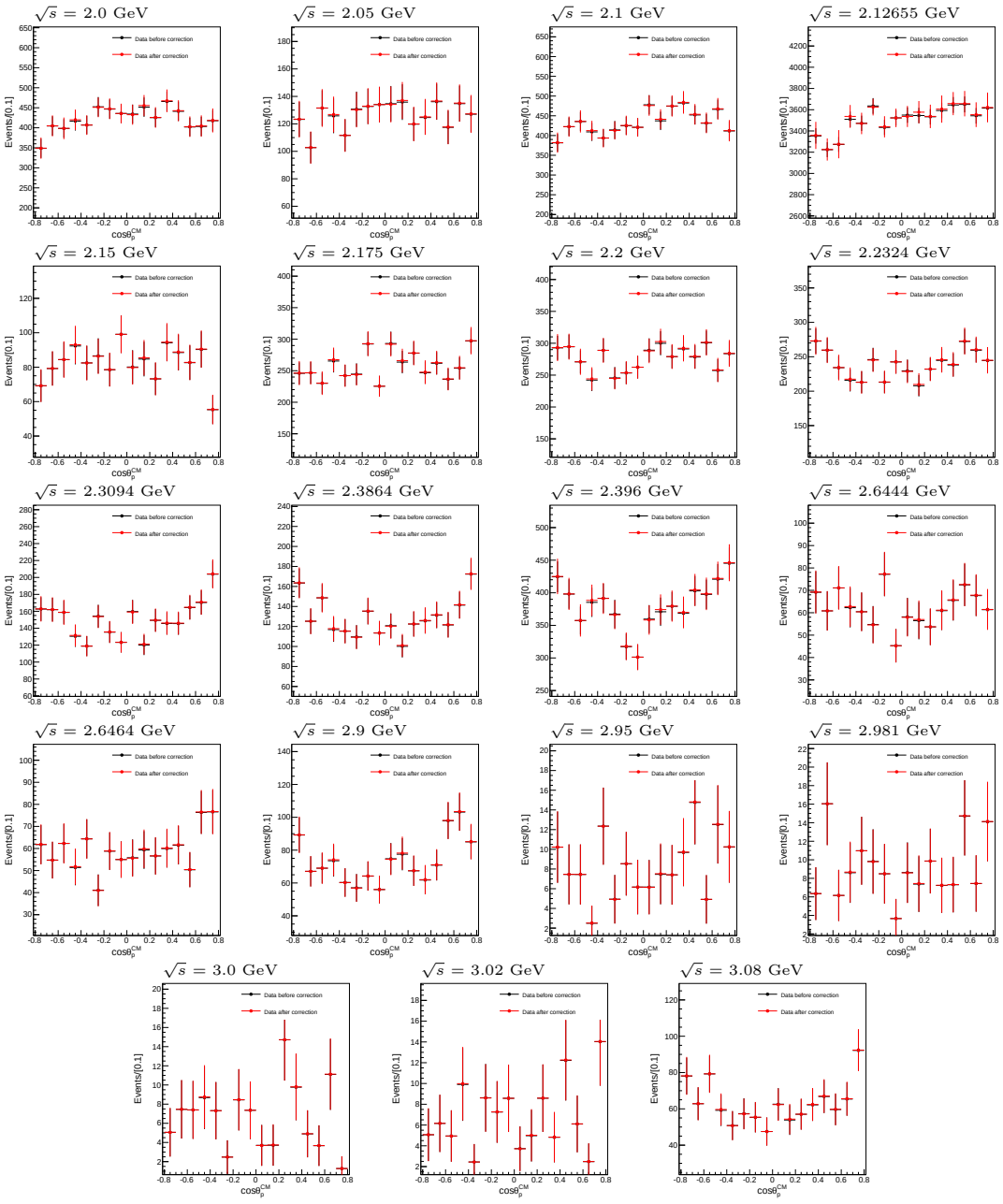

FIGURE C.10: Efficiency corrected distributions of data in $\cos\theta_p^{CM}$ before (black dots with error bars) and after (red dots with error bars) correcting for efficiency differences in tracking between data and MC for all CM energies of the 2015 scan data set.

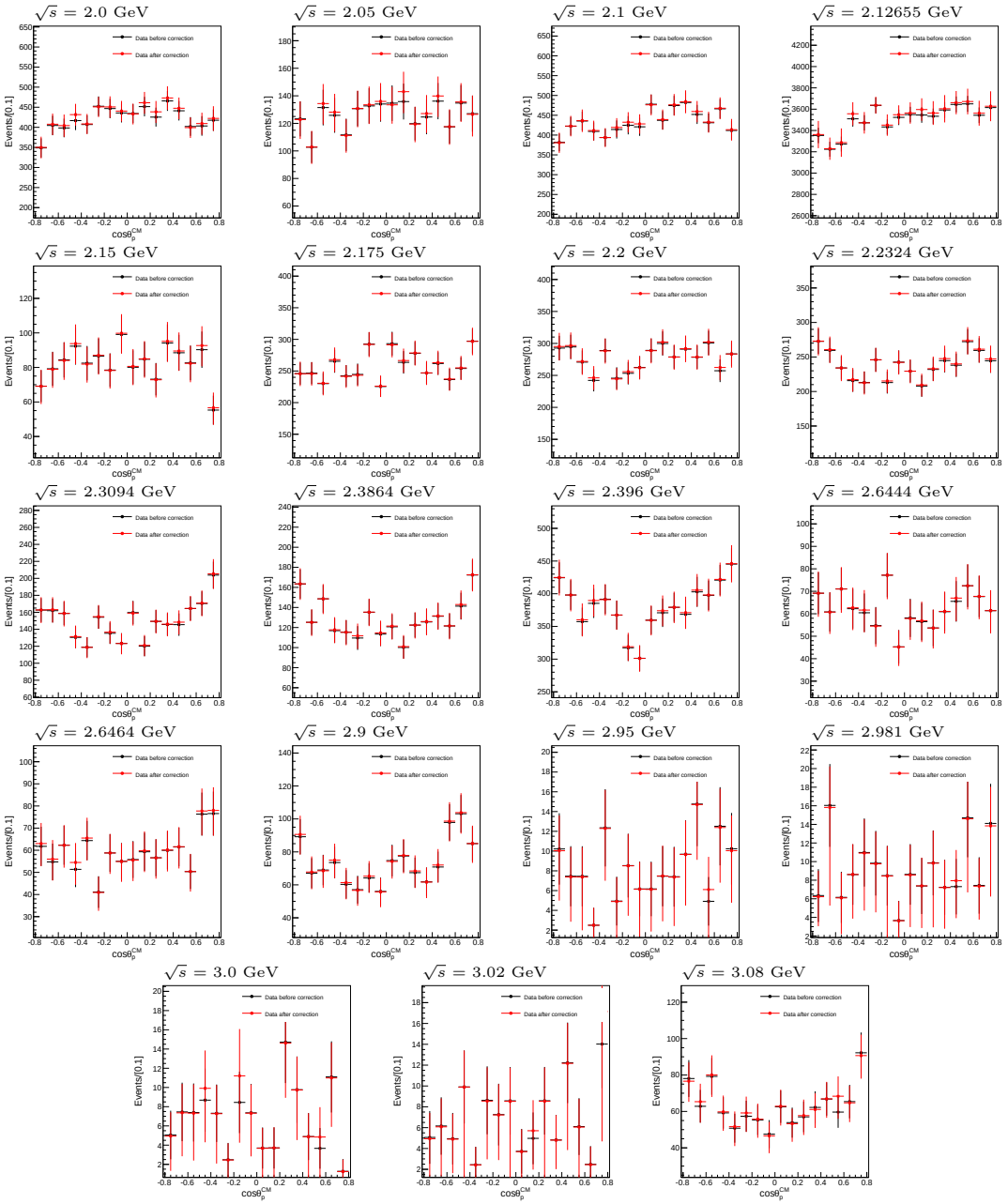

FIGURE C.11: Efficiency corrected distributions of data in $\cos\theta_p^{CM}$ before (black dots with error bars) and after (red dots with error bars) correcting for efficiency differences in tracking, PID (or PH_{norm}) and E/p selection criteria between data and MC for all CM energies of the 2015 scan data set.

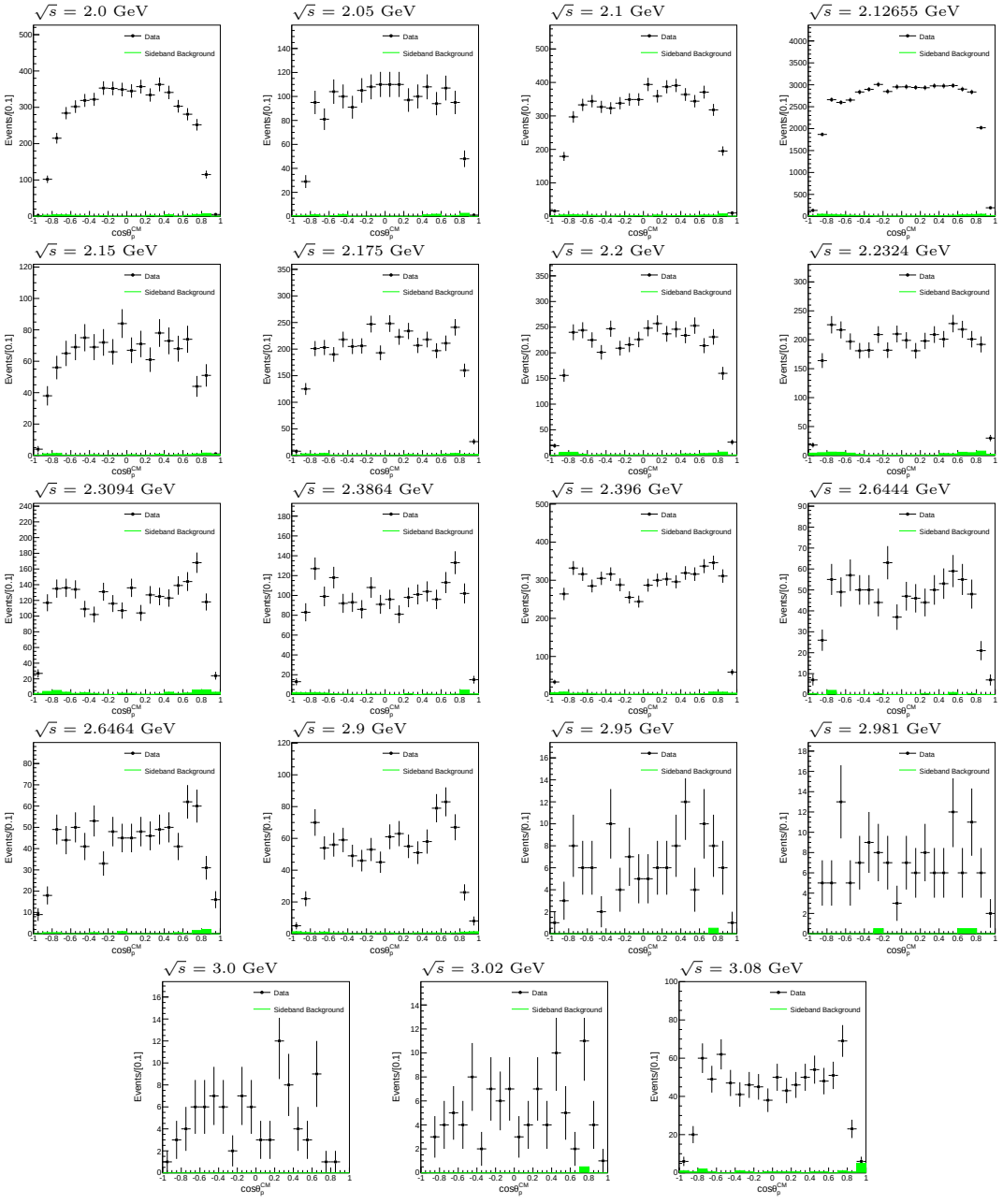

FIGURE C.12: Distributions of data in $\cos\theta_p^{CM}$ before efficiency correction (black dots with error bars) with the distribution of remaining background events extracted with the two-dimensional sideband method in $\cos\theta_p^{CM}$ (green histogram) for all CM energies of the 2015 data set.

List of Figures

List of Tables

Abbreviations

ADC	**A**nalog-to-**D**igital **C**onverter
BEPCII	**B**eijing **E**lectron **P**ositron **Collider II**
BESIII	**BE**ijing **S**pectrometer **III**
BOSS	**B**es **O**ffline **S**oftware **S**ystem
CM	**C**enter of **M**ass
CQM	**C**onstituent **Q**uark **M**odel
DAQ	**D**ata **A**c**Q**uisition
EMC	**E**lectro**M**agnetic **C**alorimeter
EM FFs	**E**lectro**M**agnetic **F**orm **F**actor**s**
E/p	energy (from EMC) over momentum (from MDC)
EWT	**E**lectro**W**eak **T**heory
FSR	**F**inal **S**tate **R**adiation
GKL	**G**ari-**K**rümpelman-**L**omon (model)
$\mathbf{G_E}$	Electric Sachs form factor
$\mathbf{G_M}$	Magnetic Sachs form factor
GR	**G**eneral **R**elativity
GUT	**G**rand **U**nified **T**heory
IJL	**I**achello, **J**ackson and **L**ande (model)
ISR	**I**nitial **S**tate **R**adiation
LHC	**L**arge **H**adron **C**ollider
LINAC	**LIN**ear **AC**cellerator
MC	**M**onte **C**arlo
MDC	**M**ultilayer **D**rift **C**hamber
MUC	**MU**on **C**ounter
NLO	**N**ext-to-**L**eading **O**rder

NNLO	**N**ext-to-**N**ext-to-**L**eading **O**rder
PH_{norm}	normalised pulse height
PID	**P**article **ID**entification
PMT	**P**hoto **M**ultiplier **T**ube
POA	**P**oint **O**f closest **A**pproach
pQCD	**p**erturbative **Q**uantum **C**hromo**D**ynamics
QCD	**Q**uantum **C**hromo**D**ynamics
QED	**Q**uantum **E**lectro**D**ynamics
QFD	**Q**uantum **F**lavour**D**ynamics
RPC	**R**esistive **P**late **C**ounters
SL	**S**pace-**L**ike
TL	**T**ime-**L**ike
TOF	**T**ime **O**f **F**light
VMD	**V**ector **M**eson **D**ominance

Bibliography

[1] CDF Collaboration. *Phys. Rev. Lett. 74*, pages 2626–2631, 1995.

[2] ATLAS Collaboration. *Physics Letters B 716*, pages 1–29, 2012.

[3] CMS Collaboration. *Physics Letters B 716*, pages 30–61, 2012.

[4] . URL https://www.quantumdiaries.org/2014/03/14/the-standard-model-a-beautiful-but-flawed-theory/.

[5] English wikipedia website of the standard model. URL https://en.wikipedia.org/wiki/StandardModel.

[6] P.A. Zyla *et al.* Review of Particle Physics. *PTEP*, 2020(8):083C01, 2020.

[7] P. Skands. Introduction to QCD. *Searching for New Physics at Small and Large Scales*, 2013.

[8] M. Eidemüller, H.G. Dosch, and M. Jamin. The field strength correlator from QCD sum rules. *Nuclear Physics B - Proceedings Supplements*, 86(1):421 – 425, 2000.

[9] Christoph Berger. *Elementarteilchenphysik*. Springer-Verlag, 2006.

[10] Professor E. Rutherford F.R.S. Lxxix. the scattering of α and β particles by matter and the structure of the atom. *The London, Edinburgh, and Dublin Philosophical Magazine and Journal of Science*, 21(125):669–688, 1911.

[11] Bogdan Povh, Klaus Rith, Christoph Scholz, and Frank Zetsche. *Teilchen und Kerne*. Springer-Verlag, 2004.

[12] C.F. Perdrisat, V. Punjabi, and M. Vanderhaeghen. Nucleon electromagnetic form factors. *Progress in Particle and Nuclear Physics*, 59(2):694–764, 2007.

[13] O. Stern. *Nature*, 132:103, 1933.

[14] R. Hofstadter and R. W. McAllister. Electron scattering from the proton. *Phys. Rev.*, 98:217–218, 1955.

[15] R. Hofstadter. Electron scattering and nuclear structure. *Rev. Mod. Phys.*, 28: 214–254, 1956.

[16] M. N. Rosenbluth. High energy elastic scattering of electrons on protons. *Phys. Rev.*, 79:615–619, 1950.

[17] E. Clementel and C. Villi. On the scattering of high energy electrons by protons. *Nuovo Cim*, 4:1207–1211, 1956.

[18] R. W. McAllister and R. Hofstadter. Elastic scattering of 188-mev electrons from the proton and the alpha particle. *Phys. Rev.*, 102:851–856, 1956.

[19] V. Punjabi, C. F. Perdrisat, M. K. Jones, E. J. Brash, and C. E. Carlson. The structure of the nucleon: Elastic electromagnetic form factors, 2015. URL https://arxiv.org/abs/1503.01452.

[20] H.-W. Hammer. Nucleon form factors in the space- and timelike regions, 2001. URL https://arxiv.org/abs/hep-ph/0105337.

[21] S. Pacetti. Nucleon form factors and dispersion relations. *Eur. Phys. J. A*, 32(4): 421–427, 2007.

[22] A. Z. Dubnickova, S. Dubnicka, and M. P. Rekalo. Investigation of nucleon electromagnetic form-factors in the unphysical region by means of the $\bar{N}N \to \pi l^+ l^-$ reactions. *Z. Phys. C*, 70:473–482, 1996.

[23] C. Adamuščín, E. A. Kuraev, E. Tomasi-Gustafsson, and F. E. Maas. Testing axial and electromagnetic nucleon form factors in time-like regions in the processes $\overline{p}+n \to \pi^- + \ell^- + \ell^+$ and $\overline{p}+p \to \pi^0 + \ell^- + \ell^+, \ell = e, \mu$. *Phys. Rev. C*, 75:045205, 2007.

[24] J. Guttmann and M. Vanderhaeghen. Theoretical analysis of the $p\bar{p} \to \pi_0 e^+ e^-$ process with a Regge framework. *Physics Letters B*, 719(1):136 – 142, 2013.

[25] J. Boucher. *Feasibility studies of the $\bar{p}p \to \pi_0 e^+ e^-$ electromagnetic channel at $\bar{P}ANDA$*. PhD thesis, University of Paris-Sud XI and Johannes Gutenberg University Mainz, 2017.

[26] G. Schneider *et al.* Double-trap measurement of the proton magnetic moment at 0.3 parts per billion precision. *Science*, 358(6366):1081–1084, 2017.

[27] S. Pacetti, R. Baldini Ferroli, and E. Tomasi-Gustafsson. Proton electromagnetic form factors: Basic notions, present achievements and future perspectives. *Phys. Rept.*, 550-551:1–103, 2015.

[28] E. Pharagmén and E. Lindelöf. Sur une extension d'un principe classique de l'analyse et sur quelques propriétés des fonctions monogènes dans le voisinage d'un point singulier. *Acta Math.*, 31:381–406, 1908.

[29] E. C. Titchmarsh. *The Theory of Functions.* Oxford science publications. Oxford University Press, 1939.

[30] L. Andivahis *et al.* Measurements of the electric and magnetic form factors of the proton from q^2=1.75 to 8.83 $(\mathrm{GeV/c})^2$. *Phys. Rev. D*, 50:5491–5517, 1994.

[31] L. N. Hand *et al.* Electric and magnetic form factors of the nucleon. *Rev. Mod. Phys.*, 35:335–349, 1963.

[32] J. Litt *et al.* Measurement of the ratio of the proton form factors, G_E/G_M, at high momentum transfers and the question of scaling. *Physics Letters B*, 31(1):40 – 44, 1970.

[33] L. E. Price *et al.* Backward-angle electron-proton elastic scattering and proton electromagnetic form-factors. *Phys. Rev. D*, 4:45–53, 1971.

[34] Ch. Berger *et al.* Electromagnetic form factors of the proton at squared four-momentum transfers between 10 and 50 fm^{-2}. *Physics Letters B*, 35(1):87 – 89, 1971.

[35] W. Bartel *et al.* Measurement of proton and neutron electromagnetic form factors at squared four-momentum transfers up to 3 $(\mathrm{GeV/c})^2$. *Nuclear Physics B*, 58(2): 429 – 475, 1973.

[36] K. M. Hanson *et al.* Large-angle quasielastic electron-deuteron scattering. *Phys. Rev. D*, 8:753–778, 1973.

[37] F. Borkowski, G. G. Simon, V.H. Walther, and R.D. Wendling. Electromagnetic form factors of the peoton at low four-momentum transfer (ii). *Nuclear Physics B*, 93(3):461 – 478, 1975.

[38] G. G. Simon, Ch. Schmitt, F. Borkowski, and V.H. Walther. Absolute electron-proton cross sections at low momentum transfer measured with a high pressure gas target system. *Nuclear Physics A*, 333(3):381 – 391, 1980.

[39] L. Andivahis *et al.* Measurements of the electric and magnetic form factors of the proton from q^2=1.75 to 8.83 $(\mathrm{GeV/c})^2$. *Phys. Rev. D*, 50:5491–5517, 1994.

[40] R. C. Walker *et al.* Measurements of the proton elastic form factors for $1 \leq Q^2 \leq 3$ $(\mathrm{GeV}/c)^2$ at SLAC. *Phys. Rev. D*, 49:5671–5689, 1994.

[41] M. E. Christy *et al.* Measurements of electron-proton elastic cross sections for $0.4 < Q^2 < 5.5$ $(\mathrm{GeV}/c)^2$. *Phys. Rev. C*, 70:015206, 2004.

[42] I. A. Qattan *et al.* Precision rosenbluth measurement of the proton elastic form factors. *Phys. Rev. Lett.*, 94:142301, 2005.

[43] D. H. Coward *et al.* Electron-proton elastic scattering at high momentum transfers. *Phys. Rev. Lett.*, 20:292–295, 1968.

[44] T. Janssens, R. Hofstadter, E. B. Hughes, and M. R. Yearian. Proton form factors from elastic electron-proton scattering. *Phys. Rev.*, 142:922–931, 1966.

[45] A. I. Akhiezer and M. P. Rekalo. Polarization phenomena in electron scattering by protons in the high energy region. *Sov. Phys. Dokl.*, 13:572, 1968.

[46] A. I. Akhiezer and M. P. Rekalo. Polarization effects in the scattering of leptons by hadrons. *Sov. J. Part. Nucl.*, 4:277, 1974.

[47] M. K. *et al.* G_{E_p}/G_{M_p} ratio by polarization transfer in $\vec{e}\ p \rightarrow e\ \vec{p}$. *Phys. Rev. Lett.*, 84:1398–1402, 2000.

[48] V. Punjabi *et al.* Proton elastic form factor ratios to $Q^2 = 3.5$ GeV^2 by polarization transfer. *Phys. Rev. C*, 71:055202, 2005.

[49] A. J. R. Puckett *et al.* Final analysis of proton form factor ratio data at $Q^2 = 4.0$, 4.8, and 5.6 GeV^2. *Phys. Rev. C*, 85:045203, 2012.

[50] A. J. R. Puckett *et al.* Recoil polarization measurements of the proton electromagnetic form factor ratio to $Q^2 = 8.5$ GeV^2. *Phys. Rev. Lett.*, 104:242301, 2010.

[51] M. Meziane *et al.* Search for effects beyond the born approximation in polarization transfer observables in $\vec{e}\ p$ elastic scattering. *Phys. Rev. Lett.*, 106:132501, 2011.

[52] M. Paolone *et al.* Polarization transfer in the $^4\mathrm{He}(\vec{e}, e'\ \vec{p})^3\mathbf{H}$ reaction at $Q^2 = 0.8$ and 1.3 $(\mathrm{GeV}/c)^2$. *Phys. Rev. Lett.*, 105:072001, 2010.

[53] G. Ron *et al.* Measurements of the proton elastic-form-factor ratio $\mu_p G_E^p/G_M^p$ at low momentum transfer. *Phys. Rev. Lett.*, 99:202002, 2007.

[54] B. Hu *et al.* Polarization transfer in the $^2\mathrm{H}(\vec{e}, e'\ \vec{p})n$ reaction up to $Q^2 = 1.61$ $(\mathrm{GeV}/c)^2$. *Phys. Rev. C*, 73:064004, 2006.

[55] G. MacLachlan *et al.* The ratio of proton electromagnetic form factors via recoil polarimetry at $q^2 = 1.13$ $(\mathrm{GeV/c}^2)$. *Nuclear Physics A*, 764:261–273, 2006.

[56] S. Strauch *et al.* Polarization transfer in the $^4\mathrm{He}(\vec{e}, e'\ \vec{p})^3\mathrm{H}$ reaction up to $Q^2 = 2.6$ $(\mathrm{GeV}/c)^2$. *Phys. Rev. Lett.*, 91:052301, 2003.

[57] O. Gayou *et al.* Measurement of G_{E_p}/G_{M_p} in $\overrightarrow{e}\ p \rightarrow e\ \overrightarrow{p}$ to $Q^2 = 5.6$ GeV^2. *Phys. Rev. Lett.*, 88:092301, 2002.

[58] O. Gayou *et al.* Measurements of the elastic electromagnetic form factor ratio $\mu_p G_{\rm ep}/G_{\rm mp}$ via polarization transfer. *Phys. Rev. C*, 64:038202, 2001.

[59] S. Dieterich *et al.* Polarization transfer in the 4he$(\overrightarrow{e}, e'\overrightarrow{p})$3h reaction. *Physics Letters B*, 500(1):47–52, 2001.

[60] Th. Pospischil *et al.* Measurement of $G_E, p/G_M, p$ via polarization transfer at $Q^2 = 0.4$ GeV/c^2. *Eur. Phys. J. A*, 12:125–127, 2001.

[61] B. Milbrath *et al.* Comparison of polarization observables in electron scattering from the proton and deuteron. *Phys. Rev. Lett.*, 80:452–455, 1998.

[62] A. J. R. Puckett *et al.* Polarization transfer observables in elastic electron-proton scattering at $Q^2 = 2.5$, 5.2, 6.8, and 8.5 GeV^2. *Phys. Rev. C*, 96:055203, 2017.

[63] M. K. Jones *et al.* Proton G_E/G_M from beam-target asymmetry. *Phys. Rev. C*, 74:035201, 2006.

[64] C. B. Crawford *et al.* Measurement of the proton's electric to magnetic form factor ratio from $^1\overrightarrow{\rm H}\ (\overrightarrow{e}, e'p)$. *Phys. Rev. Lett.*, 98:052301, 2007.

[65] A. Liyanage *et al.* Proton form factor ratio $\mu_p G_E^p/G_M^p$ from double spin asymmetry. *Phys. Rev. C*, 101:035206, 2020.

[66] B. Delcourt *et al.* Study of the reaction $e^+e^- \rightarrow p\bar{p}$ in the total energy range 1925-2180 MeV. *Physics Letters B*, 86(3):395 – 398, 1979.

[67] D. Bisello *et al.* A measurement of $e^+e^- \rightarrow p\bar{p}$ for $(1975 \leq {\rm s} \leq 2250)$ mev. *Nuclear Physics B*, 224(3):379 – 395, 1983.

[68] D. Bisello *et al.* Baryon pair production in $e^+\ e^-$ annihilation at $\sqrt{S} = 2.4$-GeV. *Z. Phys. C*, 48:23–28, 1990.

[69] M. Castellano *et al.* The reaction $e^+e^- \rightarrow p\bar{p}$ at a total energy of 2.1 GeV. *Nuovo Cim. A*, 14:1–20, 1973.

[70] A. Antonelli *et al.* First measurement of the neutron electromagnetic form factor in the time-like region. *Physics Letters B*, 313(1):283 – 287, 1993.

[71] A. Antonelli *et al.* Measurement of the electromagnetic form factor of the proton in the time-like region. *Physics Letters B*, 334(3):431 – 434, 1994.

[72] A. Antonelli *et al.* The first measurement of the neutron electromagnetic form factors in the time-like region. *Nuclear Physics B*, 517(1):3 – 35, 1998.

[73] M. Ablikim *et al.* Measurement of the cross section for $e^+e^- \to p\bar{p}$ at center-of-mass energies from 2.0 to 3.07 GeV. *Physics Letters B*, 630(1):14 – 20, 2005.

[74] T. K. Pedlar *et al.* Precision measurements of the timelike electromagnetic form factors of pion, kaon, and proton. *Phys. Rev. Lett.*, 95:261803, 2005.

[75] R. R. Akhmetshin *et al.* Study of the process $e^+e^- \to p\bar{p}$ in the c.m. energy range from threshold to 2 GeV with the CMD-3 detector. *Physics Letters B*, 759:634 – 640, 2016.

[76] G. Bassompierre *et al.* First Determination of the Proton Electromagnetic Form-Factors at the Threshold of the Timelike Region. *Phys. Lett. B*, 68:477–479, 1977.

[77] G. Bardin *et al.* Measurement of the proton electromagnetic form factor near threshold in the time-like region. *Physics Letters B*, 255(1):149 – 154, 1991.

[78] G. Bardin *et al.* Precise determination of the electromagnetic form factor of the proton in the time-like region up to s = 4.2 GeV^2. *Physics Letters B*, 257(3):514 – 518, 1991.

[79] G. Bardin *et al.* Determination of the electric and magnetic form factors of the proton in the time-like region. *Nuclear Physics B*, 411(1):3 – 32, 1994.

[80] T. A. Armstrong *et al.* Proton electromagnetic form factors in the timelike region from 8.9 to 13.0 gev^2. *Phys. Rev. Lett.*, 70:1212–1215, 1993.

[81] M. Ambrogiani *et al.* Measurements of the magnetic form factor of the proton in the timelike region at large momentum transfer. *Phys. Rev. D*, 60:032002, 1999.

[82] M. Andreotti *et al.* Measurements of the magnetic form factor of the proton for timelike momentum transfers. *Physics Letters B*, 559(1):20 – 25, 2003.

[83] M. Ablikim *et al.* Measurement of the proton form factor by studying $e^+e^- \to p\bar{p}$. *Phys. Rev. D*, 91:112004, 2015.

[84] J. P. Lees *et al.* Study of $e^+e^- \to p\bar{p}$ via initial-state radiation at BABAR. *Phys. Rev. D*, 87:092005, 2013.

[85] M. Ablikim *et al.* Study of the process $e^+e^- \to p\bar{p}$ via initial state radiation at BESIII. *Phys. Rev. D*, 99(9):092002, 2019.

[86] J. P. Lees *et al.* Measurement of the $e^+e^- \to p\bar{p}$ cross section in the energy range from 3.0 to 6.5 GeV. *Phys. Rev. D*, 88(7):072009, 2013.

[87] J. R. Dunning *et al.* Quasi-elastic electron-deuteron scattering and neutron form factors. *Phys. Rev.*, 141:1286–1297, 1966.

[88] E. Tomasi-Gustafsson and M. P. Rekalo. Search for evidence of asymptotic regime of nucleon electromagnetic form factors from a compared analysis in space- and time-like regions. *Physics Letters B*, 504(4):291 – 295, 2001.

[89] T. Massam and A. Zichichi. A one-paramenter fit to the electromagnetic form factors of the nucleon. *Nuovo Cimento A*, 43:1137–1148, 1966.

[90] F. Iachello, A. D. Jackson, and A. Lande. Semi-phenomenological fits to nucleon electromagnetic form factors. *Physics Letters B*, 43(3):191 – 196, 1973.

[91] M. Gari and W. Krümpelmann. Semiphenomenological Synthesis of Meson and Quark Dynamics and the Electromagnetic Structure of the Nucleon. *Z. Phys. A*, 322:689–693, 1985.

[92] M. Gari and W. Krümpelmann. The electromagnetic form factor of the neutron. *Physics Letters B*, 173(1):10 – 14, 1986.

[93] M. F. Gari and W. Krümpelmann. The electric neutron form factor and the strange quark content of the nucleon. *Physics Letters B*, 274(2):159 – 162, 1992.

[94] E. L. Lomon *et al.* Extended Gari-Krümpelmann model fits to nucleon electromagnetic form factors. *Phys. Rev. C*, 64:035204, 2001.

[95] E. L. Lomon. Effect of recent R_p and R_n measurements on extended Gari-Krümpelmann model fits to nucleon electromagnetic form factors. *Phys. Rev. C*, 66:045501, 2002.

[96] E. L. Lomon. Effect of revised R(n) measurements on extended Gari-Krumpelmann model fits to nucleon electromagnetic form factors. 2006.

[97] E. L. Lomon and S. Pacetti. Erratum: Timelike and spacelike electromagnetic form factors of nucleons, a unified description [phys. rev. d 85, 113004 (2012)]. *Phys. Rev. D*, 86:039901, 2012.

[98] S. Rock *et al.* Measurement of elastic electron-neutron scattering and inelastic electron-deuteron scattering cross sections at high momentum transfer. *Phys. Rev. D*, 46:24–44, 1992.

[99] A. Lung *et al.* Measurements of the electric and magnetic form factors of the neutron from q^2=1.75 to 4.00 $(\mathrm{GeV/c})^2$. *Phys. Rev. Lett.*, 70:718–721, 1993.

[100] P. Markowitz *et al.* Measurement of the magnetic form factor of the neutron. *Phys. Rev. C*, 48:R5–R9, 1993.

[101] H. Anklin *et al.* Precision measurement of the neutron magnetic form factor. *Physics Letters B*, 336(3):313 – 318, 1994.

[102] H. Gao *et al.* Measurement of the neutron magnetic form factor from inclusive quasielastic scattering of polarized electrons from polarized ^{3}He. *Phys. Rev. C*, 50: R546–R549, 1994.

[103] E. E. W. Bruins *et al.* Measurement of the neutron magnetic form factor. *Phys. Rev. Lett.*, 75:21–24, 1995.

[104] H. Anklin *et al.* Precise measurements of the neutron magnetic form factor. *Physics Letters B*, 428(3):248 – 253, 1998.

[105] G. Kubon *et al.* Precise neutron magnetic form factors. *Physics Letters B*, 524 (1):26 – 32, 2002.

[106] W. K. Brooks and J. D. Lachniet. Precise determination of the neutron magnetic form factor to higher Q^2. *Nuclear Physics A*, 755:261 – 264, 2005.

[107] B. Anderson *et al.* Extraction of the neutron magnetic form factor from quasielastic $^3\vec{\mathrm{He}}(\vec{e},e')$ at $Q^2 = 0.1{-}0.6(\mathrm{GeV}/c)^2$. *Phys. Rev. C*, 75:034003, 2007.

[108] D. I. Glazier *et al.* Measurement of the electric form factor of the neutron at Q^2 = 0.3-0.8 $(\mathrm{GeV/c})^2$. *Eur. Phys. J. A*, 24:101–109, 2005.

[109] C. Herberg *et al.* Determination of the neutron electric form-factor in the D(e,e' n)p reaction and the influence of nuclear binding. *Eur. Phys. J. A*, 5:131–135, 1999.

[110] J. Becker *et al.* Determination of the neutron electric form-factor from the reaction He-3(e,e' n) at medium momentum transfer. *Eur. Phys. J. A*, 6:329–344, 1999.

[111] M. Meyerhoff *et al.* First measurement of the electric formfactor of the neutron in the exclusive quasielastic scattering of polarized electrons from polarized ^{3}He. *Physics Letters B*, 327(3):201 – 207, 1994.

[112] T. Eden *et al.* Electric form factor of the neutron from the $^2\mathrm{H}(\mathrm{e}\rightarrow,e'\mathrm{n}\rightarrow)^1\mathrm{H}$ reaction at q^2=0.255 $(\mathrm{gev/c})^2$. *Phys. Rev. C*, 50:R1749–R1753, 1994.

[113] J. Golak *et al.* Extraction of electromagnetic neutron form factors through inclusive and exclusive polarized electron scattering on a polarized ^{3}He target. *Phys. Rev. C*, 63:034006, 2001.

[114] R. Schiavilla *et al.* Neutron charge form factor at large q^2. *Phys. Rev. C*, 64: 041002, 2001.

[115] I. Passchier *et al.* Charge form factor of the neutron from the reaction $^2\vec{H}\,(\vec{e}\,,e'n)p$. *Phys. Rev. Lett.*, 82:4988–4991, 1999.

[116] M. Ostrick *et al.* Measurement of the neutron electric form factor $G_{E,n}$ in the quasifree $^2H(\vec{e}, e' \vec{n})p$ reaction. *Phys. Rev. Lett.*, 83:276–279, 1999.

[117] M. N. Achasov *et al.* Recent results from snd experiment at VEPP-2000 collider. *EPJ Web of Conferences*, 37:09020, 2012.

[118] S. J. Brodsky and G. R. Farrar. Scaling laws for large-momentum-transfer processes. *Phys. Rev. D*, 11:1309–1330, 1975.

[119] S. J. Brodsky and G. R. Farrar. Scaling laws at large transverse momentum. *Phys. Rev. Lett.*, 31:1153–1156, 1973.

[120] P. L. Chung and F. Coester. Relativistic constituent-quark model of nucleon form factors. *Phys. Rev. D*, 44:229–241, 1991.

[121] M. R. Frank, B. K. Jennings, and G. A. Miller. Role of color neutrality in nuclear physics: Modifications of nucleonic wave functions. *Phys. Rev. C*, 54:920–935, 1996.

[122] F. Cardarelli, E. Pace, G. Salmè, and S. Simula. Nucleon and pion electromagnetic form factors in a light-front constituent quark model. *Physics Letters B*, 357(3): 267 – 272, 1995.

[123] F. Cardarelli and S. Simula. Su(6) breaking effects in the nucleon elastic electromagnetic form factors. *Phys. Rev. C*, 62:065201, 2000.

[124] S. Boffi *et al.* Covariant electroweak nucleon form-factors in a chiral constituent quark model. *Eur. Phys. J. A*, 14:17–21, 2002.

[125] F. Gross and P. Agbakpe. Shape of the nucleon. *Phys. Rev. C*, 73:015203, 2006.

[126] O. Gayou *et al.* Measurement of G_{E_p}/G_{M_p} in $\vec{e}\ p \to e\ \vec{p}$ to $Q^2 = 5.6$ GeV^2. *Phys. Rev. Lett.*, 88:092301, 2002.

[127] J. P. B. C. de Melo, T. Frederico, E. Pace, S. Pisano, and G. Salmè. Timelike and spacelike nucleon electromagnetic form factors beyond relativistic constituent quark models. *Physics Letters B*, 671(1):153 – 157, 2009.

[128] A. Denig and G. Salme. Nucleon Electromagnetic Form Factors in the Timelike Region. *Prog. Part. Nucl. Phys.*, 68:113–157, 2013.

[129] S. Boinepalli *et al.* Precision electromagnetic structure of octet baryons in the chiral regime. *Phys. Rev. D*, 74:093005, 2006.

[130] C. Alexandrou, G. Koutsou, J. W. Negele, and A. A. Tsapalis. Nucleon electromagnetic form factors from lattice QCD. *Phys. Rev. D*, 74:034508, 2006.

[131] N. Kivel and M. Vanderhaeghen. Soft spectator scattering in the nucleon form factors at large Q^2 within the SCET approach. *Phys. Rev. D*, 83:093005, 2011.

[132] G. P. Lepage and S. J. Brodsky. Exclusive processes in quantum chromodynamics: Evolution equations for hadronic wavefunctions and the form factors of mesons. *Physics Letters B*, 87(4):359 – 365, 1979.

[133] V. L. Chernyak and A. R. Zhitnitsky. Asymptotic behaviour of exclusive processes in QCD. *Physics Reports*, 112(3):173 – 318, 1984.

[134] N. Kivel. Factorizing the hard and soft spectator scattering contributions for the nucleon form factor F_1 at large Q^2. *Eur. Phys. J. A*, 48:156, 2012.

[135] N. Kivel and M. Vanderhaeghen. Description of the spacelike and timelike proton form factors at large momentum transfer in the QCD factorization approach. *Prog. Part. Nucl. Phys.*, 67:491–495, 2012.

[136] C. C. Kuo *et al.* Measurement of $\gamma\gamma \to p\bar{p}$ production at Belle. *Physics Letters B*, 621(1):41 – 55, 2005.

[137] M. Ablikim *et al.* Design and construction of the BESIII detector. *Nuclear Instruments and Methods in Physics Research Section A: Accelerators, Spectrometers, Detectors and Associated Equipment*, 614(3):345 – 399, 2010.

[138] Shou-Xian Fang and Sen-Yu Chen. The Beijing Electron Positron Collider. *Part. Accel.*, 26:51–61, 1990.

[139] J. Z. Bai *et al.* The BES detector. *Nucl. Instrum. Meth. A*, 344:319–334, 1994.

[140] F. A. Harris. BEPCII and BESIII. *Nuclear Physics B - Proceedings Supplements*, 162:345 – 350, 2006.

[141] J. Q. Wang and C. Zhang. The Beijing Electron-positron Collider and its Second Phase Construction. In *9th European Particle Accelerator Conference (EPAC 2004)*, 2004.

[142] C. Zhang, L. Ma, G. Pei, and J. Wang. Construction and Commissioning of BEPCII. In *Particle Accelerator Conference (PAC 09)*, page MO3RAI03, 2010.

[143] Webpage of the institute for high energy physics in beijing, . URL http://english.ihep.cas.cn/bes/doc/2124.html.

[144] M. Ablikim *et al.* The construction of the BESIII experiment. *Nuclear Instruments and Methods in Physics Research Section A: Accelerators, Spectrometers, Detectors and Associated Equipment*, 598(1):7 – 11, 2009.

[145] Y. Zhang *et al.* The reconstruction and calibration of the BESIII Main Drift Chamber. In *Computing in High Energy and Nuclear Physics*, 2007.

[146] S. Agostinelli *et al.* Geant4 — a simulation toolkit. *Nuclear Instruments and Methods in Physics Research Section A: Accelerators, Spectrometers, Detectors and Associated Equipment*, 506(3):250 – 303, 2003.

[147] D. M. Asner *et al.* Physics at BES-III, 2008.

[148] S. Yang *et al.* Test of high time resolution MRPC with different readout modes for the BESIII upgrade. *Nuclear Instruments and Methods in Physics Research Section A: Accelerators, Spectrometers, Detectors and Associated Equipment*, 763: 190 – 196, 2014.

[149] Y. Liu *et al.* A GEANT4-based simulation model for the BESIII endcap time-of-flight system. *Nuclear Instruments and Methods in Physics Research Section A: Accelerators, Spectrometers, Detectors and Associated Equipment*, 629(1):87 – 92, 2011.

[150] Shu-Jun Wei *et al.* Introduction to BESIII EMC sub-trigger system. *Nuclear Instruments and Methods in Physics Research Section A: Accelerators, Spectrometers, Detectors and Associated Equipment*, 598(1):323 – 327, 2009.

[151] M. *et al.* Ablikim. Determination of the number of J/ψ events with inclusive J/ψ decays. *Chinese Physics C*, 41, 2016.

[152] Webpage of the BESIII experiment. URL http://bes3.ihep.ac.cn.

[153] M. *et al.* Ablikim. Determination of the number of $\psi(3686)$ events at BESIII. *Chin. Phys. C*, 42(2):023001, 2018.

[154] M. *et al.* Ablikim. Measurement of the integrated luminosities of the data taken by BESIII at $\sqrt{s} = 3.650$ and 3.773 GeV. *Chinese Physics C*, 37(12):123001, 2013.

[155] M. *et al.* Ablikim. Precision measurement of the integrated luminosity of the data taken by BESIII at center-of-mass energies between 3.810 GeV and 4.600 GeV. *Chinese Physics C*, 39(9):093001, 2015.

[156] M. *et al.* Ablikim. Luminosity measurements for the R scan experiment at BESIII. *Chin. Phys. C*, 41(6):063001, 2017.

[157] B.X. Zhang and H.M. Hu. Luminosity measurement for the new R-QCD data, 2015. BESIII collaboration meeting.

[158] M. *et al.* Ablikim. Future physics programme of BESIII. *Chinese Physics C*, 44 (4):040001, 2020.

[159] M. Ablikim *et al.* New features in the electromagnetic structure of the neutron. Accepted by Nature Physics, in print.

[160] P. Larin. *Measurement of the Timelike Electromagnetic Form Factors of the Neutron at the BESIII Experiment with the Process* $e^+e^- \to \bar{n}n$. PhD thesis, Johannes Gutenberg University Mainz, 2020.

[161] S. Ahmed. *Measurement of the cross section of the process* $e^+e^- \to \bar{n}n$ *and the extraction of the time-like electromagnetic form factors of the neutron at the Beijing Spectrometer III* . PhD thesis, Johannes Gutenberg University Mainz, 2020.

[162] M. Ablikim *et al.* Complete measurement of the Λ electromagnetic form factors. *Phys. Rev. Lett.*, 123:122003, 2019.

[163] M. Ablikim *et al.* Measurement of integrated luminosity and center-of-mass energy of data taken by BESIII at $\sqrt{s} = 2.125$ gev. *Chinese Physics C*, 41(11):113001, 2017.

[164] Y. Sun *et al.* BESIII offline software system and performance test. *Nuclear Electronics and Detection Technology*, 27:842–846, 2007.

[165] W. Li *et al.* The offline software for the BESIII experiment. In *Computing in High Energy and Nuclear Physics*, 2006.

[166] C. Arnault. CMT: A software configuration management tool. In *11th International Conference on Computing in High-Energy and Nuclear Physics*, pages 692–695, 2000.

[167] G. Barrand *et al.* GAUDI — A software architecture and framework for building HEP data processing applications. *Computer Physics Communications*, 140(1):45 – 55, 2001.

[168] Webpage of geometry description markup language gdml. URL http://gdml.web.cern.ch/GDML/.

[169] Webpage of glast. URL http://www-glast.slac.stanford.edu/software/calib/.

[170] Webpage of root. URL https://root.cern/.

[171] S. Jadach, B. Ward, and Z. Was. The precision monte carlo event generator KK for two-fermion final states in e^+e^- collisions. *Computer Physics Communications*, 130(3):260–325, 2000.

[172] Ping Rong-Gang. Event generators at BESIII. *Chinese Physics C*, 32(8):599–602, 2008.

[173] P. Golonka and Z. Was. PHOTOS monte carlo: a precision tool for QED correctionsin Z and W decays. *The European Physical Journal C*, 45(1):97–107, 2006.

[174] E. Barberio and Z. Was. PHOTOS - a universal Monte Carlo for QED radiative corrections: version 2.0. *Computer Physics Communications*, 79(2):291 – 308, 1994.

[175] A. Ryd *et al.* EvtGen: A Monte Carlo Generator for B-Physics. 2005.

[176] T. Sjöstrand. The Pythia event generator: Past, present and future. *Computer Physics Communications*, 246:106910, 2020.

[177] C.M. Carloni Calame, G. Montagna, O. Nicrosini, and F. Piccinini. The BABAYAGA event generator. *Nuclear Physics B - Proceedings Supplements*, 131: 48 – 55, 2004.

[178] G. Balossini *et al.* Photon pair production at flavour factories with per mille accuracy. *Phys. Lett. B*, 663:209–213, 2008.

[179] G. Balossini *et al.* Matching perturbative and parton shower corrections to Bhabha process at flavour factories. *Nuclear Physics B*, 758(1-2):227–253, 2006.

[180] H. Czyz, M. Gunia, and J. H. Kühn. Simulation of electron-positron annihilation into hadrons with the event generator PHOKHARA. *Journal of High Energy Physics*, 2013(8), 2013.

[181] R. Ping *et al.* Tuning and validation of hadronic event generator for r value measurements in the tau-charm region. *Chinese Physics C*, 40, 2016. doi: 10.1088/1674-1137/40/11/113002.

[182] D. Lin. *Measurement of proton electromagnetic form factors using the initial-state-radiation process $e^+e^- \to p\bar{p}\gamma$ at BESIII.* PhD thesis, Johannes Gutenberg University Mainz, 2017.

[183] M. Ablikim *et al.* Measurement of $e^+e^- \to K^+K^-$ cross section at $\sqrt{s} = 2.00 - 3.08$ GeV. *Phys. Rev. D*, 99:032001, 2019.

[184] H. Czyz, J. H. Kühn, and S. Tracz. Nucleon form factors and final state radiative corrections to $e^+e^- \to \bar{p}p\gamma$. *Physical Review D*, 90(11), 2014.

[185] E. Tomasi-Gustafsson and M. P. Rekalo. Search for evidence of asymptotic regime of nucleon electromagnetic form factors from a compared analysis in space- and time-like regions. *Physics Letters B*, 504(4):291 – 295, 2001.

[186] A. Bianconi and E. Tomasi-Gustafsson. Periodic interference structures in the timelike proton form factor. *Phys. Rev. Lett.*, 114:232301, 2015.

[187] A. Bianconi and E. Tomasi-Gustafsson. Phenomenological analysis of near-threshold periodic modulations of the proton timelike form factor. *Phys. Rev. C*, 93:035201, 2016.

[188] I. T. Lorenz, H.-W Hammer, and Ulf-G. Meißner. New structures in the proton-antiproton system. *Phys. Rev. D*, 92:034018, 2015.

[189] D. V. Shirkov and I. L. Solovtsov. Analytic model for the QCD running coupling with universal $\overline{\alpha}_s(0)$ value. *Phys. Rev. Lett.*, 79:1209–1212, 1997.

[190] F. Iachello and Q. Wan. Structure of the nucleon from electromagnetic timelike form factors. *Phys. Rev. C*, 69:055204, 2004. doi: 10.1103/PhysRevC.69.055204.

[191] R. Bijker and F. Iachello. Reanalysis of the nucleon spacelike and timelike electromagnetic form factors in a two-component model. *Phys. Rev. C*, 69:068201, 2004.

[192] R. Bijker and F. Iachello. Reanalysis of the nucleon spacelike and timelike electromagnetic form factors in a two-component model. *Phys. Rev. C*, 69:068201, 2004.

[193] E. Tomasi-Gustafsson, A. Bianconi, and S. Pacetti. New fit of time-like proton electromagnetic form factors from e^+e^- colliders, 2021. URL https://arxiv.org/abs/2012.14656.